UNIVERSITÉ DE SHERBROOKE
Faculté de génie
Département de génie civil

SHEAR AND FLEXURAL BEHAVIOR OF LIGHTWEIGHT SELF-CONSOLIDATING CONCRETE BEAMS REINFORCED WITH GLASS- AND BASALT-FRP BARS

COMPORTEMENT À L'EFFORT TRANCHANT ET À LA FLEXION DE POUTRES EN BÉTON AUTOPLAÇANT LÉGER ARMÉ D'ARMATURE EN PRF DE FIBRES DE VERRE ET DE BASALTE

Thèse de doctorat
Spécialité : génie civil

Shehab Abdelghafar Abdelhakim MEHANY

A dissertation submitted in partial fulfilment
of the requirements for the degree of
Doctor of Philosophy
(Civil Engineering)

Sherbrooke (Québec) Canada **December 2021**

JURY MEMBERS

Prof. Brahim BENMOKRANE

Directeur de recherche/Supervisor

Prof. Sébastien LANGLOIS

Rapporteur/Examiner

Prof. Adel EL-SAFTY

Examinateur externe/External Examiner

Prof. P. VIJAY

Examinateur externe/External Examiner

DEDICATION

In the name of Allah, the most merciful, the most compassionate

This thesis work is dedicated to my parents who have always loved me unconditionally

To my brothers

To my beloved wife and my daughter who sacrifice everything for the succession of this work

To those who work hard to make the world a better place to live in

Abstract

Lightweight self-consolidating concrete (LWSCC) is being more and more widely used in different types of reinforced concrete (RC) structures due to its better structural and durability performance. No research, however, seems to have investigated LWSCC beams reinforced with fiber-reinforced polymer (FRP) bars under shear and flexural loads. In addition, present guidelines for FRP structures in North-America (ACI 440.1R-15, CSA S806-12, and CSA S6-19) do not provide guidance for LWSCC beams reinforced with FRP bars. This research takes charge of providing experimental database as well as extensive analyses and design recommendations of LWSCC beams reinforced with different FRP bars.

The experimental tests were completed through two phases. The first phase was conducted to investigate the behavior and concrete shear strength of FRP-reinforced LWSCC beams. 14 full-scale RC beams were tested up to failure. The second phase included testing of 20 full-scale RC beams to investigate the flexural behavior and serviceability performance of FRP bars in LWSCC beams. The experimental results are discussed in terms of cracking behavior, deflection, flexural capacity, concrete shear strength, and mode of failure. The findings of this study indicated that the adoption of LWSCC allowed for decreasing the self-weight of the RC beams (density of 1,800 kg/m^3) compared to normal weight concrete (NWC). By comparing the concrete shear strengths of the LWSCC beams with their predicted strengths based on a concrete density reduction factor (λ) of 0.75 and 0.8 in the CSA S806-12 and ACI 440.1R-15 design equations, respectively, revealed that these equations yielded good predictions of LWSCC beams reinforced with FRP bars compared to the NWC beams. In the second phase, the test results indicated that the experimental moment capacities of the LWSCC beams were in good agreement with the predictions based on design standards with an average accuracy of ≥ 90%. In addition, the predicted crack width values for LWSCC beams reinforced with FRP, using the bond-dependent coefficient (k_b) values recommended by the standards, were overestimated in most cases. Thus, new values for k_b have been suggested for FRP bars when used in LWSCC members. The measured deflections and the experimental values of the effective moment of inertia (I_e) were analyzed and compared with those predicted using the available models.

Keywords: Lightweight self-consolidating concrete; GFRP and BFRP bars; beams; shear; flexure; ultimate capacity, crack patterns, concrete density reduction factor; Deflection and crack width; Bond-dependent coefficient; FRP design codes.

Résumé

Le béton autoplaçant (BAP) léger est de plus en plus utilisé dans différents types de structures en béton armé en raison de ses meilleures performances structurelles et de durabilité. L'utilisation de barres d'armature en polymère renforcé de fibres (PRF) non corrosives en remplacement des barres d'acier traditionnelles dans les éléments en béton a gagné la confiance et l'acceptation dans le domaine de la construction. Aucune recherche, cependant, ne semble avoir étudié les poutres en BAP léger renforcées avec des barres de PRF sous des charges de cisaillement et de flexion. De plus, les normes de conception actuelles pour les structures en béton armé de barres d'armature en PRF en Amérique du Nord (ACI 440.1R-15, CSA S806-12 et CSA S6-19) ne fournissent pas de directives pour les poutres en BAP léger armé avec des barres en PRF. Cette recherche se charge de fournir une base de données expérimentale ainsi que des analyses approfondies et des recommandations de conception des poutres en BAP léger armé avec différentes barres en PRF.

Les tests expérimentaux se sont déroulés en deux phases. La première phase a été menée pour étudier les effets de différents paramètres sur le comportement et la résistance à l'effort tranchant des poutres en BAP léger armé de barres en PRF. Quatorze (14) poutres en béton armé grandeur nature ont été testées à l'effort tranchant. La deuxième phase a été conçue et préparée pour étudier le comportement en flexion et les performances de service des barres en PRF dans des poutres BAP léger. Vingt (20) poutres en béton armé grandeur nature ont été fabriquées et testées sous des charges de flexion. Les résultats expérimentaux sont discutés en termes de comportement à la fissuration, de flèche, de résistance à la flexion, de résistance à l'effort tranchant et du mode de rupture. Les résultats de cette étude ont indiqué que l'adoption du BAP léger a permis de diminuer le poids propre des poutres en béton (densité de 1 800 kg/m^3) par rapport au béton normal (BN). Dans la première phase de cette thèse de doctorat, une étude théorique a été menée pour évaluer la précision des équations de calcul à l'effort tranchant poutres en BAP léger armé de PRF. Cette étude a démontré que les poutres en BAP léger armé de PRF peuvent être conçues à condition qu'un facteur de réduction de densité du béton approprié (λ) soit appliqué. L'utilisation d'un facteur de réduction de 0,75 et 0,8 dans les équations du CSA S806-12 et de l'ACI 440.1R-15, respectivement, pour considérer l'influence de la densité du béton a donné une bonne prédiction similaire à celle obtenue pour des poutres en BN armé de PRF. Dans la deuxième phase, les résultats des essais sur poutres en BAP léger armé de PRF a montré que les résistances en flexion des poutres en BAP léger en BN étaient en bon accord avec

les prédictions basées sur les équations des normes de conception avec une précision moyenne ≥ 90 %. De plus, les valeurs de largeur de fissure prédites pour les poutres en BAP léger armé de PRF, en utilisant les valeurs de coefficient d'adhérence (k_b) recommandées par les normes, ont été surestimées dans la plupart des cas comparativement aux valeurs expérimentales obtenues. Par conséquent, de nouvelles valeurs pour kb ont été suggérées pour les barres en PRFV et PRFB lorsque utilisées dans des structures en BAP léger. Enfin, les flèches mesurées et les valeurs expérimentales du moment d'inertie effectif (I_e) ont été analysées et comparées à celles prédites à l'aide des modèles disponibles.

Mots-clés : Béton léger autoplaçant (BAP) ; Barres d'armature en PRFV et PRFB ; poutres ; cisaillement/effort tranchant ; flexion ; capacité ultime, modèles de fissures, facteur de réduction de la densité du béton ; flèche et largeur de fissure ; coefficient dépendant de l'adhérence ; Codes de conception sur les PRF.

Bibliography

During the research work at the University of Sherbrooke, the candidate has participated in the following publications as a first author:

Journal Papers:

1. **Mehany, S.**, Mohamed, H. M., and Benmokrane, B. (2021). "Contribution of Lightweight Self-Consolidated Concrete (LWSCC) to Shear Strength of Beams Reinforced with Basalt FRP Bars." Engineering Structures, 231, 111758. DOI: 10.1016/j.engstruct.2020.111758.
2. **Mehany, S.**, Mohamed, H. M., and Benmokrane, B. (2021). "Performance of LWSCC Beams Reinforced with GFRP Bars without Stirrups under Shear." *ACI Struct. J., In Press.*
3. **Mehany, S.**, Mohamed, H. M., and Benmokrane, B. (2021). "Flexural Behavior and Serviceability Performance of LWSCC Beams Reinforced with BFRP Bars." *ACI Struct. J., In Press.*
4. **Mehany, S.**, Mohamed, H. M., and Benmokrane, B. (2021). "Flexural Strength and Serviceability of GFRP-Reinforced Lightweight Self-Consolidating Concrete Beams." J. Comp Constr., ASCE (Under review).
5. **Mehany, S.**, Mohamed, H. M., Adel El-Safty, and Benmokrane, B. (2021). "Bond-Dependent Coefficient and Cracking Behavior of Lightweight Self-Consolidating Concrete (LWSCC) Beams Reinforced with Glass- and Basalt-FRP Bars." *J. Constr. & Build. Mat.,* Elsevier (Under review).

Refereed Conferences Publications:

6. **Mehany, S.**, Mohamed, H. M., and Benmokrane, B. (2019). "Strength and Behavior of HSC Concrete Beams Reinforced with Sand-coated Basalt FRP Bars" Proc. of *Annual Conference of the Canadian Society for Civil Engineering* (CSCE 2019), proceedings, 12-15 June 2019, Laval (Greater Montreal), Quebec, Canada, 8p.
7. **Mehany, S.**, Mohamed, H. M., and Benmokrane, B. (2021). "Flexural Response of Lightweight SCC Beams Reinforced with Basalt FRP Reinforcing Bars." Proc. of *Annual Conference of the Canadian Society for Civil Engineering* (CSCE 2021), proceedings, 26-29 May 2021, Virtual Conference, Canada, 8p.

8. **Mehany, S.**, Mohamed, H. M., and Benmokrane, B. (2021). "Shear Strength of Lightweight Self-consolidating Concrete Beams Reinforced with BFRP Bars." Proc. of the 8th *International Conference on Advanced Composite Materials in Bridges and Structures* (ACMBS-VIII), proceedings, 05-07 Aug. 2021, Sherbrooke, Quebec, Canada, 8p.
9. **Mehany, S.**, Mohamed, H. M., and Benmokrane, B. (2021). "Performance of GFRP-RC Beams Using Lightweight Self-Consolidating Concrete (LWSCC) under Flexure." *The 11th International Conference on Short and Medium Span Bridges (SMSB 2022)* (to be submitted in Dec. 2021).

Acknowledgements

First of all, I would like to thank the ***Almighty Allah*** for giving me the effort to complete this work in the proper shape.

I wish to take the opportunity to express my deep gratitude to everyone who contribute to make this research possible. I express my sincere gratitude and appreciation to my supervisor, ***Prof. Brahim BENMOKRANE,*** for giving me the opportunity to conduct such project research and providing me with the necessary support at times when it was most needed.

I am deeply grateful indebted to ***Dr. Hamdy MOHAMED*** for his constant cooperation, continuous encouragement, consulting, and unlimited help throughout the work. It is no exaggeration to say that without him this work would not be as complete.

Many thanks to ***Profs. Sébastien LANGLOIS, Adel EL-SAFTY, and P. VIJAY*** for accepting to be jury members of this dissertation and giving time to read and review.

Special thanks are extended to the Natural Science and Engineering Research Council of Canada (NSERC), Canada Research Chair in Advanced Composite Materials for Civil Structures, the Fonds de la recherché du Quebec—Nature et Technologie (FRQ-NT), and the Ministère de l'Économie, de l'Innovation et des Exportations (MEIE) of Quebec for their financial support, and ASA.TEC (Austria) and Pultrall Inc. (Canada) for donation of FRP bars.

Special thanks go also to the technical staff of the structural lab at the Department of Civil and Building Engineering of the University of Sherbrooke, ***Jerôme Lacroix*** and ***Steven MacEachern*** for their technical help during casting and testing of the beams.

Many thanks also go to all my colleagues and friends at the Université de Sherbrooke. Their friendliness streamlined and supported my studies and life style during the period of my doctoral studies.

Last but not the least, I deeply grateful indebted to my parents, who show a genuine interest in and concern for my life, my work, and my well-being. The wishes and prayers of my brothers were always a support in the distress times. I wish to extend my deepest love and appreciation to my wife for her steadfast support and continuous encouragements throughout all these years. My daughter ♥ ***Kinda*** ♥ has surely participated in this achievement. Their continuous patience, understanding, sacrifice, and prayers throughout this research means a lot for me.

Shehab Mehany

Contents

Abstract i
Résumé iii
Bibliography v
Acknowledgements vii
Contents ix
List of Figures xv
List of Tables xix
Chapter 1 Introduction 1
1.1 General 1
1.2 Research Significance 2
1.3 Objectives 3
1.4 Methodology 4
1.5 Thesis organization 5
Chapter 2 Literature review 9
2.1 General 9
2.2 FRP reinforcement 9
2.3 Lightweight concrete (LWC) 10
2.3.1 Properties of LWC 10
2.3.1.1 Compressive strength of LWC 10
2.3.1.2 Tensile strength of LWC 11
2.3.1.3 Modulus of elasticity of lightweight concrete 11
2.3.1.4 Bond strength 13
2.3.1.5 Shrinkage of LWC 13
2.4 Lightweight self-consolidating concrete (LWSCC) 14
2.5 Applications of LWC 15
2.5.1 Use of LWC in New Zealand 15
2.5.2 Use of LWC in UK 16
2.6 Shear behavior of FRP-RC beams without stirrups 17
2.6.1 Shear transfer mechanism in beams without stirrups 17
2.6.1.1 Shear resistance in un-cracked concrete 18
2.6.1.2 Interface shear transfer 18
2.6.1.3 Dowel action of the longitudinal bars 19

2.6.1.4 Residual tensile stresses across cracks 19
2.6.1.5 Arch action 20
2.6.2 Factors affecting shear capacity 20
2.6.2.1 Concrete tensile strength 20
2.6.2.2 Longitudinal reinforcement ratio 21
2.6.2.3 Shear span-to-depth ratio 21
2.6.2.4 Axial forces 23
2.6.2.5 Depth of concrete members (size effect) 24
2.6.3 Research on shear behavior of RC beams 25
2.6.4 Review of shear design equations 28
2.6.4.1 ACI 440.1R-15 design guidelines 29
2.6.4.2 Canadian Standard Code, CSA S6-19 29
2.6.4.3 Canadian Standard Code, CSA S806-12 30
2.6.4.4 Hoult et al. (2008) Equation 30
2.7 Flexural behavior and serviceability of FRP-RC beams 31
2.7.1 Research on flexural behavior and serviceability of FRP-RC beams 31
2.7.2 Flexural capacity of FRP RC members 36
2.7.3 Curvature and Deformability 37
2.7.4 Review of serviceability equations 38
2.7.4.1 Deflection equations 38
2.7.4.1.1 Effective moment of inertia models 39
2.7.4.2 Crack-Width Equations 41
Chapter 3 Contribution of Lightweight Self-Consolidated Concrete (LWSCC) to Shear Strength of Beams Reinforced with Basalt FRP Bars 43
3.1 Introduction 45
3.2 Objectives 46
3.3 Experimental Investigation 47
3.3.1 Material Properties 47
3.3.1.1 Lightweight self-consolidating concrete (LWSCC) 47
3.3.1.2 BFRP and Steel Bars 48
3.3.2 Test Specimens 49
3.3.3 Measurement Equipment 52
3.3.4 Test Setup and Procedure 52
3.4 Test Results and Discussion 53
3.4.1 General Behavior, Crack Patterns, and Failure Modes 53

3.4.2 Concrete Strains 58
3.4.3 Reinforcement Strains 59
3.5 Shear Capacity 59
3.5.1 Review of Shear Design Equations 62
3.5.1.1 ACI 440.1R-15 design guidelines 62
3.5.1.2 Canadian Standard Code, CSA S6-19 63
3.5.1.3 Canadian Standard Code, CSA S806-12 63
3.5.2 Comparison of Predicted Shear Capacity to Experimental Results 64
3.6 Summary and Conclusions 67
Chapter 4 Performance of LWSCC Beams Reinforced with GFRP Bars without Stirrups under Shear 69
4.1 Introduction 71
4.2 Research Significance 72
4.3 Test Program 73
4.3.1 Geometry and Test Matrix of the Beam Specimens 73
4.3.2 Materials 74
4.3.2.1 GFRP and Steel Bars 74
4.3.2.2 Concrete Types 75
4.3.3 Beam Fabrication 76
4.3.4 Instrumentation and Test Setup 77
4.4 Observations and Test Results 78
4.4.1 Shear Failure Mode and Cracking 78
4.4.2 Load–Deflection Behavior 80
4.4.3 Reinforcement and Concrete Strains 81
4.4.4 Ductility and Deformability 83
4.5 Analysis and Discussion 84
4.5.1 Effect of GFRP Longitudinal Reinforcement Ratio and Modulus of Elasticity on Shear Strength 84
4.5.2 Shear-Strength Predictions 85
4.5.2.1 ACI 440.1R-15 85
4.5.2.2 CSA S806-12 86
4.5.2.3 CSA S6-19 86
4.5.2.4 Hoult et al. (2008) Equation 86
4.5.3 Comparison of Current Equations for Concrete Shear Strength Predictions with the Experimental Results 88

4.5.4 Effect of Concrete Density on Shear Strength Predictions 93
4.6 Summary and Conclusions 95
Chapter 5 Flexural Behavior and Serviceability Performance of LWSCC Beams Reinforced with BFRP Bars 97
5.1 Introduction 99
5.2 Research Significance 101
5.3 Test Program 101
5.3.1 Materials 101
5.3.1.1 Concrete Mixes 101
5.3.1.2 Reinforcing Bars 102
5.3.2 Beam Details and Test Parameters 104
5.3.3 Instrumentation and Test Specimens 107
5.4 Test Results and Discussion 108
5.4.1 Crack Propagation and Mode of Failure 108
5.4.2 Cracking and Ultimate Moment 111
5.4.3 Stiffness and Moment–Deflection Behavior 113
5.4.4 Strain in Concrete and Reinforcement 115
5.4.5 Curvature and Deformability 117
5.5 Review of Current Deflection and Cracking Provisions 119
5.5.1 Deflection Provisions 119
5.5.2 Crack-Width Provisions 120
5.5.3 Comparison between Experimental Results and Code Predictions 121
5.5.3.1 Deflection 121
5.5.3.2 Crack Width 123
5.6 Summary and Conclusions 124
Chapter 6 Flexural Strength and Serviceability of GFRP-Reinforced Lightweight Self-Consolidating Concrete Beams 127
6.1 Introduction 129
6.2 Research Motivation 131
6.3 Experimental Program 131
6.3.1 Beam Details and Test Matrix 131
6.3.2 Material Properties 134
6.3.3 Measurement Equipment and Test Setup 136
6.4 Experimental Results and Discussions 138
6.4.1 Cracking Moment 138

6.4.2 Failure Mode and Resistance Moment 139
6.4.3 Deflection Behavior 142
6.4.4 Concrete Strains 143
6.4.5 Reinforcement Strains 145
6.4.6 Moment–Bar-Strain Profile along the Span 145
6.4.7 Deformability Evaluation 146
6.4.8 Deflection Prediction 147
6.4.8.1 Deflection Equations 147
6.4.8.2 Effective Moment of Inertia Models 148
6.4.8.3 Predicted Effective Moment of Inertia and Deflection Compared to Experimental Results 151
6.4.8.4 Proposed Modification to the ACI 440.1R-15 (ACI 2015) Equation for LWSCC Specimens 154
6.4.9 Crack-Width Prediction 157
6.4.9.1 Crack-Width Equations 157
6.4.9.2 Predicted Crack-Width to Experimental Results 158
6.5 Conclusions 160
Chapter 7 Bond-Dependent Coefficient and Cracking Behavior of Lightweight Self-Consolidating Concrete (LWSCC) Beams Reinforced with Glass- and Basalt-FRP Bars 163
7.1 Introduction 165
7.2 Research Objectives and Significance 167
7.3 Experimental Program 168
7.3.1 Materials 168
7.3.1.1 Concrete Types 168
7.3.1.2 GFRP and BFRP Bars 168
7.3.2 Beams Geometry and Test Matrix 170
7.3.3 Specimen Fabrication Details 172
7.3.4 Instrumentation and Test Setup 173
7.4 Test Results and Discussion 174
7.4.1 Definition of Service Load Level 174
7.4.2 First Cracking Moment 175
7.4.3 Crack Propagation, Flexural Capacity, and Mode of Failure 177
7.4.4 Crack Spacing 179
7.4.5 Moment-Strain Relationship 179

7.4.6 Moment-Crack Width Relationship 181
7.4.7 Crack Width Prediction 183
7.4.7.1 Crack Width Equations 184
7.4.7.2 Predicted Crack Width to Experimental Results 185
7.4.8 Evaluation of the Bond-Dependent Coefficient (k_b) 187
7.5 Summary and Conclusions 191
Chapter 8 Conclusions and Recommendations 193
8.1 Summary 193
8.2 Conclusion 194
8.2.1 Part I: RC Beams with GFRP and BFRP Bars without stirrups under shear loads . 194
8.2.1.1 Experimental Results 194
8.2.1.2 Theoretical Results and Design Recommendations 194
8.2.2 Part II: RC Beams with GFRP and BFRP Bars under flexural loads 195
8.2.2.1 Experimental Results 195
8.2.2.2 Theoretical Results and Design Recommendations 196
8.3 Recommendations for Future Work 197
8.4 Sommaire 198
8.5 Conclusions 199
8.5.1 Phase I : Poutres en béton armé avec des barres en PRFV et barres en PRFB sans étriers soumises à l'effort tranchant 199
8.5.1.1 Résultats expérimentaux 199
8.5.1.2 Résultats théoriques et recommandations de conception 200
8.5.2 Phase II : Poutres en béton armé avec des barres en PRFV et PRFB sous charges de flexion 200
8.5.2.1 Résultats expérimentaux 200
8.5.2.2 Résultats théoriques et recommandations de conception 201
8.6 Recommandations pour les travaux futurs 203
References 205
Appendix. Example: Bond-dependent coefficient (k_b) 215

List of Figures

Figure 2.1– Different types of FRP bars. 10
Figure 2.2– The behavior of LWC and NWC under compressive force (Gerritse 1981). 11
Figure 2.3– Modulus of elasticity (ACI 213R-14). 12
Figure 2.4– Stress-strain curves for LWC and NWC (Wight and Macgregor 1997). 12
Figure 2.5– Bond strength: pull-out tests (ACI 213R-14). 13
Figure 2.6– Drying shrinkage: normally cured concrete (ACI 213R-14). 14
Figure 2.7– Wellington Stadium, New Zealand (McSaveney 2000). 15
Figure 2.8– Guys Hospital-Tower blocks, UK (Roy 1995). 16
Figure 2.9– Office block (construction) for East Surrey Newspaper, Ltd., Redhill (Roy 1995). 17
Figure 2.10– Mechanism of shear transfer in cracked RC beams without stirrups. 18
Figure 2.11– Shear stresses transmitted by aggregate interlock (Vecchio and Collins 1986). . 19
Figure 2.12– Modes of failure of deep beams (ASCE-ACI 1973). 22
Figure 2.13– Modes of failure of short shear spans with aid ranging from 1.5 to 2.5 (ASCE-ACI 1973). 22
Figure 2.14– Typical shear failure of a slender beam. 23
Figure 2.15– Typical crack pattern without stirrups subjected to axial tension and shear (Adebar and Collins 1996). 23
Figure 2.16– Comparison of large-scale beam tested by (Shioya et al. 1989) with predictions from ACI Code and MCFT (Collins and Mitchell 1997). 24
Figure 2.17– Typical diagonal tension failure mode- Beam CN-3 (El-sayed et al. 2006). 25
Figure 2.18– Load-deflection curves at mid-span (Tomlinson and Fam 2015). 26
Figure 2.19– Beam details and test configuration (dimensions in mm) (El Refai and Abed 2015). 26
Figure 2.20– Comparison between V_{exp}/V_{pred} ratio for BFRP bars (El Refai and Abed 2015). 27
Figure 2.21– Load-deflection envelopes of all specimens (Pantelides et al. 2012a). 28
Figure 2.22– Moment-deflection relationships for the tested beams: (a) beams C1; (b) beams C2; (c) beams G1 and G2; (d) beams AR (Kassem et al. 2011). 32
Figure 2.23– Typical crack pattern of the pure bending zone at failure (El-Nemr et al. 2016).33
Figure 2.24– ultimate moment vs. reinforcement ratio curve: (a) NSC and (b) HSC (Abed et al. 2021). 34
Figure 2.25– Load–deflection response for the beam specimens. (Wu et al. 2019) 35

Figure 2.26– Specimen details (dimensions in millimeters) (Liu et al. 2020). 35
Figure 2.27– Typical cracking patterns of the constant moment zone at failure (LCC–6#8–3) (Liu et al. 2020). 36
Figure 3.1– BFRP bar types and surface characteristics. 49
Figure 3.2– Fabrication of the beam specimens (a) cages and formwork, (b) casting, and (c) beam specimens. 50
Figure 3.3– Dimensions, reinforcement details, and instrumentation of the beam specimens (dimensions in mm). 52
Figure 3.4– Test setup. 53
Figure 3.5– Cracking patterns and shear-crack angles at failure. 55
Figure 3.6– Typical crack pattern of the beam specimens. 55
Figure 3.7– Load–deflection response for all the beam specimens. 57
Figure 3.8– Strain responses for the beam specimens in (a) concrete and (b) longitudinal reinforcement. 59
Figure 3.9– Normalized shear strength versus reinforcement ratio for the LWSCC beam specimens. 60
Figure 3.10– Normalized shear strength versus concrete density. 61
Figure 3.11– Comparison between V_{exp} / V_{pred} for the beam specimens. 65
Figure 4.1– Dimensions, reinforcement details, and strain gauge locations of the test specimens. (Note: dimensions in mm; 1 mm = 0.0394 in.) 74
Figure 4.2– Overview of assembled GFRP cages. 76
Figure 4.3– Test setup: (a) schematic diagram, and (b) overview of the tested beams. 78
Figure 4.4– Typical crack pattern of beams: LS-G-1.26. 79
Figure 4.5– Load–crack width for the beam specimens. (Note: 1 mm = 0.0394 in.; 1 kN = 0.225 kip.) 80
Figure 4.6– Load–deflection response for the beam specimens. (Note: 1 mm = 0.0394 in.; 1 kN = 0.225 kip.) 81
Figure 4.7– Load versus longitudinal reinforcement and concrete strain at mid-span for the beam specimens. (Note: 1 kN = 0.225 kip.) 82
Figure 4.8– Normalized shear strength versus reinforcement ratio of the beams. 84
Figure 4.9– Predictions with the ACI 440.1R-15 design equation for all beam specimens. (Note: 1 kN = 0.225 kip.) 91
Figure 4.10– Predictions with the CSA S806-12 design equation for all beam specimens. (Note: 1 kN = 0.225 kip.) 92

Figure 4.11– Predictions with the CSA S6-19 design equation for all beam specimens. (Note: 1 kN = 0.225 kip.) 92
Figure 4.12– Comparison of experimental shear capacities to Hoult et al. (2008) shear strength predictions. (Note: 1 kN = 0.225 kip.) 92
Figure 5.1– BFRP bar types and surface characteristics. 103
Figure 5.2– Dimensions, reinforcement details, and instrumentation of the beam specimens. (Note: dimensions in mm; 1 mm = 0.0394 in) 104
Figure 5.3– Fabrication of the beam specimens (a) Cages inside the formwork; and (b) Beam specimens. 107
Figure 5.4– Test setup. 108
Figure 5.5– Crack patterns and failure modes of the tested beams. 110
Figure 5.6– Moment-to-crack-width relationships for the BFRP-LWSCC beams. (Note: 1 mm = 0.0394 in.; 1 kN.m= 0.738 kip.ft.) 111
Figure 5.7– Normalized moment capacity versus reinforcement ratio. 113
Figure 5.8– Normalized moment capacity versus concrete density. (Note: 1 kg /m^3= 0.062 lb/ft^3) 113
Figure 5.9– Moment-deflection response for the beam specimens. (Note: 1 mm = 0.0394 in.; 1 kN.m= 0.738 kip.ft.) 115
Figure 5.10– Strain responses for the beam specimens. (Note: 1 kN.m= 0.738 kip.ft.) 117
Figure 5.11– Moment-curvature for the beam specimens. (Note: 1 kN.m= 0.738 kip.ft.) 118
Figure 5.12– Comparison between the experimental and predicted deflection. (Note: 1 mm = 0.0394 in.; 1 kN.m= 0.738 kip.ft.) 122
Figure 6.1– Dimensions and reinforcement details of the beam specimens (dimensions in mm). 133
Figure 6.2– GFRP bar types and surface characteristics. 136
Figure 6.3– Schematic of the instrumentation (dimensions in mm). 137
Figure 6.4– Test setup. 137
Figure 6.5– Crack patterns and failure modes of the tested beams. 140
Figure 6.6– Moment–deflection response at the mid-span. 143
Figure 6.7– Strain responses for the beam specimens at the mid-span (a) concrete and (b) longitudinal reinforcement. 144
Figure 6.8– Tensile-strain distribution along the specimen length of the LWSCC beams after cracking: (a) GFRP Type I and (b) GFRP Type II. 146

Figure 6.9– Tensile-strain distribution along the specimen length of the LWSCC beams at failure: (a) GFRP Type I and (b) GFRP Type II. (Note: failure for LS-S-3#15M was the yielding moment). 146

Figure 6.10– The effective moment of inertia versus the applied moment for the GFRP-LWSCC specimens. 153

Figure 6.11– The modified effective moment of inertia (ACI 440.1R-15 (ACI 2015) model) versus the applied moment for GFRP-LWSCC specimens. 156

Figure 7.1– FRP bar types and surface characteristics. 170

Figure 7.2– Dimensions, reinforcement details, and instrumentation of the specimens (dimensions in mm). 172

Figure 7.3– Fabrication of the of the GFRP and BFRP cages 173

Figure 7.4– Overview of the test setup. 174

Figure 7.5– Comparison between $M_{cr\text{-}exp}/M_{cr\text{-}pred}$ for the LWSCC specimens according to: (a) ACI 440.1R-15; (b) CSA S806-12..... 177

Figure 7.6– Crack pattern and failure modes of the tested beams. 178

Figure 7.7– Moment-to-bar strain relationships: (a) Series I; (b) Series II; (c) Series III and IV. 181

Figure 7.8– Moment-to-crack-width relationships: (a) Series I; (b) Series II; (c) Series III and IV. 183

Figure 7.9– Predicted moment-to-crack-width relationships according to ACI 440.1R-15, ACI 440X-XX, AASHTO-18, and CSA S6-19 for LWSCC beams. 187

Figure 7.10– Predicted k_b values at different limits for sand-coated GFRP and BFRP bars. . 188

Figure 7.11– Predicted k_b values at different limits for helically grooved GFRP and BFRP bars. 189

List of Tables

Table 3.1 – Physical properties of aggregates 48
Table 3.2 – LWSCC and NWC mix proportions 48
Table 3.3 – Mechanical properties of the BFRP and steel reinforcements 49
Table 3.4 – Test matrix and details of test specimens 51
Table 3.5 – Test results and comparison of experimental and predicted shear capacities of specimens using different design codes 58
Table 3.6 – Relative accuracy of different design codes 65
Table 3.7 – Experimental and predicted shear capacities of the NWC beams reinforced with BFRP bars 66
Table 4.1 – Mechanical properties of the GFRP and steel reinforcement 75
Table 4.2 – Test matrix and details of the test specimens 76
Table 4.3 – Test results for the experimental shear capacities of the beam specimens 81
Table 4.4 – Design provisions for calculating the concrete contribution V_c in FRP RC members 88
Table 4.5 – Comparison of experimental results with the various code predictions 90
Table 4.6 – Characteristics of LWC specimens used for comparison of design methods 91
Table 4.7 – Characteristics of NWC specimens from past studies 94
Table 4.8 – Average, standard deviation, and coefficient of variation of the V_{exp}/V_{pred} for LWC and NWC beams. 94
Table 5.1– Physical properties of aggregates 102
Table 5.2– LWSCC and NWC mix proportions 102
Table 5.3– Mechanical properties of the BFRP and steel reinforcement 103
Table 5.4– Test matrix and details of test specimens 105
Table 5.5– Experimental and predicted cracking and ultimate moments 109
Table 5.6– Strains and curvature of the BFRP beams at failure 116
Table 5.7– Experimental-to-predicted deflection and crack-width ratios of the BFRP-LWSCC specimens 123
Table 6.1 –Test matrix and details of the test specimens 134
Table 6.2 –Physical properties of aggregates 135
Table 6.3 –Mechanical properties of the GFRP and steel reinforcement 136
Table 6.4 –Experimental and predicted cracking and ultimate moments 139
Table 6.5 –Deflections, strains and curvature of the GFRP beams at failure 144

Table 6.6 –Experimental-to-predicted deflection ratios of the GFRP-LWSCC specimens.... 154
Table 6.7 –Experimental-to-predicted crack widths of the GFRP-LWSCC specimens 159
Table 6.8 –The predicted k_b values at different limits for GFRP bars 159
Table 7.1 – LWSCC mix proportions 168
Table 7.2 – Mechanical properties of the GFRP and BFRP reinforcements 169
Table 7.3 – Test matrix and details of test specimens..... 172
Table 7.4 – Experimental cracking and ultimate moments..... 176
Table 7.5 – Experimental-to-predicted crack-width ($w_{cr\text{-}exp}$/ $w_{cr\text{-}pred}$) for LWSCC specimens 186
Table 7.6 – Average predicted k_b values for sand-coated GFRP and BFRP bars..... 190
Table 7.7 – Average predicted k_b values for helically grooved GFRP and BFRP bars 190

CHAPTER 1

Introduction

1.1 General

Lightweight concrete (LWC) allows for the production of reinforced concrete (RC) members that have a reduced own weight while maintaining a concrete strength that is of the same magnitude as normal-weight concrete (NWC). Reducing the own weight of an RC structure could considerably decrease the section dimensions of beams, slabs, columns, and foundations, which would enhance cost savings. An additional benefit of RC elements made with LWC is cutting lifting and transportation costs in the case of precast elements. The past few decades have yielded great inventions in modern concrete technology from which lightweight self-consolidating concrete (LWSCC) has emerged as a promising alternative to NWC (Okamura and Ouchi 2003). LWSCC is considered a new kind of high-performance concrete (HPC) in construction, which combines the excellent benefits and characteristics of LWC and self-consolidating concrete (SCC) (Hwang and Hung 2005). Therefore, consolidating lightweight aggregate (LWA) in SCC should enhance the quality, produce high-strength LWC (HSLWC), and prevent the segregation of LWA.

Aggressive climate and environmental changes stimulate the manufacturing of a corrosion-free material. Past years have seen valuable research work and widespread applications of concrete elements having fiber-reinforced polymer (FRP) reinforcement. Nowadays, glass-FRP (GFRP) bars are becoming the most common type of FRP bars because they cost less than other types of FRP composite materials. GFRP bars have been used in different applications, including high-rise buildings, bridges, and parking garages. Recently, basalt-FRP (BFRP) bars have been introduced in the construction field as a promising addition to the existing FRP bars family. Similar to GFRP bars, BFRP bars are characterized by high strength-to-weight ratio, good resistance to chemical attack and electromagnetic, excellent bond strength with concrete, and relatively low modulus of elasticity when compared to traditional steel bars (Wu et al. 2015; Elgabbas et al. 2017).

Extensive research programs have been conducted to study the shear and flexural behavior of NWC members reinforced with FRP bars (Razaqpur and Isgor 2006; Hoult et al. 2008; Ali et al. 2017a, b; Kassem et al. 2011; El-Nemr et al. 2016, 2018; Abdelkarim et al. 2019; Mehany et al. 2019). As a result, several equations from the current approaches (American Concrete Institute (ACI 440.1R-15), Canadian Standards Association (CSA S6-19; CSA S806-12) have been published to assess the shear and flexural behavior of members reinforced with FRP bars. In contrast, limited research has been conducted to investigate the shear and flexural behavior of LWC beams reinforced with FRP bars. Pantelides et al. (2012a) studied the behavior and shear performance of sand-LWC (SLWC) panels reinforced with GFRP bars (SLWC-GFRP). The results showed that modifying ACI 440.1R-06 equations by applying a concrete density reduction factor of 0.85 could be employed to calculate the concrete shear capacity of SLWC-GFRP panels. Kim and Jang (2014) reported that the concrete shear capacities of LWC specimens reinforced with GFRP bars (LWC-GFRP) were equal to 75 % of the capacities predicted by the equation for NWC. For the SLWC-GFRP panels presented in Pantelides et al. (2012a), however, they were equal to 85% of the capacities predicted by the equation for NWC. Wu et al. (2019) tested nine concrete beam specimens reinforced with GFRP bars under flexural loads. The specimens were made with LWC and steel fiber-reinforced LWC (SFLWC). The test results indicate that the beams made with SFLWC exhibited narrower cracks than those made with LWC. The amount of reinforcement affected the flexural stiffness after cracking of both the LWC and SFLWC beams and thus, their load–deflection behavior. Liu et al. (2020) studied the applicability of using GFRP and carbon-FRP (CFRP) bars as longitudinal reinforcement in LWC and SFLWC beams. The test results show that the failure of all specimens occurred by concrete crushing. Moreover, comparing the crack-width predictions show that the provisions in the ACI 440.1R-0.6 overestimated the predicted crack widths at service load for the LWC and SFLWC beams, while those in the ISIS Canada Research Network design manual (2007) predicted reasonable crack-width values.

1.2 Research Significance

Lightweight self-consolidating concrete (LWSCC) is being more and more widely used in different types of RC structures due to its better structural and durability performance. No research, however, seems to have investigated LWSCC beams reinforced with FRP bars under shear and flexural loads. In addition, ACI 440.1R-15, CSA S806-12, and CSA S6-19 do not provide guidance for LWSCC beams reinforced with GFRP and BFRP bars. Therefore, this

paper tries to fill this gap. The experimental program is completed at the University of Sherbrooke (Sherbrooke, QC, Canada) to study the shear and flexural behavior of FRP-reinforced LWSCC beams in which the fine aggregates are a mixture of LWA and natural sand (NS). The test results and outcomes of this study can be used to assess and explore the feasibility of using GFRP and BFRP bars as longitudinal reinforcement in LWSCC members. Moreover, the results reported in this thesis represent a significant contribution to the relevant literature and provide designers, engineers, and members of code committees with much-needed data and recommendations to advance the use of basalt FRP reinforcement in concrete structures.

1.3 Objectives

This research project aims at evaluating the feasibility of using GFRP and BFRP bars as internal reinforcement for structural LWSCC elements. This study consists of two phases. Phase I concerned the shear behavior evaluation of 14 concrete beams reinforced with different types and ratios of GFRP, BFRP, and steel bars. Phase II concerned the flexural behavior and serviceability performance evaluation of 20 concrete beams reinforced with different types and ratios of GFRP, BFRP, and steel bars. The specific objectives of the current investigation are to:

Phase I

a. Investigate the shear behavior and failure mode mechanisms of LWSCC beams reinforced with GFRP and BFRP bars under static loads.
b. Analyze the effect of types of FRP bars and reinforcement ratio on concrete shear capacity.
c. Assess the accuracy of the current FRP design provisions for estimating the concrete shear strength of the LWSCC specimens, including ACI 440.1R-15, CSA S806-12, and CSA S6-19.
d. Compare the shear behavior of FRP-reinforced LWSCC beam specimens without shear reinforcement with that of FRP-reinforced NWC specimens tested in this research program and from past studies.

Phase II

e. Investigate the flexural behavior and serviceability performance of LWSCC beams reinforced with GFRP and BFRP bars under static loads.

f. Compare the experimental cracking moment of the GFRP- and BFRP-reinforced LWSCC beams with those obtained from predicted using FRP design provisions.

g. Investigate the effect of GFRP and BFRP types and amount of reinforcement on the behavior of the LWSCC specimens.

h. Compare the recorded crack widths and deflections of LWSCC beams with those predicted by models in the FRP provisions.

i. Estimate the bond-dependent coefficient (k_b) factor of different surface conditions of GFRP and BFRP bars (sand-coated and helically grooved) in LWSCC.

1.4 Methodology

To achieve the above-described objectives, extensive experimental and theoretical programs were conducted. The experimental program comprised two phases summarized as follows:

Phase I: RC Beams with GFRP and BFRP Bars without stirrups under shear loads

This phase was designed and prepared to provide experimental data on the behavior and concrete shear strength of LWSCC beams reinforced with GFRP or BFRP bars without stirrups. This investigation considered the concrete density and the longitudinal FRP reinforcement type and ratio as the test variables. A total of fourteen RC beams, including five LWSCC beams reinforced with BFRP bars, four LWSCC beams reinforced with GFRP bars, one LWSCC beam reinforced with steel bars, two NWC beams reinforced with GFRP bars, and two NWC beams reinforced with BFRP bars, were tested up to failure. The beam specimens were 3,100 mm long × 200 mm wide × 400 mm deep with a clear shear span of 1,000 mm. The constant shear span-to-depth ratio was approximately 3.0. The thickness of the beam specimens was chosen to be greater than those in ACI 440.1R-15, where the minimum thickness for simply supported beams shall be *L/10*. The results were discussed in terms of general behavior, crack patterns, and failure modes effect of test parameters, deflection responses, and concrete shear capacities. The test results of this study were compared to the current FRP shear design equations in the design guidelines, codes, and literature. Moreover, the concrete density reduction factor (λ) of the GFRP and BFRP bars were evaluated and compared with the recommendations of the current FRP design codes and guidelines.

Phase II: RC Beams with GFRP and BFRP Bars under flexural loads

The experimental program in this phase was conducted to investigate the flexural behavior and serviceability of concrete members reinforced with GFRP or BFRP bars. A total of 20 RC beam specimens with a cross-sectional width and height of 200 mm and 300 mm, respectively, and with a total length of 3,100 mm were tested under four-point bending load up to failure. 16 beams were made with LWSCC, while the other four were made with NWC as reference specimens. The test parameters were concrete density (LWSCC and NWC); reinforcement type (GFRP and BFRP bars) with various surface conditions (sand-coated and helically grooved), and longitudinal reinforcement ratio. The experimental results were reported in terms of cracking moments, deflection responses, flexural capacity, mode of failure, crack patterns, crack spacing, and crack widths. The crack-control models in the current FRP codes and design guidelines were re-examined, extended, and applied to circular FRP-RC members. Moreover, the k_b values have been evaluated and suggested for FRP bars of different types (glass and basalt) in LWSCC. Finally, the measured deflections and experimental values of the effective moment of inertia (I_e) were analyzed and compared with those predicted using available models.

1.5 Thesis organization

This thesis is divided into eight chapters. The contents of each chapter can be summarized as follows:

Chapter 1 presents the introduction, research significance, objectives, and methodology of this investigation.

Chapter 2 introduces a review of the relevant literature. Firstly, the chapter provides a brief summary of the main characteristics and properties of the FRP composite materials used as internal reinforcement. After that, it provides a brief review of the experimental and theoretical studies carried out to investigate the shear and flexural behavior of NWC and LWC members reinforced with steel and FRP bars. Finally, the code provision that related to shear and flexural behavior of FRP-RC members are also presented.

Chapter 3 (1st article) investigates the shear behavior of LWSCC beams reinforced with BFRP bars. The influence of two different types of BFRP bars of comparable quality and commercially available (sand-coated basalt and helically grooved basalt) on shear capacity was assessed. The

tested beams included five beams reinforced with BFRP bars, one beam reinforced with steel bars and two beams constructed using NWC for comparison purposes. Comparisons between the experimental test results and the theoretical predictions by three North American codes and design guidelines are performed. Based on this study, the BFRP RC beams can be designed with LWSCC provided that an appropriate concrete density reduction factor is applied.

Chapter 4 (2nd article) presents the experimental results on the shear behavior of beams reinforced with GFRP bars and one control beam reinforced with conventional steel bars for comparison purposes. The test variables were the reinforcement type and ratio and concrete density. The analysis and discussions of these results are presented. These discussions are based on modes of failure, load–deflection behavior, reinforcement and concrete strains, ductility and deformability, and effect of various test variables on the shear strength of tested specimens. Moreover, the test results of this study and the results for 42 specimens in the literature were compared to the current FRP shear design equations in the design guidelines, codes, and literature.

Chapter 5 (3rd article) investigates experimentally and theoretically the feasibility of using BFRP bars as longitudinal reinforcement in flexural LWSCC members. The test parameters were concrete density (LWSCC and NWC); reinforcement type (sand-coated BFRP, helically grooved BFRP, thread-wrapped BFRP, or steel); and longitudinal BFRP reinforcement ratio. The test results were compared from the standpoint of the cracking and ultimate moment, deflection, and crack-width design provided in the available FRP design standards.

Chapter 6 (4th article) investigates the flexural behavior and serviceability performance of GFRP-reinforced LWSCC members experimentally and theoretically. The experimental results are reported in terms of cracking moment, failure mode and resistance moment, deflection behavior, concrete and reinforcement strains, moment-bar-strain profile along the span, and deformability evaluation. Moreover, the recorded deflections and crack widths of the GFRP-reinforced LWSCC beams are presented and compared to those predicted with the FRP design provisions and the literature.

Chapter 7 (5th article) aims at investigating the cracking behavior of LWSCC beams reinforced with GFRP and BFRP bars and evaluating the k_b values. The experimental results are reported in terms of crack patterns, crack spacing, and crack width versus the applied moment. Crack

control models in the current FRP codes and design guidelines were re-examined, extended, and applied to FRP-reinforced LWSCC members.

Chapter 8 presents a general conclusion of the results drawn from the work presented in this dissertation. Recommendations for future research are also given.

CHAPTER 2

Literature review

2.1 General

This chapter provides a brief summary of the main characteristics and properties of the fiber-reinforced polymer (FRP) materials used as internal reinforcement. After that, it provides a brief review of the studies carried out to investigate the shear and flexural behavior of normal weight concrete (NWC) and lightweight concrete (LWC) members reinforced with steel and FRP bars. Finally, the code provisions that related to shear and flexural behavior of reinforced concrete (RC) members with FRP bars are also presented.

2.2 FRP reinforcement

The use of FRP bars for reinforcing concrete structures is recommended to construct structures in highly corrosive environments and increase service life of marine infrastructure. FRP bars are known as a composite material, manufactured of a polymer matrix reinforced with fibers. In North America, glass-FRP (GFRP) bars are becoming the most common type of FRP bars because they cost less than other types of FRP composite materials. GFRP bars have been used in different applications, including high-rise buildings, bridges, and parking garages. Recently, basalt-FRP (BFRP) bars have been introduced in the construction field as a promising addition to the existing FRP bars family. Similar to GFRP bars, BFRP bars are characterized by high strength-to-weight ratio (1/6 to 1/4 times of the density of steel reinforcement), high longitudinal tensile strength, good resistance to chemical attack and electromagnetic, excellent bond strength with concrete, and relatively low modulus of elasticity when compared to traditional steel bars (Wu et al. 2015; Elgabbas et al. 2017).

The surface of the FRP rebars are either sand coated, helically wound spiral outer surface, indented, braided, or with ribs. Figure 2.1 shows some commercially available FRP bars with

different surface textures. Extensive research has been conducted since the mid-1990s to study the behaviour of beams and slabs reinforced with various FRP bars (ACI 440.1R-15).

Figure 2.1– Different types of FRP bars.

2.3 Lightweight concrete (LWC)

Over the years, RC structures have become the most common structures in the world due to their relatively low construction costs, high availability, and potentially long service lives. Sometimes, however, the relatively high self-weight of RC structures results in impractical structural solutions. Lighter concrete with high strength would be very desirable for many applications, including high-rise buildings and bridge structures. LWC benefits include lower cost by reducing the dead load, cutting substructure and foundation costs, and improving the seismic structural response. In addition, LWC provides better performance in terms of insulation, fire, and freeze–thaw resistance (Xiao et al. 2016). Since LWC was presented, different types have been introduced and evolved to meet industry requirements.

2.3.1 Properties of LWC

2.3.1.1 Compressive strength of LWC

LWC can be designed to achieve similar strength as NWC. There is usually no relationship between aggregate strength and concrete strength. The concrete strength is more dependent on the cementitious matrix. Usually, the strength of LWC ranges from 21to 35 MPa (ACI 213R-14). Using light aggregates of good quality (maximum aggregate diameter of 9 or 13 mm) made it possible to produce LWCs with compressive strengths ranging from 40 to 50 MPa (Mehta and Monteiro 2013). Figure 2.2 shows the behavior of LWC and NWC under compressive force to

understand the transmission of force in the concrete. As shown, the cracks in LWC tend to pass through lightweight aggregate (LWA) particles instead of around them.

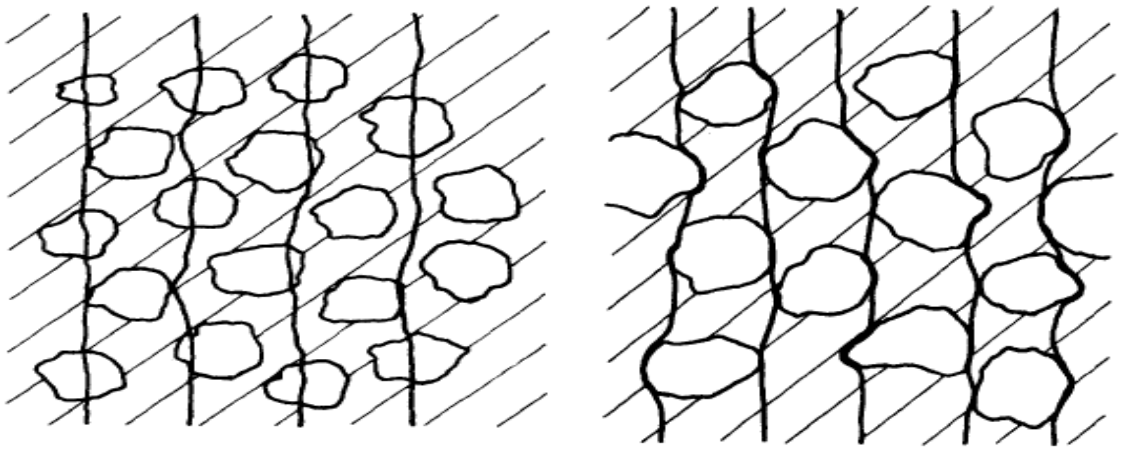

LWC **NWC**

Figure 2.2– The behavior of LWC and NWC under compressive force (Gerritse 1981).

2.3.1.2 Tensile strength of LWC

The tensile strength of concrete is only a fraction of its compressive strength and is dependent on the tensile strength of the coarse aggregate and mortar phases, and the degree to which the two phases are securely bonded. Concrete tensile strengths can be measured via a splitting test or from a modulus of rupture test. The splitting tensile strength of LWC varies from approximately 70% to 100% of NWC with similar compressive strength (ACI 213R-14).

2.3.1.3 Modulus of elasticity of lightweight concrete

The modulus of elasticity depends on the relative amounts of paste and aggregate and the modulus of each component (Pauw 1960). Generally, the modulus of elasticity of LWC can be considered to vary between 50% and 75% that of normal weight sand and gravel concrete of the same strength (Hossain 2004a, b). LWAs have lower modulus of elasticity than normal aggregates because of their high porosity. As a result, LWC has a lower modulus of elasticity than normal concrete (Mindess et al. 2002). Figure 2.3 shows the range of modulus of elasticity values for LWC.

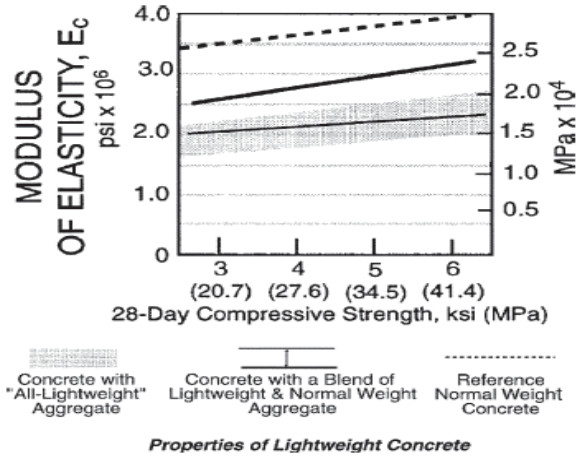

Figure 2.3– Modulus of elasticity (ACI 213R-14).

The stress-strain curve of LWC is affected by the lower modulus of elasticity and the relative strength of the aggregate and cement paste. If the aggregate is weaker than the cement paste, failure tends to occur suddenly in the aggregate, and the descending branch of the stress strain curve is very short, as shown by upper solid line in Figure 2.4. The fracture surface of those LWCs tends to be smoother than for normal weight concrete. On the other hand, if the aggregate does not fail, the stress strain curve will have a well descending branch as shown by the curved lower solid line in Figure 2.4. The strain of LWC at the maximum compressive stress is higher than NWC. This can be attributed to the higher modulus of elasticity of NWC (Wight and Macgregor 1997).

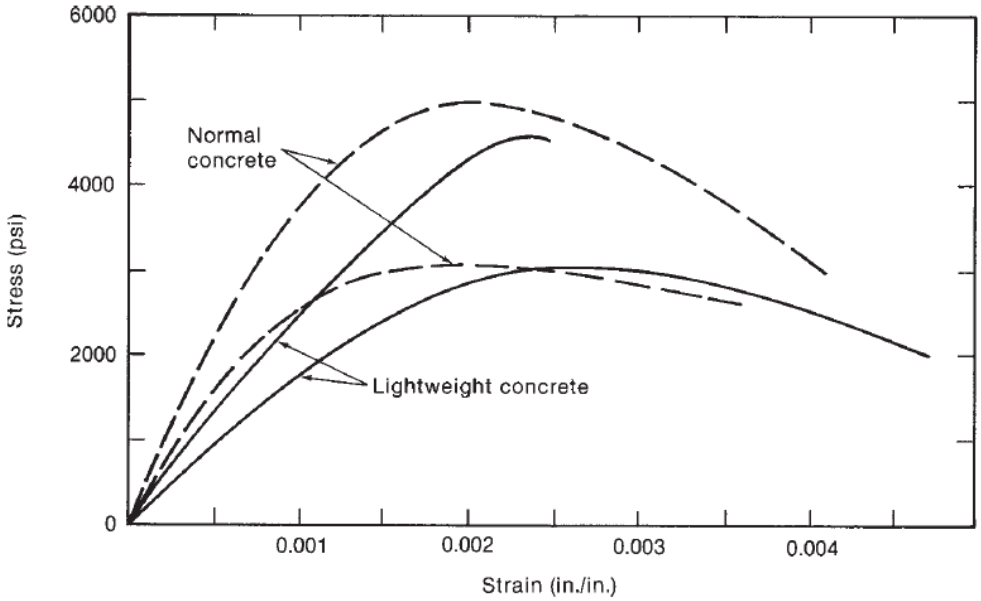

Figure 2.4– Stress-strain curves for LWC and NWC (Wight and Macgregor 1997).

2.3.1.4 Bond strength

As included in ACI 318R-19, the factor for development length of 1.3 is to reflect the lower tensile strength of LWC. Because of the lower strength of the aggregate, LWC has lower tensile strength, fracture energy, and local bearing capacity than NWC with the same compressive strength. Figure 2.5 shows the bond strength of bars cast in LWC is lower than that in NWC (Shideler 1957). Using LWC can result in bond strengths that range from nearly equal to 65% to similar or even higher values than those obtained with NWC (ACI 213R-14).

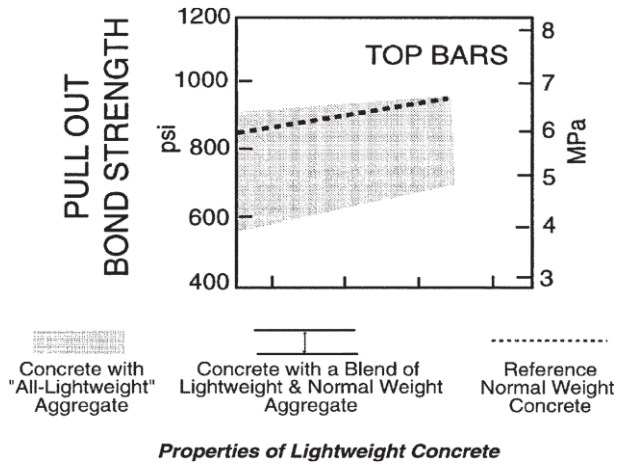

Figure 2.5– Bond strength: pull-out tests (ACI 213R-14).

2.3.1.5 Shrinkage of LWC

Shrinkage is an important property that can affect the extent of cracking, effective tensile strength, and warping. Figure 2.6 shows wide ranges of shrinkage values after one year of drying for LWC compared with NWC. It appears that low-strength LWC has greater drying shrinkage than NWC. However, some of higher strength LWC exhibit lower shrinkage. Partial or full replacement of the lightweight fine aggregate by natural sand usually reduces shrinkage for concrete made with most LWC (ACI 213R-14).

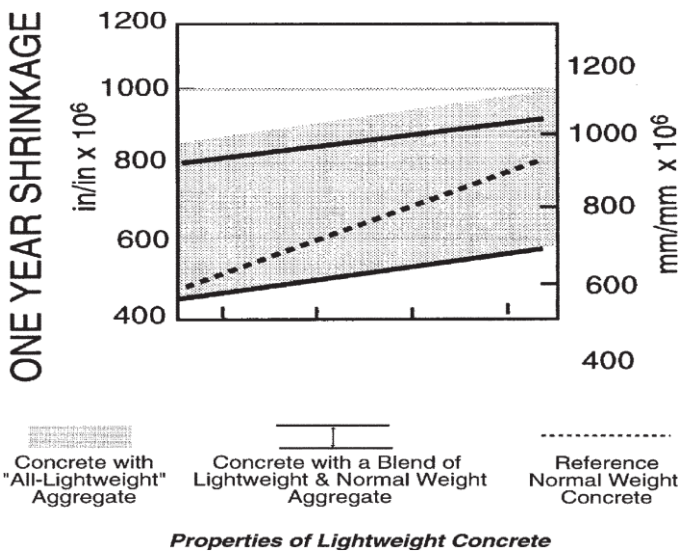

Figure 2.6– Drying shrinkage: normally cured concrete (ACI 213R-14).

2.4 Lightweight self-consolidating concrete (LWSCC)

The past few decades have yielded considerable inventions in the concrete industry, including lightweight self-consolidating concrete (LWSCC), which has appeared as an applicable alternative to NWC. LWSCC was developed to combine the excellent benefits of self-consolidating concrete (SCC) and LWC in a single package (Okamura and Ouchi 2003; Hwang and Hung 2005). SCC offers many advantages in terms of reducing labor and machinery costs, faster construction, and ability to spread in cases of highly crowded reinforcement making compaction difficult. Therefore, consolidating LWA in SCC should enhance quality, provide better strength and durability, offer excellent workability, and decrease the life-cycle cost of RC structures.

LWSCC has been used at the first time in Japan in 1922 with the construction of a cable-stayed bridge's main girder. Few years ago, LWSCC has gained a wide range of applications as a result of its unique properties, such as precast stadium benches (Hubertova and Hela 2007). The strength of LWC can be developed by a combination of the coarse lightweight and the fine stone aggregates. The strength ceiling is achieved by the concrete with aggregates of the expanded clay or slag and with the aggregate of the natural crushed stone. Furthermore, it has an influence on the cost of construction by reducing the total dead load of the structural members. LWSCC can achieve better strength and durability while offering excellent workability (Hwang and Hung 2005; Shi and Wu 2005).

2.5 Applications of LWC

The use of LWC for building and bridge construction has intrinsic and easily documented benefits that contribute to the sustainability of our built environment. The traditional benefits associated with a 20 to 30% reduction in density and up to a 50% reduction in heat conductivity as compared to NWC. For long-span bridges, the live load is a minor part of the total load and a reduction in density is translated into reductions in not only mass, but also in section size, (Clark 1993). The lower mass and density are extremely important in seismic areas where a reduction in the initial effects of the dead load may mean the difference between section survival and section failure.

LWC has been used for different purposes in the building industry, as follows:

2.5.1 Use of LWC in New Zealand

Wellington Stadium with a seating capacity of 40,000, is New Zealand's first modern sport stadium to be built with LWC with strength of 35 MPa (Figure 2.7). Expanded shale aggregates, imported from California, USA, was used to produce LWC for all the precast components in the main stadium bowl structure. The structure is located in close proximity to active earthquake fault lines, so an innovative seismic damping system has been used to ensure that the lightweight precast concrete structure is not subjected to high ductility demands. LWC, with a density of 1,850 kg/m^3, reduced the seismic loads, and offered a number of design and other construction advantages for the difficult site conditions (McSaveney 2000).

Figure 2.7– Wellington Stadium, New Zealand (McSaveney 2000).

2.5.2 Use of LWC in UK

Many interesting and challenging structures have been constructed using LWC in the last four decades. Figure 2.8 shows the view of the two towers of Guys Hospital- Users Tower and Communication Tower, respectively, 122 m and 145 m high (Roy 1995). The tower was built in 1974. Extensive use was made of LWC 31,000 m^3 with coarse and fine aggregates of about 30 MPa compressive strength. The interesting feature is the lecture theater on the 29th floor, where all the LWC beams cantilever 113 m above ground. Besides considerable savings in the foundation and framing, it added two hours of fire resistance without any extra treatment.

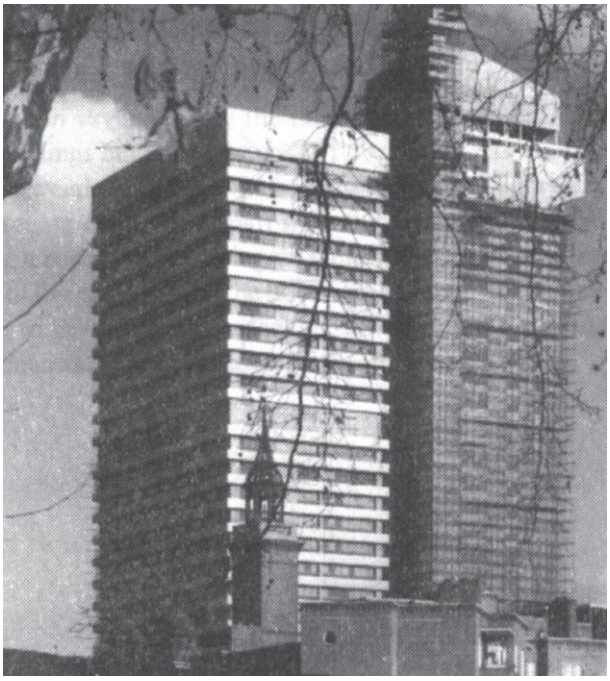

Figure 2.8– Guys Hospital-Tower blocks, UK (Roy 1995).

For precast structures, Figure 2.9 shows the construction of East Surrey Newspaper, Limited at Redhill. The structural frames with cladding panels were cast with LWC, using Solite aggregate. The concrete strength was 50 MPa with a density of 1,900 kg/m^3.

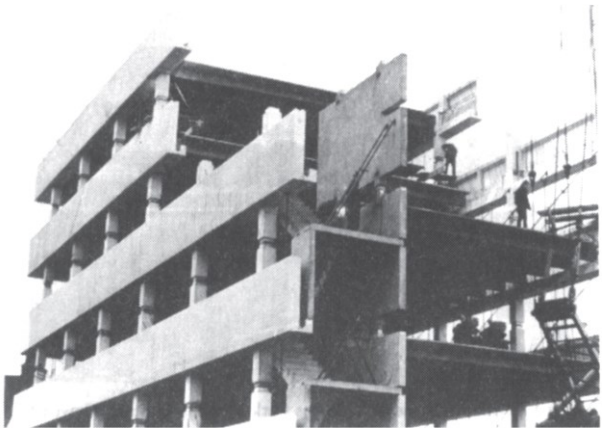

Figure 2.9– Office block (construction) for East Surrey Newspaper, Ltd., Redhill (Roy 1995).

2.6 Shear behavior of FRP-RC beams without stirrups

In the last decades, extensive researches have been carried out on the shear behavior of RC beams without web reinforcement. In this subsection, an overview of previously-conducted research on shear behavior of FRP-RC beams is presented. In addition, the influence of different factors on the shear response of beams, such as longitudinal reinforcement ratio, size effect, and span-to-depth ratio, are discussed. Moreover, the provisions of different codes namely, CSA S806-12, CSA S6-19, and ACI 440.1R-15 are also discussed.

2.6.1 Shear transfer mechanism in beams without stirrups

Five components are identified by the ASCE-ACI Committee 445 for mechanism of shear transfer in cracked RC beams: shear resistance in un-cracked concrete (compression zone) above the neutral axis; interface shear transfer along the two faces of the cracks, sometimes called "aggregate interlock or crack friction"; dowel action of the longitudinal bars; residual tensile stresses transmitted across the crack; and arch action for deep beam with a shear span-to-depth ratio less than 2.5, as shown in Figure 2.10. Taylor (1970) reported that the contribution of the shear force transferred by the various mechanisms for slender beams after the formation of a diagonal crack is, 20 to 40 percent by the un-cracked concrete of compression zone above the neutral axis; 33 to 50 percent by aggregate interlock; and 15 to 25 percent by dowel action of the longitudinal bars. While, for deep beam, the load is transferred directly from the loading points to the supports because of arch action behavior.

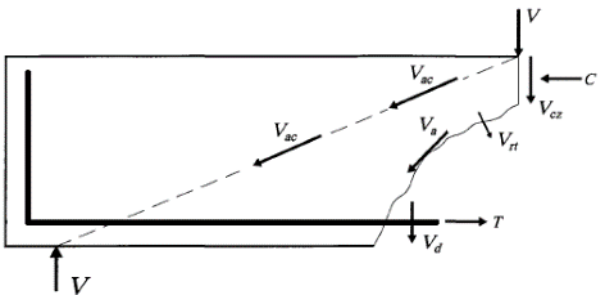

Vcz: Shear resistance in un-cracked concrete.

Va : Interface shear transfer.

Vd : Dowel action of the longitudinal bars.

Vrt : Residual tensile stresses across the crack.

Vac: Arch action for deep members.

Figure 2.10– Mechanism of shear transfer in cracked RC beams without stirrups.

2.6.1.1 Shear resistance in un-cracked concrete

In the compression zone, the force is transferred by inclined principal tensile and compressive stresses. The integration of shear stresses in un-cracked concrete zone gives a shear force component. The depth of the un-cracked zone and the concrete strength are considered the main factors in the contribution of the un-cracked concrete. Taylor (1970) reported that the shear force in the un-cracked concrete zone does not contribute significantly to the shear capacity because the depth of compression zone is relatively small. The contribution of the compression zone to the total shear by about 20 to 40 %.

2.6.1.2 Interface shear transfer

The friction along the inclined crack interface is considered the main reason for this shear transfer mechanism, which develops because of the relative slip between the two surfaces of the crack. Usually, cracking will form through the matrix and the bond zone between the matrix and the aggregate in normal strength concrete (NSC) due to the difference in strength of the aggregate and cement matrix. The protruding aggregate particles are larger than the crack width, the crack surface can increase resistance against slip and a shear force can be transferred, see Figure 2.11. While, high strength and light weight aggregate concrete, the fracture mode differs, because the cracks pass through the aggregate particles and form a smoother crack surface. However, shear transfer along the cracked surfaces occurs by friction, although to a less extent. Taylor (1970)

reported that the contribution of this mechanism indicated that between 33% and 50% of the total shear force.

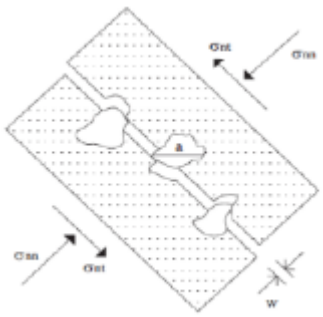

Figure 2.11– Shear stresses transmitted by aggregate interlock (Vecchio and Collins 1986).

2.6.1.3 Dowel action of the longitudinal bars

For beams without shear reinforcement, usually dowel action is less significant, because the dowel force in combination with the radial forced developed by bond forced give rise to vertical tensile stresses in the concrete surrounding the bar. Meanwhile, the ultimate shear in a dowel is limited by some factors; the amount of concrete cover, spacing of flexural cracks. However, Dowel action may be significant when using large amounts of longitudinal reinforcement in beam, particularly when distributing the longitudinal reinforcement in more than one layer (Taylor 1970; ASCE-ACI 1998). Several investigations carried out on dowel action indicated that the dowel shear force is between 15% and 25% of the total shear force (ASCE-ACI 1998).

2.6.1.4 Residual tensile stresses across cracks

The basic explanation of residual tensile stresses is that when first cracks are formed in the concrete, still tensile stresses can be transferred across the crack face. Usually, concrete does not crack by a clean break, but more gradually. At the moment or just before the tensile strength is reached, existing micro-cracks in the concrete start to grow and new micro-cracks produce due to debonding between the coarse aggregates and the matrix. With increasing strain, the micro-cracks coalesce, but still tensile stresses are present. When finally this coalescence results in a single macro-crack, the so-called residual stresses disappear. Reineck (1991) has found that the residual stresses provide a significant contribution to the shear resistance when the flexural and diagonal crack widths are small in very shallow members with depths less than about 100 mm.

2.6.1.5 Arch action

The arching action occurs in short beams which applied loads are transferred directly to the supports. The main factors influencing this action are the span-to-depth ratio and the strength of the compression strut. El-Sayed et al. (2006) reported that a significant redistribution of internal forces can be predicted after cracking. This is not a shear transfer mechanism. That means, it does not transmit a tangential force to a nearby parallel plane, but permits the transfer of a vertical concentrated force to a reaction, thereby reducing the contribution of the other types of shear transfer. In general, arch action enhances the strength of a section. For arch action to develop, a horizontal reaction component is required at the base of the arch. In beams, this is usually provided by the tie action of the longitudinal bars.

2.6.2 Factors affecting shear capacity

The ultimate shear capacity and the shear failure mode for beams without shear reinforcement are affected by the following parameters as introduced by the (ASCE-ACI 1998):

1. Concrete tensile strength.
2. Longitudinal reinforcement ratio.
3. Shear span-to-depth ratio.
4. Axial forces.
5. Depth of concrete members (size effect).

2.6.2.1 Concrete tensile strength

The cracks of concrete beams without shear reinforcement occur when the principal tensile stress of the concrete exceeds the concrete tensile strength. The shear strength increased when increasing of the increase in concrete tensile strength. The tensile strength of concrete can be measured via a splitting test or from a modulus of rupture test but the two tests can be difficult in practice. The tensile strength of concrete can be ranged between 8 and 15% of the compressive strength of concrete f'_c and is approximately proportional to the square or cubic root of the compressive strength.

2.6.2.2 Longitudinal reinforcement ratio

The beams with high amounts of reinforcement had smaller and narrower cracks than the beam specimens with low amounts of reinforcement. The smaller cracks increased the uncracked concrete contribution by increasing the compression zone depth. The narrower crack width increased the interface shear by increasing the aggregate interlock in the cracked surface and the residual tensile stress. Moreover, the dowel action contribution can be increased by increasing the amount of reinforcement because that increases the dowel area.

2.6.2.3 Shear span-to-depth ratio

Shear span-to-depth ration, *a/d*, has be influenced on the shear capacity and the mode of failure of concrete beams without shear reinforcement. The shear span can be classified based on the *a/d* into four types:

1. Very short shear span: the *a/d* equals 0 to 1.0. These beams develop inclined cracks joining the load and the support. After inclined cracks, the behavior changes from beam action to arch action which can be fail by different ways (ASCE-ACI 1973):
    a. Anchorage failure of longitudinal reinforcement, often combined with dowel splitting effect;
    b. Bearing failure occurs above a support;
    c. Flexural failure due to the yielding of tension bars or the crushing of the compression zone;
    d. Tension failure of arch-rib near the top of an edge may occur because of the eccentricity of the thrust of the compressive stresses in the inclined strut; and
    e. Crushing of compression strut along the crack.

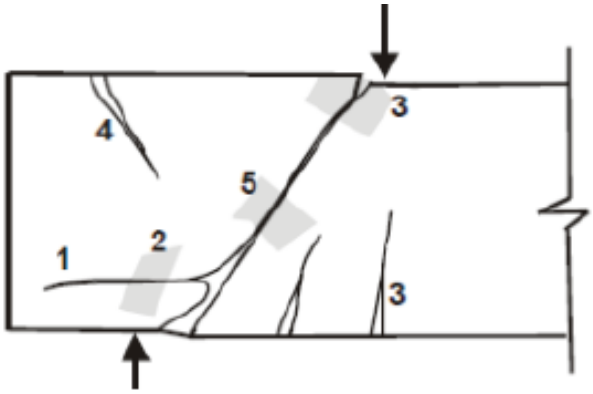

1: Anchorage failure.

2: Bearing failure.

3: Flexural failure.

4, 5: Crushing of compression strut.

Figure 2.12– Modes of failure of deep beams (ASCE-ACI 1973).

2. Short shear span: the shear span-to-depth ratio equals 1.0 to 2.5. These beams develop diagonal cracks and after redistribution of internal forces are able to carry additional load by arch action. The mode of failure of such beams will result from a bond failure, a splitting failure or a dowel failure along the longitudinal reinforcement, or by crushing of the compression zone over the shear crack, see Figure 2.26.

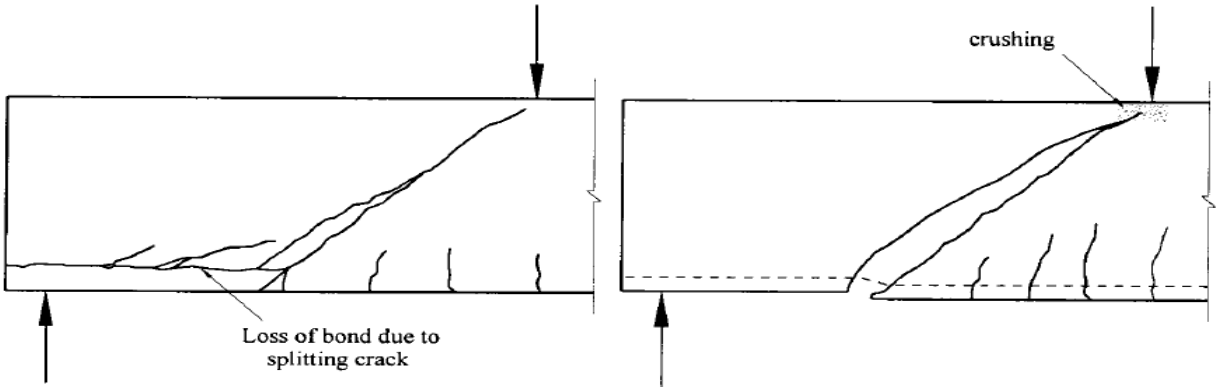

(a) Shear-tension failure (b) Shear-compression failure

Figure 2.13– Modes of failure of short shear spans with aid ranging from 1.5 to 2.5 (ASCE-ACI 1973).

3. Slender: with a/d ranges from 2.5 to 6.0. As shown in Figure 2.14, the inclined cracks propagate to reach to the beam fails at inclined cracking.

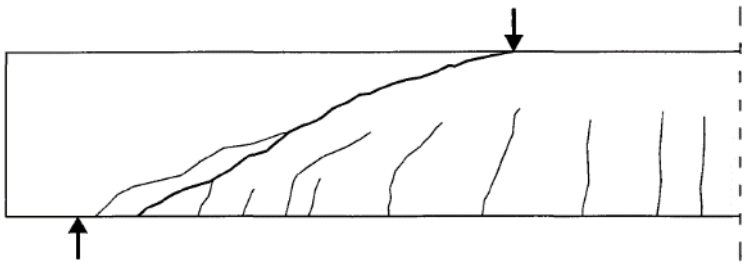

Figure 2.14– Typical shear failure of a slender beam.

4. Very slender: with a/d greater than 6.0. These beams will fail in flexure before the formation of inclined cracks.

2.6.2.4 Axial forces

The shear strength of concrete beams without stirrups will be decreased with increasing the axial tension forces. While, the axial compression forces will increase the shear resistance by delaying cracking and limiting the penetrated depth of the crack into the beam (ASCE-ACI 1998). On the other hand, the initial flexural crack will occur earlier in the member with axial tension and will extend farther resulting in a reduction in shear resistance. Beams without shear reinforcement subjected to large axial compression force and shear may fail in a very brittle manner at the instance of first diagonal cracking. While, beams subjected to tension and shear are comparatively ductile. The crack pattern for beams subjected to large axial tension and shear is shown in Figure 2.15. In the figure, the initial cracks are very steep and extend over the full depth of the member. Thus, longitudinal reinforcement is required at the top of the member, and the initial cracks. As the loading is increased, new, flatter inclined cracks form. Failure occurs only after the diagonal cracks become too flat to be controlled by the longitudinal reinforcement (Adebar and Collins 1996).

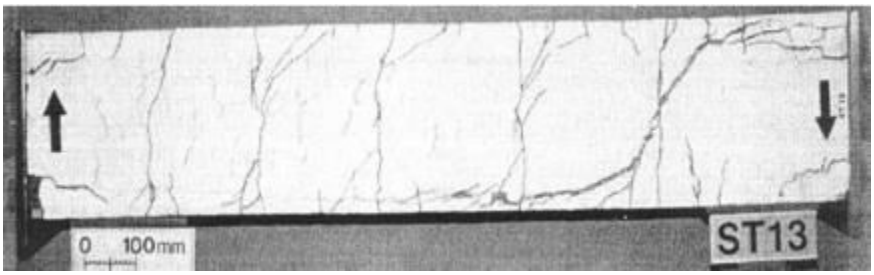

Figure 2.15– Typical crack pattern without stirrups subjected to axial tension and shear (Adebar and Collins 1996).

2.6.2.5 Depth of concrete members (size effect)

It was shown by (Kani 1967) that there is a very significant size effect on the shear strength of members without transverse reinforcement. The shear stress at failure decreases when the depth of the member increases due to a larger members will have the larger width of diagonal cracks. A larger crack width reduces the residual stresses and will reduce the ability to transmit crack interface shear stresses. The average shear stress to cause failure of the largest beam was about one-third the average shear stress to cause failure of the smallest beam (see Figure 2.16). On the other hand, the size effect will disappear when the longitudinal reinforcement is well distributed (Kuchma and Collins 1998). Figure 2.16 compares the results from large-scale beam tested by (Shioya et al. 1989) with predictions from ACI Code and modified compression field theory (MCFT).

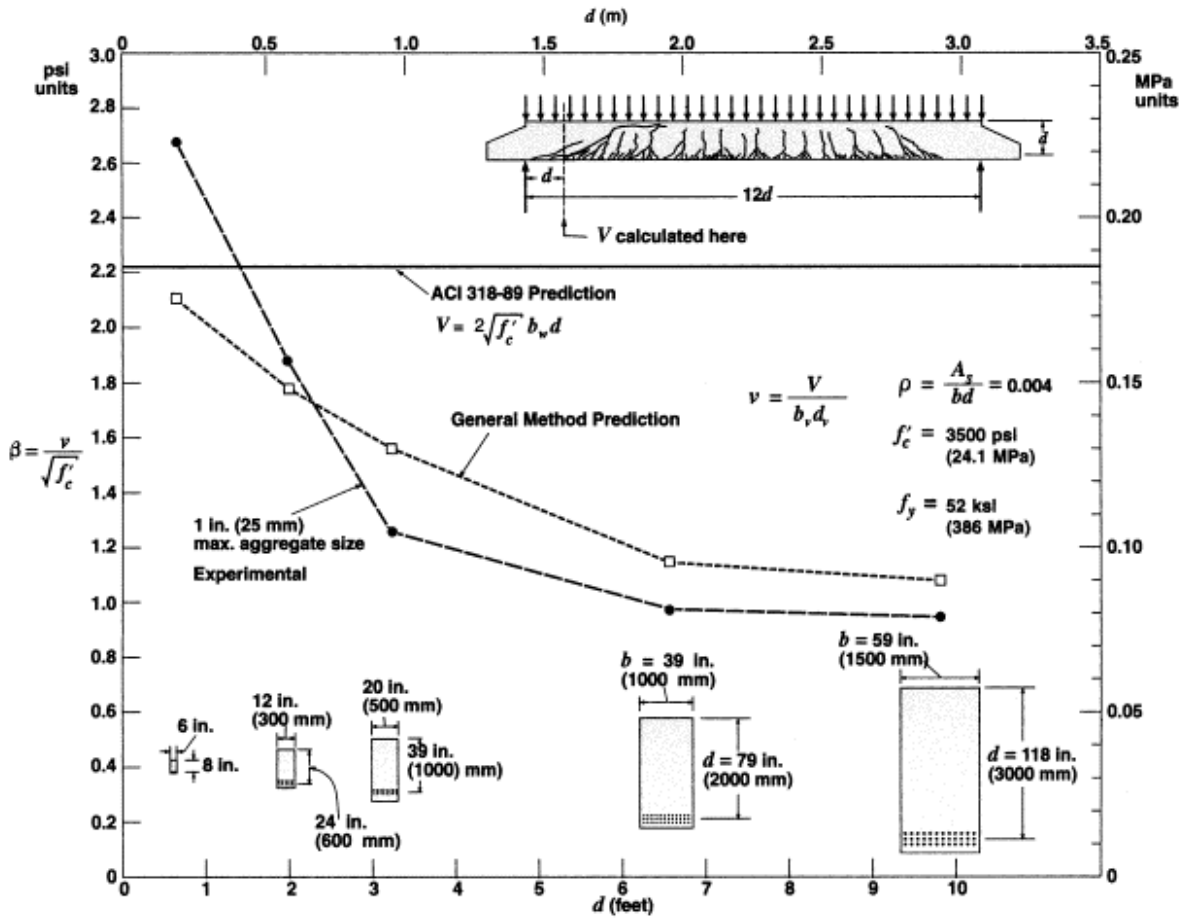

Figure 2.16– Comparison of large-scale beam tested by (Shioya et al. 1989) with predictions from ACI Code and MCFT (Collins and Mitchell 1997).

2.6.3 Research on shear behavior of RC beams

Numerous studies have been carried out on the shear behavior and performance of NWC beam and slab specimens reinforced with FRP bars without web reinforcement. Few shear studies have investigated concrete contribution to shear capacity in NWC structures incorporating BFRP bars as longitudinal reinforcement.

El-sayed et al. (2006) investigated the shear strength and behavior of concrete slender beams reinforced with FRP bars and without shear reinforcement. Nine full-scale RC beams were prepared and tested up to failure. The beams included three beams reinforced with GFRP bars, three beams reinforced with carbon-FRP (CFRP) bars, and three control beams reinforced with steel bars. All beams measured 3,250 mm long, 250 mm wide and 400 mm deep and were tested in four-point bending. The test results indicated that all nine beams failed in diagonal tension except the control beam, SN-1, which experienced steel yielding under loading simultaneously as the diagonal tension failure occurred. The typical diagonal tension failure mode of the tested beams is illustrated in Figure 2.17. In addition, the shear strength of RC beams with no stirrups is proportional to the axial stiffness of the longitudinal reinforcing bars.

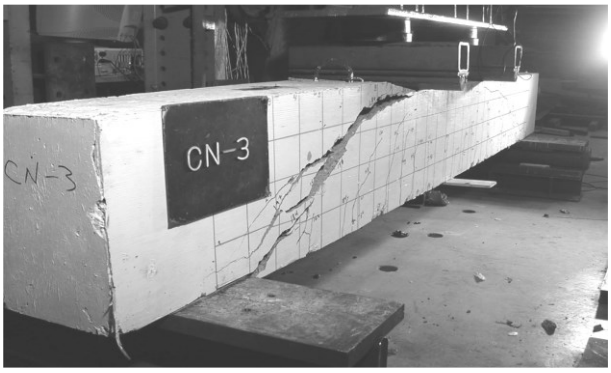

Figure 2.17– Typical diagonal tension failure mode- Beam CN-3 (El-sayed et al. 2006).

Tomlinson and Fam (2015) studied the shear performance of NWC beams reinforced with BFRP bars with/without stirrups. The beam specimens had 150 x 300 mm cross-sectional dimensions with a total length of 3,100 mm. In beam specimens without stirrups, the load at which major diagonal shear cracking occurred increased as BFRP flexural reinforcement ratio increased. The load then dropped by various amounts inversely proportional to reinforcement ratio, before it increased again to ultimate shear failure levels exceeding shear cracking load by percentages also inversely proportional to reinforcement ratio. Moreover, as a result of BFRP bars having lower axial stiffness than steel bars, the depth and width of the diagonal cracks increased due to

lower contribution of aggregate interlock and uncracked concrete in the compression zone (Tureyen and Frosch 2002).

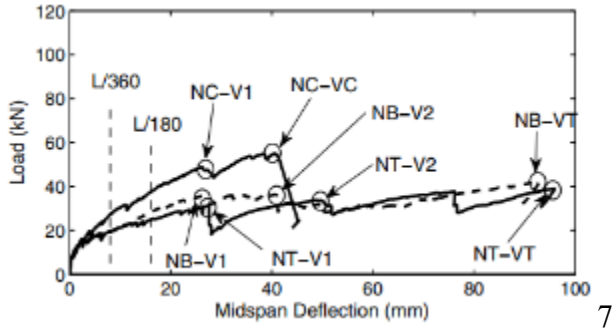

7

Figure 2.18– Load-deflection curves at mid-span (Tomlinson and Fam 2015).

El Refai and Abed (2015) investigated the shear behavior of concrete beams reinforced with BFRP bars without transverse reinforcement. The test program included eight beams reinforced with BFRP bars and two beams reinforced with longitudinal steel bars as control beams. The test parameters in this study were the longitudinal reinforcement ratio and the span-to-depth ratio of the beams. Figure 2.19 provides a schematic of the dimensions of beam specimens.

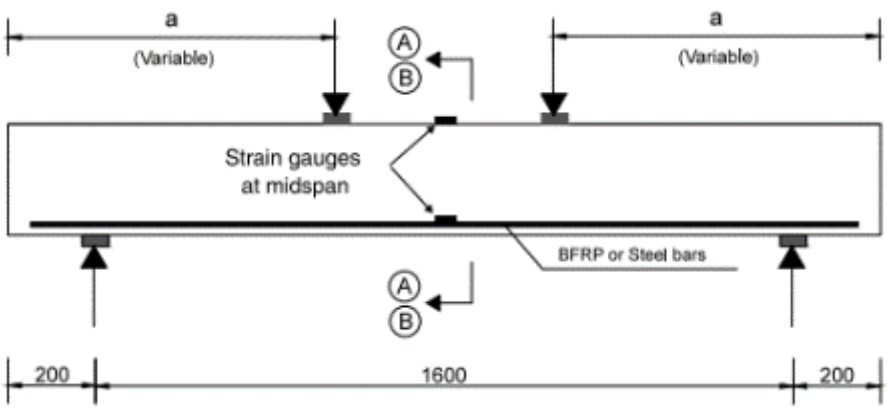

Figure 2.19– Beam details and test configuration (dimensions in mm) (El Refai and Abed 2015).

The test results were compared with predictions of different available codes and design guidelines. The test results were combined with the experimental results of a large database that included 75 specimens reinforced with different types of FRP bars. The results were also compared with shear strengths predicted using the ACI 440.1R-15, CSA 806-12, and CSA S6-10 codes and design guidelines. The main findings of this study can be summarized as follows:

1. Similar to beams reinforced with other conventional types of FRP bars, the concrete contribution to the shear strength in beams reinforced with BFRP bars increases as the axial rigidity of the longitudinal reinforcement, ρE, increases and decreases as the span-to-depth ratio, a/d, increases (for the same beam length and depth).
2. The shear design equations of CSA S806-12 standards provide the most accurate predictions for the concrete strength of beams reinforced with BFRP bars, with a mean value of 1.03 for the ratio V_{exp}/V_{pred}. However, some of the CSA 806-12 predictions are not conservative.
3. Both ACI 440.1R-15 and CSA S6-10 design methods provide conservative predictions with mean values of 1.94 and 1.57, respectively, for the ratio V_{exp}/V_{pred}.

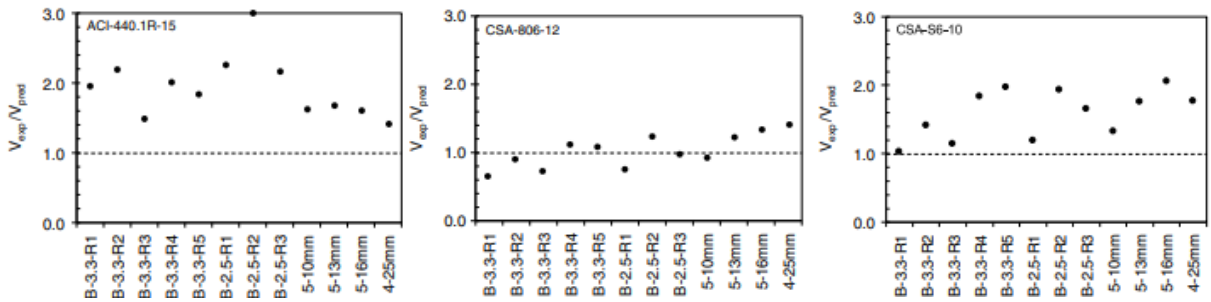

Figure 2.20– Comparison between V_{exp}/V_{pred} ratio for BFRP bars (El Refai and Abed 2015).

Generally, there is a paucity of the experimental studies regarding LWC beams reinforced with FRP bars. Pantelides et al. (2012a) studied the behavior and shear performance of RC panels reinforced with GFRP bars. Three NWC and three LWC specimens reinforced with identical GFRP reinforcement details were tested to failure. The main findings of this study can be summarized as follows:

1. The experimental shear capacity of NWC specimens reinforced with GFRP bars was greater than LWC specimens. The LWC specimens achieved 80% of the shear strength and 89% the deflection at maximum load of the NWC specimens.
2. The modifying ACI 440.1R-06 equations by applying a concrete density reduction factor of 0.85 could be employed to calculate the concrete shear capacity of sand LWC-reinforced GFRP panels.

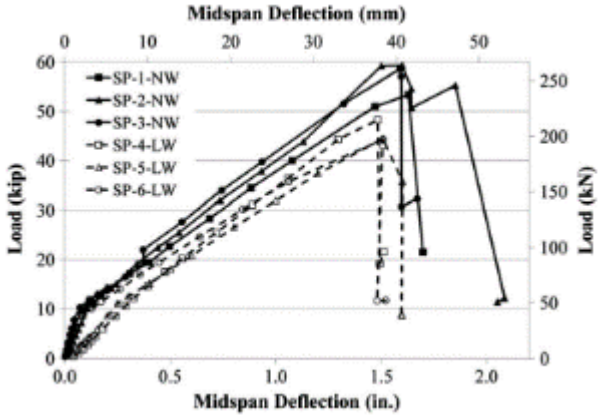

Figure 2.21– Load-deflection envelopes of all specimens (Pantelides et al. 2012a).

Kim and Jang (2014) investigated the contribution of concrete to the shear strength of NWC and LWC beams that are reinforced with FRP bars. 24 RC beams cast with LWC with two compressive strengths of 33.6 MPa and 40.3 MPa. The other beams cast with NWC with compressive strength 30 MPa. Lightweight aggregates for LWC made of mesalite and is produced in Japan and the content of the all LWC is about 1,800 kg/m^3. The dimensions of beams were 2,200 mm length, 250 mm depth, and 150 mm or 200mm width. Two FRP bars were used for each beam, and these FRP bars were CFRP and GFRP bar having 9 mm and 13 mm diameter, respectively. For each beam, two replicate specimens were fabricated to raise experimental accuracy. The test results indicated that the concrete shear capacities of LWC specimens reinforced with GFRP bars were equal to 75 % of the capacities predicted by the equation for NWC. For the sand-LWC panels reinforced with GFRP bars presented in Pantelides et al. (2012a), however, they were equal to 85% of the capacities predicted by the equation for NWC.

2.6.4 Review of shear design equations

The concrete shear capacity, V_c, of the tested BFRP RC beam specimens was computed using different shear design methods developed by several organizations in North America (CSA S806-12; CSA S6-19; ACI 440.1R-15). This section provides a brief description of the methods in current standards and guidelines. This study focused on the contribution of concrete to the shear capacity as the beam specimens had no transverse reinforcement. Therefore, equations related to the web shear-reinforcement capacity are not presented. The safety factors in the design equations used in this study were set equal to 1.0. Note that all the following equations are presented in the SI system of units, where stress is in megapascals (MPa), force is in Newtons (N), and length is in millimeters (mm).

2.6.4.1 ACI 440.1R-15 design guidelines

To account for the concrete shear capacity, V_c, of flexural elements with FRP bars as the longitudinal reinforcement, ACI Committee 440 recommends the following equations based on the uncracked concrete depth:

$$V_c = \frac{2}{5}\lambda\sqrt{f_c^{'}}b_w(kd) \tag{2.1}$$

$$k = \sqrt{2\rho_f n_f + \left(\rho_f n_f\right)^2} - \rho_f n_f \tag{2.2}$$

where kd is the cracked transformed section neutral-axis depth; $n_f = E_f / E_c$; and λ is the concrete density reduction factor for the influence of concrete weight. Based on the experiments carried out by Liu and Pantelides (2013), ACI Committee 440 specifies that λ =0.8 for SLWC in which all the fine aggregate is natural sand (NS). For sections with NSC with $f_c^{'} < 55$ MPa, the value of the modulus of elasticity of concrete, E_c, is calculated using the following equation

$$E_c = 0.043 w_c^{1.5}\sqrt{f_c^{'}} \tag{2.3}$$

where w_c is the density of concrete.

2.6.4.2 Canadian Standard Code, CSA S6-19

El-Sayed and Benmokrane (2008) proposed a new equation as a modification to the equation published in CSA standard for concrete elements reinforced with steel. The concrete shear capacity in CSA S6-19 depends on the shear resistance of the cracked concrete factor, β; the cracking strength of concrete, f_{cr}; width, b_v; and the effective shear depth, d_{long}. The computation of V_c according to CSA S6-19 provided under section 16 is expressed as:

$$V_c = 2.5\beta\phi_c f_{cr} b_v d_{long} \tag{2.4}$$

where f_{cr} shall be taken as $0.4\sqrt{f_c'}$, $0.34\sqrt{f_c'}$, or $0.3\sqrt{f_c'}$ (MPa) ≤ 3.2 MPa for normal-density concrete (NDC) with a density between 2,150 and 2,500 kg/m^3; semi-low-density concrete (SDC) with a density greater than 1,850 kg/m^3 but less than 2,150 kg/m^3; and low-density concrete (LDC) with a density less than 1,850 kg/m^3, respectively.

2.6.4.3 Canadian Standard Code, CSA S806-12

The contribution of concrete to the shear capacity in CSA S806-12 is based on the equation proposed by Razaqpur and Isgor (2006):

$$V_c = 0.05\lambda\phi_c (f_c^{'})^{\frac{1}{3}} b_w d_v k_m k_r k_s \tag{2.5}$$

$$0.11\phi_c \sqrt{f_c^{'}} b_w d_v \le V_c \le 0.22\phi_c \sqrt{f_c^{'}} b_w d_v, f_c^{'} \le 60\,MPa \tag{2.6}$$

where the coefficients of V_c shall be determined as follows:

$k_m = \sqrt{V_f d / M_f} \le 1.0$ is the coefficient accounting for the effect of moment to shear; $k_r = 1 + (E_c \rho_{Fw})^{1/3}$ is the coefficient accounting for the effect of reinforcement rigidity; $k_s = 1.0$ for ($d \le 300$ mm); and $k_s = 750/(450 + d) \le 1.0$ for (d more than 300 and $A_{Fv} \le A_{vF}$) is the coefficient accounting for the effect of member size. CSA S806-12 specifies that λ =1.0 for NDC; λ = 0.85 for structural SCD (SLWC), in which all the fine aggregate is NS; and λ = 0.75 for structural LDC in which none of the fine aggregate is NS. These values of λ are the same as those specified in ACI 318R-19.

2.6.4.4 Hoult et al. (2008) Equation

Hoult et al. (2008) proposed an equation to predict the shear strength of FRP RC members without stirrups. This equation has been used in the knowledge that the average longitudinal strain for FRP reinforcement will exceed a value of about 1×10^{-3} (0.1%). The Hoult et al. (2008) shear-strength equation of the FRP RC beam specimens is given as follows:

$$V_c = \left[\frac{0.3}{0.5 + (1000\varepsilon_x + 0.15)^{0.7}}\right]\left[\frac{1300}{(1000 + s_{ze})}\right]\sqrt{f_c^{'}} b_w d_v \tag{2.7}$$

The first term, $\left[\frac{0.3}{0.5+(1000\varepsilon_x+0.15)^{0.7}}\right]$, is related to diagonal crack width; the second term, $\left[\frac{1300}{(1000+s_{ze})}\right]$, is a correction factor for size effect. The strain effect and the size effect are included in the strain term ε_x and the size effect term s_{ze}. It should be noted that the concrete members are not subjected to axial load and are not prestressed. The strain term and the size effect term are taken to be:

$$\varepsilon_x = \frac{M_f / d_v + V_f}{2E_f A_f} \tag{2.8}$$

where M_f and V_f = bending moment and shear force at the critical section for shear.

$$s_{ze} = \frac{31.5d}{16 + a_g} \geq 0.77d \tag{2.9}$$

where a_g is the maximum aggregate size for coarse aggregate in mm. It has been found that in LWC, the cracks propagate through the aggregate particles rather than around them. Therefore, Hoult et al. (2008) recommended that a_g should be taken as zero in LWC.

2.7 Flexural behavior and serviceability of FRP-RC beams

2.7.1 Research on flexural behavior and serviceability of FRP-RC beams

Considerable research work has focused on the flexural behavior and serviceability of FRP-reinforced NWC beam specimens.

Kassem et al. (2011) assessed the performance of 24 NWC beam specimens reinforced with either FRP or steel reinforcement under flexural loads. The beams were 3,300 mm long with a rectangular cross section of 200 mm in width and 300 mm in depth. Their results show that the moment capacities of the FRP-reinforced NWC beams were higher than that of the counterpart control steel beams with the same amount of reinforcement. Moreover, since FRP bars have a modulus of elasticity lower than that of steel, the FRP-reinforced NWC beams evidenced larger deflections and crack widths than the steel beams at the same reinforcement ratio. In addition, the NWC specimens with sand-coated FRP bars showed more cracks and reduced average crack spacing than the NWC specimens with ribbed FRP bars. Figure 2.22 shows the moment–deflection relationships at the mid-span of the beam specimens.

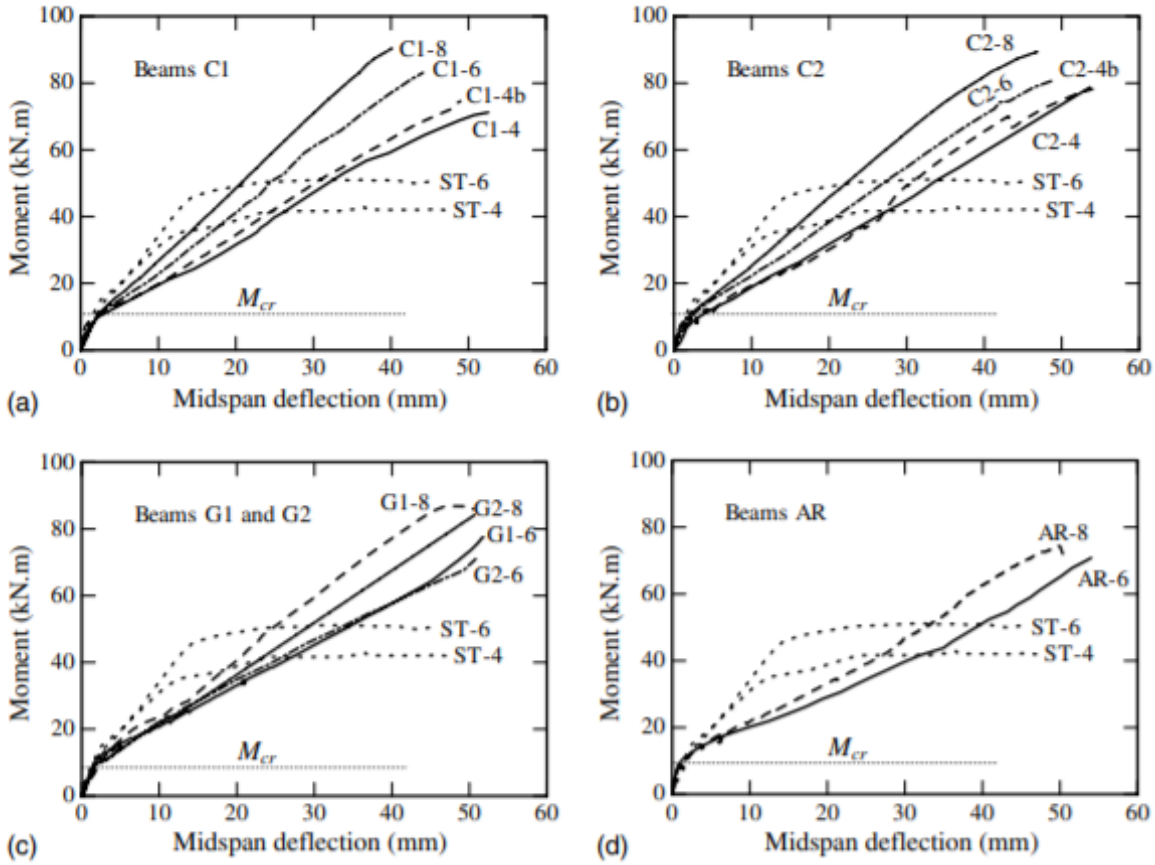

Figure 2.22– Moment-deflection relationships for the tested beams: (a) beams C1; (b) beams C2; (c) beams G1 and G2; (d) beams AR (Kassem et al. 2011).

El-Nemr et al. (2016) tested 16 NWC beams reinforced with different FRP types up to failure. The beams were reinforced with sand-coated GFRP bars, helically-grooved GFRP bars, and sand-coated CFRP bars. Their results show that the number of cracks appearing in the pure bending zone was affected by the type and diameter of the FRP reinforcing bars as well as concrete strength, which implicitly includes the effect of bond characteristics (Figure 2.23). The sand-coated GFRP bars exhibited lower bond-dependent coefficient (k_b) values than the helically grooved GFRP bars. Moreover, they found that the ACI 440.1R-06 and ISIS Canada Research Network (2007) guidelines overestimated the predicted crack widths of the NWC beams at $0.30M_n$ (service load).

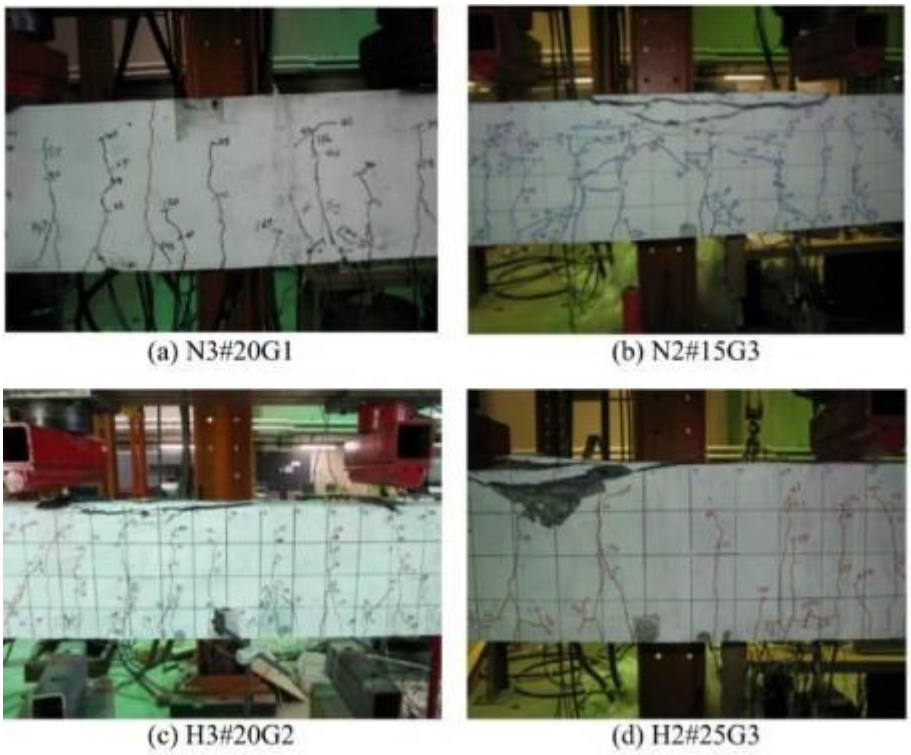

Figure 2.23– Typical crack pattern of the pure bending zone at failure (El-Nemr et al. 2016).

Tomlinson and Fam (2015) investigated the flexural performance of BFRP-reinforced NWC beams with BFRP or steel stirrups. Their results indicate that the moment capacities of the BFRP-NWC beams tested were higher than that of the counterpart control steel beam with the same amount of reinforcement. Moreover, ACI 440.1R-6 and CSA S806-12 adequately predicted the moment capacity of the BFRP-NWC beams.

Abed et al. (2021) tested 14 slender BFRP-reinforced NWC beams under flexural loads. Seven beams were made with high-strength concrete (HSC) and seven others with NSC. The beam specimens measured 180 mm wide, 230 mm high, and 2,200 mm long.

The main findings of this study can be summarized as follows:

1. The increasing moment capacity of the BFRP-NWC specimens with increasing amount of reinforcement was quite consistent with the ACI 440.1R-15 equation (see Figure 2.24). In addition, using HSC enhanced the cracking moment by 10% compared to the NSC beams.
2. The average bond-dependent coefficient kb for BFRP-reinforced NWC beams was found to be around 0.70 which indicates a good bond between the sand-coated FRP bars and

surrounding concrete. The results suggest that the value of 1.4 recommended by the ACI 440.1R-15 may be very conservative.

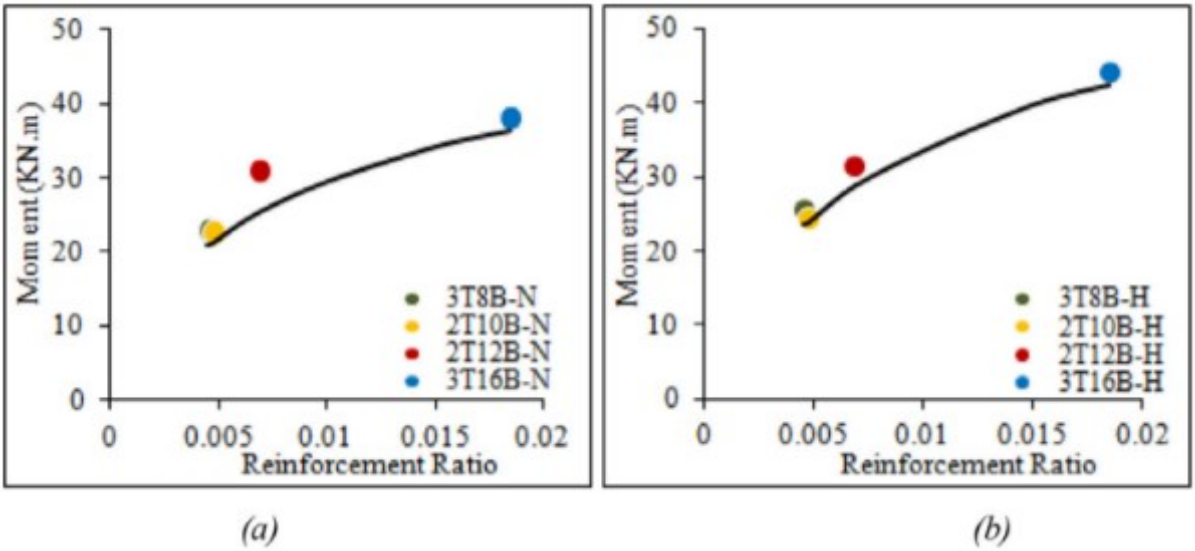

Figure 2.24– ultimate moment vs. reinforcement ratio curve: (a) NSC and (b) HSC (Abed et al. 2021).

In recent years, a few experimental studies have been conducted recently to assess the influence of FRP reinforcing bars on the flexural behavior and serviceability of LWC beam specimens. Wu et al. (2019) tested nine RC beam specimens with GFRP bars under flexural loads. The specimens were made with LWC and steel fiber-reinforced LWC (SFLWC). The test results indicate that the beams made with SFLWC exhibited narrower cracks than those made with LWC. In addition, the reinforcement ratio significantly affected serviceability performance for LWC and SFLWC beam specimens. As the reinforcement ratio increased, the specimens exhibited lower deflections at the same load levels (Figure 2-25). The ACI 440.1R-15 underestimated the load-carrying capacity of the specimens that failed by concrete crushing and overestimated the load-carrying capacity of the specimens that were damaged due to FRP rupture.

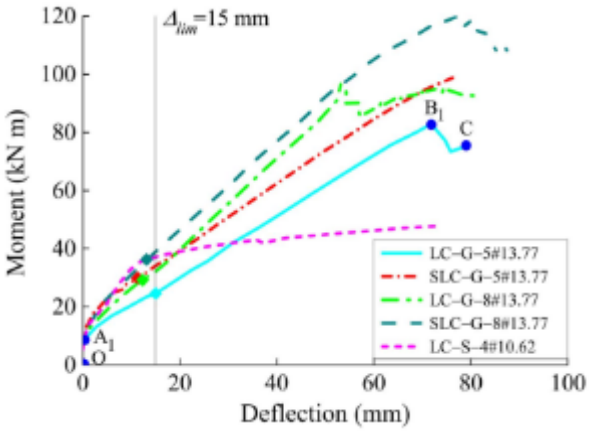

Figure 2.25– Load–deflection response for the beam specimens. (Wu et al. 2019)

Liu et al. (2020) studied the applicability of using GFRP and CFRP bars as longitudinal reinforcement in LWC beams. A total of 14 simply supported beams that measured 200 mm wide (b) × 300 mm deep (h) were fabricated and tested (Figure 2.26). All the specimens were placed into a standard curing room maintained at 20 ± 2 °C and 95 ± 10% relative humidity until testing time. The test parameters were steel fiber content, reinforcement ratio, bar diameter, and clear span.

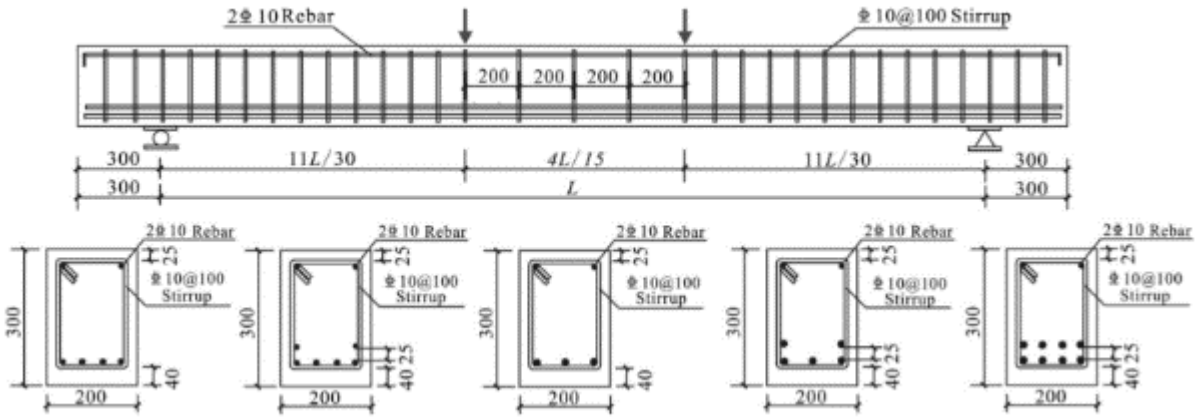

Figure 2.26– Specimen details (dimensions in millimeters) (Liu et al. 2020).

The test results show that the failure of all specimens occurred by concrete crushing, as shown in Figure 2.27. Moreover, comparing the crack-width predictions show that the provisions in the ACI 440.1R-06 overestimated the predicted crack widths at service load for the LWC beams, while those in the ISIS Canada Research Network design manual (2007) predicted reasonable crack-width values.

Figure 2.27– Typical cracking patterns of the constant moment zone at failure (LCC–6#8–3) (Liu et al. 2020).

2.7.2 Flexural capacity of FRP RC members

The theoretical flexural capacity of beams can be calculated by considering the force equilibrium and strain compatibility according to the following equations:

$$\alpha_1 f_c^{'} ba + A_f^{'} f_f^{'} = A_f f_f \tag{2.10}$$

$$\varepsilon_f = \frac{\left(d - \frac{a}{\beta_1}\right)}{\frac{a}{\beta_1}} \varepsilon_{cu} \tag{2.11}$$

$$\varepsilon_f^{'} = \frac{\left(\frac{a}{\beta_1} - d^{'}\right)}{\frac{a}{\beta_1}} \varepsilon_{cu} \tag{2.12}$$

$$f_f = \varepsilon_f E_f \tag{2.13}$$

$$f_f^{'} = \varepsilon_f^{'} E_f^{'} \tag{2.14}$$

$$M_n = A_f f_f \left(d - \frac{a}{2}\right) + A_f^{'} f_f^{'} \left(\frac{a}{2} - d^{'}\right) \tag{2.15}$$

where M_n is the nominal moment capacity (kN-m); A_f and $A^{'}_f$ are the area of the tension and compressive FRP bars (mm^2), respectively; f_f and $f^{'}_f$ are the stresses in the tension and compressive FRP bars (MPa), respectively; ε_f and $\varepsilon^{'}_f$ are the strains in the tension and compressive FRP bars, respectively; d is the distance from the compression face of the concrete

to the center of the tension FRP bars (mm); a is the depth of equivalent rectangular stress block (mm); d' is the distance from the compression face of the concrete to the center of the compressive FRP bars (mm); and b is the width of the beam. The α_1 and β_1 factors can be computed with the following equations:

ACI 440.1R-15

$$\alpha_1 = 0.85 \tag{2.16}$$

$$\beta_1 = 0.85 - 0.00714\left(f_c' - 28\right) \geq 0.65 \tag{2.17}$$

CSA S806-12

$$\alpha_1 = 0.85 - 0.0015 f_c' \geq 0.67 \tag{2.18}$$

$$\beta_1 = 0.97 - 0.0025 f_c' \geq 0.67 \tag{2.19}$$

2.7.3 Curvature and Deformability

Beam curvature is considered an important term that points out the deformation of a RC element under applied loads. The curvature (ψ) was calculated at the mid-span of the specimens using the calculated neutral-axis depth and the experimental FRP and concrete strains as follows:

$$\psi = \frac{\varepsilon_c}{c} \tag{2.20}$$

$$c = \left(\frac{\varepsilon_c}{\varepsilon_c + \varepsilon_f}\right) d \tag{2.21}$$

where ε_c is the concrete strain in the extreme fiber in compression and c is the depth of the neutral axis.

Ductility is the ability of RC elements to absorb energy without strength loss. Ductility is related to inelastic deformation, which occurs prior to complete failure. In case of steel RC elements, ductility can be estimated as the ratio of the total deformation at failure divided by the deformation at yielding. As a result of linear behavior of the BFRP bars up to failure, this approach to calculating ductility cannot be applied to BFRP-LWSCC beams. In this study, the

CSA S6 (2019) approach was used to compute the deformability factor (*J-factor*) of the BFRP-LWSCC beams. This approach is based on deformability instead of absorbed energy to ensure that the BFRP-LWSCC specimens exhibited adequate deformation prior to failure. According to CSA S6 (2019), the *J-factor* should be at least 4.0 and 6.0 for rectangular and T-sections, respectively, and is calculated as follows:

$$J = \frac{M_{ult}\psi_{ult}}{M_c\psi_c} \tag{2.22}$$

Where M_{ult} is the ultimate bending moment; ψ_{ult} is the ultimate curvature; M_c is the bending moment at a concrete strain of 0.001; and ψ_c is the curvature at a concrete strain of 0.001.

2.7.4 Review of serviceability equations

2.7.4.1 Deflection equations

The immediate mid-span deflection for a simply supported RC element can be estimated as follows:

$$\delta = \frac{(P/2)x}{24E_cI_e}\left[3L^2 - 4x^2\right] \tag{2.23}$$

where $E_c = 0.043\gamma_c^{1.5}\sqrt{f_c'}$ for the equilibrium concrete density (γ_c) between 1,440 and 2,560 kg/m^3 (ACI 318R-19).

CSA S806-12 recommends curvature integration by assuming a fully cracked section without any contribution of tension stiffness in the cracked zones. For simple loading cases, Eq. (2.24) is provided for a simply supported beam with two equal point loads *P/2* placed at a distance *x* from the supports, as follows:

$$\delta = \frac{(P/2)L^3}{24E_cI_{cr}}\left[3\left(\frac{x}{L}\right) - 4\left(\frac{x}{L}\right)^3 - 8\left(1 - \frac{I_{cr}}{I_g}\right)\left(\frac{L_g}{L}\right)^3\right] \tag{2.24}$$

where $E_c = \left[3300\sqrt{f_c'} + 6900\right]\left[\frac{\gamma_c}{2300}\right]^{1.5}$ for concrete γ_c between 1,500 and 2,500 kg/m^3; I_{cr} is the cracking moment of inertia; L is the clear span; and L_g is the distance from support to point where M_a is M_{cr}.

2.7.4.1.1 Effective moment of inertia models

The flexural stiffness of a RC member varies along its span because of the cracks that can occur from the applied moment. The flexural stiffness at cracks is affected by the concrete in compression and the reinforcement, while the concrete carries no tension. Between the cracks, however, the concrete helps resist tensile stress due to the bond between the concrete and reinforcement. This impact is often referred to as tension stiffening and is taken into account with I_e. I_e allows for a gradual transition from uncracked to cracked transformed section as the applied moment increases. The value of I_e is between I_g and I_{cr}, depending on how much of the RC element has cracked.

Several models have been introduced by various researchers and design codes to define I_e for FRP-RC members. The Benmokrane et al. (1996) model is one of the first approaches introduced to improve the performance of Branson's equation through a comprehensive experimental program on GFRP-RC beams. Benmokrane et al. (1996) initially proposed an equation for calculating the I_e for GFRP-RC beam specimens, as follows:

$$I_e = \left(\frac{M_{cr}}{M_a}\right)^3 \frac{I_g}{\beta} + \left[1 - \left(\frac{M_{cr}}{M_a}\right)^3\right] \alpha I_{cr} \leq I_g \tag{2.25}$$

where α and β are 0.84 and 7.0, respectively.

Thériault and Benmokrane (1998) continued experimentally studying the deflection behavior of GFRP-RC beam specimens, and then introduced a new modification to Branson's equation, as follows:

$$I_e = \left(\frac{M_{cr}}{M_a}\right)^3 \beta_d I_g + \left[1 - \left(\frac{M_{cr}}{M_a}\right)^3\right] I_{cr} \leq I_g \tag{2.26}$$

where β_d is the reduction factor equal to 0.6. This factor was later modified by Gao et al. (1998) [Eq. (2.27)] and adopted in ACI 440.1R-03.

$$\beta_d = \alpha_b I_g \left(\frac{E_f}{E_s} + 1\right) \tag{2.27}$$

where α_b is the bond-dependent coefficient equal to 0.5; E_f and E_s are the moduli of elasticity of the FRP and steel bars, respectively.

Based on an assessment of the experimental results from several studies, ACI 440.1R-06 proposed the following simple relationship for β_d

$$\beta_d = 0.2\left(\frac{\rho_f}{\rho_{fb}}\right) \leq 1.0 \tag{2.28}$$

Bischoff (2005) proposed an equation for estimating I_e based on the tension stiffening concepts as follows:

$$I_e = \frac{I_{cr}}{1-\left(\frac{M_{cr}}{M_a}\right)^2\left(1-\frac{I_{cr}}{I_g}\right)} \tag{2.29}$$

ISIS Canada Research Network (2007) offered an equation to calculate the I_e based on the study conducted by Mota et al. (2006) as follows:

$$I_e = \frac{I_t I_{cr}}{I_{cr}+\left(1-0.5\left(\frac{M_{cr}}{M_a}\right)^2\right)\left(I_t - I_{cr}\right)} \tag{2.29}$$

ACI 440.1R-15 recommends estimating I_e with the equation suggested by Bischoff and Gross (2011) as follows:

$$I_e = \frac{I_{cr}}{1-\gamma\left(\frac{M_{cr}}{M_a}\right)^2\left(1-\frac{I_{cr}}{I_g}\right)} \leq I_g \tag{2.30}$$

The reduction factor γ provided in the above equation to account for the variation in stiffness along the span is expressed as:

$$\gamma = \frac{3\left(\frac{x}{L}\right)-4\left(4\left(\frac{M_{cr}}{M_a}\right)-3\right)\left(\frac{x}{L}\right)^3}{3\left(\frac{x}{L}\right)-4\left(\frac{x}{L}\right)^3} \tag{2.31}$$

It should be noted that a simpler expression defined by Bischoff (2018) for the gamma factor is as follows

$$\gamma = (1+\alpha) - \alpha\left(\frac{M_{cr}}{M_a}\right) \tag{2.32}$$

$$\alpha = \frac{4}{0.75\left(\frac{L}{x}\right)^2 - 1} \tag{2.33}$$

2.7.4.2 Crack-Width Equations

CSA S6-19 specifies Eq. (2.34) to account for the crack-width of flexural elements reinforced with longitudinal FRP bars as:

$$w_{cr} = 2\frac{f_{fs}}{E_f}\frac{h_2}{h_1}k_b\sqrt{d_c^2 + (s_{\max}/2)^2} \tag{2.34}$$

where h_2 is the distance from the neutral axis to the tension face of the concrete; h_1 is the distance from the neutral axis to the center of the tension bars; and d_c is the distance from the center of the tension bars to the tension face of the concrete. The k_b value shall be calculated by using the test method in CSA S806-12 In the absence of experimental data for k_b, CSA S6-19 recommends a k_b of 0.8 and 1.0 for sand-coated and deformed FRP bars, respectively.

ACI 440.1R-15 specifies an indirect procedure that controls crack-width with a maximum bar spacing based on the approach proposed by Ospina and Bakis (2007):

$$s_{\max} = 1.15\frac{E_f}{f_{fs}}\frac{w_{cr}}{k_b} - 2.5c_c \le 0.92\frac{E_f}{f_{fs}}\frac{w_{cr}}{k_b} \tag{2.35}$$

Eq. (2.34) forms the basis of Eq. (2.35). where s_{max} is the maximum allowable bar spacing for flexural-crack control (mm); f_{fs} is the stress level induced in FRP bars at service loads (MPa); w_{cr} is the maximum permissible crack-width (mm); and c_c is the clear concrete cover (mm). k_b is the bond-dependent coefficient, which calculates the bond between the FRP bars and surrounding concrete. The k_b value shall be calculated experimentally, but, when the experimental data is not available, ACI 440.1R-15 suggests a conservative value of 1.4 for FRP

bars. The evaluation of the maximum allowable bar spacing shall be based on a d_c value that complies with the following equation

$$d_c \leq \frac{E_f w}{2 f_{fs} \beta k_b} \tag{2.36}$$

CHAPTER 3

Contribution of Lightweight Self-Consolidated Concrete (LWSCC) to Shear Strength of Beams Reinforced with Basalt FRP Bars

Foreword

Authors and Affiliation:

- Shehab Mehany: Ph.D. candidate, Department of Civil Engineering, Université de Sherbrooke, Sherbrooke, Quebec, Canada, J1K 2R1.
- Hamdy M. Mohamed: Research Associate/Lecturer, Department of Civil Engineering, Université de Sherbrooke, Sherbrooke, Quebec, Canada, J1K 2R1.
- Brahim Benmokrane: Professor, Department of Civil Engineering, Université de Sherbrooke, Sherbrooke, Quebec, Canada, J1K 2R1.

Journal Title: *Engineering Structures, Elsevier.*

Paper Status: *Published* (https://doi.org/10.1016/j.engstruct.2020.111758).

Abstract

To date, the shear contribution of lightweight self-consolidating concrete (LWSCC) members reinforced with basalt fiber-reinforced polymer (BFRP) bars (LWSCC-BFRP) has not yet been investigated. Therefore, the anticorrosion properties of BFRP bars combined with the advantages of LWSCC motivated this research to assess the behavior of such members under shear. Eight beams cast using LWSCC and normal-weight concrete (NWC) reinforced with BFRP or steel bars were prepared and tested up to failure. The specimens had a total length of 3,100 mm and concrete cross section of 200 mm in width and 400 mm in depth. The influence of two different types of BFRP bars of comparable quality and commercially available (sand-coated basalt and helically grooved basalt) on shear capacity was assessed. The tested beams included five beams reinforced with BFRP bars, one beam reinforced with steel bars and two beams constructed using NWC for comparison purposes. The experimental results indicate that the adoption of LWSCC allowed for decreasing the self-weight of the reinforced concrete (RC) beams (density of 1,800 kg/m^3) compared to NWC. Test results show that the concrete shear capacity of the LWSCC beams increased as did the axial stiffness of the longitudinal BFRP reinforcing bars. The test results were compared with the shear capacities predicted using the provisions in several standards. Using a 0.75 concrete density reduction factor in the CSA 2012 shear equation to consider the influence of concrete density yielded a more accurate value for the concrete shear capacity. In addition, using a 0.8 concrete density reduction factor in the ACI 440.1R-15 design equation yielded an appropriate degree of conservatism compared to the NWC beams.

Keywords: Lightweight self-consolidating concrete; BFRP bars; reinforced-concrete beams, shear; ultimate capacity, crack patterns, strains, modes of failure, design codes.

3.1 Introduction

Over the years, reinforced concrete (RC) structures have become the most common structures in the world due to their relatively low construction costs, high availability, and potentially long service lives. Sometimes, however, the relatively high self-weight of RC structures results in impractical structural solutions. Lighter concrete with high strength would be very desirable for many applications, including high-rise buildings and bridge structures. Lightweight concrete (LWC) benefits include lower cost by reducing the dead load, cutting substructure and foundation costs, and improving the seismic structural response. In addition, LWC provides better performance in terms of insulation, fire, and freeze–thaw resistance (Xiao et al. 2016). Since LWC was presented, different types have been introduced and evolved to meet industry requirements. One of the latest inventions in LWC industry is lightweight self-consolidating concrete (LWSCC) (Okamura and Ouchi 2003). LWSCC can be defined as a new kind of high-performance concrete (HPC) in building industry. LWSCC combines the benefits and characteristics of LWC and self-consolidating concrete (SCC). Therefore, incorporating lightweight aggregate (LWA) into SCC might produce high strength LWC (HSLWC), improve quality, and prevent the segregation of LWA (Hwang and Hung 2005, Wang 2009). In addition, the freeze/thaw resistance of LWSCC has been improved through various means, including proper moisture conditioning of LWA and proper amounts of air entrainment (ACI 213R-14).

Nowadays, fiber-reinforced polymer (FRP) bars are being more accepted in many design codes (CSA S806-12, CSA S6-19, and ACI 440.1R-15) as an alternative reinforcement to conventional steel bars in RC members. This is because of their lower weight, higher tensile strength compared to conventional steel bars, and corrosion resistance. Recently, basalt-FRP (BFRP) bars have been introduced into the building industry as an alternative type of FRP bars. BFRP has been shown to be noncorrodible (Elgabbas et al. 2015) as well as exhibiting higher tensile strength compared to GFRP and good bond strength between BFRP and concrete (Ovitigala and Issa 2013). BFRP also provides good thermal resistance, excellent freeze/thaw resistance, and excellent resistance to acidic environments (Wei et al. 2010).

Numerous studies have been carried out on the shear behavior and performance of normal-weight concrete (NWC) beam and slab specimens reinforced with FRP bars (NWC-GFRP) without web reinforcement (El-Sayed et al. 2006, Razaqpur et al. 2011, Kim and Jang 2014, and Ali et al. 2017a). Few shear studies (Tomlinson and Fam 2014, El Refai and Abed 2015, and

Issa et al. 2015) have investigated concrete contribution to shear capacity in NWC structures incorporating BFRP bars as longitudinal reinforcement. Tomlinson and Fam (2014) studied the shear performance of NWC beams reinforced with BFRP bars (NWC-BFRP) with/without stirrups. In beam specimens without stirrups, the concrete shear capacity increased as the amount of the longitudinal BFRP reinforcement increased. Moreover, as a result of BFRP bars having lower axial stiffness than steel bars, the depth and width of the diagonal cracks increased due to lower contribution of aggregate interlock and uncracked concrete in the compression zone (Tureyen and Frosch 2002). ACI-ASCE Committee 445 (1998) reported that a cracked reinforced concrete beam without web reinforcement resists shear stresses by means of (1) uncracked concrete, (2) aggregate interlock, (3) dowel action of the longitudinal reinforcement, (4) arch action, and (5) residual tensile stresses across the inclined crack. El Refai and Abed (2015) and Issa et al. (2015) demonstrated that the behavior and the predicted concrete shear capacity of NWC-BFRP beam specimens were consistent with those of NWC beams reinforced with other types of FRP bars.

Generally, there is a paucity of the experimental studies regarding LWC beams reinforced with FRP bars (Pantelides et al. 2012a, b, Liu and Pantelides 2013, and Kim and Jang 2014). Pantelides et al. (2012a) studied the behavior and shear performance of sand-LWC (SLWC) panels reinforced with GFRP bars (SLWC-GFRP). The results showed that modifying ACI 440.1R-06 equations by applying a concrete density reduction factor of 0.85 could be employed to calculate the concrete shear capacity of SLWC-GFRP panels. This is comparable to the ACI 318R-19. Kim and Jang (2014) reported that the concrete shear capacities of LWC specimens reinforced with GFRP bars (LWC-GFRP) were equal to 75 % of the capacities predicted by the equation for NWC. For the SLWC-GFRP panels presented in Pantelides et al. (2012a), however, they were equal to 85% of the capacities predicted by the equation for NWC. On the other hand, Sathiyamoorthy (2016) studied the shear behavior of LWSCC beam specimens reinforced with steel bars (LWSCC-steel) and estimated the contribution of concrete to overall shear capacity. The test results showed that all shear design codes conservatively predicted the shear capacity of the LWSCC beam specimens.

3.2 Objectives

To date, all the research on LWC has focused on LWC members with GFRP reinforcement. The authors know of no experimental data on the use of LWSCC with BFRP bars as longitudinal

reinforcement. In addition, the design standards and guidelines (CSA S806-12, CSA S6-19, and ACI 440.1R-15) do not provide specific information about BFRP-reinforced LWSCC beams. This paper focuses on LWSCC beams reinforced with various types of BFRP longitudinal reinforcement at different reinforcement ratios. Accordingly, this study has various objectives: (1) to evaluate the behavior and concrete shear capacity of the BFRP-reinforced LWSCC members, (2) to analyze the effect of types of BFRP bars and reinforcement ratio on concrete shear capacity, (3) to compare the shear behavior of BFRP-reinforced LWSCC beam specimens without shear reinforcement with that of BFRP-reinforced NWC specimens tested in this research program and from past studies, and (4) to assess the accuracy of the current design provisions (CSA S806-12, CSA S6-19, and ACI 440.1R-15).

3.3 Experimental Investigation

3.3.1 Material Properties

3.3.1.1 Lightweight self-consolidating concrete (LWSCC)

The beams were cast in the laboratory with two types of concrete (LWSCC and NWC) with an average cylinder capacity of 40 MPa at 28-day. NWC, supplied by a local supplier, was ready-mixed concrete, while LWSCC was mixed in the University of Sherbrooke's laboratories. The LWSCC mixtures were made with two types of LWAs—Solite 307 and Solite 343—from a single source (Northeast Solite). The LWA properties met the current requirements in ASTM C330/C330M-17a (2017). Table 3.1 presents the physical properties of aggregates. In addition, the cement was a TerC3 cement consisting of 75%, 20%, and 5% for GU cement, class F fly ash, and silica fume, respectively. Table 3.2 gives the details of the mix proportions of the two types of concrete (LWSCC and NWC). The equilibrium density of the LWSCC was 1,800 kg/m^3 (112.8 lb/ft^3) and was measured according to ASTM C567/C567M (2014). The actual compressive strengths of concrete, f'_c, were determined in accordance with ASTM C39/C39M (2018) from six concrete cylinders (100 x 200 mm) for the LWSCC and NWC. The actual slump-flow value of LWSCC prior to casting ranged between 670 and 710 mm. Table 3.4 presents the actual concrete compressive strengths for the beam specimens. All cylinders were cured under identical conditions with the beams. The average tensile strengths were 3.1 and 3.6 for the LWSCC and NWC, respectively. The split cylinder tests were conducted on cylinders 100 mm in diameter × 200 mm in length.

Table 3.1 – Physical properties of aggregates

Materials	Specific Gravity	Water Absorption (%)	Maximum Particle-Size (mm)
Lightweight coarse aggregates	1.47	11.2	15
Lightweight sand	1.65	18.5	5
Natural sand	2.65	0.98	5.15

Table 3.2 – LWSCC and NWC mix proportions

LWSCC		NWC	
Type TerC3 cement	543 kg /m^3	Type GU cement	244 kg/m^3
		Type GUb-SF cement	216 kg/m^3
w/c	0.33	w/c	0.35
Lightweight coarse aggregate	369 kg /m^3	Crushed stone: 5–20 mm	730 kg /m^3
Lightweight sand	488 kg /m^3	Crushed stone: 5–10mm	272 kg/m^3
Natural sand	381 kg /m^3	Natural sand	719 kg/m^3
Air entrainment	70 mL/100 kg	Air entrainment	80 mL/100 kg
Superplasticizer	3.5 L/ m^3	Water reducer	300 mL/100 kg

3.3.1.2 BFRP and Steel Bars

Two types of BFRP bars were selected to use as longitudinal reinforcement in the beam specimens. The selected BFRP bars are commercially available and have mechanical properties comparable to those specified in CSA/S807-19. Figure 3.1 shows the No. 6 sand-coated BFRP bars (d_b=19.1 mm) and the No. 5 helically grooved BFRP bars (d_b=15.9 mm) used in this study. All BFRP bars were manufactured by the pultrusion method with a fiber content 81% and 80% (by weight), respectively, in a vinyl-ester resin. The mechanical properties of the BFRP and steel bars including modulus of elasticity, E_f, and ultimate tensile strength, f_{fu}, were estimated according to ASTM D7205 (2011). One size No. 20M deformed steel bars was selected to use as longitudinal reinforcement in the reference beam specimen. Table 3.3 presents the mechanical properties of the BFRP and steel bars.

Figure 3.1– BFRP bar types and surface characteristics.

Table 3.3 – Mechanical properties of the BFRP and steel reinforcements

Reinforcement Type		Bar Size	d_b (mm)	A_f [a] (mm²)	A_{im} [c] (mm²)	E_f (GPa)	f_{fu} (MPa)	ε_{fu} (%)
BFRP bars	Type I	No. 6	19.1	285	346±2.2	63.7±0.80	1646±40	2.50±0.1
	Type II	No. 5	15.9	199	201.1±1	64.8±3.3	1724±64	2.67±0.17
Steel bars		20M	19.5	300	---	200.0	f_y [b] = 460±15	ε_y [b] = 0.2

[a] Nominal cross-sectional area.

[b] f_y and ε_y are the yield strength and strain of the steel bars, respectively.

[c] Immersed cross-sectional area (measured).

Note: Properties calculated based on the nominal cross-sectional area.

3.3.2 Test Specimens

Eight RC beams were fabricated, cast, and tested to investigate their behavior and concrete shear capacity (see Figure 3.2). The beam specimens were designed without web reinforcement to assess the concrete shear capacity. The beam specimens were designed to allow the specimen to fail in shear rather than flexure. Therefore, the BFRP-reinforced specimens were reinforced with the amounts of longitudinal reinforcement higher than the balanced reinforcement ratio, ρ_{fb}, to prevent flexural failure. While, the reinforcement ratio of the steel RC beam was lower than the balanced one.

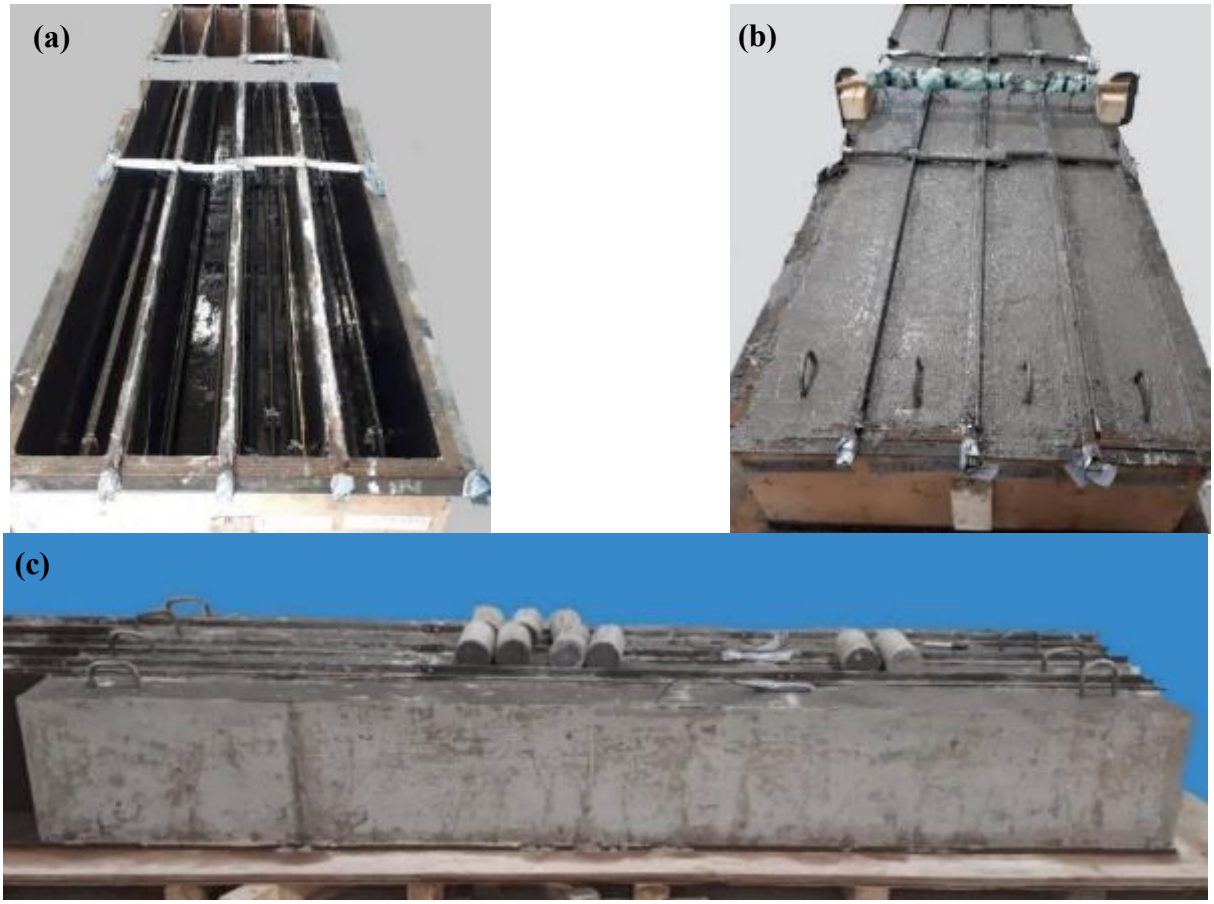

Figure 3.2– Fabrication of the beam specimens (a) cages and formwork, (b) casting, and (c) beam specimens.

The ρ_{fb} is defined as the reinforcement ratio at which concrete crushing and tension-FRP bar rupture or -steel bars yielding occur at the same time. According to ACI 440.1R-15 and CSA S806-12, the ρ_{fb} can be determined by the following equations, respectively:

$$\rho_{fb} = 0.85\beta_1 \frac{f_c^{'}}{E_f \varepsilon_{fu}} \frac{\varepsilon_{cu}}{\varepsilon_{cu} + \varepsilon_{fu}} \tag{3.1}$$

$$\rho_{fb} = \alpha_1 \beta_1 \frac{f_c^{'}}{E_f \varepsilon_{fu}} \frac{\varepsilon_{cu}}{\varepsilon_{cu} + \varepsilon_{fu}} \tag{3.2}$$

where the factors of the equivalent rectangular stress block α_1 and β_1 are calculated as follows:

ACI 440.1R-15:

$$\beta_1 = 0.85 - 0.00714\left(f_c^{'} - 28\right) \geq 0.65 \tag{3.3}$$

CSA S806-12:

$$\alpha_1 = 0.85 - 0.0015 f_c^{'} \geq 0.67 \tag{3.4}$$

$$\beta_1 = 0.97 - 0.0025 f_c^{'} \geq 0.67 \tag{3.5}$$

In this study, the longitudinal-reinforcement ratios ranged from 0.58% to 1.75%. Figure 3.3 provides a schematic of the beam dimensions and their cross sections. Table 3.4 gives the reinforcement ratio to balanced-reinforcement ratio, ρ_f/ρ_{fb}, for the beam specimens. The beam specimens had 200 x 400 mm cross-sectional dimensions with a total length of 3,100 mm. The thickness of the beam specimens was selected to be larger than those used in ACI 440.1R-15, which stipulates a minimum thickness of $L/10$ for simply supported beams. The clear shear span and the constant moment region for the beam specimens were 1000 and 600 mm, respectively. The shear span-to- depth ratio was almost equal to 3.0. As the anchorage of the longitudinal reinforcement affects the failure of slender beams, the longitudinal bars had a 250 mm anchorage length beyond the supports on each side. Each beam is identified with a label consisting of numbers and letters, beginning with "LS" or "N," referring to the types of concrete weight: LWSCC, or NWC, respectively. The letters "BI," "BII," and "S" represent the type of longitudinal reinforcement: BFRP Type I, BFRP Type II, and steel, respectively. The numbers are used to indicate the reinforcement ratio of the longitudinal bars. Table 3.4 gives the test matrix of the beam specimens.

Table 3.4 – Test matrix and details of test specimens

Beam ID	Reinforcing Material	$f_c^{'}$ (MPa)	Flexural Reinforcement		ρ_f/ρ_{fb}		E_rA_r, N × 10^6	Beam Details
			Bars	ρ_f(%)	ACI 440.1R-15	CSA S806-12		
LSBI-1.75	BFRP-Type I	54	4 No.6	1.75	7.23	6.96	72.62	Sec 3-3
LSBI-1.26	BFRP-Type I	54	3 No.6	1.26	5.20	5.01	54.46	Sec 2-2
LSBI-0.83	BFRP-Type I	54	2 No.6	0.83	3.43	3.30	36.31	Sec 1-1
LSBII-0.86	BFRP-Type II	54	3 No.5	0.86	3.82	3.68	38.69	Sec 2-2
LSBII-0.58	BFRP-Type II	54	2 No.5	0.58	2.57	2.48	25.79	Sec 1-1
LSS-0.88	Steel	54	2#20M	ρ_s[a]=0.88	0.19	0.19	120.00	Sec 1-1
NBI-0.83	BFRP-Type I	41.3	2 No.6	0.83	4.32	4.06	36.31	Sec 1-1
NBII-0.86	BFRP-Type II	41.3	3 No.5	0.86	4.81	4.52	38.69	Sec 2-2

[a] ρ_s is the reinforcement ratio of the beam reinforced with steel bars.

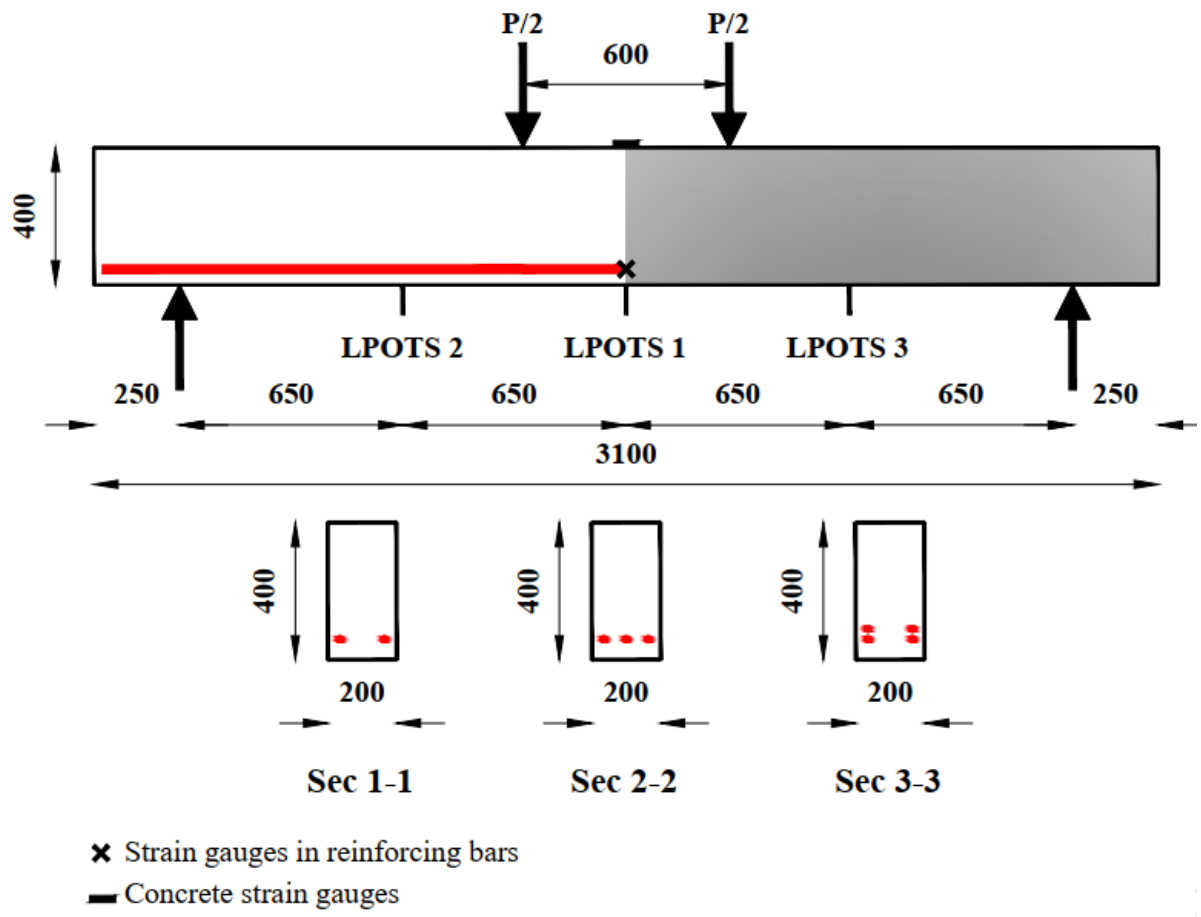

Figure 3.3– Dimensions, reinforcement details, and instrumentation of the beam specimens (dimensions in mm).

3.3.3 Measurement Equipment

As presented in Figure 3.3, the beam specimens were equipped with two electrical resistance strain gages with 6 mm gage lengths bonded to the reinforcing bars at mid-span to record reinforcement strain. In addition, two electric strain gages with 60 mm gage lengths were placed at the center span on the top face of the specimen to measure the strains in the concrete. Beam deflection was captured during testing with three linear potentiometers (LPOTS) located on each specimen at different locations. Furthermore, during testing, one high-accuracy linear variable differential transformer (LVDT) was placed to measure the crack width of the first vertical crack (flexural crack) between the two loading points.

3.3.4 Test Setup and Procedure

Before testing began, the surface of the beam specimens was painted white and marked with vertical and horizontal lines (100 × 100 mm grid) to facilitate observation of crack propagation.

The beam specimens were a simply supported with one end on a hinged support and the other on a roller support attached to two steel plates (width =150 mm) with a span of 2,600 mm, see Figure 3.4. The beams were tested under monotonic concentrated load with a 1,000 kN hydraulic actuator attached to a stiff steel beam (spreader beam). This stiff steel beam was used to transfer two identical loads to the beam specimen. The distance between the two loading points was 600 mm. The load was applied at a stroke-controlled rate of 0.6 mm/minute to achieve the shear failure in 30–60 minutes (see Figure 3.4). During loading, the beam specimens were observed to mark the crack formation and take photographs. Detailed data consisting of the load cell, strain gages, LPOT, and LVDT readings were monitored and recorded with a 20-channel computer data-acquisition system (DAS) and saved in a personal laptop.

Figure 3.4– Test setup.

3.4 Test Results and Discussion

3.4.1 General Behavior, Crack Patterns, and Failure Modes

All eight beam specimens in this study failed after the formation of a critical shear crack under loading. Crack propagation during the loading history was closely observed. Figure 3.5

illustrates the cracking and failure modes of the beam specimens. The first crack was observed in all beam specimens in the early phases of loading, appearing as a flexural crack in the pure moment region, followed by additional flexural cracks at mid-span as loading increased. The inclined crack that eventually led to failure in shear began as a flexural crack in the shear span and propagated close to the edge of the support. Lastly, all beam specimens experienced diagonal tension failure. In the case of LSBII-0.86 and NBII-0.86, a secondary bond–anchorage failure was noticed after formation of the critical inclined crack at the same time as the shear failure. In other words, cracks developed another branch—normally at the level between the concrete and longitudinal reinforcement—that propagated horizontally toward the support. This phenomenon was observed in past shear studies (El-Sayed et al. 2006 and Issa et al. 2015). It is important to mention the tendency for cracks to pass through LWA particles instead of around them. In addition, it was observed that, because of the relatively low modulus of elasticity of BFRP bars, the BFRP RC beams, LSBI-0.83 and LSBII-0.86, developed wider and deeper cracks than the steel RC beam LSS-0.88. On the other hand, the LWSCC beams had wider and deeper cracks than the NWC beams. This could be attributed to the interlocking action of aggregate along the diagonal cracked concrete surfaces being higher in the NWC beams than in the LWSCC beams. Figure 3.6 presents an example of a typical failure pattern.

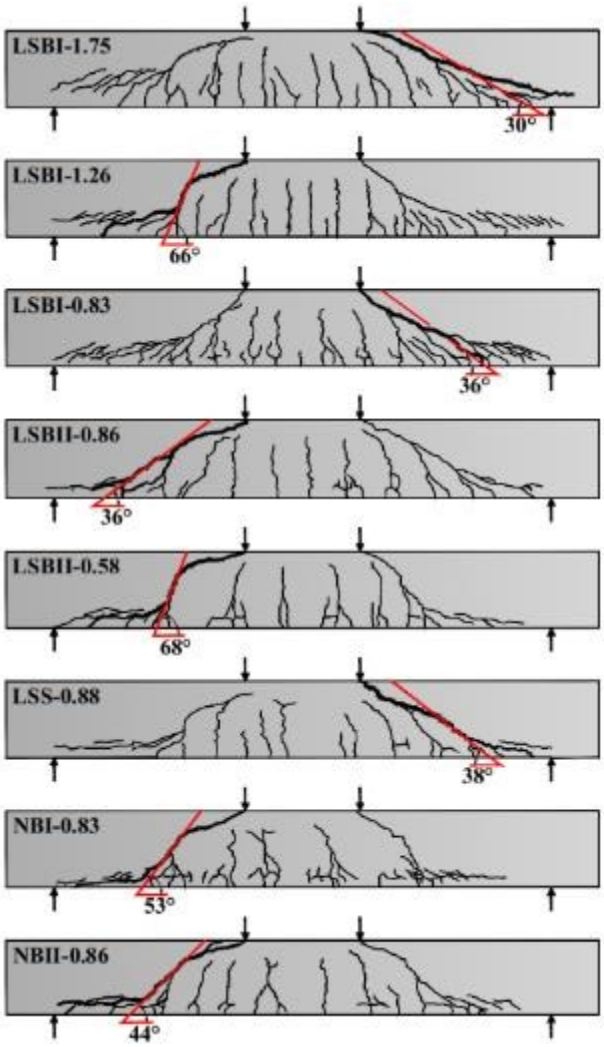

Figure 3.5– Cracking patterns and shear-crack angles at failure.

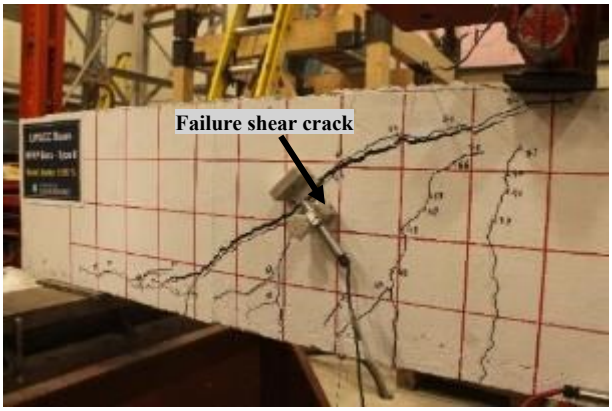

Figure 3.6– Typical crack pattern of the beam specimens.

The angle between the diagonal crack and the horizontal axis of the specimen was measured and noted on the figures. According to most building codes, the angle of inclination of the diagonal crack, θ, depends on the longitudinal straining of the beam, ε_x, while the longitudinal strain is a

function of the amount of reinforcement. Therefore, θ is a function of the amount of longitudinal reinforcement. Although the crack angle is not used to calculate V_c, it does influence the amount of transverse reinforcement required (MacGregor and Wight 2005).

The crack angle, θ, was computed with Eqns. (3.6) and (3.7), which are given in Section 8.4.4.9 of CSA S806-12 and in Section 8.9.3.7 of CSA S6-19 as

$$\theta = (30 + 7000\varepsilon_x) \tag{3.6}$$

$$\theta = (29 + 7000\varepsilon_x) \tag{3.7}$$

where the longitudinal strain is represented as follows:

$$\varepsilon_x = \frac{M_f / d_v + V_f}{2E_{FRP}A_{FRP}} \tag{3.8}$$

Figure 3.5 shows that the crack angle varied from 30° to 68° from the longitudinal axis. The average crack angle of inclination in the LWSCC-BFRP beams was 47.2°, while it was 48.5° in the NWC-BFRP beams. Moreover, it is similar to what has been observed before in FRP-reinforced NWC (NWC-FRP) beams, where the average crack inclination was 48° with the longitudinal axis (Razaqpur et al. 2004). The average crack angle is within code requirements: CSA S806-12 states that the value of θ shall not be considered greater than 60° nor less than 30°.

Figure 3.7 shows the applied load–deflection curve for the beam specimens at mid-span to present the influence of each parameter on shear behavior. In general, the typical load–deflection curve of the beam specimens can be defined by two main phases. The 1st phase is prior to flexural cracking, where the behavior of the curve was almost linear. Despite the difference in the amount and type of reinforcement of the tested beam specimens, the values of flexural stiffness in the 1st phase were almost identical. This behavior could be attributed to the significant contribution of the gross-section properties of the tested beam specimens in the uncracked phase. When the load increased, the beams converted from an uncracked to cracked phase, which gradually decreased inertia and flexural stiffness. In this 2nd phase, the flexural stiffness of the beams was dependent on the amount and type of reinforcement. In other words, it depended on the axial stiffness of the longitudinal bars, which is a function of the modulus of elasticity, E, and area, A, of the bar. The figure shows that increasing the reinforcement ratio for the same type of BFRP

reinforcement increased the flexural stiffness in the post-cracking phase. LSBI-1.75 was stiffer than LSBI-1.26 and LSBI-0.83 at the phase after cracking. This behavior was observed for the other types of BFRP reinforcement (LSBII-0.86 and LSBII-0.58). While, because the steel bars had the highest modulus of elasticity, the LWSCC-steel beam specimen, LSS-0.88, showed higher flexural stiffness than the other beam specimens. In addition, for the same type of bars, the LWSCC beam reinforced with the sand-coated BFRP bars (LSBI-1.75) exhibited lower deflection than LSBI-1.26 and LSBI-0.83 at the same load level. The observations were similar for the LWSCC beams reinforced with the helically grooved BFRP bars (LSBII-0.86 and LSBII-0.58). Generally, at the same load level, decreased deflection can be attributable to the increase in reinforcement ratio for specimens with the same type of reinforcement.

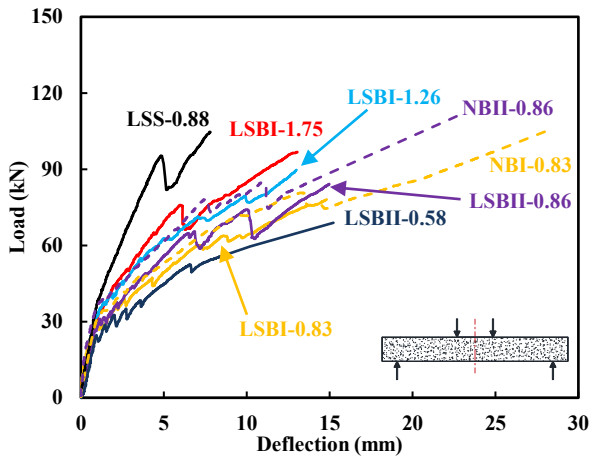

Figure 3.7– Load–deflection response for all the beam specimens.

On the other hand, Figure 3.7 presents the load–deflection curve of the beam specimens that had different concrete weights (LWSCC and NWC) with the same reinforcement ratio (LSBI-0.83, LSBII-0.86, NBI-0.83, and NBII-0.86). After the flexural cracks formed, the cracking stiffness of the beam specimens suddenly decreased in both LWSCC and NWC beam specimens. The figure indicated that LSBI-0.83 exhibited slightly lower relative cracking stiffness than NBI-0.83. Similar behavior of the cracking stiffness was observed for the beam specimens reinforced with helically grooved BFRP bars (LSBII-0.86 and NBII-0.86). Figure 3.7 shows that, similar to the influence of the amount of reinforcement on the obtained ultimate load, the lower the modulus of elasticity of LWSCC, the lower the ultimate load. Table 3.5 presents the failure loads of the tested beams.

Table 3.5 – Test results and comparison of experimental and predicted shear capacities of specimens using different design codes

Beam ID	Failure Load,[a] kN	V_{exp}, kN	V_{nor}	Maximum Strain, με		ACI 440.1R-15		CSA S6-19		CSA S806-12	
				Bars	Conc.	V_{pred}, kN	V_{exp}/V_{pred}	V_{pred} [b], kN	V_{exp}/V_{pred}	V_{pred}, kN	V_{exp}/V_{pred}
LSBI-1.75	96.80	48.40	0.196	2394	927	39.46	1.23	48.51	1.00	52.18	0.93
LSBI-1.26	89.70	44.85	0.174	3185	1449	35.71	1.26	47.22	0.95	49.43	0.91
LSBI-0.83	78.10	39.05	0.152	2820	1230	29.68	1.32	47.22	0.83	43.63	0.89
LSBII-0.86	84.20	42.10	0.163	3648	1055	30.56	1.38	47.50	0.89	44.60	0.94
LSBII-0.58	68.90	34.45	0.133	3464	736	25.58	1.35	47.50	0.73	39.70	0.87
LSS-0.88	104.70	52.35	0.204	1533	949	50.20†	1.04†	45.28	1.16	45.28 †	1.16†
NBI-0.83	105.44	52.72	0.224	4933	1408	29.79	1.77	66.06	0.80	53.20	0.99
NBII-0.86	111.58	55.79	0.236	3850	1329	30.69	1.82	66.35	0.84	54.38	1.03

[a] Failure loads do not include beam self-weight.

[b] β was calculated using the simplified method in CSA S6-19.

† Shear strength of the steel-reinforced beams was calculated using ACI 318R-19 and CSA A23.3-19.

3.4.2 Concrete Strains

Figure 3.8a presents the measured applied load versus the concrete strain. The measured strain in the concrete was dependent on the amount of reinforcement, the bar type, and the type of concrete. As indicated in this figure, before cracking, the concrete strains at mid-span were insignificant and ranged approximately from 100 to 200 με. After the 1st phase, the concrete strains started to increase progressively, reaching to less than 1,500 με. For the same type of bars, the beam specimens with the high amount of longitudinal reinforcement experienced lower concrete strains than those with the low amount of longitudinal reinforcement. For example, given the same load level, the concrete strain recorded in LSBII-0.86 was lower than that in LSBII-0.58. In addition, the LWSCC beam specimens showed lower concrete strains than the NWC beam specimens. The maximum concrete strains in LSBI-0.83 and LSBII-0.86 at failure were 1,250 and 1,050 με, respectively, compared to 1,400 and 1,350 με in NBI-0.83 and NBII-0.86, respectively. No signs of flexural compression failure were observed during testing. Therefore, none of the beam specimens exceed the ultimate compressive strain of 3,000 με in the ACI 440.1R-15 or 3,500 με in CSA S806-12 and CSA S6-19.

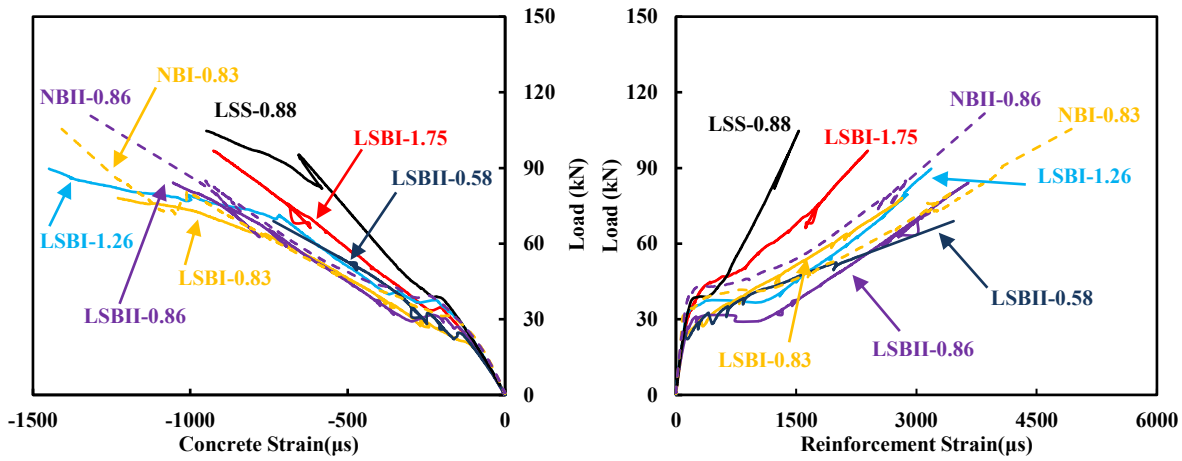

(a) (b)

Figure 3.8– Strain responses for the beam specimens in (a) concrete and (b) longitudinal reinforcement.

3.4.3 Reinforcement Strains

Table 3.5 provides the measured reinforcement strains of the tested beam specimens. Figure 3.8b gives the measured reinforcement strains at mid-span. The figure shows that increasing the amount of reinforcement decreased the reinforcement strain in the BFRP bars at the same load level for both reinforcement types. As example, the reinforcement strain recorded in LSBI-1.75 was lower than that in LSBI-1.26 and LSBI-0.83 at the same load level. Moreover, the sand-coated and helically grooved BFRP bars improved the cross-sectional area of the specimen by enhancing a transformed area due to their higher modulus of elasticity. In addition, the reinforcement strains in the LWSCC-steel beam were lower than those in the LWSCC-BFRP beams at the same load level after cracking occurred. This is because of the high modulus of elasticity of the steel bars. In general, these reinforcement strains at failure show that the shear failure was not caused by the tension-bars rupture. The maximum measured reinforcement strains in the BFRP bars ranged from 2,400 to 3,700 με, which did not exceed 50% of the ultimate tensile strain the bars during the test of beams.

3.5 Shear Capacity

Research on the performance of FRP RC beams without stirrups under shear has shown that the concrete shear capacity can be assessed by considering account the axial stiffness of the longitudinal reinforcement (El-Sayed et al. 2006; Tureyen and Frosch 2002). Figure 3.9 presents the influence of axial stiffness on the normalized shear capacity, V_{nor}, of the tested LWSCC beam

specimens. The vertical axis is the V_{nor} of the beam specimens with respect to $(f_c')^{1/3}bd$, as given by Eq. (3.9), where the shear design equations of several codes (BSI-85; JSCE-97; CSA S806-12) contain the variation of the shear capacity with the cubic root of f'_c, whereas the horizontal axis represents the reinforcement ratio.

$$V_{nor} = {V_{exp}}/{(f_c')^{1/3}bd} \tag{3.9}$$

As shown in this figure, the specimen reinforced with helically grooved BFRP bars (LSBII-0.86) experienced larger V_{nor} in comparison to that reinforced with sand-coated BFRP bars (LSBI-0.83), indicating the influence of axial stiffness. The increase in V_{nor} for LSBII-0.86 over LSBI-0.83 was 7%. On the other hand, the increase in V_{nor} for sand-coated BFRP RC beams LSBI-0.83, LSBI-1.26, and LSBI-1.75 was 13% and 29% for approximately 52% and 110% increases in the amount of reinforcement from 0.83% to 1.26% and 1.75%, respectively. The increase in V_{nor} for helically grooved BFRP RC beams LSBII-0.58 and LSBII-0.86 was 23% for an approximately 48% increase in the amount of reinforcement from 0.58% to 0.86%. This reveals that an increase in reinforcement was accompanied by an increase in V_{nor}. On the other hand, as indicated in Table 3.5, because of steel bars had the highest modulus of elasticity, the LWSCC-steel beam specimen (LSS-0.88) had the highest V_{nor} of the beam specimens.

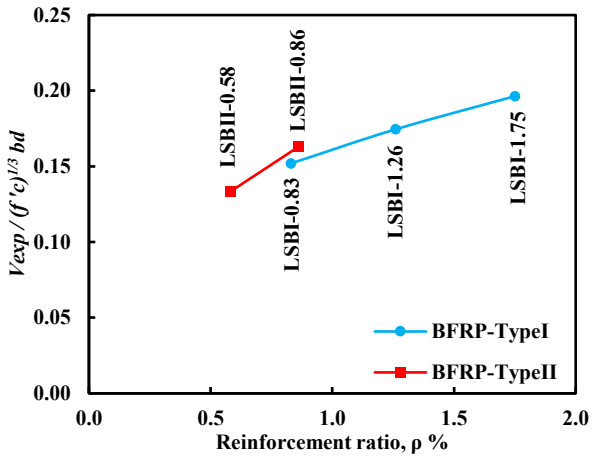

Figure 3.9– Normalized shear strength versus reinforcement ratio for the LWSCC beam specimens.

In addition, the increases in longitudinal reinforcement and/or modulus of elasticity had virtually no effect on crack width or depth at the same load level. The beams with high amounts of reinforcement and/or moduli of elasticity had smaller and narrower cracks than the beam specimens with low amounts of reinforcement and/or moduli of elasticity. The smaller cracks

increased the uncracked concrete contribution by increasing the compression zone depth. The narrower crack width increased the interface shear by increasing the aggregate interlock in the cracked surface and the residual tensile stress. Moreover, the dowel action contribution can be increased by increasing the amount of reinforcement because that increases the dowel area. Therefore, the tensile stresses in the surrounding concrete decreased. These results are in good agreement with the previous database from other test results on FRP beam specimens without web reinforcement (El-Sayed et al. 2006; El Refai and Abed 2015). It is important to mention that the contribution of dowel action of BFRP bars can be lower than that of steel due to the anisotropic behavior of FRP bars (Machial et al.2010).

The type of concrete is a parameter that can significantly affect the shear capacity mechanisms. Figure 3.10 plots the V_{nor} versus concrete unit weight for the beam specimens. The vertical axis denotes the V_{nor}, while the horizontal axis is the concrete unit weight (refer to concrete type). At the reinforcement ratio of 0.83%, LWSCC beam specimen LSBI-0.83 had a V_{nor} of 0.15 compared to 0.22 for NWC beam specimen NBI-0.83, whereas keeping a very close amount of reinforcement (0.86%) increased the V_{nor} from 0.16 to 0.24 for beam specimens LSBII-0.86 (LWSCC) and NBII-0.86 (NWC), respectively. This could be attributed to the brittle nature of porous LWA compared to normal-weight aggregate, as reported by Gerritse (1981). In other words, the interlocking action of aggregate along the diagonal cracked concrete surfaces in the NWC beams was higher than that in the LWSCC beams. This is attributed to the fact that the strength of gravel aggregate in NWC is higher than that of LWA in LWSCC. Sathiyamoorthy (2016) reported a similar observation for LWSCC-steel beam specimens compared to those made with NWC (NWC-steel).

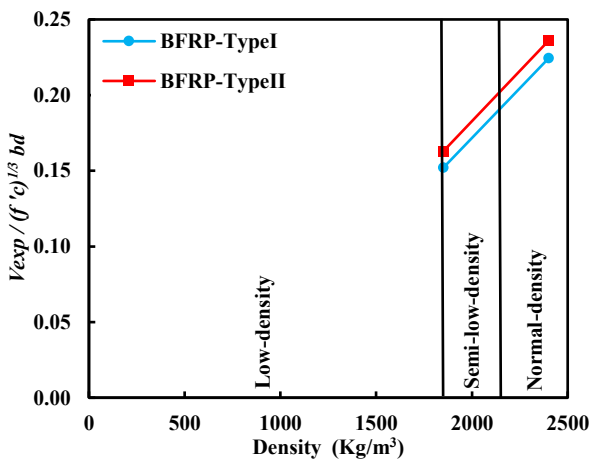

Figure 3.10– Normalized shear strength versus concrete density.

3.5.1 Review of Shear Design Equations

The concrete shear capacity, V_c, of the tested BFRP RC beam specimens was computed using different shear design methods developed by several organizations in North America (CSA S806-12; CSA S6-19; ACI 440.1R-15). This section provides a brief description of the methods in current standards and guidelines. This study focused on the contribution of concrete to the shear capacity as the beam specimens had no transverse reinforcement. Therefore, equations related to the web shear-reinforcement capacity are not presented. The safety factors in the design equations used in this study were set equal to 1.0. Note that all the following equations are presented in the SI system of units, where stress is in megapascals (MPa), force is in newtons (N), and length is in millimeters (mm).

3.5.1.1 ACI 440.1R-15 design guidelines

To account for the concrete shear capacity, V_c, of flexural elements with FRP bars as the longitudinal reinforcement, ACI Committee 440 recommends the following equations based on the uncracked concrete depth:

$$V_c = \frac{2}{5}\lambda\sqrt{f_c^{'}}b_w(kd) \tag{3.10}$$

$$k = \sqrt{2\rho_f n_f + \left(\rho_f n_f\right)^2} - \rho_f n_f \tag{3.11}$$

where kd is the cracked transformed section neutral-axis depth; $n_f = E_f / E_c$; and λ is the concrete density reduction factor for the influence of concrete weight. Based on the experiments carried out by Liu and Pantelides (2013), ACI Committee 440 specifies that λ=0.8 for SLWC in which all the fine aggregate is natural sand (NS). For sections with normal strength concrete (NSC) with $f_c^{'} < 55$ MPa, the value of the modulus of elasticity of concrete, E_c, is calculated using the following equation

$$E_c = 0.043 w_c^{1.5}\sqrt{f_c^{'}} \tag{3.12}$$

where w_c = the density of concrete.

3.5.1.2 Canadian Standard Code, CSA S6-19

El-Sayed and Benmokrane (2008) proposed a new equation as a modification to the equation published in CSA standard for concrete elements reinforced with steel. The concrete shear capacity in CSA S6-19 depends on the shear resistance of the cracked concrete factor, β; the cracking strength of concrete, f_{cr}; width, b_v; and the effective shear depth, d_{long}. The computation of V_c according to CSA S6-19 provided under section 16 is expressed as:

$$V_c = 2.5\beta\phi_c f_{cr} b_v d_{long} \tag{3.13}$$

where f_{cr} shall be taken as $0.4\sqrt{f_c'}$, $0.34\sqrt{f_c'}$, or $0.3\sqrt{f_c'}$ (MPa) ≤ 3.2 MPa for normal-density concrete (NDC) with a density between 2,150 and 2,500 kg/m^3; semi-low-density concrete (SDC) with a density greater than 1,850 kg/m^3 but less than 2,150 kg/m^3; and low-density concrete (LDC) with a density less than 1,850 kg/m^3, respectively.

3.5.1.3 Canadian Standard Code, CSA S806-12

The contribution of concrete to the shear capacity in CSA S806-12 is based on the equation proposed by Razaqpur and Isgor (2006):

$$V_c = 0.05\lambda\phi_c (f_c^{'})^{\frac{1}{3}} b_w d_v k_m k_r k_s \tag{3.14}$$

$$0.11\phi_c\sqrt{f_c^{'}} b_w d_v \le V_c \le 0.22\phi_c\sqrt{f_c^{'}} b_w d_v, f_c^{'} \le 60\,MPa \tag{3.15}$$

where the coefficients of V_c shall be determined as follows:

$k_m = \sqrt{V_f d/M_f} \le 1.0$ is the coefficient accounting for the effect of moment to shear; $k_r = 1 + (E_F\rho_{Fw})^{1/3}$ is the coefficient accounting for the effect of reinforcement rigidity; $k_s = 1.0$ for ($d \le 300$ mm); and $k_s = 750/(450 + d) \le 1.0$ for (d more than 300 and $A_{Fv} \le A_{vF}$) is the coefficient accounting for the effect of member size. CSA S806-12 specifies that λ =1.0 for NDC; λ = 0.85 for structural SCD (SLWC), in which all the fine aggregate is NS; and λ = 0.75 for structural LDC in which none of the fine aggregate is NS. These values of λ are the same as those specified in ACI 318R-19.

3.5.2 Comparison of Predicted Shear Capacity to Experimental Results

The concrete shear capacities of the LWSCC-BFRP and NWC-BFRP beam specimens were compared to the shear design provisions in several standards (CSA S806-12; CSA S6-19; ACI 440.1R-15). In this study, two types of fine aggregate were used in the LWSCC mixtures: LWA (Solite 307) and natural fine aggregate (NS), leading to a concrete density of 1,800 kg/m^3. Therefore, the value of λ in the current study was taken according to ACI 440.1R-15 and CSA S806-12 to be equal 0.8 (SLWC) and 0.75 (structural LDC), respectively, while according to CSA S6-19, f_{cr} was taken to be equal $0.3\sqrt{f_c'}$ (MPa) (LDC).

Table 3.6 provides the statistical results of the ratio of the experimental shear capacity of the LWSCC beam specimens over the predicted values (V_{exp}/V_{pred}), while Figures 3.11a, 3.11b and 3.11c show the comparison between the rations of V_{exp}/V_{pred} for different design methods. We used this information to assess the relative accuracy of several codes and design guidelines (CSA S806-12; CSA S6-19; ACI 440.1R-15). The predictions based on CSA S806-12 are comparable with the experimental results with the least scattered values. The average value of the ratio V_{exp}/V_{pred} using CSA S806-12 is 0.91 with a standard deviation (SD) and coefficient of variation (COV) equal to 0.03 and 3.24, respectively. The average value of V_{exp}/V_{pred} is closer to 1.0 ($V_{exp}/V_{pred} < 1$), as can be seen in Figure 3.11c. It is important to point out that all predicted values using CSA S806-12 could be conservative if the concrete reduction factor of $\phi_c = 0.65$ is applied. On the other hand, CSA S6-19 overestimates the contribution of concrete to the shear capacity as the average value of V_{exp}/V_{pred} ranged from 0.73 to 1.00. Furthermore, CSA S6-19 shows the most scattered predictions with a SD and high COV equal to 0.11 and 12.16%, respectively (see Figure 3.11b). By contrast, ACI 440.1R-15 slightly underestimates the contribution of concrete to the shear capacity of the tested beams, providing an average value of V_{exp}/V_{pred} equal to 1.30 (a value > 1.0 indicates a conservative prediction) with a SD of 0.06 and a COV of 4.80%. This level of conservatism is predictable as ACI 440.1R-15 takes into that the concrete shear capacity of an element is based only by the uncracked concrete depth (Tureyen and Frosch 2002). It is important to mention that the LWSCC-steel beam specimen (LSS-0.88) is not included in the average, SD, and COV of the ratio V_{exp}/V_{pred}. As shown in Table 3.5, the ratio of V_{exp}/V_{pred} for that beam ranges between 1.04 and 1.16.

Table 3.6 – Relative accuracy of different design codes

Design Method	Minimum	Maximum	Average	SD	COV (%)
ACI 440.1R-15	1.23	1.38	1.30	0.06	4.80
CSA S6-19	0.73	1.00	0.88	0.11	12.16
CSA S806-12	0.87	0.94	0.91	0.03	3.24

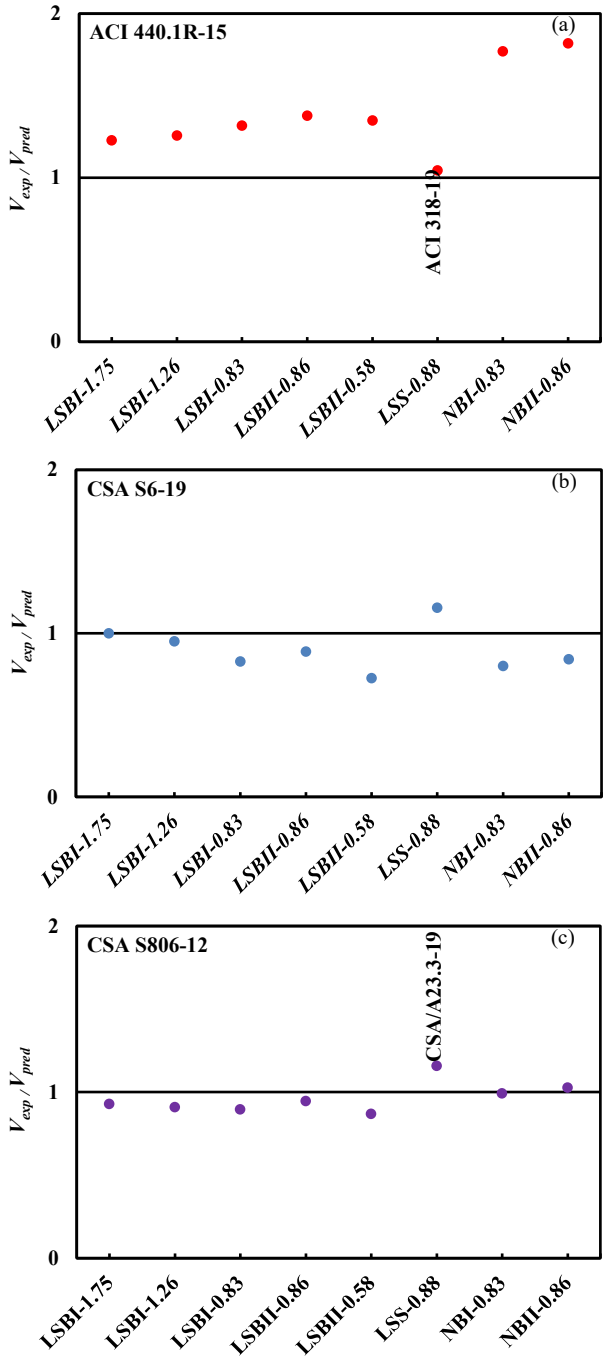

Figure 3.11– Comparison between V_{exp} / V_{pred} for the beam specimens.

To investigate the influence of concrete density on the shear capacity predictions of BFRP RC members, the results of the predictions of the current tested LWSCC-BFRP beams were

compared with the results for predictions for the NWC-BFRP beams tested in the current research and others found in the literature (El Refai and Abed 2015; Issa et al. 2015). Table 3.7 presents the ratios of V_{exp}/V_{pred} for the NWC-BFRP beams. The comparison shows that ACI 440.1R-15 predictions are more scattered for the NWC-BFRP beams than the LWSCC-BFRP beams, as the average values were 1.81 and 1.30, respectively. The SD value of V_{exp}/V_{pred} for NWC beams is 0.43, with a COV of 23.91%. This means that the ACI 440.1R-15 experimental-to-predicted shear capacity of the LWSCC-BFRP members is considerably lower than that for NWC-BFRP members. These results are in a good agreement with those obtained for SLWC-GFRP members (Liu and Pantelides 2013). On the other hand, CSA S6-19 predicts comparable ratios of V_{exp}/V_{pred} for both NWC and LWSCC. As shown in Table 3.7, CSA S6-19 overestimates the experimental shear capacity for the LWSCC and NWC beams, with average values of the V_{exp}/V_{pred} equal to 0.88 and 0.70, respectively. On the other hand, CSA S806-12 is the most accurate method for predicting the shear capacity for both NWC and LWSCC. The comparison demonstrates that using λ = 0.75 in CSA S806-12 provides good predictions that consider the influence of concrete density. They are quite consistent with the results for the NWC beams tested in this study and past studies, showing a similar degree of conservatism (approximately).

Table 3.7 – Experimental and predicted shear capacities of the NWC beams reinforced with BFRP bars

Reference	Beam ID	Failure Load,[a] kN	V_{exp}, kN	V_{nor}	ACI 440.1R-15		CSA S6-19		CSA S806-12	
					V_{pred}, kN	V_{exp}/V_{pred}	V_{pred}[b], kN	V_{exp}/V_{pred}	V_{pred}, kN	V_{exp}/V_{pred}
El Refai and Abed (2015)	B-3.3-R1	33.8	16.9	0.138	8.66	1.95	40.45	0.42	19.31	0.88
	B-3.3-R2	46.2	23.1	0.190	10.60	2.18	40.29	0.57	21.77	1.06
	B-3.3-R3	37.2	18.6	0.153	12.50	1.49	40.14	0.46	24.07	0.77
	B-3.3-R4	55.7	27.9	0.240	14.53	1.92	38.74	0.72	26.11	1.07
	B-3.3-R5	59.8	29.9	0.261	16.93	1.77	38.27	0.78	28.74	1.04
	B-2.5-R1	39	19.5	0.159	8.66	2.25	40.45	0.48	22.19	0.88
	B-2.5-R2	63.2	31.6	0.259	10.60	2.98	40.29	0.78	25.01	1.26
	B-2.5-R3	54	27	0.223	12.50	2.16	40.14	0.67	27.65	0.98
Issa et al. (2015)	5-10N5	58.6	29.3	0.174	19.45	1.51	54.86	0.53	34.8	0.84
	5-13N5	77.4	38.7	0.230	24.12	1.60	54.86	0.71	47.6	0.81
	5-16N5	90.4	45.2	0.269	29.20	1.55	54.86	0.82	42.94	1.05
	6-16N7	80.4	40.2	0.239	31.55	1.27	54.86	0.73	34.17	1.18
	3-25N7	96.8	48.4	0.296	32.80	1.48	53.46	0.91	33.39	1.45
	4-25N7	103	51.5	0.296	36.94	1.31	53.46	0.91	47.3	1.09

[a] Failure loads do not include beam self-weight.

[b] β was calculated using the simplified method in CSA S6-19.

3.6 Summary and Conclusions

The behavior and shear performance of LWSCC beams reinforced with two different types of BFRP bars were investigated. A total of eight RC beam specimens measuring 3,100 mm long × 200 mm wide × 400 mm deep were fabricated. Six beam specimens, including one conventional steel RC beam, were cast with LWSCC; two reference beam specimens were cast with NWC. The beam specimens were tested under four-point bending to failure. Based on the results, the main conclusions of this research are as follows.

1. Using LWSCC made it possible to fabricate beams with lower self-weight (density of 1,800 kg/m^3) than with NWC. The LWSCC-BFRP beams with LWA and NS behaved similarly to the NWC-BFRP beams.
2. The sand-coated and helically grooved BFRP-reinforced LWSCC beam specimens had cracking behavior similar to the counterpart LWSCC-steel beam.
3. Using high reinforcement ratios and/or moduli of elasticity reduced the crack width in the LWSCC beams. This increased the contribution of uncracked concrete and the interface shear by increasing the depth of compression zone, the aggregate interlock in the cracked surface, and the residual tensile stress.
4. Diagonal tension failure was the dominant failure mode of the BFRP-reinforced LWSCC beam specimens.
5. This study demonstrated that BFRP RC beams can be designed with LWSCC provided that an appropriate concrete density reduction factor is applied. Using a concrete density reduction factor of 0.75 in the CSA S806-12 equation to consider the influence of concrete density yielded a more accurate prediction of the concrete shear capacity. On the other hand, CSA S6-19 overestimated the concrete contribution to shear capacity for the LWSCC-BFRP and NWC-BFRP beams.
6. Using a concrete density reduction factor of 0.8 in the ACI 440.1R-15 equation to consider the influence of concrete density for LWSCC-BFRP beams yielded an appropriate degree of conservatism compared to the NWC-BFRP beams.

CHAPTER 4

Performance of LWSCC Beams Reinforced with GFRP Bars without Stirrups under Shear

Foreword

Authors and Affiliation:

- Shehab Mehany: Ph.D. candidate, Department of Civil Engineering, Université de Sherbrooke, Sherbrooke, Quebec, Canada, J1K 2R1.
- Hamdy M. Mohamed: Research Associate/Lecturer, Department of Civil Engineering, Université de Sherbrooke, Sherbrooke, Quebec, Canada, J1K 2R1.
- Brahim Benmokrane: Professor, Department of Civil Engineering, Université de Sherbrooke, Sherbrooke, Quebec, Canada, J1K 2R1.

Journal Title: *ACI Structural Journal.*

Paper Status: *Accepted*.

Abstract

Integrating glass fiber-reinforced polymer (GFRP) bars into lightweight self-consolidating concrete (LWSCC) would effectively contribute to producing lighter and more durable reinforced concrete (RC) structures. Nonetheless, the shear behavior of GFRP RC structures cast with LWSCC has not yet been fully defined. This paper reports experimental results on the behavior and shear strength of LWSCC beams reinforced with GFRP bars. The beams measured 3,100 mm (122.05 in.) long, 200 mm (7.87 in.) wide, and 400 mm (15.75 in.) deep. The test program included six beams reinforced with GFRP bars and one control beam reinforced with conventional steel bars for comparison purposes. The test variables were the reinforcement type and ratio and concrete density. The experimental results indicate that using LWSCC allowed for decreasing the self-weight of the RC beams (density of 1,800 kg/m^3) (112.4 lb/ft^3) compared to normal-weight concrete (NWC). All beams failed as a result of diagonal tension cracking. Increasing the axial stiffness of the longitudinal GFRP reinforcing bars improved the concrete shear capacity of the LWSCC beams. The test results of this study and the results for 42 specimens in the literature were compared to the current FRP shear design equations in the design guidelines, codes, and literature. Applying a concrete density reduction factor of 0.8 and 0.75 in the ACI 440.1R-15 and CSA S806-12 shear design equations, respectively, to take into account the influence of concrete density achieved an appropriate degree of conservatism equal to that of the equations for NWC beams.

Keywords: Beams; lightweight self-consolidating concrete (LWSCC); GFRP bars; lightweight aggregate (LWA); shear strength; shear failure and cracking; load deflection; strain; shear strength predictions; design codes.

4.1 Introduction

Lightweight concrete (LWC) allows for the production of reinforced concrete (RC) members that have a reduced own weight while maintaining a concrete strength that is of the same magnitude as normal-weight concrete (NWC). Reducing the own weight of an RC structure could considerably decrease the section dimensions of beams, slabs, columns, and foundations, which would enhance cost savings. An additional benefit of RC elements made with LWC is cutting lifting and transportation costs in the case of precast elements. On the other hand, self-consolidating concrete (SCC) is a substitute for conventional concrete in the case of highly crowded reinforcement. SCC is self-compacting and consequently, it can consolidate under its self-weight, avoiding the need for vibration. The past few decades have yielded great inventions in modern concrete technology from which lightweight self-consolidating concrete (LWSCC) has emerged as a promising alternative to NWC (Okamura and Ouchi 2003). LWSCC is considered a new kind of high-performance concrete (HPC) in construction, which combines the excellent benefits and characteristics of LWC and SCC (Hwang and Hung 2005). Therefore, consolidating lightweight aggregate (LWA) in SCC should enhance the quality, produce high-strength LWC (HSLWC), and prevent the segregation of LWA.

Since fiber-reinforced polymer (FRP) reinforcement is noncorroding, its use as an alternative to steel reinforcement has been accepted as an effective solution to corrosion problems (Mohamed and Benmokrane 2014; Ali et al. 2016; Hadhood et al. 2017; Hadhood et al. 2018). Glass-FRP (GFRP) bars are one of the most common and high-performance types of FRP bars used as longitudinal reinforcement in North America. In addition to its excellent corrosion resistance, GFRP reinforcement has a high strength-to-weight ratio, good fatigue properties as well as good resistance to chemical attack and electromagnetic resistance. Integrating GFRP bars into LWSCC would effectively contribute in producing lighter and more durable RC members for precast concrete applications (slabs, girders, and piles) (Sanni et al. 2021; Bakouregui et al. 2021).

Extensive research programs have been conducted to study the shear and flexural behavior of NWC members reinforced with FRP bars (Razaqpur and Isgor 2006; Hoult et al. 2008; Soltanzadeh et al. 2016; Ali et al. 2017a, b; Hadhood et al. 2019; Mousa et al. 2018, 2019; Mehany et al. 2019; Abdelazim et al. 2020). As a result, several equations from the current approaches (American Concrete Institute (ACI 440.1R-15), Canadian Standards Association

(CSA S6-19 and CSA S806-12) have been published to assess the shear and flexural behavior of members reinforced with FRP bars. Yost et al. (2001) tested full-scale NWC beams under shear load. Their experimental results showed that the cracking shear behavior of the GFRP RC beams was comparable to that of conventional steel RC beams with similar reinforcement ratios. The concrete shear strength was lower, however, for the GFRP RC beams than the steel RC beams. El-Sayed et al. (2006) investigated the shear strength and behavior of NWC beams reinforced with FRP bars and without shear reinforcement. The test results showed that the shear strength was proportional to the axial stiffness of the longitudinal reinforcing bars. In addition, they reported that the shear behavior of cracked RC members reinforced with FRP bars without web reinforcement resisted as the result of uncracked concrete, aggregate interlock, dowel-action mechanisms, arch action, and residual tensile stresses across the inclined crack.

In recent years, limited research has been conducted to investigate the shear behavior and strength of LWC beams reinforced with FRP bars (Pantelides et al. 2012 a, b; Liu and Pantelides 2013; Mehany et al. 2021). The results from these studies indicated that sand LWC (SLWC) can be used for panels reinforced with GFRP bars. The researchers found that using a reduction factor of 0.85 in ACI 440.1R-06 equations would make it possible to predict the concrete shear strength of GFRP-reinforced SLWC panels. Kim and Jang (2014) investigated the shear behavior of LWC beams reinforced with FRP bars. They used several equations to predict the contribution of LWC to the shear strength of beams, including the equation recommended in CSA S806-12. Their results indicate that the concrete shear strength of the LWC beams was equivalent to 75% of the strength predicted for NWC beams. On the other hand, Hossain et al. (2020) investigated the shear behavior of LWSCC beams reinforced with steel bars as longitudinal reinforcement. According to their analysis, all structural design codes conservatively predicted the shear capacity of the LWSCC beams reinforced with steel bars.

4.2 Research Significance

LWSCC is being more and more widely used in different types of RC structures due to its better structural and durability performance. No research, however, seems to have investigated LWSCC beams reinforced with GFRP bars under shear. In addition, ACI 440.1R-15, CSA S806-12, and CSA S6-19 do not provide guidance for LWSCC beams reinforced with GFRP bars. Therefore, this paper tries to fill this gap. A targeted experimental program is underway at the University of Sherbrooke (Sherbrooke, QC, Canada) to study the behavior and shear strength of

GFRP-reinforced LWSCC beams in which the fine aggregates are a mixture of LWA and natural sand (NS). The provisions in ACI 440.1R-15, CSA S6-19, and CSA S806-12 were also examined in light of the test results of this study and for 42 LWC specimens found in the literature. In addition, the Hoult et al. (2008) equation was reviewed and compared to the experimental results. The test results and outcomes of this study can be used to assess and explore the feasibility of using GFRP bars in LWSCC members to resist shear loads. Moreover, the knowledge gained in this experimental investigation is valuable for designers, engineers, and members of code committees using GFRP reinforcement in LWC structures and for the development of codes and standards.

4.3 Test Program

4.3.1 Geometry and Test Matrix of the Beam Specimens

The test program herein was designed and prepared to provide experimental data on the behavior and shear strength of LWSCC beams reinforced with GFRP bars without stirrups. This investigation considered the concrete density and the longitudinal GFRP reinforcement type and ratio as the test variables. A total of seven RC beams, including four LWSCC beams reinforced with GFRP bars, one LWSCC beam reinforced with steel bars, and two NWC beams reinforced with GFRP bars, were tested up to failure. The beam specimens were 3,100 mm (122.05 in.) long × 200 mm (7.87 in.) wide × 400 mm (15.75 in.) deep with a clear shear span of 1,000 mm (39.37 in.). The constant shear span-to-depth ratio was approximately 3.0. The thickness of the beam specimens was chosen to be greater than those in ACI 440.1R-15, where the minimum thickness for simply supported beams shall be *L/10*. Figure 4.1 shows the layout, rectangular cross sections, and reinforcement arrangement of the beam specimens. Three-part identification was used for each specimen. The first part identifies the concrete density: LS for LWSCC and N for NWC. The second part indicates the reinforcement type: G for GFRP and S for steel. The third part represents the longitudinal reinforcement ratio. The GFRP RC specimens were designed to be over-reinforced to avoid the brittle fracture of FRP reinforcement. Hence, the reinforcement ratios of the specimens reinforced with GFRP were greater than the balanced reinforcement ratio, ρ_{fb}. On the other hand, the reinforcement ratio of the beam specimen reinforced with steel was lower than the balanced ratio. The beams were designed to fail in shear with a safety margin against flexural failure.

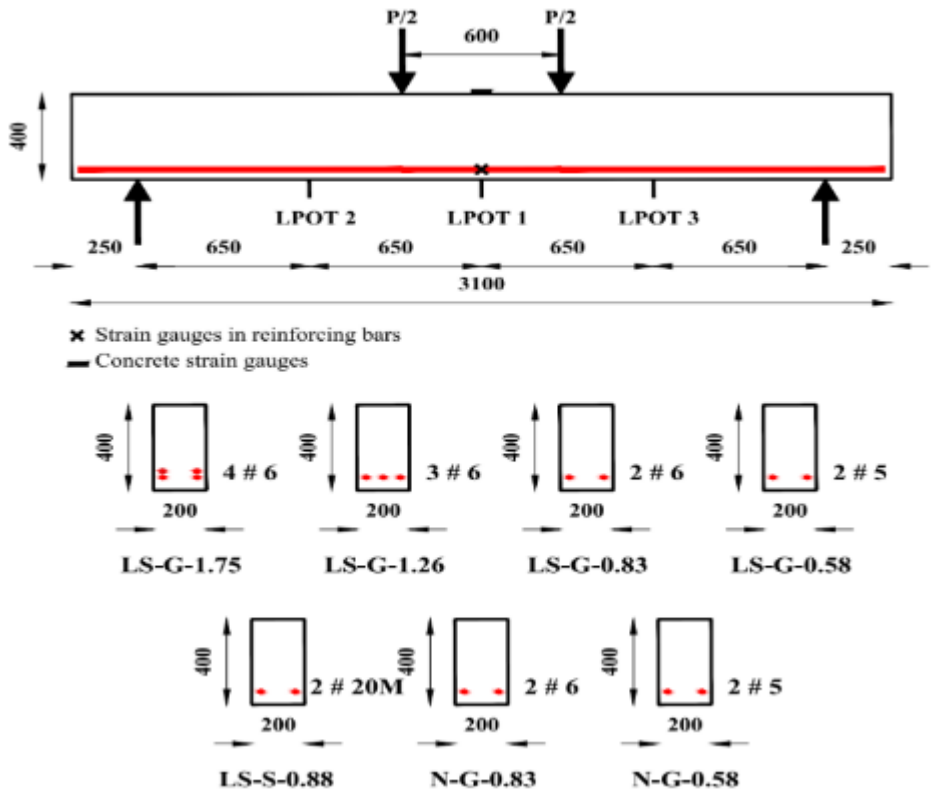

Figure 4.1– Dimensions, reinforcement details, and strain gauge locations of the test specimens. (Note: dimensions in mm; 1 mm = 0.0394 in.)

4.3.2 Materials

4.3.2.1 GFRP and Steel Bars

Two types of bars were used as flexural reinforcement: GFRP and steel. The GFRP bars were fabricated by a pultrusion process using E-glass fibers impregnated in a vinyl-ester resin with a fiber content of 83% (by weight). A sand coating was chosen to enhance bond and force transfer between the bars and the surrounding concrete. Number 6 (20 mm (0.79 in.) diameter) and Number 5 (15.9 mm (0.63 in.) diameter) bars with nominal cross-sectional areas of 285 and 199 mm^2 (0.44 and 0.31 $in.^2$), respectively, were used to reinforce the GFRP specimens in the longitudinal direction. Both Number 6 and Number 5 bars are classified as Grade III. In this investigation, the nominal values were selected for use in designing the beam specimens and in all analyses. The modulus of elasticity, ultimate tensile strength, and strain at rupture were estimated according to ASTM D7205. In addition, Number 20M deformed conventional steel bars with a ribbed surface were selected as longitudinal reinforcement for the reference beam specimen. Table 4.1 presents the mechanical characteristics of the GFRP and steel bars.

Table 4.1 – Mechanical properties of the GFRP and steel reinforcement

RFT Type	Bar Size	d_b (mm)	A_f [a] (mm²)	A_{im} [c] (mm²)	E_f (GPa)	f_{fu} (MPa)	ε_{fu} (%)
GFRP bars	No. 6	20	285	325±1	64.2±0.48	1382±12	2.15±0.1
	No. 5	15.9	199	229.1±0.6	65.3±0.5	1451±28	2.22±0.03
Steel	20M	19.5	300	---	200.0	f_y [b] = 460±15	ε_y [b] = 0.2

[a] Nominal cross-sectional area.

[b] f_y and ε_y are the yield strength and strain of the steel bars, respectively.

[c] Immersed cross-sectional area (measured).

Note: Properties calculated based on the nominal cross-sectional area; 1 mm= 0.0394 in.; 1 mm^2 = 0.00155 in.^{2}; 1 GPa = 145 ksi; 1 MPa = 145 psi.

4.3.2.2 Concrete Types

Two concrete mixtures (LWSCC and NWC) were used to investigate the effect of concrete density on shear strength. The designed concrete strength was 40 MPa (5800 psi). The NWC was provided by a local supplier, while the LWSCC was mixed in the University of Sherbrooke laboratory. The mixture proportion per cubic meter of NWC was 730 and 272 kg (1610 and 600 lb) of coarse aggregate in size ranges of 5–20 mm (0.20–0.79 in.) and 5–10 mm (0.20–0.39 in.), respectively; 719 kg (1585 lb) of fine aggregates, 460 kg (1015 lb) of cement, a 0.35 water-to-cement ratio (w/c), 80 mL/100 kg (1.23 oz /100 lb) of entrained air, and 300 mL/100 kg (4.60 oz /100 lb) of water-reducing agent. The LWSCC mixtures contained two types of LWAs—Solite 307 and Solite 343—from a single source: Northeast Solite. The properties of the LWAs met the requirements of the current ASTM C330 / C330M-17a. The mixture proportion per cubic meter of LWSCC was 369 kg (815 lb) of lightweight coarse aggregate (Solite 343), 488 kg (1075 lb) of lightweight fine aggregate (Solite 307), 381 kg (840 lb) of fine aggregate (NS), 543 kg (1200 lb) of cement (Type TerC3), 0.33 water-cement ratio (w/c), 3.5 L (118.3 oz) of superplasticizer, and 70 mL/100 kg (1.07 oz /100 lb) of entrained air. The actual slump-flow value for the LWSCC ranged between 670 and 710 mm (26.4 and 28 in.). The density of the LWSCC was 1800 kg/m^3 (112.4 lb/ft^3) as measured according to ASTM C567 (ASTM C567/C567M 2014). The actual concrete compressive strengths (f'_c) were determined in accordance with ASTM C39/C39M from nine 100 × 200 mm (3.94 × 7.87 in.) cylinders for both the LWSCC and NWC. The cylinders were tested on the same day as the start of testing of the beam specimens. Table 4.2 presents the actual compressive strengths of the LWSCC and NWC for the beam specimens. Split cylinder tests were carried out on 100 mm (3.94 in.) in diameter

× 200 mm (7.87 in.) long cylinders. The average tensile strengths were 3.1 and 3.6 MPa (450 and 520 psi) for the LWSCC and NWC, respectively.

Table 4.2 – Test matrix and details of the test specimens

Beam ID	Reinforcing Material	f'_c (MPa)	a/d	Flexural Reinforcement		ρ_f / ρ_{fb}	
				Amount of reinforcement	ρ_f (%)	ACI 440.1R-15	CSA S806-12
LS-G-1.75	GFRP	54.00	3.07	4 No.6	1.75	5.16	4.99
LS -G-1.26	GFRP	54.00	2.94	3 No.6	1.26	3.71	3.59
LS -G-0.83	GFRP	54.00	2.94	2 No.6	0.83	2.45	2.37
LS -G-0.58	GFRP	54.00	2.92	2 No.5	0.58	1.85	1.78
LS -S-0.88	Steel	54.00	2.94	2#20M	0.88	0.19	0.19
N-G--0.83	GFRP	41.30	2.94	2 No.6	0.83	3.08	2.91
N-G-0.58	GFRP	41.30	2.92	2 No.5	0.58	2.33	2.19

Note: 1 MPa = 145 psi.

4.3.3 Beam Fabrication

GFRP and steel reinforcement cages were tied with tie wraps outside the formwork (see Figure 4.2). The beam specimens were prepared and carefully placed inside the wooden molds for casting. The clear concrete cover was 50 mm (1.97 in.), which was set in accordance with CSA S806-12. Plastic spacers were used to keep the reinforcement cage at the correct distance from the wooden molds. Prior to casting, the clear cover was checked in different positions along the length of the cage. The reinforcement cages were trimmed 20 mm (0.79 in.) from each end to fit into the 3,100 mm (122.05 in.) long forms. Five beams were cast with LWSCC, while the remaining two were cast with NWC as reference beams. The beams were covered after one hour with wet burlap and plastic sheeting for curing. The LWSCC and NWC cylinders were cast under the same conditions to evaluate the concrete compressive strengths. All cylinders were cured under the same conditions as the beam specimens.

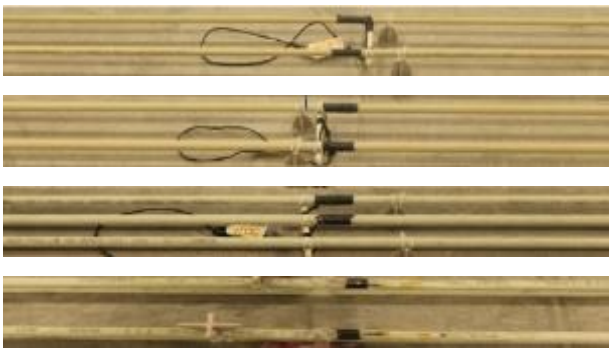

Figure 4.2– Overview of assembled GFRP cages.

4.3.4 Instrumentation and Test Setup

Instrumentation of the beam specimens included three linear potentiometers (LPOTs) at different locations for deflection measurement. Two electrical strain gauges with a gauge length of 6 mm (0.24 in.) were used at mid-span to measure the reinforcement strain. In addition, two electric strain gauges with a gauge length of 60 mm (2.36 in.) were placed at the center span on the top face of the specimen to measure the strains in the concrete. Epoxy was used to bond the strain gauges to the compression beam surface after it was cleaned. Figure 4.1 shows the locations of the LPOTs and the concrete and reinforcement strain gauges. Moreover, a high-accuracy linear variable differential transformer (LVDT) was mounted during testing on the first flexural crack at the constant moment region to measure the crack width.

The beam specimens were about three months old at the time of testing. Prior to their testing, the beams were painted white and marked with vertical and horizontal lines (100 × 100 mm) (3.94 × 3.94 in.) to help in monitoring crack propagation. Each beam specimen consisted of a 2,600 mm (102.36 in.) simply supported span with 250 mm (9.85 in.) projections from each end to avoid bond–anchorage failure of the longitudinal reinforcement. Two steel plates 150 mm (5.90 in.) wide were placed under the beam specimen on the top of the hinged and roller supports. The vertical load was applied with a 1,000 kN (224.80 kip) hydraulic actuator through a spreader beam at a stroke-controlled rate of 0.6 mm/min (0.024 in. /min). This rigid steel beam was used to transfer two equal loads to the specimen. Figure 4.3 provides the details of test setup and its schematic diagram. The load was removed from the test beams immediately after reaching the failure load. The applied load, strain gauges, LPOTs, and LVDT readings were automatically recorded during the test using a 20-channel computer data-acquisition system and stored on a personal computer.

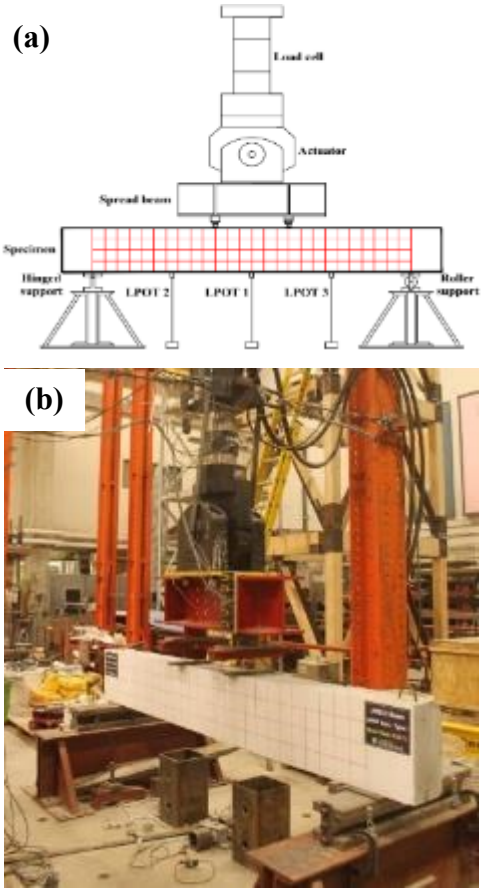

Figure 4.3– Test setup: (a) schematic diagram, and (b) overview of the tested beams.

4.4 Observations and Test Results

4.4.1 Shear Failure Mode and Cracking

The LWSCC and NWC beams clearly failed in shear failure mode before reaching their flexural capacities. Vertical flexural cracks were observed in all beam specimens perpendicular to the direction of the maximum principal stress induced by pure bending moment in the flexural span zone. Cracking outside the flexural span zone started as the load increased, similarly to flexural cracking. As more load was applied, the shear stress became more dominant and developed curving in both shear spans toward the loading points. It is important to mention the tendency for cracks in LWSCC specimens to pass through LWA particles instead of around them. The shear failure was sudden and brittle and always by diagonal tension. Figure 4.4 illustrates the typical failure mode of the tested beam specimens. Specimen LS-G-0.83 experienced a secondary bond-anchorage failure within the shear span at the same time as the shear failure. As the aggregate interlock was lost as the inclined crack continued to widen, a sudden increase in the dowel action in the flexural reinforcement occurred to maintain cross-sectional equilibrium.

This caused vertical tensile stresses in the concrete surrounding the bars. These vertical tensile stresses combined with the existing bond stresses resulted in secondary bond-anchorage failure. The same failure sequence with GFRP-reinforced NWC members has been reported in past shear studies (El-Sayed et al. 2006; Issa et al. 2015).

Figure 4.4– Typical crack pattern of beams: LS-G-1.26.

Figure 4.5 presents the maximum width of the first crack at beam center versus the applied load. As shown, increasing the reinforcement ratio reduced the width of the first crack at the same load level. The crack in LS-G-0.58 was wider than in LS-G-0.83, LS-G-1.26, and LS-G-1.75 at the same load level. In addition, the measured crack widths in the LWSCC beam specimens were greater than those of their counterparts made with NWC. The reason behind that is the brittle nature of the porous LWA in LWSCC compared to gravel aggregate in NWC, as reported by Gerritse (1981). In other words, the interlocking action of LWA, along the diagonal cracked concrete surfaces in the LWSCC beams, was lower than that of the NWC beams. Hossain et al. (2020) reported a similar observation for LWSCC beam specimens reinforced with steel bars compared to those made with NWC. On the other hand, the number of cracks increased significantly as the amount of reinforcement increased. This can be attributed to the number of cracks being related to the applied load.

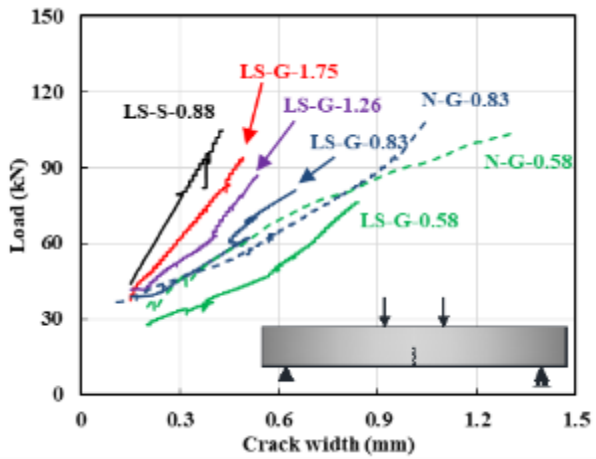

Figure 4.5– Load–crack width for the beam specimens. (Note: 1 mm = 0.0394 in.; 1 kN = 0.225 kip.)

4.4.2 Load–Deflection Behavior

Figure 4.6 presents the relationship between the applied load and the measured deflection at mid-span. Linear behavior was observed up to the formation of the first flexural crack, followed by nearly linear behavior up to failure. Beam stiffness before the formation of the flexural cracks was almost identical regardless of concrete density and reinforcement type and ratio. This can be attributed to the behavior of the uncracked beam with the gross moment of inertia of the concrete cross section. After cracking occurred, the flexural stiffness of the LWSCC beam specimens was dependent on the amount and type of reinforcement. As illustrated in Figure 4.6, increasing the reinforcement ratio of the GFRP reinforcement increased the flexural stiffness at the post-cracking stage. On the other hand, the measured deflection in specimen LS-G-0.58 with a 0.58% longitudinal reinforcement ratio was higher than that in specimens LS-G-0.83, LS-G-1.26, and LS-G-1.75 with ratios of 0.83%, 1.26%, and 1.75%, respectively, at the same load level. Similar observations were noted for the NWC specimens (N-G-0.83 and N-G-0.58). The beam specimen reinforced with Grade 460 MPa (66717 psi) steel reinforcement (LS-S-0.88) recorded the highest flexural stiffness after cracking of the all the beam specimens. At the same load level, specimen LS-S-0.88 exhibited less post-cracking deflection than specimen LS-G-0.83 with the same reinforcement ratio (approximately). This behavior can be attributed to the high modulus of elasticity of steel bars. Table 4.3 presents the experimental results of the tested beams.

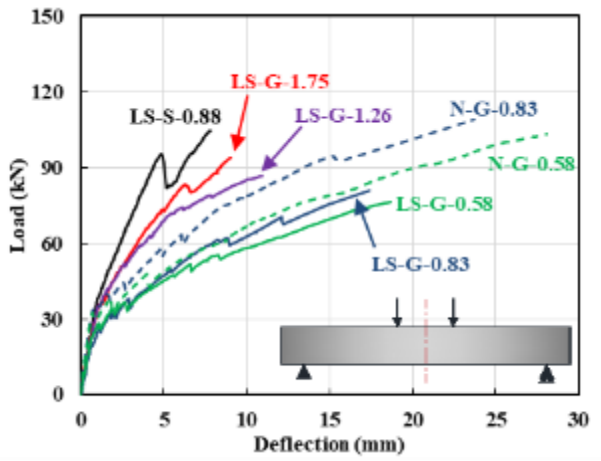

Figure 4.6– Load–deflection response for the beam specimens. (Note: 1 mm = 0.0394 in.; 1 kN = 0.225 kip.)

Table 4.3 – Test results for the experimental shear capacities of the beam specimens

Beam ID	Failure Load [a], kN	V_{exp}, kN	Normalized Shear	Maximum Strain, με		Ductility Index, μ_e
				Bars	Concrete	
LS-G-1.75	93.80	46.90	0.190	2400	980	1.52
LS -G-1.26	86.80	43.40	0.169	2300	1100	2.08
LS -G-0.83	81.00	40.50	0.158	4000	1180	2.13
LS -G-0.58	76.50	38.25	0.148	4700	1200	2.29
LS -S-0.88	104.70	52.35	0.204	1530	950	1.39
N-G--0.83	109.00	54.50	0.232	4890	1050	2.47
N-G-0.58	103.50	51.75	0.219	5960	840	2.54

[a] Failure loads do not include beam self-weight.

Note: 1 kN = 0.225 kip.

A comparison of the deflection behavior of the LWSCC beams to the NWC beams was investigated with four beam specimens. After formation of the flexural crack, the cracking stiffness of both the LWSCC and NWC beams suddenly decreased. Although the reinforcement ratio was the same, the cracking stiffness of LWSCC specimens LS-G-0.83 and LS-G-0.58 was slightly lower than that of N-G-0.83 and N-G-0.58, their NWC counterparts. In addition, as shown in Figure 4.6, the LWSCC beam specimens exhibited higher deflection than NWC beam specimens. This can be attributed to the slightly higher modulus of elasticity of NWC.

4.4.3 Reinforcement and Concrete Strains

Figure 4.7 depicts the recorded mid-span strains in the top concrete surface as well as in longitudinal reinforcement versus the applied load. In general, the reinforcement strains were

small up to the formation of cracks, at which point they increased rapidly up to failure. The rate of increase in the reinforcement strains was inversely proportional to the GFRP reinforcement ratio. The maximum recorded reinforcement strains in the GFRP-reinforced LWSCC beams were 2,400, 2,300, 4,000, and 4,700 με in LS-G-1.75, LS-G-1.26, LS-G-0.83, and LS-G-0.58, respectively, which represents approximately 11%, 10%, 18%, and 21% of the rupture strain of the GFRP reinforcement. CSA S806-12 specifies a usable reinforcement strain limit of 7,000 με, independent of the ultimate tensile strain of the FRP reinforcement. The recorded reinforcement strains in the GFRP bars did not reach the CSA S806-12 limit regardless of the failure mode. In addition, the reinforcement strains in the steel-reinforced LWSCC beam were less than those in the GFRP-reinforced LWSCC beams after cracking occurred. This can be attributed to the high modulus of elasticity of steel bars. On the other hand, the reinforcement strain in the longitudinal GFRP bars increased in LWSCC beams LS-G-0.83 and LS-G-0.58, compared to NWC beams N-G-0.83 and N-G-0.58 at the same load level. This can be attributed to the high modulus of elasticity of NWC.

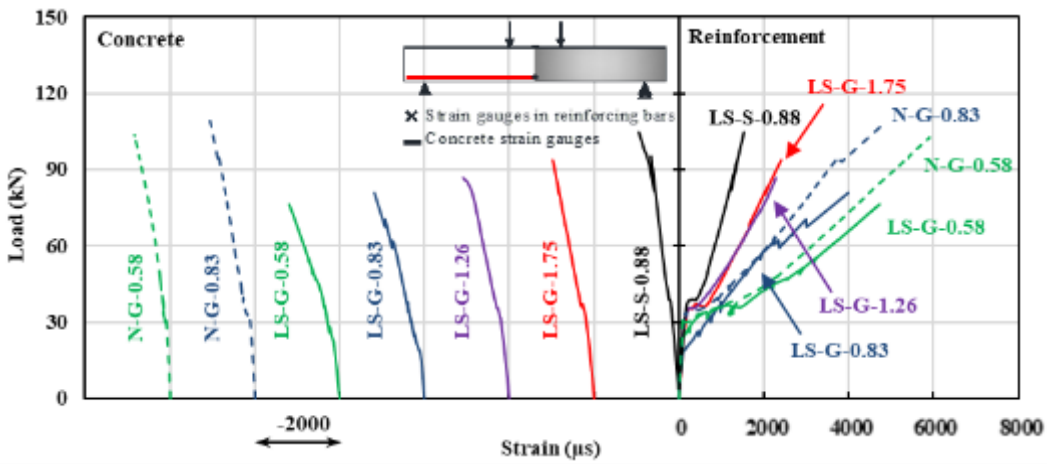

Figure 4.7– Load versus longitudinal reinforcement and concrete strain at mid-span for the beam specimens. (Note: 1 kN = 0.225 kip.)

As shown in Figure 4.7, prior to cracking, the corresponding compressive strains in the concrete at mid-span were insignificant in the tested beams and ranged approximately from 100 to 200 με. After cracking occurred, the strains began to increase progressively, reaching no more than 1,200 με, which is less than the ultimate compressive strain of 3,000 με in ACI 440.1R-15 guidelines and 3,500 με in CSA S806-12 and CSA S6-19. The LWSCC beam having high GFRP reinforcement ratio experienced lower concrete strains than those having low reinforcement ratio. The maximum concrete strain recorded in specimen LS-G-1.75 was 980 με, compared to 1,100, 1,180, and 1,200 με in specimens LS-G-1.26, LS-G-0.83, and LS-G-0.58, respectively.

In addition, similar to the influence of the LWSCC on the reinforcement strain, the concrete strain in LWSCC beams LS-G-0.83 and LS-G-0.58 was 1,180 and 1,200 με, respectively, compared to 1,050 and 840 με in NWC beams N-G-0.83 and N-G-0.58, respectively.

4.4.4 Ductility and Deformability

Ductility is the ability of an RC element to absorb energy without loss of strength. Ductility is related to inelastic deformation, which occurs prior to complete failure. In the case of steel RC elements, ductility can be estimated as the ratio of the total deformation at failure divided by the deformation at yielding. As a result of the linear behavior of GFRP bars up to failure, this approach to calculating ductility cannot be applied to GFRP-reinforced LWSCC beams. Several methods have been proposed to calculate the ductility of FRP RC structures. Naaman and Jeong (1995) defined ductility as the ratio of the total energy to the elastic energy and proposed an equation to compute the ductility index (μ_e), which can be applied to steel- and FRP RC members:

$$\mu_e = 0.5\left[\frac{E_{tot}}{E_{el}} + 1\right] \tag{4.1}$$

where E_{tot} is the total energy computed as the area under the load–deflection curve, and E_{el} is the elastic energy released upon failure computed as the area of the triangle formed at failure load by the line having the weighted average slope of the two initial straight lines of the load–deflection curve. Table 4.3 lists the computed μ_e for the GFRP and steel beams. We observed an inverse relationship between μ_e and the amount of reinforcement. In other words, decreasing the amount of reinforcement from 1.75% in LS-G-1.75 to 1.26%, 0.83%, and 0.58% increased the μ_e of specimens LS-G-1.26, LS-G-0.83, and LS-G-0.58 by 35%, 40%, and 50%, respectively. The higher μ_e relates to higher deformation and therefore gives ample warning of the failure of GFRP-reinforced LWSCC beams.

4.5 Analysis and Discussion

4.5.1 Effect of GFRP Longitudinal Reinforcement Ratio and Modulus of Elasticity on Shear Strength

This section presents the contribution of longitudinal reinforcement ratio and modulus of elasticity on the shear strength of the tested beams. The shear strength of the beams was normalized with respect to $(f'_c)^{1/3}$ to maintain the consistency with CSA S806-12, JSCE-1997, and BS8110-85, where the shear equations of these standards are a function of the cubic root of the concrete's compressive strength. Figure 4.8 presents the normalized shear strength $V_{exp}/(f'_c)^{1/3}bd$ versus the longitudinal reinforcement ratio. As can be seen, the normalized shear strength increased when the longitudinal reinforcement ratio was increased. In other words, increasing the amount of reinforcement by 45%, 120%, and 200% (from 0.58% in LS-G-0.58 to 0.83%, 1.26%, and 1.75%) increased the normalized shear strength of specimens LS-G-0.83, LS-G-1.26, and LS-G-1.75 by 7%, 15%, and 30 %, respectively. This could be attributed to a decrease in the depth and width of the shear crack when the longitudinal reinforcement was increased. As a result, the depth of the compression zone was higher to maintain the equilibrium of the cross section. In addition, the contribution of aggregate interlock increased. In addition, increasing the reinforcement ratio increased the dowel capacity (dowel area) of the LWSCC beams, therefore increasing the LWSCC shear strength of the beams. Similarly, an increase in the shear capacity was observed for the NWC beams reinforced with GFRP bars (N-G-0.58 and N-G-0.83).

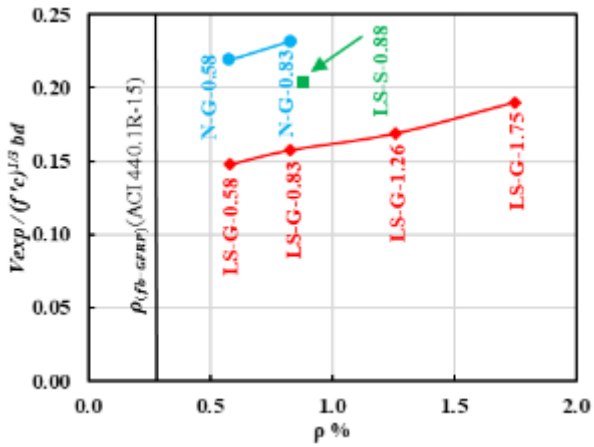

Figure 4.8– Normalized shear strength versus reinforcement ratio of the beams.

Figure 4.8 also presents the influence of modulus of elasticity on the normalized shear strength of the tested LWSCC beams. As shown in the figure, a higher modulus of elasticity of the reinforcing material yielded higher normalized shear strength. Due to the relatively low modulus of elasticity of GFRP bars compared to that of steel bars, specimen LS-G-0.83 exhibited lower normalized shear strength than steel-reinforced beam LS-S-0.88 with the approximatively same amount of reinforcement.

4.5.2 Shear-Strength Predictions

This section provides first a brief description of the methods in current codes, standards, and design guidelines. The FRP shear design equations available in ACI 440.1R-15, CSA S806-12, and CSA S6-19, as shown in Table 4.4, are presented and discussed. A brief description of the shortcomings of the existing shear design provisions related to LWC is presented. Moreover, the shear design equation proposed by Hoult et al. (2008) is also introduced and discussed. As the study focused on the contribution of concrete to the shear strength, no equations related to the shear reinforcement contribution are presented.

4.5.2.1 ACI 440.1R-15

ACI 440.1R-15 design guidelines provide a design equation to determine the concrete shear strength of members reinforced with GFRP reinforcement. This equation, however, does not distinguish between the different types of LWC, considering only concrete density. The shear capacity of concrete is given as follows:

$$V_c = \frac{2}{5}\lambda\sqrt{f_c^{'}}b_w(kd) \tag{4.2}$$

where λ is the concrete density reduction factor to consider the influence of concrete density and k is the ratio of depth of neutral axis to reinforcement depth. ACI 440.1R-15 specifies that $\lambda=0.8$ for SLWC in which all the fine aggregate is NS.

Generally, this equation leads to very conservative predictions of the shear strength of NWC, as it is based on a linear elastic approach. The size effect, the effect of the *a/d* ratio, and the effect of moment–shear interaction are not included in the equation. In addition, this equation predicts zero concrete shear strength for RC members with low reinforcement or without longitudinal reinforcement.

4.5.2.2 CSA S806-12

For members without applied axial load and $f'_c \leq 60\ MPa$ (8700 psi), the shear strengths of the GFRP RC specimens without shear reinforcement are predicted using the following equation:

$$V_c = 0.05\lambda\phi_c (f'_c)^{\frac{1}{3}} b_w d_v k_m k_r k_s \tag{4.3}$$

CSA S806-12 specifies that $\lambda=1.0,\ 0.85$, and 0.75 for normal density concrete, structural semi-low density concrete in which all the fine aggregate is NS, and structural low-density concrete in which none of the fine aggregate is NS, respectively. According to CSA S806-12, V_c shall not be taken as less than $0.11\emptyset_c\sqrt{f_c'}b_w d_v$, nor more than $0.22\emptyset_c\sqrt{f_c'}b_w d_v$.

4.5.2.3 CSA S6-19

For FRP RC elements, CSA S6-19 recommends Eq. (4.4) to calculate concrete shear contribution as:

$$V_c = 2.5\beta\phi_c f_{cr} b_v d_{long} \tag{4.4}$$

The concrete shear strength in CSA S6-19 depends on the shear resistance of the cracked concrete factor β, the cracking strength of concrete f_{cr}, width b_v, and the effective shear depth d_{long}. The coefficient β considers the effect of applied moment, shear, and stiffness of the longitudinal reinforcement.

4.5.2.4 Hoult et al. (2008) Equation

Hoult et al. (2008) proposed an equation to predict the shear strength of FRP RC members without stirrups. This equation has been used in the knowledge that the average longitudinal strain for FRP reinforcement will exceed a value of about 1×10^{-3} (0.1%). Figure 4.7 indicates that the strains in the GFRP longitudinal bars were higher than 1×10^{-3}. The Hoult et al. (2008) shear-strength equation of the FRP RC beam specimens is given as follows:

$$V_c = \left[\frac{0.3}{0.5+\left(1000\varepsilon_x+0.15\right)^{0.7}}\right]\left[\frac{1300}{(1000+s_{ze})}\right]\sqrt{f'_c}b_w d_v \tag{4.5}$$

The first term, $\left[\frac{0.3}{0.5+(1000\varepsilon_x+0.15)^{0.7}}\right]$, is related to diagonal crack width; the second term, $\left[\frac{1300}{(1000+s_{ze})}\right]$, is a correction factor for size effect. The strain effect and the size effect are included in the strain term ε_x and the size effect term s_{ze}. It should be noted that the concrete members are not subjected to axial load and are not prestressed. The strain term and the size effect term are taken to be:

$$\varepsilon_x = \frac{M_f / d_v + V_f}{2E_f A_f} \tag{4.6}$$

where M_f and V_f = bending moment and shear force at the critical section for shear.

$$s_{ze} = \frac{31.5d}{16+a_g} \geq 0.77d \tag{4.7}$$

where a_g= maximum aggregate size for coarse aggregate in mm. It has been found that in LWC, the cracks propagate through the aggregate particles rather than around them. Therefore, Hoult et al. (2008) recommended that a_g should be taken as zero in LWC. Hoult et al. (2008) reported that this equation can be expected to yield more accurate estimations of shear strength.

Table 4.4 – Design provisions for calculating the concrete contribution V_c in FRP RC members

Reference	Eq. Number	Information about Equation Use	Details
ACI 440.1R-15 (2015)	Eq. (4.2)	$k=\sqrt{2\rho_f n_f+\left(\rho_f n_f\right)^2}-\rho_f n_f$	$n_f = E_f / E_c$
		$E_c = 0.043 w_c^{1.5}\sqrt{f_c'}$	For sections with NSC with f_c' < 55 MPa.
		$\lambda = 0.8$	For SLWC in which all the fine aggregate is NS.
CSA S806-12 (2012)	Eq. (4.3)	$k_m = \sqrt{V_f d / M_f} \le 1.0$	Coefficient accounting for the effect of moment-to-shear.
		$k_r = 1 + (E_F \rho_{Fw})^{1/3}$	Coefficient accounting for the effect of reinforcement rigidity.
		$k_s = 1$ for (d ≤ 300)	Coefficient accounting for the effect of member size.
		$= 750/(450+d) \le 1$ for (d > 300 and $A_{Fv} \le A_{vF}$)	
		$=1$	For normal density concrete.
		$\lambda = 0.85$	For structural semi-low density concrete in which all the fine aggregate is NS.
		$= 0.75$	For structural low density concrete in which none of the fine aggregate is NS.
CSA S6-19 (2019)	Eq. (4.4)	$\beta = \left[\frac{0.4}{(1+1500\varepsilon_x)}\right]\left[\frac{1300}{(1000+s_{ze})}\right]$	
		$\varepsilon_x = \left[\left(M_f / d_v\right)+V_f\right] / \left[2E_f A_f\right] \le 0.003$	M_f and V_f = bending moment and shear force at the critical section for shear.
		$s_{ze} = 35 s_z / (15 + a_g) \ge 0.85 s_z$	s_{ze} = 300 mm for sections containing at least the minimum shear reinforcement. $s_z = d_v$ or the distance between layers of the shrinkage reinforcement. $a_g = 0$ for LWC or $f_c' \ge 70\,MPa$
		$=0.40\sqrt{f_c'}$	For normal-density concrete with a density between 2150 and 2500 kg/m^3.
		$f_{cr} = 0.34\sqrt{f_c'} \le 3.2$	For semi-low density concrete with a density greater than 1850 kg/m^3 but less than 2150 kg/m^3.
		$=0.30\sqrt{f_c'}$	For low density concrete with a density less than 1850 kg/m^3.

4.5.3 Comparison of Current Equations for Concrete Shear Strength Predictions with the Experimental Results

The concrete shear strengths of the tested FRP RC specimens were compared to predictions based on the shear design equations in ACI 440.1R-15, CSA S806-12, and CSA S6-19.

Moreover, the experimental values were compared to the predicted values based on the shear design equation proposed by Hoult et al. (2008). The design equations in CSA S6-19 and Hoult et al. (2008) are both based on the modified compression field theory (MCFT) (Vecchio and Collins 1986).

The value of λ in CSA S806-12 was considered in the predictions as 0.85 and 0.75 as recommended for the structural semi-low density concrete in which all the fine aggregate is NS, and structural low density concrete in which none of the fine aggregate is NS. On the other hand, λ was taken as 0.8 as recommended in ACI 440.1R-15. To consider the concrete density in CSA S6-19, the cracking strength of concrete f_{cr} was taken to be equal to $0.3\sqrt{f'_c}$, in MPa (see Table 4.4). The safety factors in the design equations were considered to be equal to 1.0.

Table 4.5 provides the comparison between the experimental results (V_{exp}) and the corresponding predicted values (V_{pred}) using the shear design equations from the various codes and guidelines. This table indicates that reducing the concrete density reduction factor in the CSA S806-12 design equation from 0.85 to 0.75 increased the safety margin for the LWSCC beams. The authors found that the values then ranged from 0.88 to 0.96 (closer to 1.0) instead of from 0.77 to 0.85 when using λ equal to 0.75 and 0.85, respectively. It is important to note that all values prediction with CSA S806-12 could be conservative if the reduction factors of materials are used. In contrast, CSA S6-19 and ACI 440.1R-15 underestimated the concrete contribution to the shear strength of the LWSCC beams. Indeed, the V_{exp}/V_{pred} values ranged from 1.25 to 1.50 and from 1.20 to 1.50 with the ACI 440.1R-15 and CSA S6-19 design provisions, respectively, (a value greater than 1.0 indicates a conservative estimation).

Table 4.5 – Comparison of experimental results with the various code predictions

Beam ID	V_{exp}, kN	ACI 440.1R-15		CSA S806-12				CSA S6-19	
		λ=0.8		λ=0.75		λ=0.85		$f_{cr} = 0.3\sqrt{f_c'}$	
		V_{pred}, kN	V_{exp}/V_{pred}	V_{pred}, kN	V_{exp}/V_{pred}	V_{pred}, kN	V_{exp}/V_{pred}	V_{pred} [a], kN	V_{exp}/V_{pred}
LS-G-1.75	46.90	39.59	1.20	52.30	0.90	59.28	0.79	37.28	1.25
LS -G-1.26	43.40	35.83	1.20	49.54	0.88	56.15	0.77	34.40	1.25
LS -G-0.83	40.50	29.78	1.35	43.73	0.93	49.56	0.82	29.01	1.40
LS -G-0.58	38.25	25.67	1.50	39.79	0.96	45.10	0.85	25.28	1.50
LS -S-0.88	52.35	50.20†	1.04	45.28†	1.16	51.32†	1.02	46.22	1.13
N-G--0.83	54.50	29.90	1.82	53.32	1.02	53.32	1.02	40.77	1.34
N-G-0.58	51.75	25.73	2.01	48.52	1.07	48.52	1.07	35.50	1.46

† Shear strength of steel-reinforced beams was calculated according to ACI 318-19 and CSA A23.3-19.

[a] β was calculated according to the general method in CSA S6-19.

Note: 1 kN = 0.225 kip.

The tests results on shear strength of LWC beams (Kim and Jang 2014) available in the literature were used to help in assessing the accuracy of these shear design equations in predicting the shear capacity of LWC members, Table 4.6 gives the characteristics and material properties of these beams. The equilibrium density of the LWC was 1,850 kg/m^3 (115.5 lb/ft^3). Figures 4.9 to 4.11 show the relationship between the experimental and predicted shear strength for the test results of the current study and other beams tested by Kim and Jang (2014). As shown, using *λ=0.75* in the CSA S806-12 equation provides more accurate predictions for the concrete shear strength of LWC beams with the least scattered values. The average value of the V_{exp}/V_{pred} is 1.12 with a standard deviation and coefficient of variation equal to 0.20 and 18.50%, respectively. The ACI 440.1R-15 equation underestimated the shear strength of the LWC beams, as the average value of the V_{exp}/V_{pred} was 1.90. This high level of conservatism is expected for ACI 440.1R-15 because the predicted shear strength of a member is based on the uncracked concrete depth above the neutral axis (Tureyen and Frosch 2002). Moreover, the ACI 440.1R-15 equation produced the most scattered predictions with a standard deviation and coefficient of variation equal to 0.60 and 30%, respectively, followed by CSA S6-19. The average value of the V_{exp}/V_{pred} with the CSA S6-19 design equation was 1.70, with a standard deviation equal to 0.45 and a coefficient of variation of 26%. On other hand, the Hoult et al. (2008) equation provided more accurate predictions compared to the experimental results, as the average value of the V_{exp}/V_{pred} was 1.02 (see Figure 4.12). This is because Hoult et al. (2008) equation was optimized based on

a nonlinear correlation between ε_x and the diagonal crack width. These results indicate that the concrete density reduction factor of the shear strength for LWC beams is unnecessary when using the Hoult et al. (2008) equation.

Table 4.6 – Characteristics of LWC specimens used for comparison of design methods

Ref.	Specimen ID	f'_c (MPa)	Geometrical Characteristics					Flexural Reinforcement			
			b (mm)	h (mm)	d (mm)	L (mm)	Lc (mm)	Type	ρ_f (%)	f_{fu} (MPa)	E_f (GPa)
Kim and Jang 2014	G-L-18-R1-1	33.6	200	250	215	2200	2000	GFRP	0.33	1020	41
	G-L-18-R2-1	33.6	150	250	215	2200	2000	GFRP	0.44	1020	41
	G-L-18-R2-2	33.6	150	250	215	2200	2000	GFRP	0.44	1020	41
	G-L-27-R1-1	40.3	200	250	215	2200	2000	GFRP	0.33	1020	41
	G-L-27-R1-2	40.3	200	250	215	2200	2000	GFRP	0.33	1020	41
	G-L-27-R2-1	40.3	150	250	215	2200	2000	GFRP	0.44	1020	41
	G-L-27-R2-2	40.3	150	250	215	2200	2000	GFRP	0.44	1020	41
	G-L-27-R3-1	40.3	150	250	213	2200	2000	GFRP	0.79	900	40
	G-L-27-R3-2	40.3	150	250	213	2200	2000	GFRP	0.79	900	40
	C-L-18-R1-1	33.6	200	250	215	2200	2000	CFRP	0.33	2130	146.2
	C-L-18-R2-1	33.6	150	250	215	2200	2000	CFRP	0.44	2130	146.2
	C-L-18-R2-2	33.6	150	250	215	2200	2000	CFRP	0.44	2130	146.2
	C-L-27-R1-1	40.3	200	250	215	2200	2000	CFRP	0.33	2130	146.2
	C-L-27-R1-2	40.3	200	250	215	2200	2000	CFRP	0.33	2130	146.2
	C-L-27-R2-1	40.3	150	250	215	2200	2000	CFRP	0.44	2130	146.2
	C-L-27-R2-2	40.3	150	250	215	2200	2000	CFRP	0.44	2130	146.2
	C-L-27-R3-1	40.3	150	250	213	2200	2000	CFRP	0.79	2023	147.9
	C-L-27-R3-2	40.3	150	250	213	2200	2000	CFRP	0.79	2023	147.9

Note: 1 mm= 0.0394 in.; 1 MPa = 145 psi; 1 GPa = 145 ksi.

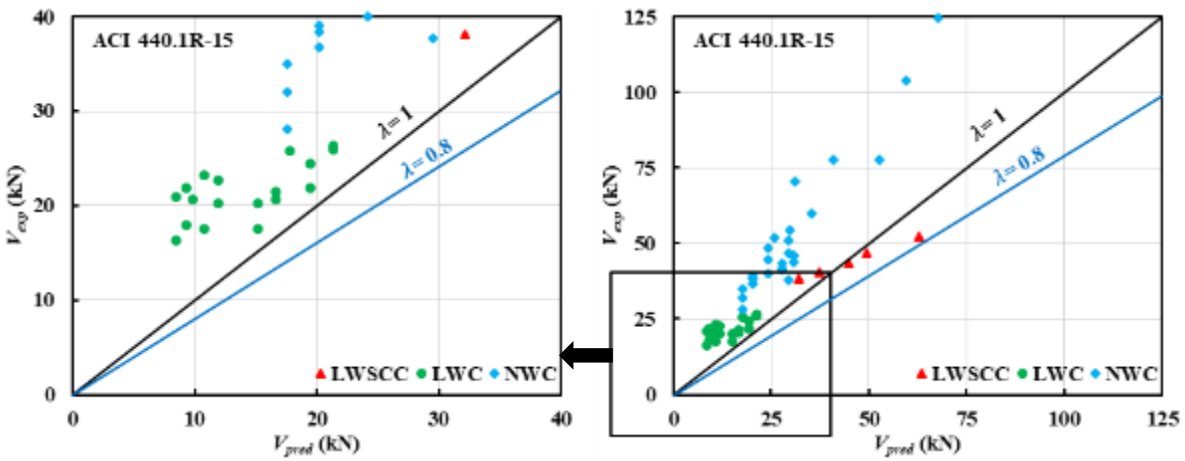

Figure 4.9– Predictions with the ACI 440.1R-15 design equation for all beam specimens. (Note: 1 kN = 0.225 kip.)

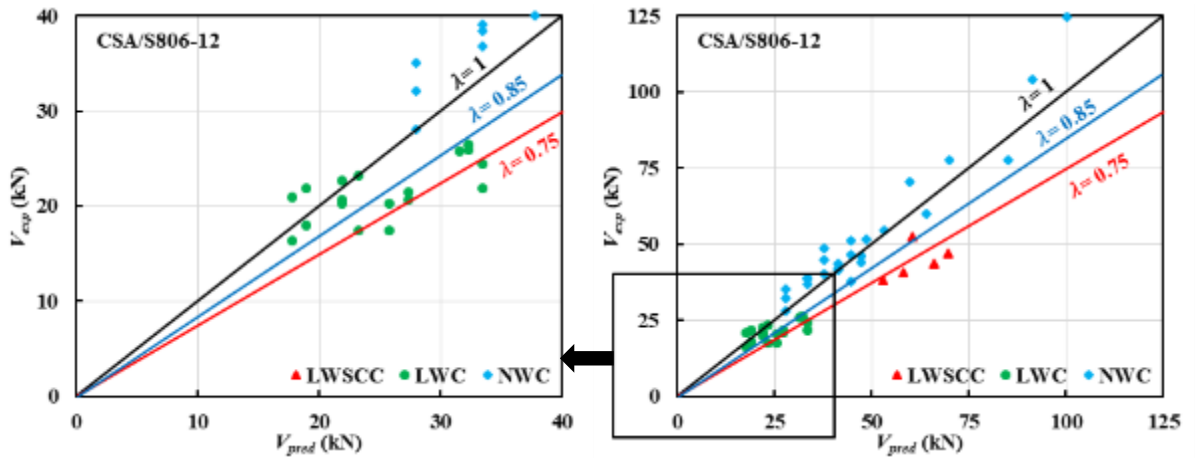

Figure 4.10– Predictions with the CSA S806-12 design equation for all beam specimens. (Note: 1 kN = 0.225 kip.)

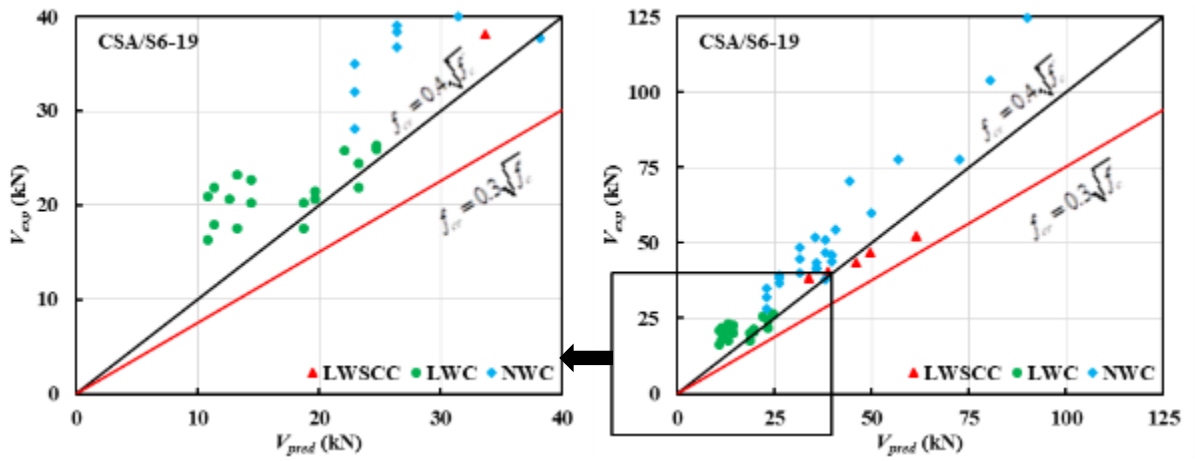

Figure 4.11– Predictions with the CSA S6-19 design equation for all beam specimens. (Note: 1 kN = 0.225 kip.)

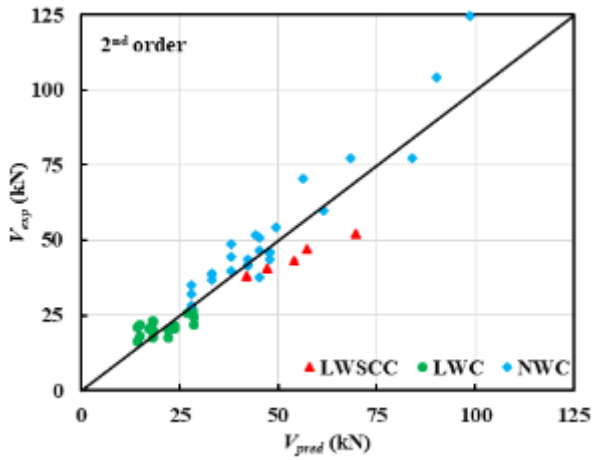

Figure 4.12– Comparison of experimental shear capacities to Hoult et al. (2008) shear strength predictions. (Note: 1 kN = 0.225 kip.)

4.5.4 Effect of Concrete Density on Shear Strength Predictions

The test results of the current study and other available in the literature for LWC beams and NWC beams were compared to show how concrete density affected the concrete shear strength predictions for FRP-reinforced concrete members. Table 4.7 gives the characteristics and material properties of the NWC beams tested by El-Sayed et al. (2006) and Yost et al. (2001). The test variables included the amount of reinforcement and the modulus of elasticity of the longitudinal FRP bars. The amount of reinforcement of the specimens ranged between 0.87% and 2.27% in the longitudinal direction without transverse reinforcement. Table 4.8 presents the average, standard deviation, and coefficient of variation of the V_{exp}/V_{pred} ratio for the LWC and NWC beams. In general, the LWC beams had lower concrete shear strength than the NWC beams. A concrete density reduction factor of 0.75 and 0.8 were applied in the CSA S806-12 and ACI 440.1R-15 shear design equations, respectively, to consider the influence of concrete density. Table 4.8 indicates that doing so resulted in a degree of conservatism equal to that of the shear design equations for NWC beams. The CSA S806-12 and ACI 440.1R-15 equations yielded V_{exp}/V_{pred} values 1.12 and 1.90, respectively, for the LWC beams. The corresponding values for the NWC beams were 1.07 and 1.75. The CSA S6-19 equation underestimated the experimental shear strength of the LWC and NWC beams, with average V_{exp}/V_{pred} values of 1.70 and 1.30, respectively. The comparison shows that the ACI 440.1R-15 and CSA S6-19 predictions were more scattered for the LWC beams than the NWC beams, as the values of the standard deviation of the V_{exp}/V_{pred} for the NWC beams were 0.23 and 0.16, respectively, with coefficients of variation equal to 13.35% and 12%. On the other hand, the Hoult et al. (2008) equation provided comparable V_{exp}/V_{pred} results for both the LWC and NWC beams, with average V_{exp}/V_{pred} values equal to 1.02 and 1.08, respectively.

Table 4.7 – Characteristics of NWC specimens from past studies

Ref.	Beam ID	f_c (MPa)	Geometrical Characteristics					Flexural Reinforcement			
			b (mm)	h (mm)	d (mm)	L (mm)	Lc (mm)	Type	ρ_f (%)	f_{fu} (MPa)	E_f (GPa)
El-Sayed et al. (2006)	CN-1	50	250	400	326	3250	2750	CFRP	0.87	1536	128
	GN-1	50	250	400	326	3250	2750	GFRP	0.87	608	39
	CN-2	44.6	250	400	326	3250	2750	CFRP	1.24	986	134
	GN-2	44.6	250	400	326	3250	2750	GFRP	1.22	754	42
	CN-3	43.6	250	400	326	3250	2750	CFRP	1.72	986	134
	GN-3	43.6	250	400	326	3250	2750	GFRP	1.71	754	42
Yost et al. (2001)	1FRP-a	36.3	229	286	225	2284	2132	GFRP	1.11	689.5	40.3
	1FRP-b	36.3	229	286	225	2284	2132	GFRP	1.11	689.5	40.3
	1FRP-c	36.3	229	286	225	2284	2132	GFRP	1.11	689.5	40.3
	2FRP-a	36.3	178	286	225	2284	2132	GFRP	1.42	689.5	40.3
	2FRP-b	36.3	178	286	225	2284	2132	GFRP	1.42	689.5	40.3
	2FRP-c	36.3	178	286	225	2284	2132	GFRP	1.42	689.5	40.3
	3FRP-a	36.3	229	286	225	2284	2132	GFRP	1.66	689.5	40.3
	3FRP-b	36.3	229	286	225	2284	2132	GFRP	1.66	689.5	40.3
	3FRP-c	36.3	229	286	225	2284	2132	GFRP	1.66	689.5	40.3
	4FRP-a	36.3	279	286	225	2284	2132	GFRP	1.81	689.5	40.3
	41FRP-b	36.3	279	286	225	2284	2132	GFRP	1.81	689.5	40.3
	4FRP-c	36.3	279	286	225	2284	2132	GFRP	1.81	689.5	40.3
	5FRP-a	36.3	254	286	225	2284	2132	GFRP	2.05	689.5	40.3
	5FRP-b	36.3	254	286	225	2284	2132	GFRP	2.05	689.5	40.3
	5FRP-c	36.3	254	286	225	2284	2132	GFRP	2.05	689.5	40.3
	6FRP-a	36.3	229	286	225	2284	2132	GFRP	2.27	689.5	40.3
	6FRP-b	36.3	229	286	225	2284	2132	GFRP	2.27	689.5	40.3
	6FRP-c	36.3	229	286	225	2284	2132	GFRP	2.27	689.5	40.3

Note: 1 mm= 0.0394 in.; 1 MPa = 145 psi; 1 GPa = 145 ksi.

Table 4.8 – Average, standard deviation, and coefficient of variation of the V_{exp}/V_{pred} for LWC and NWC beams.

		ACI 440.1R-15	CSA S806-12		CSA S6-19	Hoult et al. (2008)
		λ=0.8	λ=0.75	λ=0.85	$f_{cr} = 0.3\sqrt{f_c'}$	
LWC	Average	1.90	1.12	0.98	1.70	1.02
	SD	0.60	0.20	0.18	0.45	0.21
	COV (%)	30.0	18.50	18.57	26.0	20.60
NWC	Average	1.75	1.07		1.30	1.08
	SD	0.23	0.11		0.16	0.12
	COV (%)	13.35	10.50		12.0	11.15

4.6 Summary and Conclusions

This research investigated the concrete contribution to the shear strength of reinforced LWSCC beams using a mixture design for LWSCC with an equilibrium density of 1,800 kg/m^3 (112.4 lb/ft^3) and compressive strength of 54 MPa (7830 psi). Simply supported beams reinforced with GFRP bars were tested under four-point bending up to failure. The experimental results were combined with the collected database (LWC and NWC beams) and compared to the shear strength predictions produced with the shear design equations of the American Concrete Institute (ACI), the Canadian Standards Association (CSA), and the equation proposed by Hoult et al. (2008). The main findings of this investigation can be summarized as follows:

1. The tested LWSCC and NWC beams reinforced with GFRP bars failed in the same manner: diagonal tension failure.
2. The experimental results show that the GFRP-reinforced LWSCC beams exhibited cracking behavior similar to that of the counterpart GFRP-reinforced NWC beams, with the exception of an earlier onset of flexural cracking.
3. The normalized shear strength in the beams cast with LWSCC was proportional to the GFRP longitudinal reinforcement ratio. Increasing the GFRP reinforcement ratio from 0.58% to 1.75% increased the normalized shear strength of the beams by 30%. On the other hand, increasing the GFRP longitudinal reinforcement ratio increased the number of cracks.
4. Comparing the concrete shear strengths of the LWC beams with their predicted strengths based on a concrete density reduction factor of 0.75 in the CSA S806-12 design equation revealed that this equation yielded the most accurate predictions of LWC beams reinforced with FRP bars, as the safety margin was 1.12.
5. Using a concrete density reduction factor of 0.8 in the ACI 440.1R-15 equation to consider the influence of concrete density yielded a degree of conservatism equal to that of the equation for NWC beams. ACI 440.1R-15, however, yielded the most conservative predictions for LWC and NWC beams.
6. The Hoult et al. (2008) equation provided less conservative results for LWC beams reinforced with FRP bars than did the CSA S6-19 equation. Moreover, the safety margin

was 1.02 in LWC beams, indicating that the concrete density reduction factor of the shear strength for LWC beams is not required when using the Hoult et al. (2008) equation.

CHAPTER 5

Flexural Behavior and Serviceability Performance of LWSCC Beams Reinforced with BFRP Bars

Foreword

Authors and Affiliation:

- Shehab Mehany: Ph.D. candidate, Department of Civil Engineering, Université de Sherbrooke, Sherbrooke, Quebec, Canada, J1K 2R1.
- Hamdy M. Mohamed: Research Associate/Lecturer, Department of Civil Engineering, Université de Sherbrooke, Sherbrooke, Quebec, Canada, J1K 2R1.
- Brahim Benmokrane: Professor, Department of Civil Engineering, Université de Sherbrooke, Sherbrooke, Quebec, Canada, J1K 2R1.

Journal Title: *ACI Structural Journal.*

Paper Status: *Accepted*.

Abstract

This study investigates the flexural behavior and serviceability performance of lightweight self-consolidating concrete (LWSCC) beams reinforced with basalt fiber-reinforced-polymer (BFRP) bars. Eleven reinforced concrete beam specimens with a cross-sectional width and height of 200 mm (7.87 in) and 300 mm (11.81 in), respectively, and with a total length of 3,100 mm (122.05 in) were tested under four-point bending load up to failure. Nine specimens were made with LWSCC, while the other two were made with normal-weight concrete (NWC) as reference specimens. The test parameters were concrete density (LWSCC and NWC); reinforcement type (sand-coated BFRP, helically grooved BFRP, thread-wrapped BFRP, or steel); and longitudinal BFRP reinforcement ratio. The test results indicate that the LWSCC yielded lower beam self-weight (density of 1,800 kg/m^3) (112.4 lb/ft^3) than the NWC. Increasing the BFRP reinforcement ratio increased the normalized moment capacity of the LWSCC specimens. The test results were compared from the standpoint of the cracking and ultimate moment, deflection, and crack-width design provided in the available design standards for FRP reinforced elements. The comparison indicates that the experimental moment capacities of the LWSCC and NWC beams were in good agreement with the predictions based on FRP design standard with an average accuracy of ≥ 90%. The crack width of the LWSCC beams was affected by the surface configuration of the BFRP bars, while the deflection was not significantly affected by the concrete density. The Canadian design code yielded accurate predictions with a bond-dependent coefficient of 0.8 and 1.0 for the sand-coated and helically grooved BFRP bars, respectively, in LWSCC.

Keywords: Lightweight self-consolidating concrete (LWSCC) beams; Basalt fiber-reinforced polymer (BFRP) bars; Flexural behavior; Experimental and analytical investigation; Strength and serviceability; Deflection and crack width; Bond-dependent coefficient, Deformability; Design codes.

5.1 Introduction

Lightweight self-consolidating concrete (LWSCC) is deemed as an applicable alternative to normal-weight concrete (NWC) in reinforced concrete (RC) structures. It was developed to combine the excellent benefits of lightweight concrete (LWC) and self-consolidating concrete (SCC) in a single package. LWC makes it possible to reduce the self-weight of RC members, while maintaining concrete strength similar to NWC. Reducing the self-weight of a structure reduces the dimensions of elements (beams, slabs, columns, and foundations), thereby leading to lower cost. SCC yields non-segregating concrete that can spread into place and fill the formwork without any mechanical consolidation. Using SCC for RC members also reduces labor and machinery costs. Therefore, LWSCC provides better strength and durability, while offering excellent workability. LWSCC has been used in different applications, including the construction of bridge main girders, composite floor slabs, and precast concrete elements.

In the last two decades, the use of noncorroding fiber-reinforced polymer (FRP) bars as a replacement for traditional steel bars in RC members has gained the trust of and acceptance in the construction field. Recently, researchers' attention has been turned to the favorable characteristics of basalt FRP (BFRP) as a new reliable FRP type. BFRP provides benefits that are equivalent or superior to other types of FRP, while being significantly more cost-effective (Wei et al. 2010). BFRP also provides excellent freeze/thaw resistance, excellent resistance to acidic environments, and good thermal resistance. Similar to other FRP bars, BFRP bars are characterized by high strength-to-weight ratio, greater chemical stability than E-glass FRP, excellent bond strength with concrete, and relatively low modulus of elasticity when compared to traditional steel bars, in addition to being noncorroding (Wu et al. 2015; Elgabbas et al. 2017).

Although BFRP bars are commercially available, they are still not widely used as internal reinforcement in North America in comparison to the other FRPs due to the lack of research and design standards. A few experimental studies have been conducted to assess the influence of BFRP reinforcing bars on the flexural behavior of NWC beam specimens. Tomlinson and Fam (2015) investigated the flexural performance of BFRP-reinforced NWC (BFRP-NWC) beams with BFRP or steel stirrups. Their results indicate that the moment capacities of the BFRP-NWC beams tested were higher than that of the counterpart control steel beam with the same amount of reinforcement. Moreover, ACI 440.1R (2006) and CSA S806 (2012) adequately predicted the moment capacity of the BFRP-NWC beams. Abed et al. (2021) tested 14 slender BFRP-NWC

beams under flexural loads. Seven beams were made with high-strength concrete (HSC) and seven others with normal-strength concrete (NSC). The beam specimens measured 180 mm (7.09 in) wide, 230 mm (9.06 in) high, and 2,200 mm (86.61 in) long. The test results show that the increasing moment capacity of the BFRP-NWC specimens with increasing amount of reinforcement was quite consistent with the ACI 440.1R (2015) equation. In addition, using HSC enhanced the cracking moment by 10% compared to the NSC beams.

Due to the relative low modulus of elasticity of FRP bars compared to that of steel bars, FRP-RC elements will exhibit larger deflections and crack widths. Thus, serviceability requirements are crucial in the design of FRP-RC members to ensure the important serviceability aspects, such as appearance or watertightness. Valuable research efforts have focused on the serviceability performance of BFRP-RC members, including crack width and deflection response. Steel-based crack models have been modified to account for FRP-bar properties using the bond-dependent coefficient (k_b) factor (ACI 440.1R (2015)). The k_b term is a factor that accounts for the degree of bond between FRP bars and the surrounding concrete. Elgabbas et al. (2016) carried out an experimental investigation on the serviceability performance of NWC beams reinforced with sand-coated BFRP bars. The beams had a total length of 3,100 mm (122.05 in) and a rectangular cross section of 200 mm (7.87 in) in width and 300 mm (11.81 in) in height. They found that the k_b factor was 0.76 for the sand-coated BFRP bars, which is consistent with the CSA S6 (2019) recommendation of k_b = 0.8 for sand-coated FRP bars. Elgabbas et al. (2017) reported that ACI 440.1R (2015) underestimated the deflection of the BFRP-NWC specimens, while CSA S806 (2012) provided reasonable yet conservative deflection values. In addition, the average k_b was 0.83 for the ribbed BFRP bars, which is lower than the CSA S6 (2019) recommendation of k_b = 1.0 for ribbed FRP bars (Elgabbas et al. 2017).

Integrating BFRP bars into LWSCC would effectively contribute to producing lighter and more durable RC structures. So far, limited studies have been conducted to investigate the flexural behavior of FRP-reinforced LWC (FRP-LWC) members (Wu et al. 2019; Liu et al. 2020). In addition, no experimental studies seem to have investigated BFRP-reinforced LWSCC (BFRP-LWSCC) beams under flexural loads. Wu et al. (2019) studied the flexural behavior of RC beams with glass-FRP (GFRP) bars. The beams were fabricated with LWC and steel fiber-reinforced LWC (SFLWC). The test results indicate that the failure of the GFRP-reinforced LWC (GFRP-LWC) and GFRP-reinforced SFLWC (GFRP-SFLWC) specimens occurred by concrete crushing. They found that, as the reinforcement ratio increased, the beams exhibited smaller

crack widths and lower deflections at the same load levels (Wu et al. 2019). Liu et al. (2020) reported that the SFLWC yielded narrower crack widths than the LWC. In addition, using steel fibers in the LWC specimens having low reinforcement ratios decreased the crack width at service load.

5.2 Research Significance

The literature review revealed no studies investigating the flexural behavior of LWSCC beams reinforced with BFRP bars. In addition, BFRP bars have not yet been included in design standards and guidelines (CSA S806 (2012), CSA S6 (2019), AASHTO (2019), and ACI 440.1R (2015)). The main objectives of this investigation were to assess the flexural behavior and serviceability performance of BFRP-LWSCC beams. The test parameters included concrete density (LWSCC and NWC), reinforcement type, and longitudinal BFRP reinforcement ratio. Three different types of BFRP bars—sand-coated, helically grooved, and thread-wrapped—were considered in the study as being representative of those commercially available and for having the properties specified in the new edition of CSA S807 (2019). The test results and outcomes of this study can be used to assess and explore the feasibility of using BFRP bars as longitudinal reinforcement in flexural LWSCC members. In addition, the results of this investigation will contribute to integrating BFRP bars into FRP design codes and guidelines considering the effect of concrete density. Moreover, the results reported in this paper represent a significant contribution to the relevant literature and provide designers, engineers, and members of code committees with much-needed data and recommendations to advance the use of basalt FRP reinforcement in concrete structures.

5.3 Test Program

5.3.1 Materials

5.3.1.1 Concrete Mixes

Both the LWSCC and NWC specimens were cast with a target concrete strength of 40 MPa. The NWC was provided by a local supplier, while the LWSCC was mixed in the laboratory at the University of Sherbrooke. The LWSCC mixtures contained two crushed lightweight aggregate (LWA) types—Solite 307 and Solite 343—from a single source. The properties of the LWAs met the requirements of the current version of ASTM C330 / C330M-17a (2017). Table 5.1

presents the physical properties of aggregates. Table 5.2 gives the details of the mix proportions of the LWSCC and NWC. The density of the LWSCC was 1,800 kg/m^3 (112.4 lb/ft^3) as measured according to ASTM C567 (ASTM C567/C567M (2014). The exact concrete compressive and tensile strengths were determined on the day of testing from three 100 × 200 mm (3.94 × 7.87 in) concrete cylinders for each test in accordance with ASTM C39/C39M (2018) and ASTM C496 (2011), respectively. The exact concrete compressive strength for the LWSCC ranged from 42 to 43.8 MPa (6,090 to 6,350 psi), while that of the NWC was 41.3 MPa (5,990 psi). The average tensile strengths were 3.0 and 3.6 MPa (435 and 520 psi) for the LWSCC and NWC, respectively.

Table 5.1– Physical properties of aggregates

Materials	Specific Gravity	Water Absorption (%)	Maximum Particle-Size (mm)
Lightweight coarse aggregates	1.47	11.2	15
Lightweight sand	1.65	18.5	5
Natural sand	2.65	0.98	5.15

Note: 1 mm = 0.0394 in.

Table 5.2– LWSCC and NWC mix proportions

LWSCC		NWC	
Type TerC3 cement	*520* kg /m^3	Type GU cement	244 kg/m^3
		Type GUb-SF cement	216 kg/m^3
w/c	0.34	w/c	0.35
Lightweight coarse aggregate	369 kg /m^3	Crushed stone: 5–20 mm	730 kg /m^3
Lightweight sand	488 kg /m^3	Crushed stone: 5–10mm	272 kg/m^3
Natural sand	381 kg /m^3	Natural sand	719 kg/m^3
Air entrainment	70 mL/100 kg	Air entrainment	80 mL/100 kg
Superplasticizer	3 L/ m^3	Water reducer	300 mL/100 kg

Note: 1 kg /m^3= 0.062 lb/ft^3; 1 mL/100 kg= 0.015 oz/100 lb; l/ m^3=1.04 oz/ft^3.

5.3.1.2 Reinforcing Bars

Three different types of BFRP bars—referred to as BFRP Type I (No. 6), BFRP Type II (No. 5), and BFRP Type III (No. 3)—were used (see Figure 5.1). The BFRP bars were sand-coated, helically grooved, or thread-wrapped for sizes No. 6, No. 5, and No. 3, respectively, with "nominal" diameters of 19.1, 15.9, and 9.5 mm (0.75, 0.63, and 0.37 in). The bars had typical

fiber contents of 81%, 80%, and 73.3% by weight, respectively. The modulus of elasticity, ultimate tensile strength, and tensile strain at rupture of the BFRP bars were estimated by testing five representative specimens in accordance with ASTM D7205 (2011). In addition, grade 450 15M steel bars served as longitudinal reinforcement in the reference specimen. Furthermore, one size (10M) of steel stirrups was fabricated as transverse reinforcement for all the beams. Table 5.3 summarizes the mechanical properties of the BFRP and steel bars.

Figure 5.1– BFRP bar types and surface characteristics.

Table 5.3– Mechanical properties of the BFRP and steel reinforcement

RFT Type		Bar Size	Surface Configuration	d_b (mm)	A_f [a] (mm²)	A_{im} [b] (mm²)	E_f (GPa)	f_{fu} (MPa)	ε_{fu} (%)
BFRP bars	Type I	No. 6	Sand-coated	19.1	285	346	63.7	1646	2.50
	Type II	No. 5	Helically grooved	15.9	199	201.1	64.8	1724	2.67
	Type III	No. 3	Thread-wrapped	9.5	71	104	47.8	911	2.0
Steel bars		15M	Ribbed	16.0	200	---	E_s [c]=203	f_y [d] = 450	ε_y [d] = 0.22

[a] Nominal cross-sectional area.

[b] Immersed cross-sectional area (measured).

[c] E_s is the modulus of elasticity of the steel bars.

[d] f_y and ε_y are the yield strength and strain of the steel bars, respectively.

Note: Properties calculated based on the nominal cross-sectional area; 1 mm = 0.0394 in; 1 mm^2 = 0.00155 in^2; 1 GPa = 145 ksi; 1 MPa = 145 psi.

5.3.2 Beam Details and Test Parameters

A total of 11 RC beams measuring 3,100 mm (122.05 in) long with a 200 × 300 mm (7.87 × 11.81 in) rectangular cross section were fabricated including four beams reinforced with sand-coated BFRP bars; four beams reinforced with helically grooved BFRP bars; two beams reinforced with thread-wrapped BFRP bars; and one beam reinforced with steel bars for comparison purposes. It is worth mentioning that nine specimens, including the traditional steel RC specimen, were made with LWSCC; two reference specimens were made with NWC. The beams were designed according to the geometry recommendations in Annex S of CSA S806 (2012). The constant shear span-to-depth ratio was approximately 4.50. Figure 5.2 shows the layout, rectangular cross sections, and reinforcement arrangement of the beam specimens. Table 5.4 shows the test matrix, details of test specimens, and the actual compressive strengths of the LWSCC and NWC for the beam specimens.

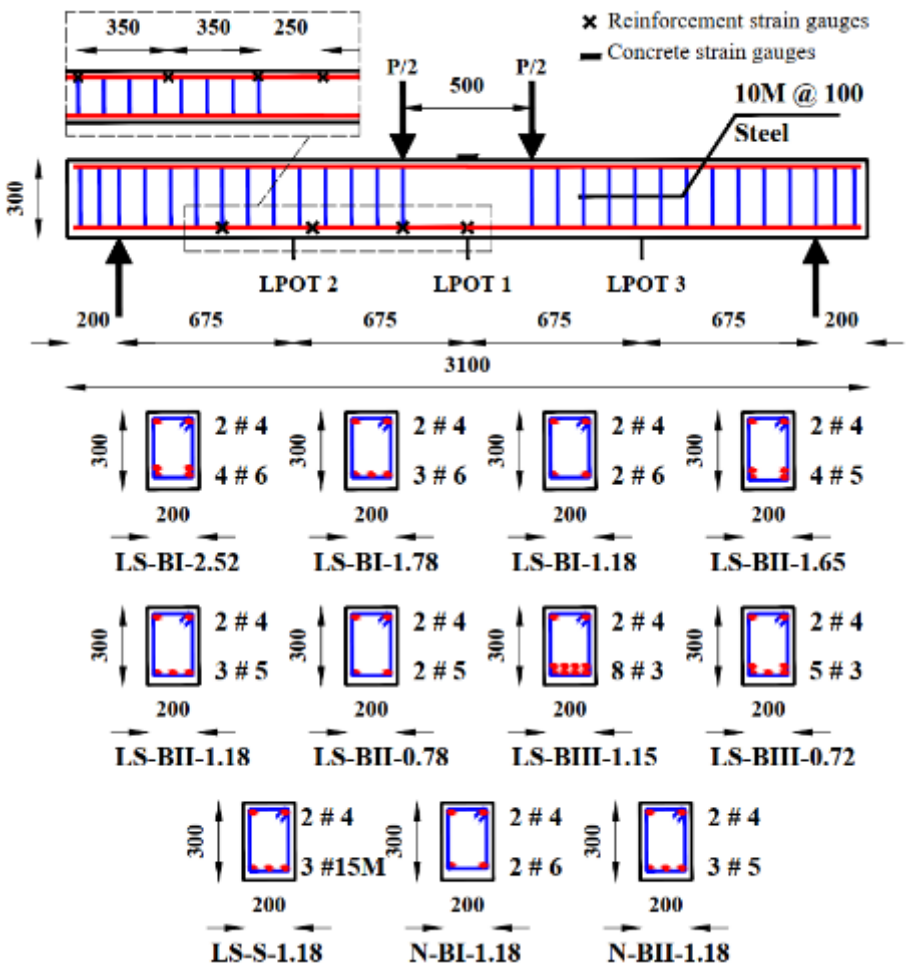

Figure 5.2– Dimensions, reinforcement details, and instrumentation of the beam specimens. (Note: dimensions in mm; 1 mm = 0.0394 in)

Table 5.4– Test matrix and details of test specimens

Beam ID	Reinforcing Material	f'_c (MPa)	Flexural Reinforcement		ρ_f/ρ_{fb}		E_fA_f, N × 10^6
			Bars	ρ_f (%)	ACI 440.1R (2015)	CSA S806 (2012)	
LS-BI-2.52	BFRP- Type I	42.0	4 No.6	2.52	15.0	13.75	72.50
LS-BI-1.78	BFRP- Type I	42.0	3 No.6	1.78	10.60	9.50	54.45
LS-BI-1.18	BFRP- Type I	42.0	2 No.6	1.18	7.05	6.35	36.30
LS-BII-1.65	BFRP- Type II	43.0	4 No.5	1.65	10.35	9.40	51.60
LS-BII-1.18	BFRP- Type II	43.0	3 No.5	1.18	7.30	6.60	38.70
LS-BII-0.78	BFRP- Type II	42.0	2 No.5	0.78	5.0	4.50	25.80
LS-BIII-1.15	BFRP- Type III	43.0	8 No.3	1.15	2.65	2.45	27.15
LS-BIII-0.72	BFRP- Type III	43.0	5 No.3	0.72	1.65	1.50	17.00
LS-S-1.18	Steel	43.8	3#15M	ρ_s [a]= 1.18	0.27	0.26	120.00
N-BI-1.18	BFRP- Type I	41.3	2 No.6	1.18	7.15	6.40	36.30
N-BII-1.18	BFRP- Type II	41.3	3 No.5	1.18	7.55	6.80	38.70

[a] ρ_s is the reinforcement ratio of the beam reinforced with steel bars.

Note: 1 MPa = 145 psi; 1 N= 0.000225 kips.

Each beam was identified with a tripartite numbering code. The first part (LS or N) refers to the type of concrete density: LWSCC or NWC, respectively. The second part (BI, BII, BIII, or S) indicates the reinforcement: sand-coated BFRP, helically grooved BFRP, thread-wrapped BFRP or steel bars, respectively. The numbers represent the longitudinal reinforcement ratio. The test parameters were concrete density (LWSCC and NWC), reinforcement type, and longitudinal BFRP reinforcement ratio. The influence of concrete density on the flexural behavior was considered by testing two NWC beams (N-BI-1.18 and N-BII-1.18) and two LWSCC beams (LS-BI-1.18 and LS-BII-1.18) (density equal to 1,800 kg/m^3 (112.4 lb/ft^3)) with the same reinforcement ratio (1.18%). Since the BFRP beams were designed to fail by concrete crushing between the two loading points, they were designed based on the over-reinforced concept. The reinforcement ratios have been selected to be greater than the balanced reinforcement ratio (ρ_{fb}). This is the common design concept for FRP-RC members according to CSA S806 (2012) and ACI 440.1R (2015). The ρ_{fb} was estimated with the following equation:

$$\rho_{fb} = \alpha_1 \beta_1 \frac{f'_c}{f_{fu}} \frac{E_f \varepsilon_{cu}}{E_f \varepsilon_{cu} + f_{fu}} + \rho'_f \frac{\varepsilon'_f E'_f}{f_{fu}} \tag{5.1}$$

The factors of the equivalent rectangular stress block α_1 *and* β_1 are calculated from the following equations:

ACI 440.1R (2015)

$$\alpha_1 = 0.85 \tag{5.2}$$

$$\beta_1 = 0.85 - 0.00714\left(f_c^{'} - 28\right) \geq 0.65 \tag{5.3}$$

CSA S806 (2012)

$$\alpha_1 = 0.85 - 0.0015 f_c^{'} \geq 0.67 \tag{5.4}$$

$$\beta_1 = 0.97 - 0.0025 f_c^{'} \geq 0.67 \tag{5.5}$$

The influence of BFRP reinforcement ratio on the flexural behavior was investigated by testing three beams reinforced longitudinally with No. 6 sand-coated BFRP bars with reinforcement ratios of 2.52%, 1.78%, and 1.18%; three beams reinforced longitudinally with No. 5 helically grooved BFRP bars with reinforcement ratios of 1.65%, 1.18%, and 0.78%; and two specimens reinforced longitudinally with No.3 thread-wrapped BFRP bars with reinforcement ratios of 1.15% and 0.72%.

All specimens had two BFRP bars as top reinforcement to hold the stirrups. 10M steel stirrups spaced at 100 mm were used in the transverse direction in both shear spans to avoid shear failure. To reduce the confining influence of the transverse reinforcement on the flexural behavior, no stirrups were used in the pure moment region between the two loading points. The clear bottom cover was 50 mm (1.97 in) for the No. 6 bars and 38 mm (1.50 in) for the No. 3 and No. 5 bars, which was set in accordance with Annex S in CSA S806 (2012). Figure 5.3 shows the fabrication of the beam specimens (cages inside the formwork and the specimens).

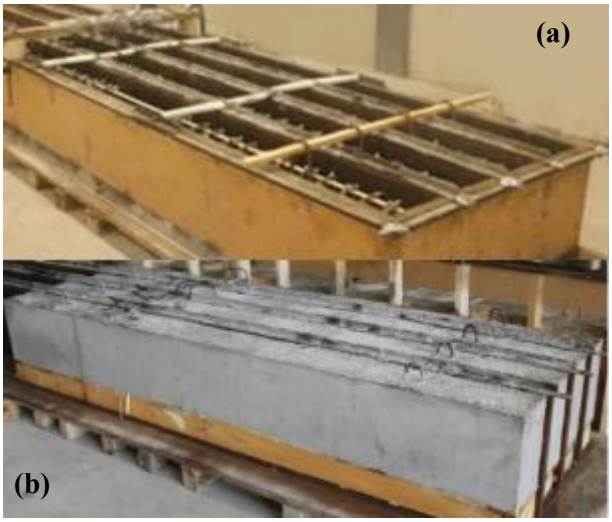

Figure 5.3– Fabrication of the beam specimens (a) Cages inside the formwork; and (b) Beam specimens.

5.3.3 Instrumentation and Test Specimens

Instrumentation of the beam specimens included three linear potentiometers (LPOTs) (LPOT1 at mid-span, and LPOT2 and LPOT3 at quarter-span) for deflection measurement. The initial crack width was measured and recorded manually with a 50× handheld microscope. Three horizontal linear variable differential transducers (LVDTs) were installed to measure the crack widths. Epoxy was used to fix the LVDTs during testing at the location of the first three flexural cracks. In addition, four electrical strain gauges with a gauge length of 6 mm (0.24 in) were used to measure the reinforcement strains in the longitudinal bars at four locations. The compressive concrete strains were measured at mid-span with two electrical strain gauges with a gauge length of 60 mm (2.36 in). Epoxy was used to attach the strain gauges to the compression beam surface after it was cleaned. Figure 5.2 shows the instrumentation details of the beam specimens.

After casting and curing, the beams were stored for two to three months outdoors prior to being brought back into the laboratory for testing. Prior to testing, the beams were painted white and marked with vertical and horizontal lines (100 × 100 mm) (3.94 × 3.94 in) to help in observing crack propagation during testing. The specimens were subjected to four-point flexural testing on a clear span length of 2,700 mm (106.30 in). The beams were supported by two steel plates measuring 150 mm (5.90 in) wide set on the hinged and roller supports. The vertical load was applied with a 1,000 kN (224.80 kip) hydraulic actuator through a steel spreader beam at a stroke-controlled rate of 0.6 mm/min (0.024 in/min). This rigid steel beam was used to transfer two equal concentrated loads to the beam specimen. The details of test setup are shown in Figure

5.4. The applied load, strain gauges, LPOTs, and LVDTs readings were automatically recorded during the test with a 20-channel computer data-acquisition system and stored on a personal computer.

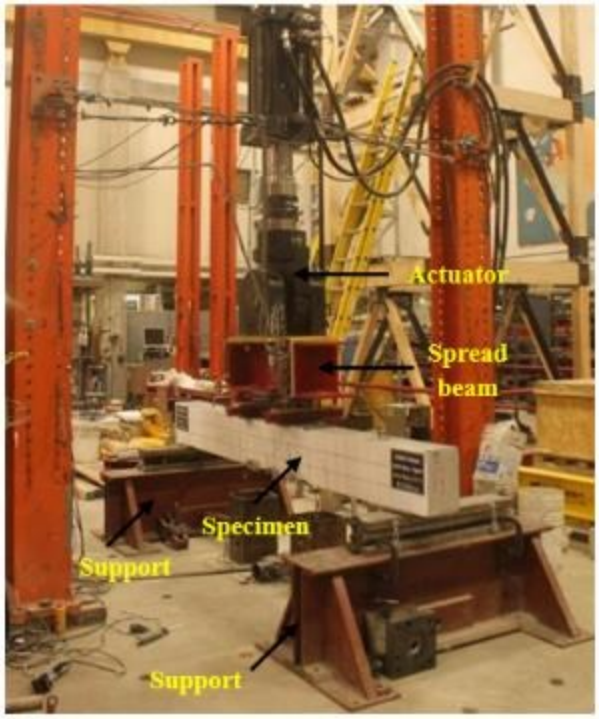

Figure 5.4– Test setup.

5.4 Test Results and Discussion

5.4.1 Crack Propagation and Mode of Failure

The LWSCC and NWC test specimens had similar crack patterns up to the peak load. The initial vertical crack appeared and propagated between the two loading points from the bottom of the specimen, where pure bending (flexural) stress is highest and shear stress is zero. As the load increased, additional vertical cracks appeared in the pure bending region and propagated progressively in a vertical direction. With further loading, cracks formed along the shear span, becoming wider and deeper. The cracks outside the pure bending region were affected by a combination of flexural and shear stresses. Table 5.5 summarizes the observed failure modes of the specimens. The BFRP-reinforced LWSCC and NWC beams failed in flexure by crushing of concrete in the pure bending region because the beams were designed to be over-reinforced. ACI 440.1R (2015) and CSA S806 (2012) recommend this failure mode for FRP-RC members since it is more gradual, less brittle, and less catastrophic with higher deformability compared to the

tensile rupture of FRP bars. On the other hand, the under-reinforced steel RC beam failed in flexure by yielding of the steel reinforcement, followed by concrete crushing. Figure 5.5 provides the crack propagation and failure mode of the tested specimens. As seen in this figure, the neutral-axis depths of the BFRP-LWSCC specimens (LS-BI-1.18, LS-BII-1.18, and LS-BIII-1.15) were less than that of the steel-reinforced LWSCC (steel-LWSCC) beam (LS-S-1.18) with a similar reinforcement ratio. This could be attributed to the fact that the steel bars had a higher modulus of elasticity than that of the BFRP bars. Moreover, the neutral-axis depth of the BFRP-LWSCC specimens increased as did the reinforcement ratio. The equilibrium of forces requires a larger concrete compression segment for the greater forces arising from larger areas of tensile reinforcement.

Table 5.5– Experimental and predicted cracking and ultimate moments

Beam ID	Experimental			Normalized Moment Capacity	$M_{cr\text{-}exp}/M_{cr\text{-}pred}$		$M_{n\text{-}exp}/M_{n\text{-}pred}$
	$M_{cr\text{-}exp}$ (kN.m)	$M_{n\text{-}exp}$ (kN.m)	Failure Mode[a]		ACI 440.1R (2015)	CSA S806 (2012)	ACI 440.1R (2015)
LS-BI-2.52	8.2	87.0	C.C.	0.203	0.80	0.88	1.07
LS-BI-1.78	8.5	85.5	C.C.	0.176	0.83	0.91	1.04
LS-BI-1.18	8.0	73.0	C.C.	0.150	0.80	0.87	1.03
LS-BII-1.65	8.5	87.0	C.C.	0.174	0.83	0.90	1.02
LS-BII-1.18	8.0	85.0	C.C.	0.153	0.78	0.85	1.02
LS-BII-0.78	7.5	73.5	C.C.	0.136	0.75	0.82	1.05
LS-BIII-1.15	8.2	78.0	C.C.	0.148	0.81	0.89	1.12
LS-BIII-0.72	8.5	70.0	C.C.	0.133	0.85	0.94	1.22
LS-S-1.18	9.5	58.5 [b]	S.Y. + C.C.	0.104	0.82	0.89	1.06
N-BI-1.18	10.3	80.0	C.C.	0.168	0.85	0.87	1.13
N-BII-1.18	9.5	91.0	C.C.	0.171	0.78	0.80	1.08

[a] C.C. = crushing of concrete; S.Y.+ C.C. = yielding of steel followed by concrete crushing.

[b] Yielding moment.

Note: 1 kN.m= 0.738 kip.ft.

Figure 5.5 also reveals that increasing the amount of reinforcement in the BFRP-LWSCC beams increased the total number of cracks that formed between the two loading points and, therefore, decreased the crack spacing. In addition, it should be mentioned that the crack spacing was affected by the surface conditions of the BFRP bars. For instance, the average crack spacing in the sand-coated BFRP-reinforced LWSCC beam (LS-BI-1.18) was narrower than the average crack spacing observed in the helically grooved BFRP-reinforced LWSCC beam (LS-BII-1.18) with the same reinforcement ratio (ρ_f of 1.18%).

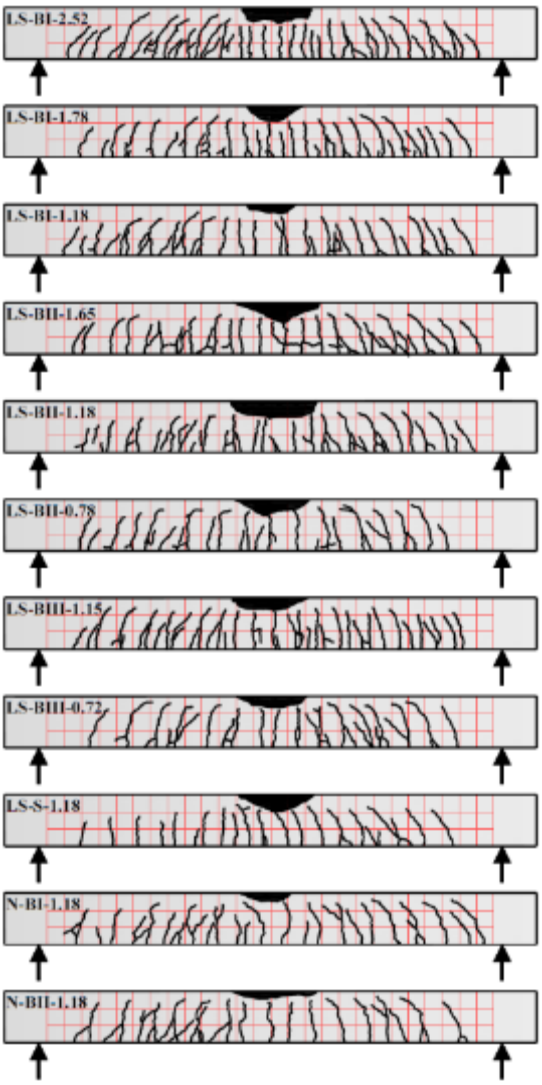

Figure 5.5– Crack patterns and failure modes of the tested beams.

Figure 5.6 presents the typical behavior of the experimental width of the first crack versus the applied moment for the BFRP-LWSCC beams. As shown in this figure, increasing the reinforcement ratio reduced the width of the first crack at the same load level. The crack in LS-BI-1.18 was wider than in LS-BI-1.78 and LS-BI-2.52 at the same load level. Similar observations were noted for the LWSCC beams reinforced with BFRP Type II and BFRP Type IIII bars. Moreover, beam LS-BII-1.18 (ρ_f of 1.18%) showed wider crack widths than beam LS-BI-1.18 (ρ_f of 1.18%) at the same load level. This could be attributed to the fact that the sand-coated BFRP bars bonded better to the concrete than the helically grooved BFRP bars.

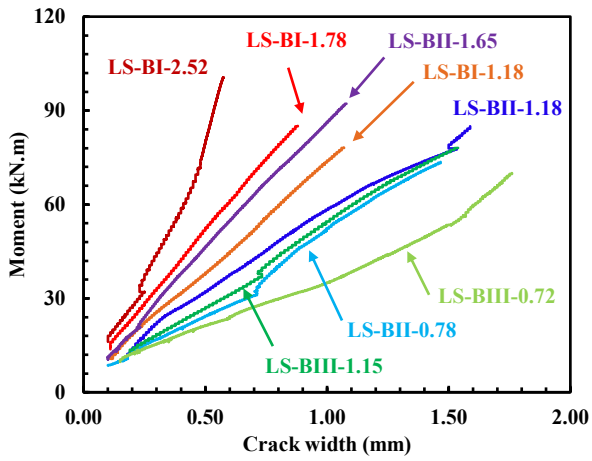

Figure 5.6– Moment-to-crack-width relationships for the BFRP-LWSCC beams. (Note: 1 mm = 0.0394 in.; 1 kN.m= 0.738 kip.ft.)

5.4.2 Cracking and Ultimate Moment

Table 5.5 provides the experimental cracking moment ($M_{cr\text{-}exp}$) at the first flexural crack for each tested beam. The $M_{cr\text{-}exp}$ values were verified from the moment–deflection and moment–strain relationships. The $M_{cr\text{-}exp}$ of the BFRP-LWSCC specimens ranged between 7.5 and 8.5 kN·m (5.53 and 6.30 kip·ft) with an average value of 8.2 kN·m (6.05 kip·ft) compared with 9.9 kN·m (7.30 kip·ft) for the BFRP-NWC specimens. The cracking moment (M_{cr}) depends on the concrete tensile strength (f_r), while the f_r is a function of the compressive strength. Therefore, the M_{cr} is a function of the compressive strength. The M_{cr} was calculated with the following equation:

$$M_{cr} = \frac{f_r \times I_g}{y_t} \tag{5.6}$$

The f_r was estimated with the following equations:

ACI 440.1R (2015)

$$f_r = 0.62\lambda\sqrt{f_c'} \tag{5.7}$$

CSA S806 (2012)

$$f_r = 0.6\lambda\sqrt{f_c'} \tag{5.8}$$

Where λ is the concrete density reduction factor. For LWC in which the fine aggregate is a combination of LWA and NS, ACI 318 (2019) specifies that λ= linear interpolation from 0.75 to 0.85 based on the absolute volume of the NS as a fraction of the total absolute volume of fine

aggregate. CSA S806 (2012) specifies that λ=1.0, 0.85, and 0.75 for normal-density concrete, structural semi-low density concrete in which all the fine aggregate is NS, and structural low-density concrete in which none of the fine aggregate is NS, respectively. In this study, the value of λ was taken to be equal to 0.8 and 0.75 in estimating the predicted cracking moment according to ACI 440.1R (2015) and CSA S806 (2012) provisions, respectively. Table 5.5 compares the experimental and predicted values of the cracking moments. The average $M_{cr\text{-}exp}$ of the BFRP-LWSCC beams was generally 19% and 12% lower, respectively, than those predicted according to ACI 440.1R (2015) and CSA S806 (2012). CSA S806 (2012) yielded slightly better predictions of cracking moments than ACI 440.1R (2015) because of the lower modulus of rupture.

The ultimate moment capacities of the BFRP specimens were predicted using the strain compatibility approach available in ACI 440.1R (2015). Table 5.5 provides the experimental-to-predicted ultimate moment capacity ($M_{n\text{-}exp}/M_{n\text{-}pred}$) of the beam specimens. The comparison shows that the ACI 440.1R (2015) slightly underestimated the moment capacities of the LWSCC beams, providing average value of $M_{n\text{-}exp}/M_{n\text{-}pred}$ equal to 1.07, with a COV equal to 6.0%.

Figure 5.7 shows the influence of BFRP reinforcement ratio on the normalized moment capacity (M_{nor}) of the LWSCC beams. As can be seen, the M_{nor} increased when the BFRP reinforcement ratio increased. In other words, increasing the amount of reinforcement by 50% and 110% (from 1.18% in LS-BI-1.18 to 1.78% and 2.52%) increased the M_{nor} of specimens LS-BI-1.78 and LS-BI-2.52 by 15% and 35%, respectively. Similarly, the increase in the M_{nor} for BFRP-Type II-reinforced LWSCC beams (LS-BII-0.78, LS-BII-1.18, and LS-BII-1.65) was 13% and 30% for approximately 50% and 110% increases in the amount of reinforcement from 0.78% to 1.18% and 1.65%, respectively. In contrast, the M_{nor} for the Type III BFRP-reinforced LWSCC beams (LS-BIII-0.72 and LS-BIII-1.15) increased by 12% for approximately 60% increases in the amount of reinforcement from 0.72% to 1.15%. Elgabbas et al. (2017) made similar remarks for BFRP-NWC beams, reporting that increasing the amount of reinforcement by 50% from 0.79% to 1.19% increased the ultimate moment capacity by 23%. On the other hand, the LWSCC beams (LS-BI-1.18 and LS-BII-1.18) and NWC beams (N-BI-1.18 and N-BII-1.18) with the same reinforcement ratio (1.18%) were compared to investigate the effect of concrete density on the M_{nor}. Figure 5.8 plots the M_{nor} versus concrete density for the beam specimens. As can be seen, the normalized moment capacities of the LWSCC beams (LS-BI-1.18 and LS-BII-1.18) (0.150 and 0.153), respectively, were not significantly affected (approximately 10% less) compared to

the NWC counterparts (N-BI-1.18 and N-BII-1.18) (0.168 and 0.171), respectively. This could be attributed to the fact that the strength of the gravel aggregate in the NWC was higher than that of the LWA in the LWSCC.

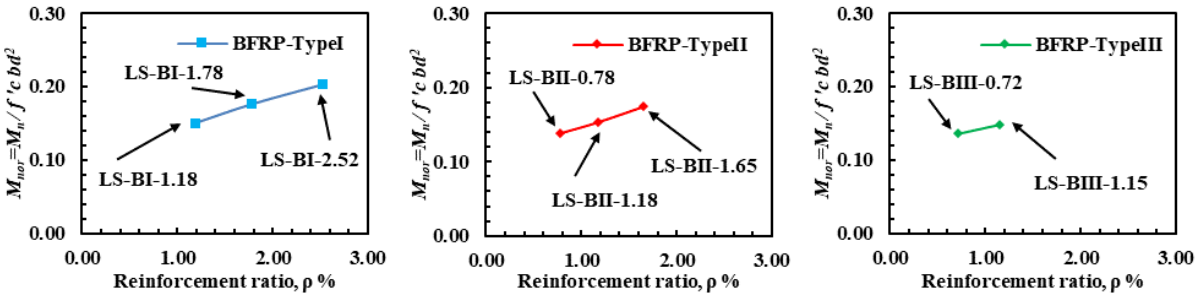

Figure 5.7– Normalized moment capacity versus reinforcement ratio.

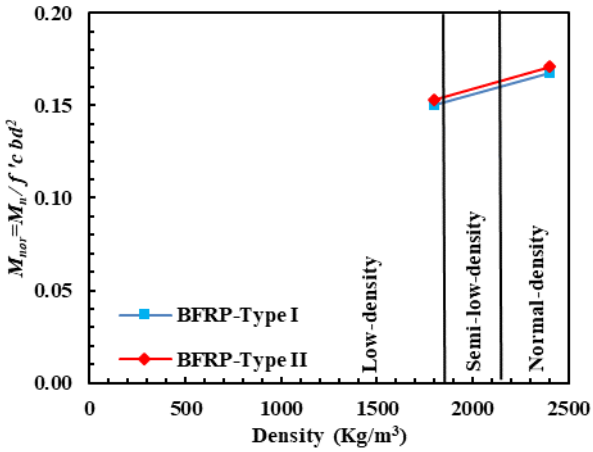

Figure 5.8– Normalized moment capacity versus concrete density. (Note: 1 kg /m^3= 0.062 lb/ft^3)

5.4.3 Stiffness and Moment–Deflection Behavior

Figure 5.9 shows the moment–deflection relationships at the mid-span of the beam specimens**.** As shown in the figure, the moment–deflection relationships consisted of two main phases (the pre-cracking phase and the post-cracking phase). The moment–deflection behavior before cracking was almost identical in all the beams because of the nonsignificant impact of reinforcement type and amount on the gross-section properties of the specimens. At this stage, specimen deflection increased linearly with the applied load. Once the first flexural crack occurred, the flexural stiffness was reduced in both the LWSCC and NWC beams. The figure reveals that the reinforcement type and amount had a direct effect on specimen stiffness and therefore on the moment–deflection relationship. Figures 5.9a, b, and c indicate that increasing the amount of reinforcement of the same type of BFRP reinforcement improved the flexural

stiffness in the post-cracking phase, thereby decreasing the deflection after cracking. The stiffness after cracking was calculated as the average slope of the curve. The stiffness after cracking of specimen LS-BI-2.52 (reinforcement ratio of 2.52%) was 12% higher than that of specimen LS-BI-1.78 (reinforcement ratio of 1.78%) and 37% higher than that of specimen LS-BI-1.18 (reinforcement ratio of 1.18%) (see Figure 5.9a). The same behavior was observed with the other two types of BFRP reinforcement (helically grooved and thread-wrapped). The steel-LWSCC beam (LS-S-1.18) showed higher flexural stiffness than the other beams. This is attributed to the high modulus of elasticity of steel bars.

Figure 5.9d shows that specimens LS-BI-1.18 and LS-BII-1.18 exhibited almost the same moment–deflection behavior. This was because both specimens had approximately the same axial stiffness (E_fA_f). Similarly, specimen LS-BI-1.78 had a moment–deflection behavior very close to that of specimen LS-BII-1.65 with almost the same axial stiffness. **T**he comparisons showed that **t**he moment–deflection relationships were not significantly affected by BFRP bar surface configuration when the axial stiffness of bars was achieved. These results are in good agreement with those obtained for beams reinforced with GFRP bars with different surface configurations (El-Nemr et al. 2013). On the other hand, Figure 5.9e illustrates the effect of concrete density on the moment–deflection behavior. As shown, the decrease in the cracking stiffness of the NWC specimens was less obvious than that of the LWSCC specimens because of the high modulus of elasticity of NWC. Specimen LS-BI-1.18 exhibited lower relative stiffness after cracking than specimen N-BI-1.18 (see Figure 5.9e). Similar behavior of the flexural stiffness after cracking was observed for the beams reinforced with helically grooved BFRP bars (specimens LS-BII-1.18 and N-BII-1.18).

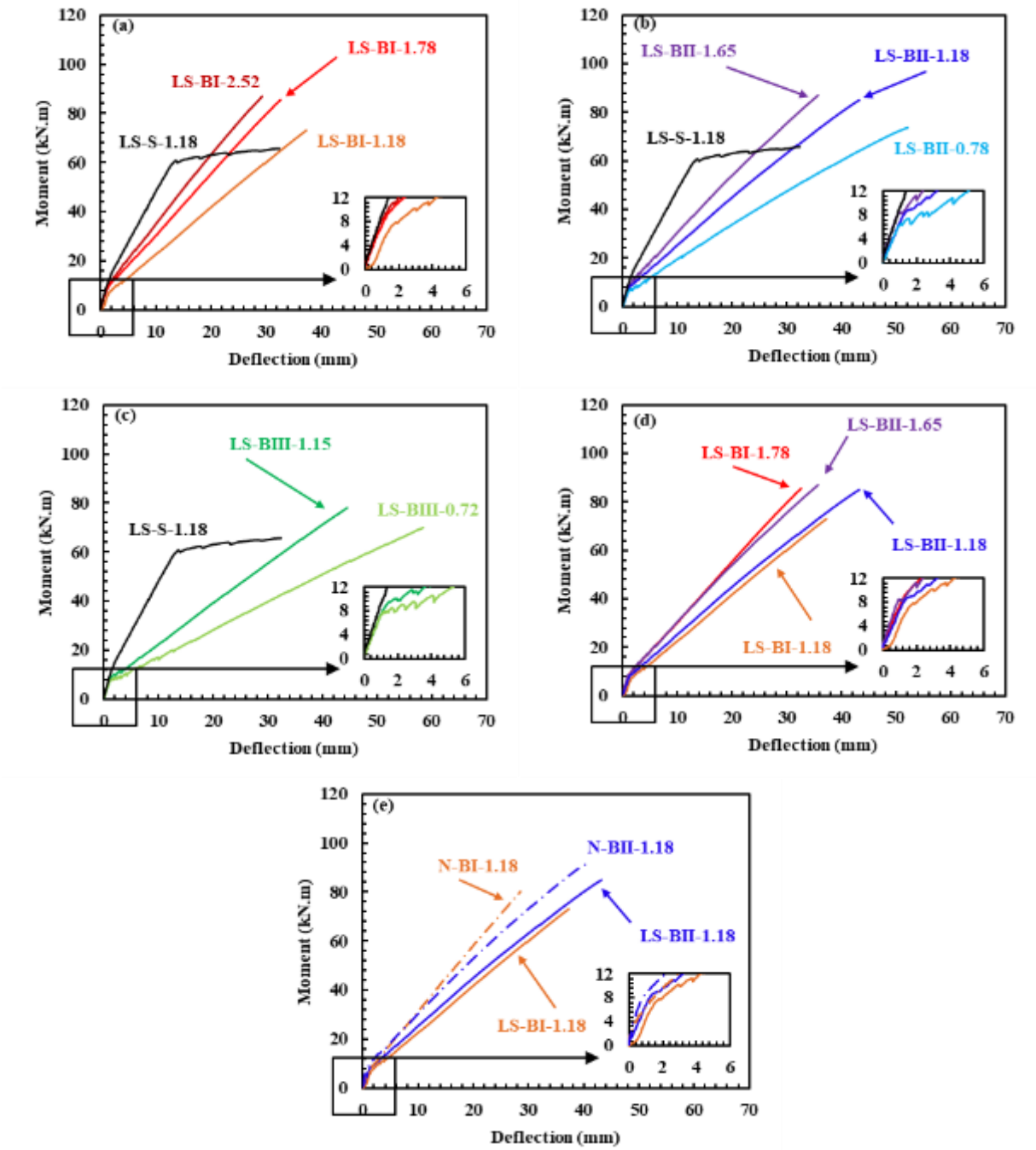

Figure 5.9– Moment-deflection response for the beam specimens. (Note: 1 mm = 0.0394 in.; 1 kN.m= 0.738 kip.ft.)

5.4.4 Strain in Concrete and Reinforcement

Figure 5.10 illustrates the mid-span strains on the top surface of the concrete and the tensile bottom reinforcements versus the applied moment. All the beams initially behaved similarly and exhibited linear moment–strain behavior up to the formation of the first flexural crack, followed by nearly linear behavior up to failure. As shown in the figure, the beams with high longitudinal

reinforcement ratios experienced lower tensile strains than those with low longitudinal reinforcement ratios given the same load level. The maximum tensile strains in the BFRP Type I bars in the BFRP-LWSCC beams ranged between 7,300 and 10,000 με (see Table 5.6), which is less than the rupture strain of the BFRP Type I bars (25,000 με). The same observation for the BFRP Type II and BFRP Type IIII beams, which had maximum tensile strains of 14,900 and 19,300 με, respectively, which is less than the rupture strain of the BFRP Type II and BFRP Type III bars in Table 5.3. In contrast, beam LS-S-3#15M yielded at an applied moment of 58.5 kN.m with a corresponding strain of 2,600 με, followed by a rapid increase in the tensile strain values up to failure at a maximum strain of 9,500 με. Four beam specimens were used to compare the maximum BFRP tensile strains in the LWSCC beams to that of the NWC beams. The maximum BFRP tensile strains of the NWC specimens were 7,950 and 10,390 με for specimens N-BI-1.18 and N-BII-1.18, respectively, which corresponds to approximately 32% and 39% of the rupture strains of the BFRP Type I and BFRP Type II bars in Table 5.3, respectively. Using LWSCC increased the maximum BFRP tensile strains to 1.25 and 1.18 times that of the NWC specimens, respectively (see Table 5.6). These results indicate that the BFRP-LWSCC beams represented good designs with a reasonable margin of safety compared to the BFRP-NWC beams.

Table 5.6– Strains and curvature of the BFRP beams at failure

Beam ID	Maximum Strain (με)		Curvature Ψ (*1 /d*)	Deformability *J*
	Bars	Concrete		
LS-BI-2.52	7300	2050	0.009	5.75
LS-BI-1.78	8370	2330	0.011	7.15
LS-BI-1.18	9980	2900	0.013	7.23
LS-BII-1.65	10400	3630	0.014	9.80
LS-BII-1.18	12350	3660	0.016	10.80
LS-BII-0.78	14980	3840	0.019	14.00
LS-BIII-1.15	11900	3500	0.015	12.30
LS-BIII-0.72	19300	3520	0.023	12.45
N-BI-1.18	7950	2400	0.010	4.70
N-BII-1.18	10390	3200	0.014	7.30

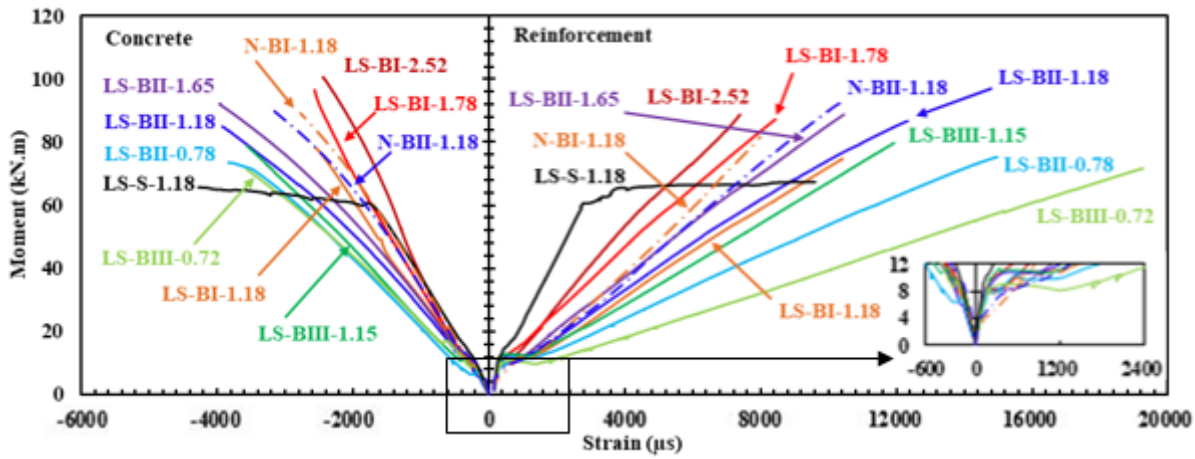

Figure 5.10– Strain responses for the beam specimens. (Note: 1 kN.m= 0.738 kip.ft.)

The concrete strains ranged approximately from 100 to 200 με in all the beam specimens before the first crack occurred. After cracking, the concrete strains increased almost linearly up to failure. Figure 5.10 exhibits that increasing the amount of reinforcement for the same type of BFRP reinforcement decreased concrete strains at the same load level. Table 5.6 presents the recorded concrete strains at failure for the beam specimens. For instance, at the same load level, the concrete strains recorded in LS-BI-2.52, LS-BII-1.65, and LS-BIII-1.15 were lower than those in LS-BI-1.18, LS-BII-0.78, and LS-BIII-0.72, respectively. In addition, the BFRP-LWSCC beams showed lower concrete strains than the BFRP-NWC beams at the same load level (see Figure 5.10). The maximum concrete strains in LS-BI-1.18 and LS-BII-1.18 at failure were 2,900 and 3,600 με, respectively, compared to 2,400 and 3,200 με in specimens N-BI-0.83 and N-BII-0.86, respectively. This can be attributed to the higher modulus of elasticity of NWC. In addition, the recorded concrete strain for the steel-LWSCC beam (LS-S-3#15M) just before steel yielding was 1,640 με.

5.4.5 Curvature and Deformability

Beam curvature is considered an important term that points out the deformation of a RC element under applied loads. The curvature (ψ) was calculated at the mid-span of the specimens using the calculated neutral-axis depth and the experimental BFRP and concrete strains as follows:

$$\psi = \frac{\varepsilon_c}{c} \tag{5.9}$$

$$c = \left(\frac{\varepsilon_c}{\varepsilon_c + \varepsilon_f}\right) d \tag{5.10}$$

where ε_c is the concrete strain in the extreme fiber in compression and c is the depth of the neutral axis. Figure 5.11 illustrates the moment–curvature relationship for the beam specimens at different reinforcement ratios of either steel or BFRP bars. Table 5.6 summarizes the maximum curvature of the BFRP specimens at failure as a function of $1/d$, where d is the effective depth of beam. As shown in Figure 5.11, the moment–curvature relationship is very similar to that of reinforcement strain. Prior to cracking, the position of the neutral axis of the cross section was at the same position. Once the first flexural crack formed, a considerable increase in curvature occurred in both the LWSCC and NWC beams. After cracking, the curvature increased almost linearly with applied moment until concrete crushing. Beam curvature was dependent on the amount of reinforcement. The depth of the neutral axis was increased by increasing the BFRP reinforcement ratio to maintain the equilibrium of the cross section and therefore, the maximum beam curvature decreased. For instance, the maximum curvature in specimen LS-BII-0.78 was 0.019/d, compared to 0.016/d and 0.014/d in specimens LS-BII-1.18 and LS-BII-1.65, respectively. In addition, the maximum curvature in the LWSCC specimens is greater than that in the NWC specimens. The maximum curvatures of the LWSCC specimens (LS-BI-1.18 and LS-BII 1.18) were 0.013/d and 0.016/d, respectively, compared to 0.010/d and 0.014/d for the NWC specimens (N-BI-1.18 and N-BII-1.18), respectively.

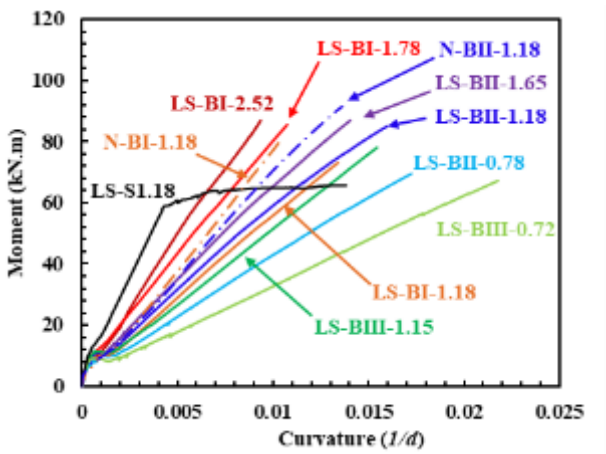

Figure 5.11– Moment-curvature for the beam specimens. (Note: 1 kN.m= 0.738 kip.ft.)

Ductility is the ability of RC elements to absorb energy without strength loss. Ductility is related to inelastic deformation, which occurs prior to complete failure. In case of steel RC elements, ductility can be estimated as the ratio of the total deformation at failure divided by the deformation at yielding. As a result of linear behavior of the BFRP bars up to failure, this approach to calculating ductility cannot be applied to BFRP-LWSCC beams. In this study, the CSA S6 (2019) approach was used to compute the deformability factor (*J-factor*) of the BFRP-

LWSCC beams. This approach is based on deformability instead of absorbed energy to ensure that the BFRP-LWSCC specimens exhibited adequate deformation prior to failure. According to CSA S6 (2019), the *J-factor* should be at least 4.0 and 6.0 for rectangular and T-sections, respectively, and is calculated as follows:

$$J = \frac{M_{ult}\psi_{ult}}{M_c\psi_c} \tag{5.11}$$

Where M_{ult} is the ultimate bending moment; ψ_{ult} is the ultimate curvature; M_c is the bending moment at a concrete strain of 0.001; and ψ_c is the curvature at a concrete strain of 0.001. Table 5.6 summarizes the values of *J-factor* for the BFRP beam specimens. Table 5.6 indicates that all the BFRP beams exhibited adequate deformability (from 5.75 to 14.0), which is higher than the CSA-S6 (2019) code limit of 4.0. The higher *J-factor* refers to a higher deformation and, therefore, gives ample warning of failure in the BFRP-RC beams. This implies that the *J-factor* reveals the amount of cracks and deflections that a BFRP-RC element will exhibit in its load history from service to ultimate conditions. Given the same type of BFRP reinforcement, higher values are inversely related to low amounts of reinforcement and vice versa. For instance, the *J-factor* for the BFRP Type I-reinforced LWSCC beams increased by 25% when the amount of reinforcement was reduced from 2.52% to 1.18%.

5.5 Review of Current Deflection and Cracking Provisions

5.5.1 Deflection Provisions

The immediate mid-span deflection for a simply supported RC element with a clear span of (L) is given as follows:

$$\delta = \frac{(P/2)a}{24E_cI_e}\left[3L^2 - 4a^2\right] \tag{5.12}$$

Where E_c is the modulus of elasticity of the concrete, taken as $E_c = 0.043w_c^{1.5}\sqrt{f_c'}$; and I_e is the effective moment of inertia. ACI 440.1R (2015) recommends calculating the I_e with the equation proposed by Bischoff and Gross (2011) as follows:

$$I_e = \frac{I_{cr}}{1-\gamma\left(\frac{M_{cr}}{M_a}\right)^2\left(1-\frac{I_{cr}}{I_g}\right)} \le I_g \tag{5.13}$$

The reduction factor γ in the above equation accounts for the variation in stiffness along the span and is expressed as:

$$\gamma = \frac{3\left(\frac{a}{L}\right)-4\left(4\left(\frac{M_{cr}}{M_a}\right)-3\right)\left(\frac{a}{L}\right)^3}{3\left(\frac{a}{L}\right)-4\left(\frac{a}{L}\right)^3} \tag{5.14}$$

CSA S806 (2012) employs curvature integration by assuming a fully cracked section without any contribution of tension stiffness in the cracked zones. For simple loading cases, CSA S806 (2012) gives the following equation for a simply supported beam with a clear span L with two equal point loading $P/2$ placed at a distance a from the supports

$$\delta = \frac{(P/2)L^3}{24E_cI_{cr}}\left[3\left(\frac{a}{L}\right)-4\left(\frac{a}{L}\right)^3-8\left(1-\frac{I_{cr}}{I_g}\right)\left(\frac{L_g}{L}\right)^3\right] \tag{5.15}$$

where $E_c = \left[3300\sqrt{f_c'}+6900\right]\left[\frac{\gamma_c}{2300}\right]^{1.5}$ for concrete γ_c between 1500 and 2500 kg/m^3; I_{cr} is the cracking moment of inertia; and L_g is the distance from support to point where M_a=M_{cr}.

5.5.2 Crack-Width Provisions

CSA S6 (2019) specifies Eq. (5.16) to account for the crack width of flexural elements reinforced with FRP longitudinal bars:

$$w_{cr} = 2\frac{f_f}{E_f}\frac{h_2}{h_1}k_b\sqrt{d_c^2+(s/2)^2} \tag{5.16}$$

where f_f is the stress in the FRP bars; E_f is the modulus of elasticity of the FRP bars; h_2 is the distance from the tension surface of the concrete to the neutral axis; h_1 is the distance from the center of the tension reinforcement to the neutral axis; d_c is the distance from the tension surface of concrete to the center of the tension reinforcement; and k_b is the bond-dependent coefficient, which gives the bond between FRP bars and the surrounding concrete. The bond-dependent

coefficient is determined according to the test method in CSA S806 (2012). In the absence of experimental data for k_b, CSA S6 (2019) recommends a k_b of 0.8 and 1.0 for sand-coated and deformed bars, respectively.

ACI 440.1R-15 specifies an indirect procedure that controls flexural-crack width with a maximum reinforcing-bar spacing based on the approach proposed by Ospina and Bakis (2007) as:

$$s_{\max} = 1.15\frac{E_f}{f_{fs}}\frac{w}{k_b} - 2.5c_c \le 0.92\frac{E_f}{f_{fs}}\frac{w}{k_b} \tag{5.17}$$

where s_{max} is the maximum allowable center-to-center bar spacing for flexural-crack control (mm); E_f is the design or guaranteed modulus of elasticity of FRP reinforcement defined as the mean modulus of sample of test members (MPa); f_{fs} is the stress level induced in FRP at service loads (MPa); w is the maximum allowable crack width (mm); and c_c is the clear concrete cover (mm). The k_b value is determined experimentally, but, when experimental data is not available, ACI 440.1R (2015) suggests a conservative value of 1.4 for FRP bars.

5.5.3 Comparison between Experimental Results and Code Predictions

5.5.3.1 Deflection

In this investigation, the empirical equations recommended in ACI 440.1R (2015) and CSA S806 (2012) were used to assess the serviceability performance of the BFRP specimens at service and higher load levels. The service load is defined as 30% of the nominal moment capacity ($0.30M_n$) as suggested by Bischoff et al. (2009), as a reasonable value for the service load of an FRP-RC member. Figure 5.12 illustrates the experimental and predicted deflection responses. Table 5.7 presents the average, standard deviation, and coefficient of variation for the ratios of the experimental-to-predicted deflections ($\delta_{exp}/\delta_{pred}$) at $0.30M_n$ as well as at $0.67M_n$ (a higher load level). Based on the predictions, ACI 440.1R (2015) underestimated the predicted deflections of the BFRP-LWSCC beams at $0.30M_n$ and $0.67M_n$, where the average $\delta_{exp}/\delta_{pred}$ was 1.26 with a COV of 9.0% and 1.11 with a COV of 8.0%, respectively. In contrast, CSA S806 (2012) provided reasonable predictions at $0.30M_n$ and at $0.67M_n$, where the average $\delta_{exp}/\delta_{pred}$ was 0.95 with a COV of 9.0% and 1.04 with a COV of 9.0%, respectively. Considering the overall average (average of all predicted deflections at $0.30M_n$ and $0.67M_n$), CSA S806 (2012) provided better predictions than ACI 440.1R (2015), with an average $\delta_{exp}/\delta_{pred}$ of 1.0 and 1.19, respectively.

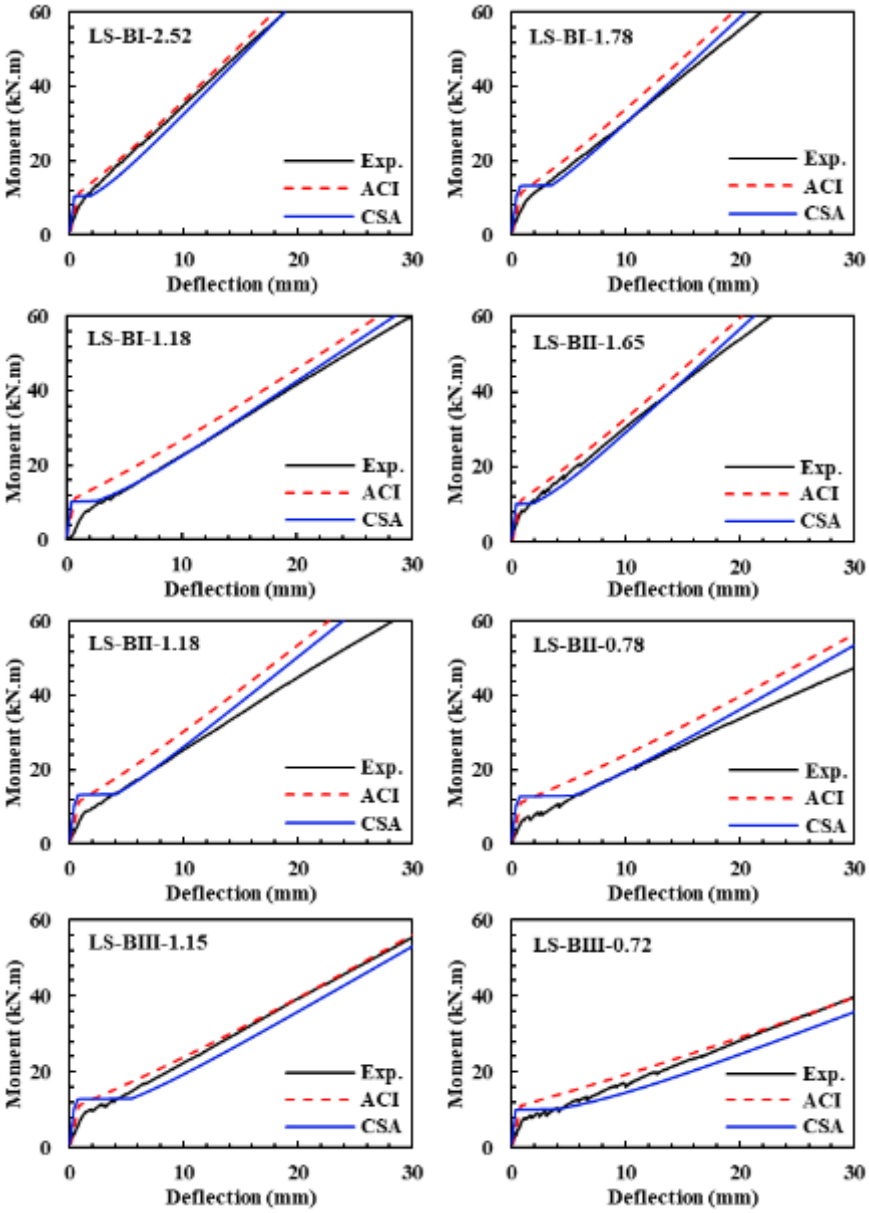

Figure 5.12– Comparison between the experimental and predicted deflection. (Note: 1 mm = 0.0394 in.; 1 kN.m= 0.738 kip.ft.)

Table 5.7– Experimental-to-predicted deflection and crack-width ratios of the BFRP-LWSCC specimens

Beam ID	Deflection						Crack Width					
	δ_{exp} (mm)		$\delta_{exp}/\delta_{pred}$				w_{exp} (mm)		w_{exp}/w_{pred}			
	0.30 M_n	*0.67* M_n	ACI 440.1R (2015)		CSA S806 (2012)		*0.30* M_n	*0.67* M_n	ACI 440.1R (2015)		CSA S6 (2019)	
			0.30 M_n	*0.67* M_n	*0.30* M_n	*0.67* M_n			*0.30* M_n	*0.67* M_n	*0.30* M_n	*0.67* M_n
LS-BI-2.52	6.5	16.5	1.08	1.02	0.87	0.96	0.32	0.51	0.57	0.42	0.94	0.70
LS-BI-1.78	8.0	20.0	1.21	1.14	0.98	1.07	0.28	0.66	0.55	0.58	0.88	0.92
LS-BI-1.18	9.0	23.0	1.32	1.12	0.98	1.05	0.43	0.92	0.51	0.48	0.86	0.81
LS-BII-1.65	8.5	22.0	1.18	1.13	0.97	1.07	0.42	1.11	0.72	0.85	1.00	1.19
LS-BII-1.18	10.0	26.0	1.33	1.24	1.05	1.17	0.40	0.75	0.78	0.66	1.08	0.91
LS-BII-0.78	11.5	30.5	1.44	1.22	1.05	1.14	0.55	1.17	0.63	0.58	0.90	0.83
LS-BIII-1.15	9.5	25.0	1.19	1.02	0.86	0.94	0.40	0.91	0.73	0.74	1.04	1.06
LS-BIII-0.72	11.5	29.5	1.32	1.00	0.84	0.90	0.50	1.37	0.58	0.74	0.88	1.11
Average			1.26	1.11	0.95	1.04			0.63	0.64	0.95	0.94
SD			0.11	0.09	0.08	0.09			0.10	0.15	0.10	0.17
COV (%)			9.0	8.0	9.0	9.0			15.50	22.65	9.40	17.70

Note: 1 mm= 0.0394 in

5.5.3.2 Crack Width

Table 5.7 compares the maximum crack width of the first three flexural cracks with the predicted results based on ACI 440.1R (2015) and CSA S6 (2019). The comparison was conducted at $0.30M_n$ (the service-load level) and at $0.67M_n$ (the average load level at which the crack patterns stabilized). In the absence of test data, the value of k_b in ACI 440.1R (2015) was considered in the predictions as 1.4 for the sand-coated and helically grooved BFRP bars. On the other hand, as recommended in CSA S6 (2019), k_b was taken 0.8 and 1.0 for the sand-coated and helically grooved BFRP bars, respectively. For thread-wrapped BFRP bars, the value of k_b was considered in the predictions as 1.4 and 1.0 as in ACI 440.1R (2015) and CSA S6 (2019), respectively. The results indicate that the predicted crack widths were generally higher than the experimental results at the both load levels. ACI 440.1R (2015) overestimated the predicted crack widths of the BFRP-LWSCC beams at $0.30M_n$ and $0.67M_n$. The experimental-to-predicted crack width values (w_{exp}/w_{pred}) ranged from 0.51 to 0.78 at $0.30M_n$ with an average of 0.63 and a corresponding COV of 15.50% and ranged from 0.42 to 0.85 at $0.67M_n$ with an average of 0.64 and a corresponding COV of 22.65%. The conservative value of k_b (1.4 for all types of BFRP bars), as suggested in ACI 440.1R (2015) when the experimental data is not available, can be

attributed to overestimating the crack widths. On the other hand, CSA S6 (2019) yielded more accurate predictions of the crack widths at $0.30M_n$ and $0.67M_n$. The average value of the w_{exp}/w_{pred} was 0.95 with a corresponding COV of 9.40% at $0.30M_n$ and 0.94 with a corresponding COV of 17.70% at $0.67M_n$. The recommended small value of k_b (0.8 for sand-coated BFRP bars and 1.0 for helically grooved and thread-wrapped BFRP bars) resulted in more accurate predictions of the crack widths.

5.6 Summary and Conclusions

The flexural behavior and serviceability performance of LWSCC beams reinforced with three different types of BFRP bars were investigated. A total of 11 RC beams measuring 3,100 mm (122.05 in) long × 200 mm (7.87 in) wide × 300 mm (11.81 in) deep were fabricated. Nine specimens, including one traditional steel RC specimen, were made with LWSCC; two reference specimens were made with NWC. The beams were tested under four-point bending up to failure. Based on the results and discussions presented herein, the main findings of this investigation can be summarized as follows:

1. The tested BFRP-LWSCC beams failed due to concrete crushing as they were designed as over-reinforced; a high degree of deformability was attained before failure by all the BFRP specimens with a deformability factor higher than 4, which satisfied the CSA S6 (2019) requirement.
2. ACI 440.1R (2015) and CSA S806 (2012) yielded very close predicted moment capacities for the BFRP-LWSCC specimens. The predictions were in good agreement with the experimental results with an average accuracy of ≥ 90%.
3. The normalized moment capacity was proportional to the amount of BFRP reinforcement bars. Increasing the amount of BFRP reinforcement from 1.18% to 2.52% increased the normalized moment capacity of the beams by 35%. In addition, the normalized moment capacity of the LWSCC beams was not significantly affected (approximately 10% less) compared to the NWC beam.
4. The amount and type of reinforcement significantly affected the serviceability performance of the LWSCC specimens. Increasing the amount of reinforcement resulted in smaller crack widths and lower deflections. The specimens reinforced with sand-coated BFRP bars produced smaller crack widths than those reinforced with helically

grooved or thread-wrapped BFRP bars. This tends to confirm BFRP bars with a sand-coated surface have better flexural bond characteristics.

5. ACI 440.1R (2015) underestimated the predicted deflections of the BFRP-LWSCC beams at both $0.30M_n$ and $0.67M_n$, with an average $\delta_{exp}/\delta_{pred}$ of 1.26 and 1.11, respectively. In contrast, CSA S806 (2012) provided reasonable predictions at $0.30M_n$ and $0.67M_n$, where the average $\delta_{exp}/\delta_{pred}$ was 0.95 and 1.04, respectively.

6. The k_b factor of 1.4 in ACI 440.1R (2015) is conservative for sand-coated, helically grooved, or thread-wrapped BFRP bars in LWSCC, where the w_{exp}/w_{pred} is 0.63 and 0.64 at $0.30M_n$ and $0.67M_n$, respectively. On the other hand, CSA S6 (2019) yielded accurate predictions with a k_b value of 0.8 for the sand-coated BFRP bars and 1.0 for the helically grooved and thread-wrapped BFRP bars in LWSCC.

CHAPTER 6

Flexural Strength and Serviceability of GFRP-Reinforced Lightweight Self-Consolidating Concrete Beams

Foreword

Authors and Affiliation:

- Shehab Mehany: Ph.D. candidate, Department of Civil Engineering, Université de Sherbrooke, Sherbrooke, Quebec, Canada, J1K 2R1.
- Hamdy M. Mohamed: Research Associate/Lecturer, Department of Civil Engineering, Université de Sherbrooke, Sherbrooke, Quebec, Canada, J1K 2R1.
- Brahim Benmokrane: Professor, Department of Civil Engineering, Université de Sherbrooke, Sherbrooke, Quebec, Canada, J1K 2R1.

Journal Title: *Journal of Composites for Construction, ASCE.*

Paper Status: *Under review.*

Abstract

Considering the limited experimental work carried out on fiber-reinforced polymer (FRP) bars in lightweight concrete (LWC) beams, there is a need for more investigation to understand their flexural behavior and serviceability performance. This paper reports on an investigation based upon experimental study that evaluated the flexural capacity and serviceability performance of lightweight self-consolidating concrete (LWSCC) beams reinforced with glass-FRP (GFRP) bars. Ten reinforced concrete (RC) beam specimens (200 wide × 300 high × 3,100 mm long) were prepared and tested under four-point bending up to failure. Eight specimens were made with LWSCC while the other two were made with normal-weight concrete (NWC) as reference specimens. The test variables were concrete density (LWSCC and NWC); reinforcement type (sand-coated GFRP, helically grooved GFRP, or steel bars); and longitudinal GFRP reinforcement ratio. Two types of fine aggregate were used in the LWSCC mixtures: lightweight aggregate (Solite 307) and natural fine aggregate, leading to a concrete density of 1,800 kg/m^3. The test results indicate that the GFRP-RC beams failed as a result of concrete crushing. The normalized moment capacity of the GFRP-reinforced LWSCC beams was approximately 0.90 times that of the counterpart GFRP-reinforced NWC beams. The predicted moment capacities of the GFRP beams were estimated based on the strain-compatibility approach in the design standards, which showed good agreement between the predicted and experimental results. Moreover, the recorded deflections and crack widths of the GFRP-reinforced LWSCC beams are presented and compared to those predicted with the FRP design provisions and the literature. The comparisons reveal that the deflections and crack widths of the GFRP-reinforced LWSCC beams can be estimated with the FRP design provisions with a variable degree of conservativeness.

Keywords: Lightweight self-consolidating concrete (LWSCC); beam specimens; GFRP bars; flexural behavior; deflection; crack-width; FRP design codes.

6.1 Introduction

The past few decades have yielded considerable innovations in the concrete industry, including lightweight self-consolidating concrete (LWSCC), which has appeared as an applicable alternative to normal-weight concrete (NWC). LWSCC was developed to combine the excellent benefits of self-consolidating concrete (SCC) and lightweight concrete (LWC) as a combined application (Okamura and Ouchi 2003; Hwang and Hung 2005). The lower density of LWC allows for the production of reinforced concrete (RC) elements (beams, slabs, columns, and foundations) that have a reduced self-weight and a smaller cross-sectional dimension, therefore leading to increased cost savings. SCC offers many advantages in terms of reducing labor and machinery costs, faster construction, and ability to spread in cases of congested reinforcement making compaction difficult. LWSCC has been used in various applications such as multistory buildings, precast elements, and bridges (Okamura and Ouchi 2003; Hubertova and Hela 2007). Recently, fiber-reinforced polymer (FRP) bars have been deemed an acceptable alternative to traditional steel bars in RC structures. Glass-FRP (GFRP) bars are one of the most common types of FRP bars in North America (ACI 440.1R-15 (ACI 2015)). In addition to their corrosion-free nature, they offer high strength-to-weight ratio, good fatigue properties, good resistance to chemical attack, and electromagnetic resistance. Combining LWSCC and GFRP bars provides the advantages of both materials and produces RC members that weigh less and are more durable (ACI 440.1R-15 (ACI 2015)).

Considerable research work has focused on the flexural behavior and serviceability of FRP-reinforced NWC (FRP-NWC) beam specimens (Kassem et al. 2011; El-Nemr et al. 2016, 2018; Abdelkarim et al. 2019). Kassem et al. (2011) assessed the performance of 24 NWC beam specimens reinforced with either FRP or steel reinforcement under flexural loads. Their results show that the moment capacities of the FRP-NWC beams were higher than that of the counterpart control steel beams with the same amount of reinforcement. Moreover, since FRP bars have a modulus of elasticity lower than that of steel, the FRP-NWC beams evidenced larger deflections and crack widths than the steel beams at the same reinforcement ratio. In addition, the NWC specimens with sand-coated FRP bars showed more cracks and reduced average crack spacing than the NWC specimens with ribbed FRP bars. El-Nemr et al. (2016) tested 16 NWC beams reinforced with different FRP types up to failure. The authors concluded that the sand-coated GFRP bars exhibited lower bond-dependent coefficient (k_b) values than the helically grooved GFRP bars. Moreover, they found that the ACI 440.1R-06 (ACI 2006) and ISIS Canada

Research Network (2007) guidelines overestimated the predicted crack widths of the NWC beams at $0.30M_n$ (service load). Abdelkarim et al. (2019) reported that the effect of increasing the amount of GFRP reinforcement on the resistance moment was approximately the same in the normal- and high-strength concrete (NSC and HSC) beams tested. The resistance moment increased by 71.3% and 68.8% when the amount of GFRP reinforcement was increased by 329% (from 0.38% to 1.63%) for the NSC and HSC specimens, respectively.

A few experimental studies have been conducted recently to assess the influence of GFRP reinforcing bars on the flexural behavior and serviceability of LWC beam specimens. Wu et al. (2019) tested five LWC beam specimens reinforced with GFRP bars under flexural loads. The test results indicate that the reinforcement ratio significantly affected the serviceability performance of the LWC beam specimens. As the reinforcement ratio increased, the specimens exhibited lower deflections and narrower crack widths at the same load levels. The provisions of ACI 440.1R-15 (ACI 2015) underestimated the load-carrying capacity of the specimens that failed by concrete crushing and overestimated the load-carrying capacity of the specimens that were damaged due to FRP rupture. Liu et al. (2020) studied the applicability of using GFRP and carbon-FRP (CFRP) bars as longitudinal reinforcement in the LWC beams. The test results show that the failure of all specimens occurred by concrete crushing. Moreover, comparing the crack-width predictions show that the provisions in ACI 440.1R-06 (ACI 2006) overestimated the predicted crack widths for the LWC beams at service load, while those in the ISIS Canada Research Network design manual (2007) predicted reasonable crack-width values.

This investigation is a part of an extensive research program on the behavior of LWSCC beams reinforced with GFRP and basalt-FRP (BFRP) bars under various loading conditions, which was carried out at the University of Sherbrooke. The objectives of this study were (1) to explore the feasibility and efficiency of using GFRP bars in LWSCC beams under flexural loads; (2) to investigate the influence of GFRP types and amount of reinforcement on the flexural behavior of the LWSCC specimens; (3) to compare the experimental cracking and resistance moment of the GFRP-reinforced LWSCC (GFRP-LWSCC) beams with those obtained predicted using FRP design provisions; and (4) to compare the recorded deflections and crack widths with those predicted by models in the FRP provisions as well as in the literature.

6.2 Research Motivation

A literature search revealed no reported research on the flexural behavior of LWSCC beams reinforced with GFRP bars. In addition, ACI 440.1R-15 (ACI 2015), CSA S806-12 (CSA 2012) (Re-approved in 2017), and CSA S6-19 (CSA 2019) do not provide guidance for LWSCC beams reinforced with GFRP bars. Therefore, there is a need to investigate the flexural behavior of GFRP-LWSCC beams. Accordingly, this investigation shed light on the behavior of GFRP-LWSCC beams under flexural load. The influence of the test parameters on the flexural strength and serviceability requirements were investigated, including concrete density (LWSCC and NWC), reinforcement type, and longitudinal GFRP reinforcement ratio. Two types of GFRP bars representative of the current world market were selected for this test program (sand-coated and helically grooved bars). The deflection equations in the FRP design provisions and literature were examined in light of this study. Moreover, the measured crack widths were used to assess the current k_b values recommended in FRP design provisions. The outcomes of this study can be used to assess and explore the feasibility of using GFRP bars as longitudinal reinforcement in flexural LWSCC members. In addition, the experimental data and theoretical analysis are valuable for designers, engineers, and members of code committees using GFRP reinforcement in LWC structures and for the development of codes and standards.

6.3 Experimental Program

6.3.1 Beam Details and Test Matrix

Ten simply supported RC beams—including eight LWSCC beams reinforced with various reinforcement ratios of either GFRP or steel bars and two NWC beams reinforced with GFRP bars as reference beams—were fabricated and tested. Each specimen had a cross section measuring 300 mm in depth, 200 mm in width, and 3,100 mm in length. The total length of the test specimens included an overhang of 200 mm past both supports to ensure the appropriate anchorage of the longitudinal bars. The clear bottom cover was 38 mm for No. 5 bars and 50 mm for No. 8 and No. 6 bars, which was determined according to Annex S in CSA S806-12 (CSA 2012). All specimens were reinforced with two No. 4 GFRP bars as top reinforcement to hold the stirrups. Traditional steel stirrups (10 mm in diameter) were selected to use in the nonconstant-moment regions and were spaced 100 mm apart in all beam specimens to avoid shear failure. To reduce the confining influence of the transverse reinforcement on the flexural

behavior, no stirrups were used in the pure moment region between the two loading points. Figure 6.1 presents specimen geometry and reinforcement details. Table 6.1 gives the test matrix and details of the test specimens. Each beam was identified with a tripartite numbering code. The first part—LS or N—refers to the type of concrete density: LWSCC or NWC, respectively. The second part—GI, GII, or S—identifies the beam as being reinforced with GFRP Type I, GFRP Type II, or steel reinforcement, respectively. The third part refers to the number of bars followed by the bar size. The test variables were concrete density, reinforcement type, and amount of GFRP reinforcement. The reinforcement ratios of the beams reinforced with GFRP bars were selected to be greater than the balanced reinforcement ratio (ρ_{fb}), which led to failure due to concrete compression. This is the common design concept for FRP RC members according to CSA S806-12 (CSA 2012) and ACI 440.1R-15 (ACI 2015). The ρ_{fb} can be estimated with the following equations:

ACI 440.1R-15 (ACI 2015)

$$\rho_{fb} = 0.85\beta_1 \frac{f_c^{'}}{f_{fu}} \frac{E_f \varepsilon_{cu}}{E_f \varepsilon_{cu} + f_{fu}} \tag{6.1}$$

where ε_{cu} is the ultimate compressive strain in concrete, taken as equal to 0.003 in ACI 440.1R-15 (ACI 2015).

$$\beta_1 = 0.85 - 0.00714\left(f_c^{'} - 28\right) \geq 0.65 \tag{6.2}$$

CSA S806-12 (CSA 2012)

$$\rho_{fb} = \alpha_1 \beta_1 \frac{\phi_c}{\phi_f} \frac{f_c^{'}}{f_{fu}} \frac{E_f \varepsilon_{cu}}{E_f \varepsilon_{cu} + f_{fu}} \tag{6.3}$$

where ϕ_c and ϕ_f are the resistance factors for concrete and FRP, respectively, taken as equal to 1.0 in this study. The ε_{cu} is taken equal to 0.0035 in CSA S806-12 (CSA 2012).

$$\alpha_1 = 0.85 - 0.0015 f_c^{'} \geq 0.67 \tag{6.4}$$

$$\beta_1 = 0.97 - 0.0025 f_c^{'} \geq 0.67 \tag{6.5}$$

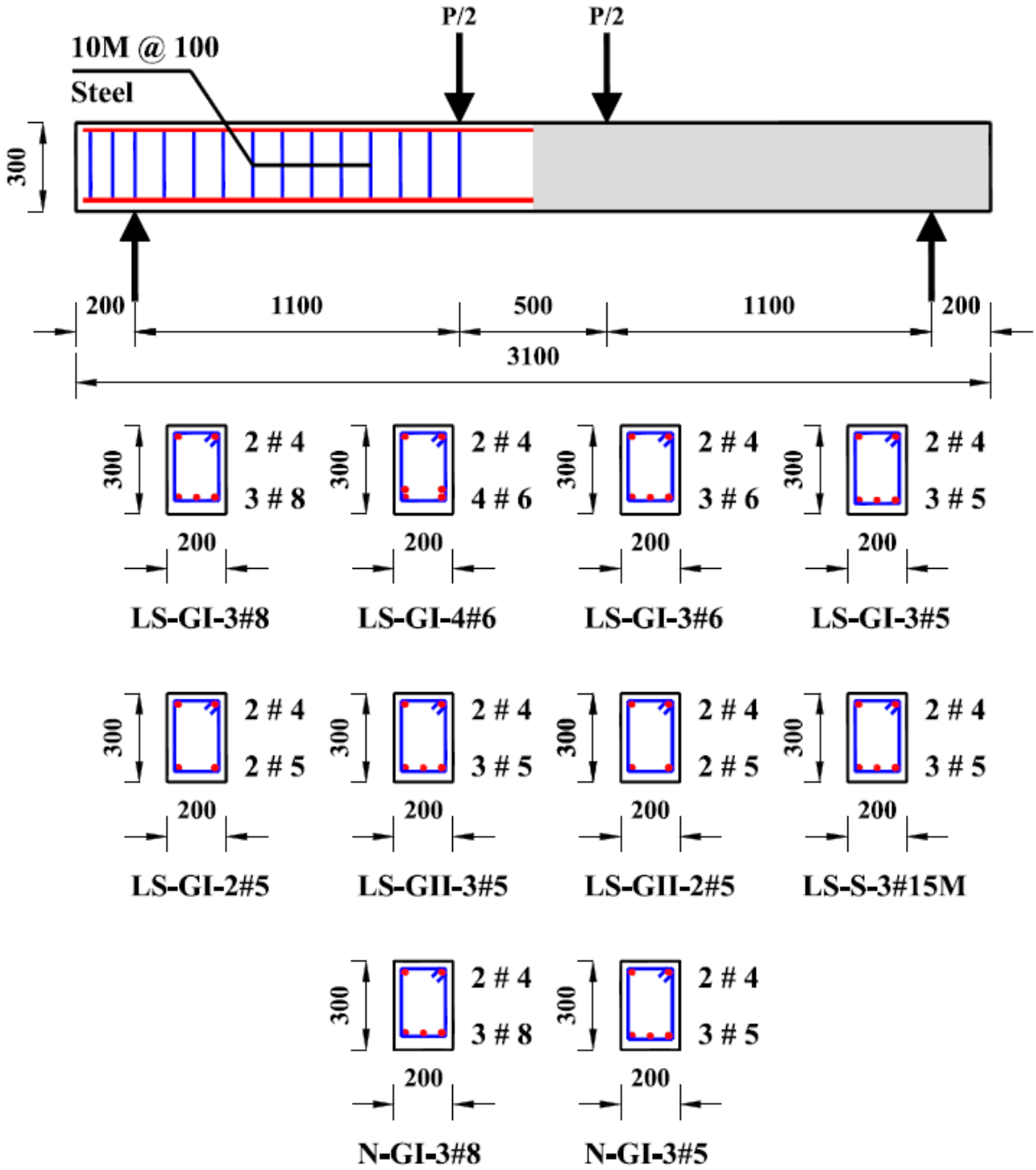

Figure 6.1– Dimensions and reinforcement details of the beam specimens (dimensions in mm).

The influence of the reinforcement ratio (ρ_f) of GFRP bars on the flexural behavior was investigated by testing five beams reinforced with GFRP Type I bars with reinforcement ratios of 3.22%, 2.52%, 1.78%, 1.18%, and 0.78%, and two beams reinforced with GFRP Type II bars with reinforcement ratios of 1.18% and 0.78%. The ratio ρ_f/ρ_{fb} for the GFRP-LWSCC specimens ranged from 2.86 to 10.49 and from 2.34 to 8.55 according to ACI 440.1R-15 (ACI 2015) and CSA S806-12 (CSA 2012), respectively, which is higher than 1.4, as recommended in ACI

440.1R-15 (ACI 2015). The steel-reinforced reference beam was reinforced with 15M steel bars with a ρ_s of 1.18%, which is lower than the balanced one. The influence of concrete density on the flexural behavior was considered by testing two NWC beams (N-GI-3#8 and N-GI-3#5) and two LWSCC beams (LS-GI-3#8 and LS-GI-3#5) (density equal to 1,800 kg/m^3).

Table 6.1 –Test matrix and details of the test specimens

Beam ID	Reinforcing Material	f'_c (MPa)	Concrete Tensile Strength (MPa)	Flexural Reinforcement		ρ_f/ρ_{fb}		E_rA_r, N × 10^6
				Reinforcement configuration	ρ_f (%)	ACI 440.1R-15 (ACI 2015)	CSA S806-12 (CSA 2012)	
LS-GI-3#8	GFRP Type I	43.0	2.95	3#8 - 1 layer	3.22	9.85	8.06	98.70
LS-GI-4#6 [a]	GFRP Type I	43.0	3.05	4#6 - 2 layers	2.52	10.49	8.55	73.20
LS-GI-3#6	GFRP Type I	43.8	3.05	3#6 -1 layer	1.78	7.33	5.95	54.90
LS-GI-3#5	GFRP Type I	43.8	3.05	3#5 - 1 layer	1.18	5.24	4.26	39.00
LS-GI-2#5	GFRP Type I	43.8	3.05	2#5 - 1 layer	0.78	3.48	2.83	26.00
LS-GII-3#5	GFRP Type II	43.0	2.95	3#5 - 1 layer	1.18	4.31	3.52	35.50
LS-GII-2#5	GFRP Type II	43.0	2.95	2#5 - 1 layer	0.78	2.86	2.34	23.70
LS-S-3#15M	Steel	43.8	3.05	3#15M -1 layer	1.18	0.34	0.30	120.0
N-GI-3#8	GFRP Type I	41.3	3.6	3#8 - 1 layer	3.22	10.10	8.32	98.70
N-GI-3#5	GFRP Type I	41.3	3.6	3#5 - 1 layer	1.18	5.43	4.46	39.00

Note: [a] The spacing between the two layers was 12 mm.

6.3.2 Material Properties

The beams were made with LWSCC and ready-mix NWC with a specified compressive strength of 40 MPa after 28 days. The NWC was provided by a local supplier, while the LWSCC was mixed in the University of Sherbrooke's laboratory with two LWA types (Solite 307 and Solite 343). The properties of the LWAs met the requirements of the current version of ASTM C330 / C330M-17a. Table 6.2 presents the physical properties of the aggregates. The mix proportions per cubic meter of LWSCC were as follows: 369 kg of lightweight coarse aggregate (Solite 343), 488 kg of lightweight fine aggregate (Solite 307), 381 kg of fine aggregate (natural sand (NS)), 520 kg of cement (Type TerC3), a water–cement ratio (w/c) of 0.34, 3 L of superplasticizer, and 70 mL/100 kg of entrained air. The density of the LWSCC was 1,800 kg/m^3, as measured according to ASTM C567 (ASTM C567/C567M 2014). The slump-flow value of the LWSCC before casting was 690 mm. Table 6.1 provides the measured concrete compressive strengths of the NWC and LWSCC based on testing three concrete cylinders (100 × 200 mm). In addition,

split cylinder tests were carried out on cylinders 100 mm in diameter × 200 mm in length. The average tensile strengths were 3.6 and 3.0 MPa for the NWC and LWSCC, respectively.

Table 6.2 –Physical properties of aggregates

Materials	Specific Gravity	Water Absorption (%)	Maximum Particle Size (mm)
Lightweight coarse aggregates	1.47	11.2	15
Lightweight sand	1.65	18.5	5
Natural sand	2.65	0.98	5.15

Two commercially available types of GFRP bars (referred to as GFRP Type I and GFRP Type II) were selected as bottom longitudinal reinforcement. The GFRP Type I bars were No. 8 (d_b = 25.4 mm), No. 6 (d_b = 19.1 mm), and No. 5 (d_b = 15.9 mm) with nominal cross-sectional areas of 510, 285, and 199 mm^2, respectively (CSA S807-19 (CSA 2019)). The GFRP Type II bars were No. 5 (d_b = 15.9 mm) with a nominal cross-sectional area of 199 mm^2 (CSA S807-19 (CSA 2019)). The GFRP Type I bars were sand-coated and manufactured by Pultrall Inc. (Thetford Mines, Quebec, Canada). The GFRP Type II bars had a helically grooved surface and were manufactured by Fiberline Composites Inc. (Kitchener, Ontario, Canada). Figure 6.2 illustrates the surface characteristics of the GFRP bars. For comparison purposes, Grade 450 15M steel bars served as longitudinal reinforcement for the reference beam. The properties of the GFRP and steel bars were taken from the manufacturer's data sheet. Table 6.3 summarizes the mechanical properties of the two types of GFRP and the steel bars employed in this investigation. Number 4 (d_b = 12.7 mm) GFRP bars were used for top reinforcement in all the beams. Furthermore, one size (10M) of steel stirrups was fabricated to use as transverse reinforcement in all specimens.

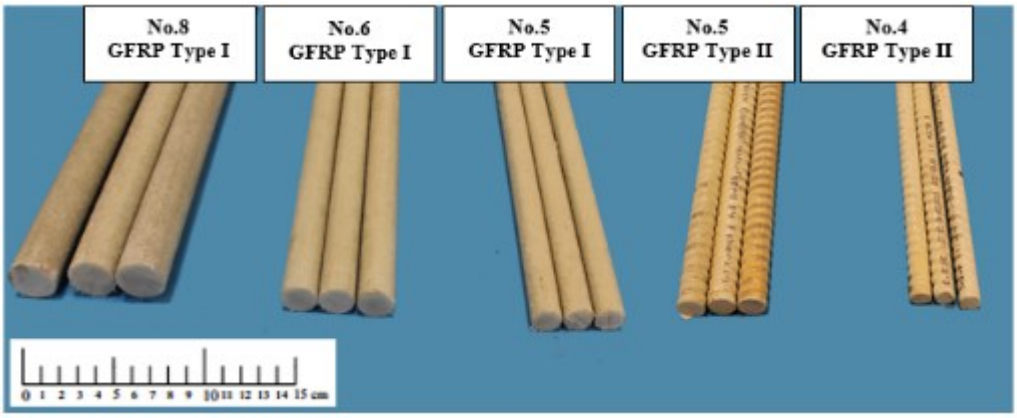

Figure 6.2– GFRP bar types and surface characteristics.

Table 6.3 –Mechanical properties of the GFRP and steel reinforcement

RFT Type		Bar Size	Surface Configuration	d_b (mm)	A_f [a] (mm²)	A_{im} [c] (mm²)	E_f (GPa)	f_{fu} (MPa)	ε_{fu} (%)
GFRP bars	Type I	No. 8	Sand-coated	25.4	510	557	64.5	1175	1.82
		No. 6		19.1	285	325	64.2	1382	2.15
		No. 5		15.9	199	229	65.3	1451	2.22
	Type II	No. 5	Helically grooved	15.9	199	221	59.5	1245	2.09
		No. 4		12.7	129	151	58.3	1170	2.01
Steel bars		15M	Ribbed	16.0	200	---	200	f_y [b] = 450	ε_y [b] = 0.2

[a] Nominal cross-sectional area.

[b] f_y and ε_y are the yield strength and strain of the steel bars, respectively.

[c] Immersed cross-sectional area (measured).

Note: Properties calculated based on the nominal cross-sectional area.

6.3.3 Measurement Equipment and Test Setup

The beams were instrumented with three linear potentiometers (LPOTs) (LPOT1 at mid-span; LPOT2 and LPOT3 at the quarter spans) to monitor deflection (see Figure 6.3). Two strain gauges (length of 60 mm) were bonded on the compression surface at mid-span of each specimen to measure the compressive concrete strains. In addition, four strain gauges (length of 6 mm) were used to monitor the reinforcement strains in the bottom longitudinal bars at four locations. Figure 6.3 illustrates the distribution of strain gauges along the bottom longitudinal bars. Moreover, during testing, three horizontal linear variable differential transducers (LVDTs) were placed at the position of the first three flexural cracks to measure crack widths.

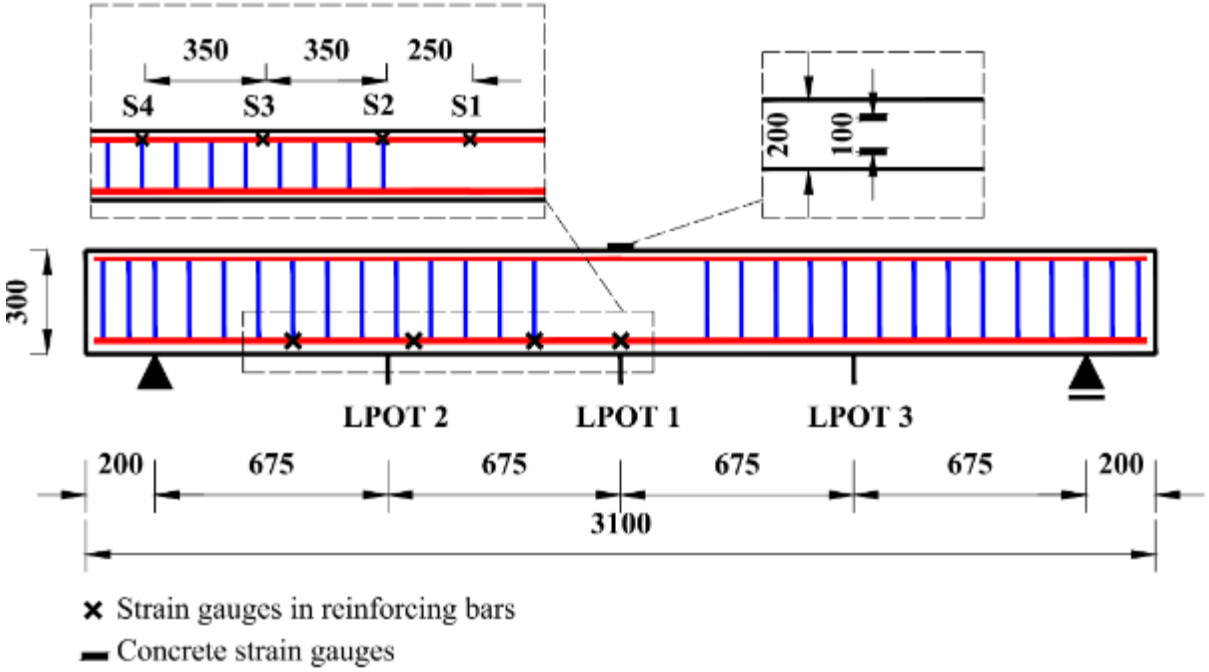

Figure 6.3– Schematic of the instrumentation (dimensions in mm).

The beam specimens were painted and marked after curing to facilitate the monitoring of crack propagation during testing. Each specimen was loaded under four-point loading with a clear span of 2,700 mm between supports. The distance (shear span) from each load to the support was 1,100 mm. A 1,000 kN hydraulic actuator was employed to apply monotonic concentrated loading through a steel spreader beam at a stroke-controlled rate of 0.6 mm/min. Figure 6.4 presents the details of the test setup. A complete test up to failure took approximately 45 to 60 min. The time interval for recording of measurements was 10 readings/s. The measured data (applied load, strain gauges, and LVDT and LPOT readings) were automatically recorded during the test by a 20-channel computer data-acquisition system and stored on a personal computer.

Figure 6.4– Test setup.

6.4 Experimental Results and Discussions

6.4.1 Cracking Moment

The load at the appearance of the first flexural crack was observed and recorded during testing for all specimens. The experimental cracking moment ($M_{cr\text{-}exp}$) of the GFRP-LWSCC specimens, including the self-weight of the beams, ranged between 7.0 and 10.5 kN-m with an average value of 8.6 kN-m compared to 11.5 kN-m for the GFRP-reinforced NWC (GFRP-NWC) specimens. The cracking moment (M_{cr}) depends on the tensile stresses that develop in the concrete from restraint to shrinkage (provided by the internal reinforcement) in addition to the concrete's tensile strength, which is a function of the concrete compressive strength. Therefore, the M_{cr} is a function of the concrete compressive strength. The M_{cr} is estimated with the following equations:

ACI 440.1R-15 (ACI 2015)

$$M_{cr} = \frac{0.62\lambda\sqrt{f_c^{'}} \times I_g}{y_t} \tag{6.6}$$

CSA S806-12 (CSA 2012)

$$M_{cr} = \frac{0.6\lambda\sqrt{f_c^{'}} \times I_g}{y_t} \tag{6.7}$$

where λ is the concrete density reduction factor; I_g is the gross moment of inertia (mm^4). In the case of LWC with a combination of LWA and NS as fine aggregate, ACI 318-19 (ACI 2019) and CSA S806-12 (CSA 2012) specify that λ is the linear interpolation from 0.75 to 0.85 based on the absolute volume of NS as a fraction of the total absolute volume of fine aggregate. In this study, the value of λ was taken to be equal to 0.8 in estimating the predicted cracking moment in accordance with ACI 440.1R-15 (ACI 2015) and CSA S806-12 (CSA 2012) provisions. In addition, normalizing the measured tensile strength of the concrete with respect to $\sqrt{f_c'}$, for both the LWSCC and NWC, indicates the average normalized tensile strength of the LWSCC was 81% of the NWC value and is in good agreement with the λ value of 0.8 used in this study for computing M_{cr}. Table 6.4 provides the experimental-to-predicted cracking moment ($M_{cr\text{-}exp} / M_{cr\text{-}pred}$) at the first flexural crack for each tested beam. As shown, the two approaches provided

approximately similar values of the cracking moment. ACI 440.1R-15 (ACI 2015) and CSA S806-12 (CSA 2012) overestimated the cracking moment values of the GFRP-LWSCC beams, as the value of $M_{cr\text{-}exp}/M_{cr\text{-}pred}$ ranged from 0.69 to 0.99 with an average of 0.84 and from 0.71 to 1.01 with an average of 0.86, respectively. Therefore, the cracking moment was controlled by the λ value for LWC.

Table 6.4 –Experimental and predicted cracking and ultimate moments

Beam ID	Failure Mode [a]	$M_{cr\text{-}exp}$ (KN-m)	$M_{n\text{-}exp}$ (kN-m)	Normalized Moment Capacity	$M_{cr\text{-}exp}/M_{cr\text{-}pred}$		$M_{n\text{-}exp}/M_{n\text{-}pred}$
					ACI 440.1R-15 (ACI 2015)	CSA S806-12 (CSA 2012)	ACI 440.1R-15 (ACI 2015)
LS-GI-3#8	C.C.	10.5	106.5	0.220	0.99	1.01	1.02
LS-GI-4#6	C.C.	9.5	85.5	0.196	0.92	0.95	0.99
LS-GI-3#6	C.C.	8.0	89.0	0.176	0.77	0.79	1.02
LS-GI-3#5	C.C.	9.0	81.0	0.143	0.87	0.89	0.96
LS-GI-2#5	C.C.	8.5	67.5	0.119	0.83	0.86	0.94
LS-GII-3#5	C.C.	8.0	78.0	0.141	0.78	0.80	0.96
LS-GII-2#5	C.C.	7.0	65.5	0.118	0.69	0.71	0.95
LS-S-3#15M [b]	S.Y. + C.C.	9.5	58.5	0.104	0.82	0.83	1.06
N-GI-3#8	C.C.	12.0	104.5	0.225	0.96	0.99	1.03
N-GI-3#5	C.C.	11.0	81.5	0.153	0.90	0.92	0.99

Note: The cracking and ultimate moment included the self-weight of the beams.

[a] C.C. = crushing of concrete; S.Y.+ C.C. = yielding of steel followed by concrete crushing.

[b] Yielding moment.

6.4.2 Failure Mode and Resistance Moment

Figure 6.5 presents the crack patterns and failure modes of the beams. A limited number of cracks were observed within the pure bending region, where the shear stress is zero and pure bending (flexural) stress is highest. As more load was applied, these cracks widened and propagated progressively in a vertical direction, while new cracks appeared in the flexural span and along the specimens' shear span. With further loading, the inclined cracks formed along the shear span and propagated towards the two loading points. As depicted in Figure 6.5, the GFRP-RC beams clearly failed in flexural mode by concrete compression between the two loading points, regardless of the amount of reinforcement and concrete density as expected. The ACI 440.1R-15 (ACI 2015) and CSA S806-12 (CSA 2012) provisions recommend this failure mode for FRP-RC members since it is more gradual, less brittle, and less catastrophic than the tensile rupture of FRP bars. On the other hand, the steel specimen failed in flexural mode by yielding

of the steel reinforcement, followed by concrete failure in compression. It should be mentioned that the steel specimen (LS-S-3#15M) had fewer cracks than the GFRP specimens (LS-GI-3#5 and LS-GII-3#5) with the same amount of reinforcement (1.18%) (see Figure 6.5). Table 6.4 presents the failure mode for each beam in the experimental program.

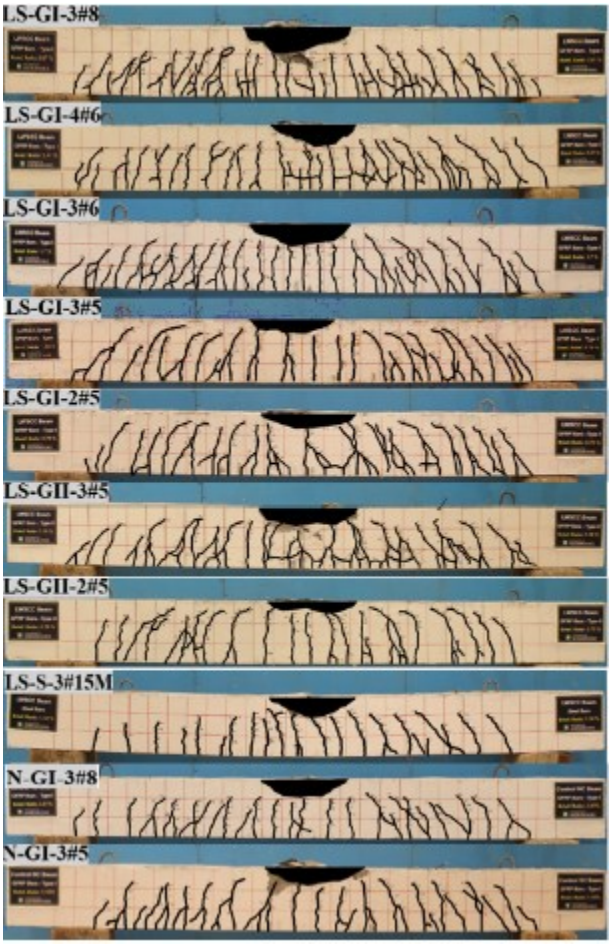

Figure 6.5– Crack patterns and failure modes of the tested beams.

The predicted ultimate moment capacities of the GFRP beams were determined using the strain compatibility approach in ACI 440.1R-15 (ACI 2015). The M_n can be calculated by considering the force equilibrium and strain compatibility according to the following equations:

$$\alpha_1 f_c^{'} ba + A_f^{'} f_f^{'} = A_f f_f \tag{6.8}$$

$$\varepsilon_f = \frac{\left(d - \frac{a}{\beta_1}\right)}{\frac{a}{\beta_1}} \varepsilon_{cu} \tag{6.9}$$

$$\varepsilon_f^{'} = \frac{\left(\frac{a}{\beta_1} - d^{'}\right)}{\frac{a}{\beta_1}} \varepsilon_{cu} \tag{6.10}$$

$$f_f = \varepsilon_f E_f \tag{6.11}$$

$$f_f^{'} = \varepsilon_f^{'} E_f^{'} \tag{6.12}$$

$$M_n = A_f f_f \left(d - \frac{a}{2}\right) + A_f^{'} f_f^{'} \left(\frac{a}{2} - d^{'}\right) \tag{6.13}$$

where M_n is the nominal moment capacity (kN-m); α_1 and β_1 are the values of the rectangular stress block factors; A_f and $A^{'}_f$ are the area of the tension and compressive FRP bars (mm^2), respectively; f_f and $f^{'}_f$ are the stresses in the tension and compressive FRP bars (MPa), respectively; ε_f and $\varepsilon^{'}_f$ are the strains in the tension and compressive FRP bars, respectively; d is the distance from the compression face of the concrete to the center of the tension FRP bars (mm); a is the depth of equivalent rectangular stress block (mm); $d^{'}$ is the distance from the compression face of the concrete to the center of the compressive FRP bars (mm); and b is the width of the beam. Table 6.4 provides the experimental-to-predicted ultimate moment capacity ($M_{n\text{-}exp}/M_{n\text{-}pred}$) of the beam specimens. The comparison shows that the predicted moment capacities for the GFRP-LWSCC specimens using the ACI 440.1R-15 (ACI 2015) equation were in good agreement with the experimental results as the value of $M_{n\text{-}exp}/M_{n\text{-}pred}$ ranged from 0.94 to 1.02 with an average of 0.98. It should be mentioned that the self-weight of the beams was included in the experimental moment capacity.

The influence of the GFRP reinforcement ratio on the normalized moment capacity ($M_n/f^{'}_c bd^2$) of the LWSCC beams was investigated. As shown in Table 6.4, increasing the GFRP Type I reinforcement ratio by 50%, 130%, 220%, and 310% (from 0.78% in LS-GI-2#5 to 1.18%, 1.78%, 2.52%, and 3.22%) increased the normalized moment capacity of specimens LS-GI-3#5, LS-GI-3#6, LS-GI-4#6, and LS-GI-3#8 by 20%, 50%, 65%, and 85%, respectively. Similarly, the increase in the normalized moment capacity for LWSCC specimens reinforced with GFRP Type II bars (LS-GII-2#5 and LS-GII-3#5) was 20% for an approximately 50% increase in the GFRP reinforcement ratio from 0.78% to 1.18%. In addition, an increase in the normalized moment capacity was noted for the GFRP-NWC beams (N-GI-3#8 and N-GI-3#5) as the

reinforcing ratio increased. El-Nemr et al. (2013) made similar observations for GFRP-NWC beam specimens, reporting that an approximately threefold increase in the GFRP reinforcement ratio resulted in an average increase of 83% in the moment capacity of the NWC beams. On the other hand, a comparison was made between the LWSCC beams (LS-GI-3#8 and LS-GI-3#5) and NWC beams (N-GI-3#8 and N-GI-3#5) with reinforcement ratios of 3.22% and 1.18%, respectively, to show how concrete density affected the normalized moment capacity of the GFRP-RC members. Table 6.4 shows that the normalized moment capacity of the LWSCC beams (LS-GI-3#8 and LS-GI-3#5) (0.220 and 0.143, respectively), was not significantly affected (approximately 3.0% and 7.0% less) compared to the NWC counterparts (N-GI-3#8 and N-GI-3#5) (0.225 and 0.153), respectively.

6.4.3 Deflection Behavior

Figure 6.6 illustrates the relationship between the applied moment and the deflection at mid-span. Initially, all the GFRP RC beams behaved linearly up to the appearance of the first flexural crack, followed by nearly linear moment–deflection behavior up to failure. On the other hand, the moment–deflection curve of the steel-reinforced LWSCC (steel-LWSCC) beam was trilinear with a yielding plateau. The LWSCC beams had nearly identical stiffness before the first flexural crack appeared because of the nonsignificant impact of reinforcement type and amount on the gross-section properties of the specimens. In addition, the NWC beams had slightly higher stiffness than the LWSCC beams before cracking due to the higher modulus of elasticity of NWC. After cracking occurred, the flexural stiffness of the LWSCC beams decreased. The curve reveals that the amount of GFRP-bar reinforcement had a direct influence on the flexural stiffness of the beams and, therefore, on their moment–deflection relationship. As expected, less deflection was obtained for higher amounts of GFRP-bar reinforcement and vice versa. The flexural stiffness after cracking of LS-GI-3#8 (ρ_f of 3.22%) was 26% higher than that of LS-GI-4#6 (ρ_f of 2.52%), 57% higher than that of LS-GI-3#6 (ρ_f of 1.78%), 92% higher than that of LS-GI-3#5 (ρ_f of 1.18%), and 140% higher than that of LS-GI-2#5 (ρ_f of 0.78%), Similarly, the flexural stiffness after cracking increased by 28% when the GFRP Type II reinforcement ratio was increased by 60% (from 0.78% in LS-GII-2#5 to 1.18% in LS-GII-3#5). Moreover, the decrease in the flexural stiffness after cracking of the NWC specimens was less obvious than that in the LWSCC specimens because of the high modulus of elasticity of NWC. LS-GI-3#8 and LS-GI-3#5 exhibited lower relative stiffness after cracking than N-GI-3#8 and N-GI-3#5, respectively (see Figure 6.6).

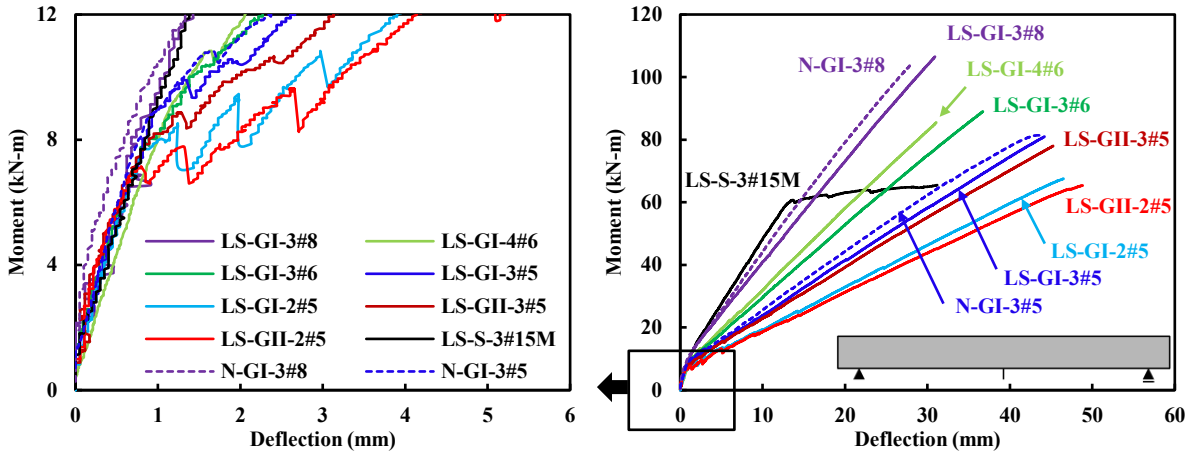

Figure 6.6– Moment–deflection response at the mid-span.

6.4.4 Concrete Strains

Figure 6.7(a) illustrates the relationship between the applied moment and the mid-span concrete strains on the top surface of the beam. Generally, prior to the first crack occurring, the concrete strains ranged approximately from 100 to 200 $\mu\varepsilon$ in all the beams. After cracking, the concrete strains increased almost linearly up to failure. The figure exhibits that increasing the amount of reinforcement of the same type of GFRP reinforcement decreased concrete strain at the same load level. In other words, the concrete strains recorded in LS-GI-3#8 and LS-GII-3#5 were lower than those in LS-GI-2#5 and LS-GII-2#5, respectively, at the same load level. Table 6.5 shows the recorded concrete strains at failure for the beams. The GFRP-LWSCC and GFRP-NWC beams failed by concrete compression at a concrete strain ranging from 3,300 to 3,950 $\mu\varepsilon$ and from 2,850 to 3,500 $\mu\varepsilon$, respectively. The lower concrete strains at failure in the GFRP-NWC beams could be attributed to the higher modulus of elasticity of the NWC. In addition, the recorded concrete strain for the steel-LWSCC beam (LS-S-3#15M) just before steel yielding and at failure was 1,650 $\mu\varepsilon$ and 4,150 $\mu\varepsilon$, respectively.

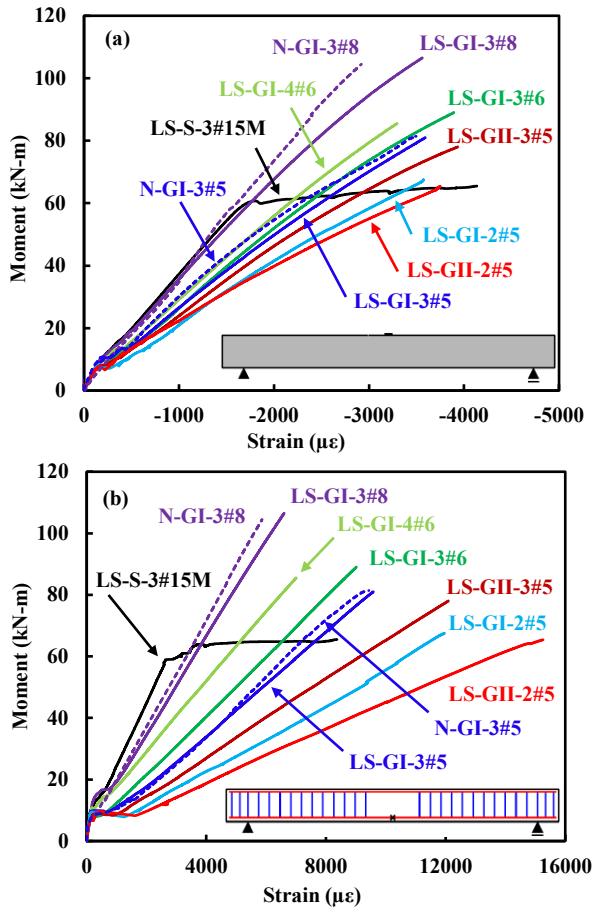

Figure 6.7– Strain responses for the beam specimens at the mid-span (a) concrete and (b) longitudinal reinforcement.

Table 6.5 –Deflections, strains and curvature of the GFRP beams at failure

Beam ID	δ_{exp} (mm)	Maximum Strain ($\mu\varepsilon$)		J
		Bars	Concrete	
LS-GI-3#8	31.0	6600	3560	9.85
LS-GI-4#6	31.0	7000	3300	10.00
LS-GI-3#6	36.7	9000	3890	11.10
LS-GI-3#5	44.2	9600	3590	11.00
LS-GI-2#5	46.5	12000	3570	11.40
LS-GII-3#5	45.2	12100	3950	11.10
LS-GII-2#5	48.8	15400	3750	11.20
N-GI-3#8	28.0	5900	2850	7.80
N-GI-3#5	43.5	9450	3500	8.00

6.4.5 Reinforcement Strains

Figure 6.7(b) illustrates a typical behavior of the tensile strains versus the applied moment for the GFRP and steel bars. Initially, the moment–strain relationships of the tensile reinforcement are comparable to their moment–deflection relationships, including a steep linear branch prior to cracking, followed by a nearly linear branch with a reduced slope after the first crack occurred. As shown in the figure, the LWSCC beams reinforced with the GFRP Type I bars exhibited progressively increasing strain up to failure with recorded tensile strains of 12,000, 9,600, 9,000, 7,000 and 6,600 $\mu\varepsilon$ (54%, 43%, 42%, 33%, and 36% of the rupture strain of the GFRP Type I bars) for LS-GI-2#5, LS-GI-3#5, LS-GI-3#6, LS-GI-4#6, and LS-GI-3#8, respectively. The same observation was made with the GFRP Type II beams, which had maximum tensile strains of 12,100 and 15,400 (as shown in Table 6.5), which is less than the rupture strain of the GFRP Type II bars. The bar tensile strain in the GFRP-LWSCC beams with 1.18% reinforcement (LS-GI-3#5 and LS-GII-3#5) was greater than that of the counterpart steel-LWSCC beam (with the same amount of reinforcement) at the same load level. This is attributed to the steel bars having a higher modulus of elasticity than the GFRP bars. On the other hand, similarly to the influence of the GFRP reinforcement ratio on the tensile strain, the LWSCC beams recorded higher tensile strains than the NWC beams. The maximum GFRP tensile strain in the LWSCC specimen (LS-GI-3#8) was 1.13 times that of the NWC specimen (N-GI-3#8) (see Table 6.5).

6.4.6 Moment–Bar-Strain Profile along the Span

An analysis of strains along the span of the LWSCC beams was conducted using the results from the four bar-strain gauges. The strain gauges were labeled S1 to S4 (S1 at mid-span and S2, S3, and S4 at 20%, 45%, and 70%, respectively, from mid-span). Figures 6.8 and 6.9 present the bar-strain distribution along the span at two different levels of applied moment (immediately after the first crack occurred and at failure). Generally, the bar strains increased with increasing distance from the support to the mid-span of each beam at the two moment levels. For instance, after the first crack occurred, the bar strain at mid-span (S1) in LS-GSI-2#5 was 3,500 $\mu\varepsilon$ compared to 3,400, 1,500, and 120 $\mu\varepsilon$ at S2, S3, and S4, respectively, from mid-span. The same observation was noted at failure, which had bar strains of 12,000, 11,000, 9,400, and 5,950 $\mu\varepsilon$ at S1, S2, S3, and S4, respectively. This indicates that no significant slip occurred during testing. Furthermore, Figures 6.8 and 6.9 confirm that increasing the amount of reinforcement for the two types of GFRP bars reduced longitudinal tensile strains at both moment levels. Beam LS-

GI-3#8 (with the highest ρ_f of 3.22%) exhibited lower bar strain along the span compared to beams LS-GI-4#6, LS-GI-3#6, LS-GI-3#5, LS-GI-2#5 (with reinforcement ratios of 2.52%, 1.78%, 1.18%, and 0.78%), respectively, at all load levels.

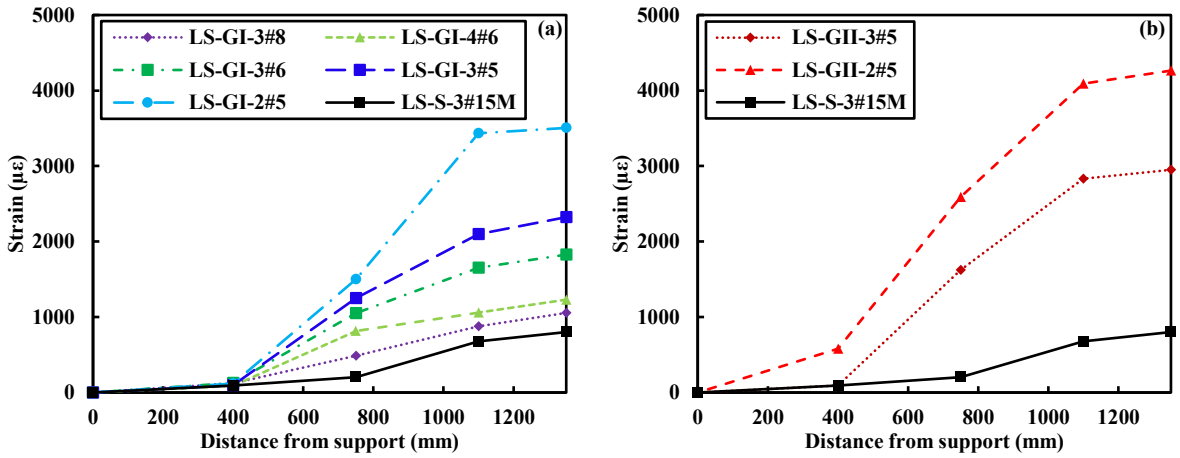

Figure 6.8– Tensile-strain distribution along the specimen length of the LWSCC beams after cracking: (a) GFRP Type I and (b) GFRP Type II.

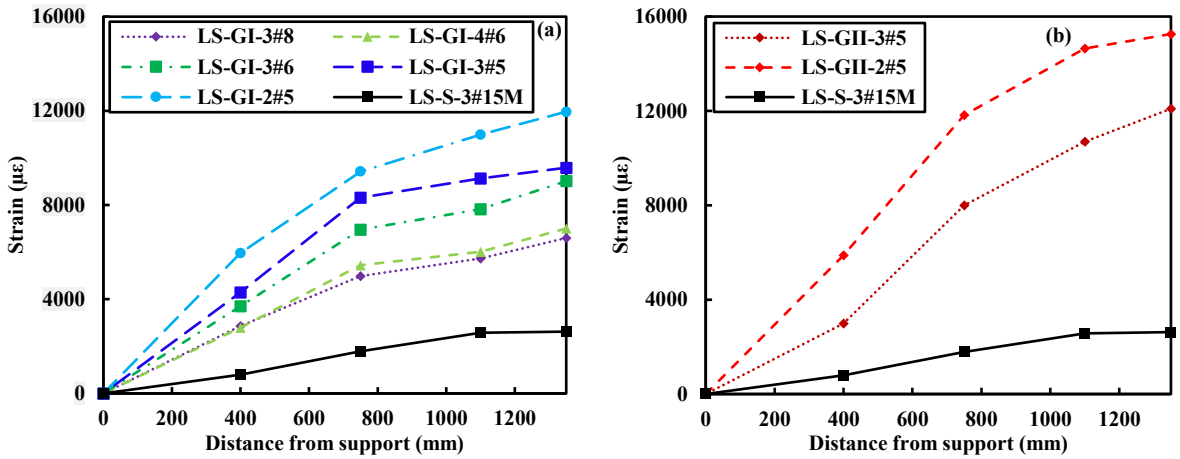

Figure 6.9– Tensile-strain distribution along the specimen length of the LWSCC beams at failure: (a) GFRP Type I and (b) GFRP Type II. (Note: failure for LS-S-3#15M was the yielding moment).

6.4.7 Deformability Evaluation

Since GFRP bars respond linearly up to failure, the definition of ductility for steel-RC elements that considers the yielding of steel bars as a reference point is not applicable to GFRP-LWSCC beams. In this study, the CSA S6-19 (CSA 2019) approach was used to compute the deformability factor (*J-factor*) of the GFRP-LWSCC beams. This approach is based on

deformability instead of absorbed energy to ensure that the GFRP-LWSCC specimens exhibited adequate deformation prior to failure. The *J-factor* is estimated from the following equation:

$$J = \frac{M_{ult}\psi_{ult}}{M_c\psi_c} \tag{6.14}$$

where M_{ult} is the ultimate bending moment; ψ_{ult} is the ultimate curvature; M_c is the bending moment at a concrete strain of 0.001; and ψ_c is the curvature at a concrete strain of 0.001. CSA S6-19 (CSA 2019) adopted this concept for the ductility of FRP-RC beams based on the Jaeger et al. (1997) and Newhook et al. (2002) methods. Newhook et al. (2002) stated that the ultimate moment is equal to the nominal moment. In this investigation, the curvature at ultimate limit states was calculated using the actual experimental values, rather than the theoretical values. Similarly, the ultimate moment is given as the maximum moment recorded during the test. According to CSA S6-19 (CSA 2019), the *J-factor* should be at least 4.0 for rectangular RC sections. Table 6.5 summarizes the *J-factor* values for the GFRP beam specimens. The results indicate that the GFRP beams exhibited adequate deformability (7.80 to 11.40), which was higher than the CSA S6-19 (CSA 2019) code limit of 4.0. It was observed that higher *J-factor* values were associated with lower amounts of reinforcement and vice versa. In other words, decreasing the amount of reinforcement from 3.22% to 0.78% in LS-GI-3#8 and LS-GI-2#5, respectively, increased the *J-factor* by 16% from 9.85 to 11.40. A higher *J-factor* correlates to higher deformation, therefore, providing ample warning of the failure of the GFRP-RC beams.

6.4.8 Deflection Prediction

This section presents the details of estimating the deflection and effective moment of inertia (I_e) for the tested GFRP-LWSCC beams. The experimental results are compared with the theoretical results yielded by the ACI 440.1R-15 (ACI 2015), ISIS Canada Research Network (2007), Benmokrane et al. (1996), and Bischoff (2005) equations. The effect of the concrete density can be taken into account in the I_e, which is a function of the M_{cr} and the modulus of elasticity (E_c), which are both affected by concrete density.

6.4.8.1 Deflection Equations

The immediate mid-span deflection for a simply supported RC element can be estimated as follows:

$$\delta = \frac{(P/2)x}{24E_c I_e}\left[3L^2 - 4x^2\right] \tag{6.15}$$

where $E_c = 0.043\gamma_c^{1.5}\sqrt{f_c'}$ for the concrete density (γ_c) between 1,440 and 2,560 kg/m^3 (ACI 318-19 (ACI 2019)).

CSA S806-12 (CSA 2012) recommends curvature integration by assuming a fully cracked section without any contribution of tension stiffness in the cracked zones. For simple loading cases, Eq. (6.16) is provided for a simply supported beam with two equal point loads *P/2* placed at a distance *x* from the supports, as follows:

$$\delta = \frac{(P/2)L^3}{24E_c I_{cr}}\left[3\left(\frac{x}{L}\right) - 4\left(\frac{x}{L}\right)^3 - 8\left(1 - \frac{I_{cr}}{I_g}\right)\left(\frac{L_g}{L}\right)^3\right] \tag{6.16}$$

where $E_c = \left[3300\sqrt{f_c'} + 6900\right]\left[\frac{\gamma_c}{2300}\right]^{1.5}$ for concrete γ_c between 1,500 and 2,500 kg/m^3; I_{cr} is the cracking moment of inertia; L is the clear span; and L_g is the distance from support to point where M_a *is* M_{cr}.

6.4.8.2 Effective Moment of Inertia Models

The flexural stiffness of a RC member varies along its span because of the cracks that can occur from the applied moment. The flexural stiffness at cracks is affected by the concrete in compression and the reinforcement, while the concrete carries no tension. Between the cracks, however, the concrete helps resist tensile stress due to the bond between the concrete and reinforcement. This impact is often referred to as tension stiffening and is taken into account with I_e. I_e allows for a gradual transition from uncracked to cracked transformed section as the applied moment increases. The value of I_e is between I_g and I_{cr}, depending on how much of the RC element has cracked.

Several models have been introduced by various researchers and design codes to define I_e for FRP-RC members. The Benmokrane et al. (1996) model is one of the first approaches introduced to improve the performance of Branson's equation through a comprehensive experimental program on GFRP-RC beams. Benmokrane et al. (1996) initially proposed an equation for calculating the I_e for GFRP-RC beam specimens, as follows:

$$I_e = \left(\frac{M_{cr}}{M_a}\right)^3 \frac{I_g}{\beta} + \left[1 - \left(\frac{M_{cr}}{M_a}\right)^3\right] \alpha I_{cr} \leq I_g \tag{6.17}$$

where α and β are 0.84 and 7.0, respectively.

Thériault and Benmokrane (1998) continued experimentally studying the deflection behavior of GFRP-RC beam specimens, and then introduced a new modification to Branson's equation, as follows:

$$I_e = \left(\frac{M_{cr}}{M_a}\right)^3 \beta_d I_g + \left[1 - \left(\frac{M_{cr}}{M_a}\right)^3\right] I_{cr} \leq I_g$$

(6.18)

where β_d is the reduction factor equal to 0.6. This factor was later modified by Gao et al. (1998) [Eq. (6.19)] and adopted in ACI 440.1R-03 (ACI 2003).

$$\beta_d = \alpha_b I_g \left(\frac{E_f}{E_s} + 1\right) \tag{6.19}$$

where α_b is the bond-dependent coefficient equal to 0.5; E_f and E_s are the moduli of elasticity of the FRP and steel bars, respectively.

Based on an assessment of the experimental results from several studies, ACI 440.1R-06 (ACI 2006) proposed the following simple relationship for β_d

$$\beta_d = 0.2\left(\frac{\rho_f}{\rho_{fb}}\right) \leq 1.0 \tag{6.20}$$

Bischoff (2005) proposed an equation for estimating I_e based on the tension stiffening concepts as follows:

$$I_e = \frac{I_{cr}}{1 - \left(\frac{M_{cr}}{M_a}\right)^2 \left(1 - \frac{I_{cr}}{I_g}\right)} \tag{6.21}$$

ISIS Canada Research Network (2007) offered an equation to calculate the I_e based on the study conducted by Mota et al. (2006) as follows:

$$I_e = \frac{I_t I_{cr}}{I_{cr} + \left(1 - 0.5\left(\frac{M_{cr}}{M_a}\right)^2\right)\left(I_t - I_{cr}\right)} \tag{6.22}$$

where M_{cr} is calculated using Eq. (6.7) (CSA S806-12 (CSA 2012)).

ACI 440.1R-15 (ACI 2015) recommends estimating I_e with the equation suggested by Bischoff and Gross (2011a) as follows:

$$I_e = \frac{I_{cr}}{1 - \gamma\left(\frac{M_{cr}}{M_a}\right)^2\left(1 - \frac{I_{cr}}{I_g}\right)} \leq I_g \tag{6.23}$$

The reduction factor γ provided in the above equation to account for the variation in stiffness along the span is expressed as:

$$\gamma = \frac{3\left(\frac{x}{L}\right) - 4\left(4\left(\frac{M_{cr}}{M_a}\right) - 3\right)\left(\frac{x}{L}\right)^3}{3\left(\frac{x}{L}\right) - 4\left(\frac{x}{L}\right)^3} \tag{6.24}$$

It should be noted that a simpler expression is defined by Bischoff (2018) for the gamma factor is as follows

$$\gamma = (1 + \alpha) - \alpha\left(\frac{M_{cr}}{M_a}\right) \tag{6.25}$$

$$\alpha = \frac{4}{0.75\left(\frac{L}{x}\right)^2 - 1} \tag{6.26}$$

6.4.8.3 Predicted Effective Moment of Inertia and Deflection Compared to Experimental Results

A comparison was made between the experimental values of the effective moment of inertia (I_{e-exp}) and I_e predicted by four models for FRP-RC members (ACI 440.1R-15 model [Eq. (6.23)], ISIS Canada Research Network (2007) model [Eq. (6.22)], Bischoff (2005) model [Eq. (6.21)], and Benmokrane et al. (1996) model [Eq. (6.18)]). This analysis was conducted to provide a smooth and gradual transition between I_g and I_{cr}, and to investigate the efficiency of each model in accurately predicting I_e. The I_{e-exp} values for the GFRP-LWSCC beams were determined using the recorded deflection data as follows:

$$I_{e-\exp} = \frac{P_{\exp+self}\,x}{48E_{c-\exp}\delta_{\exp}}\left(3L^2 - 4x^2\right) \tag{6.27}$$

where $P_{exp+self}$ is the recorded applied load plus the magnitude of the equivalent load due to the self-weight of the tested beam, taken as $P_{exp+self} = P_{exp} + bt\gamma_c L$; E_{c-exp} is the experimental modulus of elasticity (E_{c-exp}=18,000 MPa); and δ_{exp} is the immediate mid-span deflection. Figure 6.10 shows the experimental and theoretical predictions of I_e versus the applied moment for the seven tested GFRP-LWSCC beams. The experimental and theoretical results in this investigation were evaluated at service load. The service load is defined as 30% of the nominal moment capacity ($0.30M_n$) as recommended by Bischoff et al. (2009). Additional selected comparison was made at the load level corresponding to 67% of the nominal moment capacity ($0.67M_n$) to allow for the assessment of model accuracy at a higher load level. The figure reveals that the ACI 440.1R-15 model overestimated I_e and therefore, underestimated deflections at $0.30M_n$ and $0.67M_n$ for the two types of GFRP bars, regardless of the amount of reinforcement. The average value of the experimental-to-predicted deflections ($\delta_{exp}/\delta_{pred}$) was 1.31 with a COV of 7.90% at $0.30M_n$ and 1.26 with a COV of 5.95% at $0.67M_n$. Both the Bischoff (2005) and Benmokrane et al. (1996) models' predictions were lower than the predictions of the ACI 440.1R-15 (ACI 2015) model at $0.30M_n$ and $0.67M_n$. The average $\delta_{exp}/\delta_{pred}$ at $0.30M_n$ was 1.17 and 1.25, respectively, with a COV of 7.00% and 8.00%, while, at $0.67M_n$, the average $\delta_{exp}/\delta_{pred}$ was 1.22 and 1.23, respectively, with a COV of 5.75% and 6.10%. The ISIS Canada Research Network model, however, provided better predictions at $0.30M_n$ and $0.67M_n$, where the average $\delta_{exp}/\delta_{pred}$ was 1.06 with a COV of 5.30% and 1.19 with a COV of 5.90%, respectively. On the other hand, CSA S806-12 (CSA 2012) provided closer predictions at $0.30M_n$ and underestimated the deflection at

$0.67M_n$, where the average $\delta_{exp}/\delta_{pred}$ was 1.04 with a COV of 4.30% and 1.18 with a COV of 6.05%, respectively. Table 6.6 presents the values of $\delta_{exp}/\delta_{pred}$ at $0.30M_n$ and $0.67M_n$.

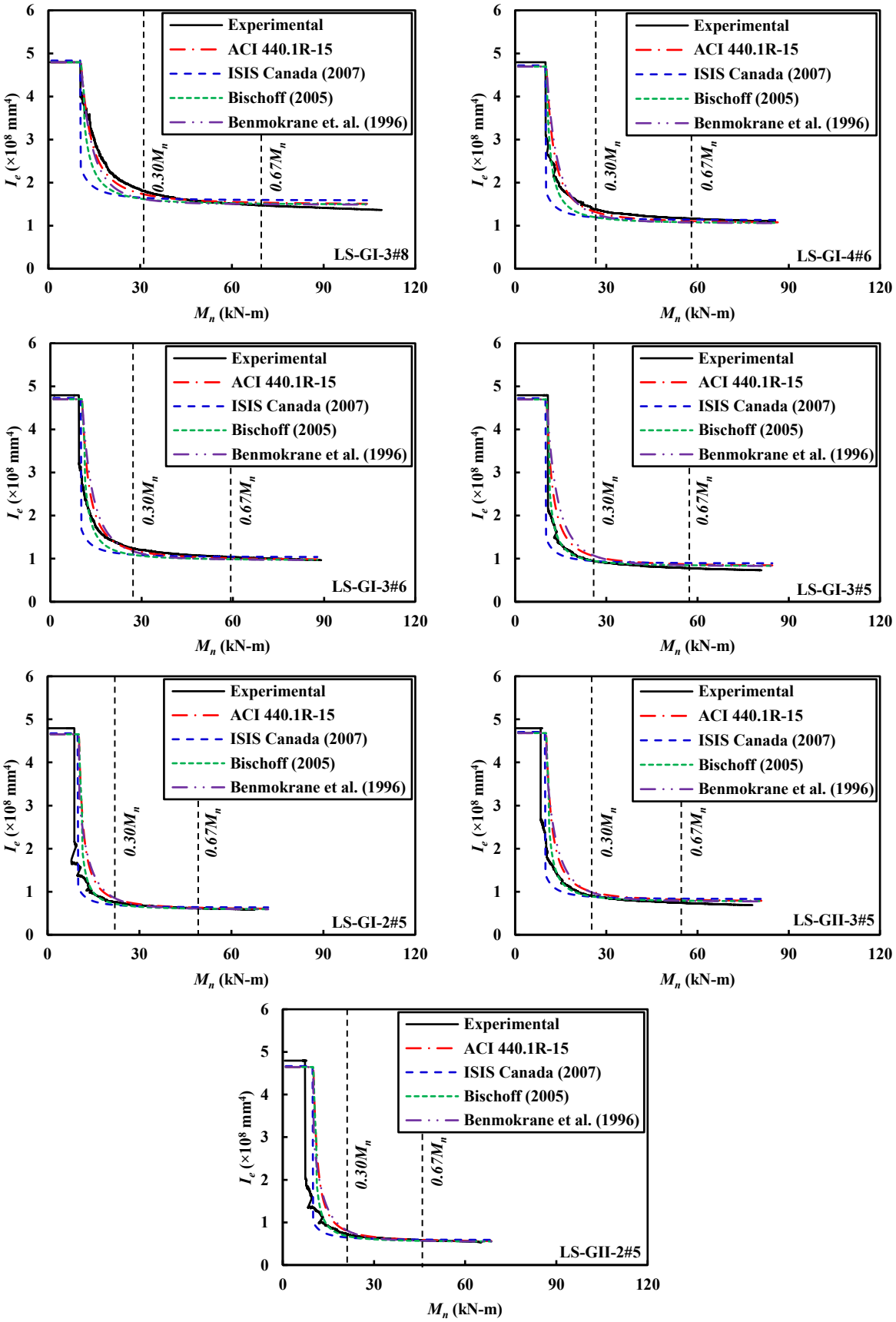

Figure 6.10– The effective moment of inertia versus the applied moment for the GFRP-LWSCC specimens.

Table 6.6 –Experimental-to-predicted deflection ratios of the GFRP-LWSCC specimens

Beam ID	δ_{exp} (mm)		$\delta_{exp}/\delta_{pred}$									
	0.30 M_n	*0.67 M_n*	CSA S806-12 (CSA 2012)		ACI 440.1R-15 Model		ISIS (2007) Model		Bischoff (2005) Model		Benmokrane et al. (1996) Model	
			0.30 M_n	*0.67 M_n*	*0.30 M_n*	*0.67 M_n*	*0.30 M_n*	*0.67 M_n*	*0.30 M_n*	*0.67 M_n*	*0.30 M_n*	*0.67 M_n*
LS-GI-3#8	7.0	19	1.03	1.20	1.19	1.27	1.04	1.21	1.11	1.24	1.11	1.23
LS-GI-4#6	7.7	20	1.01	1.09	1.18	1.16	1.01	1.10	1.08	1.13	1.15	1.12
LS-GI-3#6	8.9	22.7	1.00	1.12	1.22	1.19	1.03	1.13	1.10	1.16	1.19	1.15
LS-GI-3#5	11.3	29.2	1.12	1.28	1.41	1.37	1.16	1.29	1.31	1.33	1.35	1.33
LS-GI-2#5	11.9	32.0	1.01	1.16	1.38	1.26	1.05	1.18	1.19	1.22	1.37	1.22
LS-GII-3#5	11.3	29.8	1.08	1.25	1.38	1.34	1.11	1.26	1.23	1.30	1.28	1.30
LS-GII-2#5	11.8	31.8	1.01	1.13	1.37	1.24	1.01	1.15	1.17	1.19	1.30	1.20
Average			1.04	1.18	1.31	1.26	1.06	1.19	1.17	1.22	1.25	1.23
SD			0.04	0.07	0.10	0.07	0.06	0.07	0.08	0.07	0.10	0.07
COV (%)			4.30	6.05	7.90	5.95	5.30	5.90	7.00	5.75	8.00	6.10

Based on the experimental results, the current ACI 440.1R-15 (ACI 2015) model overestimated the I_e of the tested LWSCC specimens, in most cases, and needs modification to account for the actual response of the LWSCC specimens. In the following section, the ACI 440.1R-15 (ACI 2015) model is addressed and modified to calculate the actual deflection of the LWSCC specimens.

6.4.8.4 Proposed Modification to the ACI 440.1R-15 (ACI 2015) Equation for LWSCC Specimens

The magnitude of M_{cr} has a direct effect on I_e. Therefore, the experimental and deflection values predicted according to the ACI 440.1R-15 model (ACI 2015) were compared considering M_{cr} as being equal to $M_{cr\text{-}exp}$ (the experimental cracking moment of the LWSCC beams), $0.80M_{cr}$ (the reduced cracking moment suggested by Bischoff and Gross (2011b) for FRP-RC), and $0.67M_{cr}$ (the reduced cracking moment provided by ACI 318-19 (ACI 2019) for steel). Figure 6.11 shows the experimental and modified predictions of I_e (ACI 440.1R-15 (ACI 2015) model) versus the applied moment for the tested GFRP-LWSCC beams. The comparison indicates that the ACI 440.1R-15 (ACI 2015) predictions underestimated the deflection values with a cracking moment of $M_{cr\text{-}exp}$ at $0.30M_n$ and $0.67M_n$, where the average $\delta_{exp}/\delta_{pred}$ was 1.20 with a COV of 6.50% and 1.24 with a COV of 5.90%, respectively. Similarly, ACI 440.1R-15 (ACI 2015) yielded underestimated predictions of the deflection values with a cracking moment of $0.80M_{cr}$. The

average $\delta_{exp}/\delta_{pred}$ at $0.30M_n$ was 1.19 with a COV of 6.10%, while, at $0.67M_n$, the average $\delta_{exp}/\delta_{pred}$ was 1.23 with a COV of 6.00%.

Using $0.67M_{cr}$ as in ACI 440.1R-15 (ACI 2015), which is currently used in ACI 318-19 (ACI 2019) for steel, provided better predictions at $0.30M_n$ and $0.67M_n$, where the average $\delta_{exp}/\delta_{pred}$ was 1.13 with a COV of 5.65% and 1.22 with a COV of 5.40%, respectively. Therefore, a modified ACI 440.1R-15 (ACI 2015) model was suggested using $0.67M_{cr}$ instead of M_{cr} to predict the actual deflection of the LWSCC specimens.

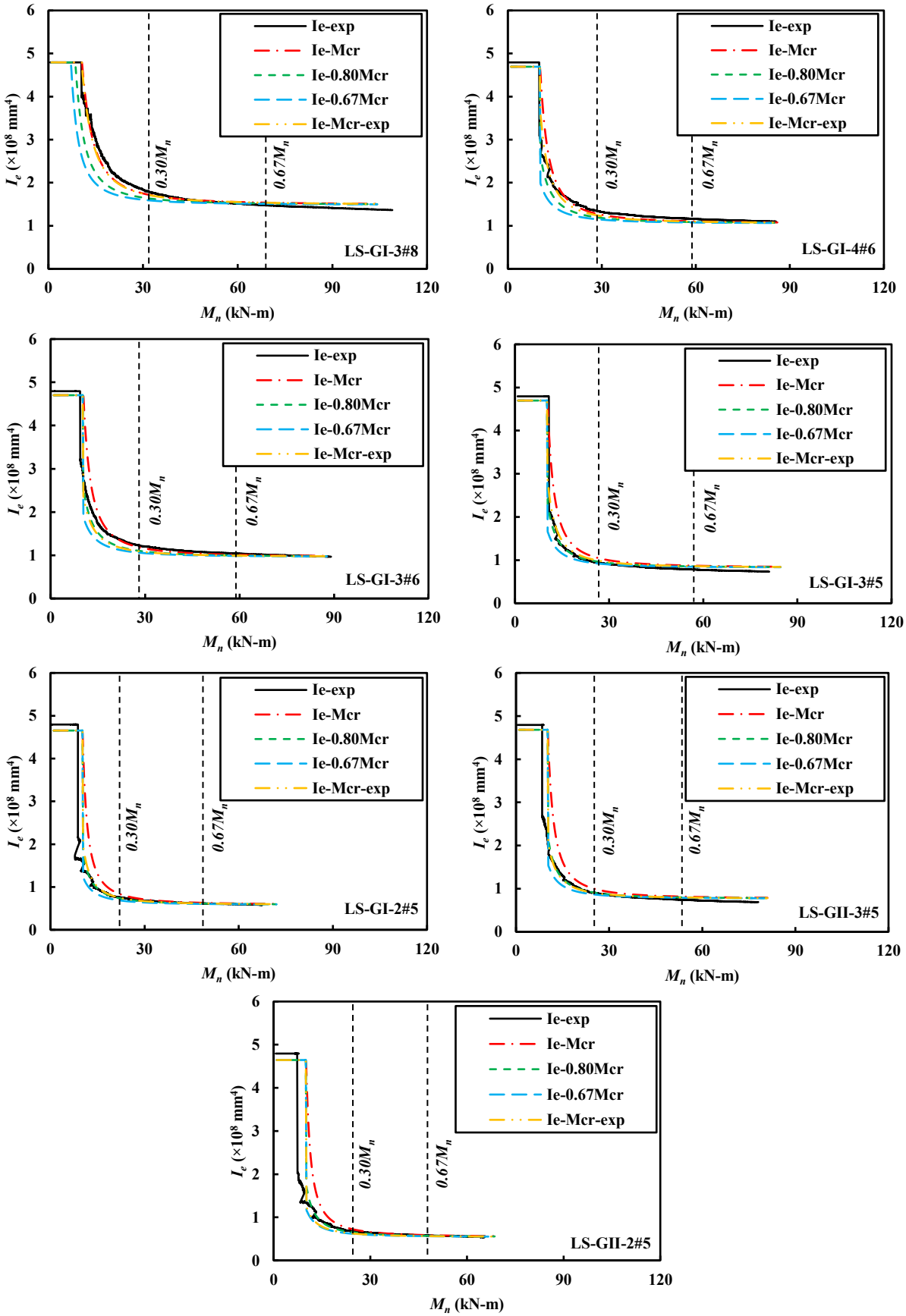

Figure 6.11– The modified effective moment of inertia (ACI 440.1R-15 (ACI 2015) model) versus the applied moment for GFRP-LWSCC specimens.

6.4.9 Crack-Width Prediction

This section presents the theoretical approaches used for calculating the crack-width predictions for the FRP-RC elements, including a direct procedure in which the crack width is estimated and an indirect procedure in which a maximum reinforcing-bar spacing limit is recommended. The experimental and predicted results are compared.

6.4.9.1 Crack-Width Equations

CSA S6-19 (CSA 2019) specifies Eq. (6.28) to account for the crack-width of flexural elements reinforced with longitudinal FRP bars as:

$$w_{cr} = 2\frac{f_{fs}}{E_f}\frac{h_2}{h_1}k_b\sqrt{d_c^2 + (s_{\max}/2)^2} \tag{6.28}$$

where h_2 is the distance from the neutral axis to the tension face of the concrete; h_1 is the distance from the neutral axis to the center of the tension bars; and d_c is the distance from the center of the tension bars to the tension face of the concrete. The k_b value is calculated using the test method in CSA S806-12 (CSA 2012). In the absence of experimental data for k_b, CSA S6-19 (CSA 2019) recommends a k_b of 0.8 and 1.0 for sand-coated and deformed FRP bars, respectively.

ACI 440.1R-15 (ACI 2015) specifies an indirect procedure that controls crack width with a maximum bar spacing based on the approach proposed by Ospina and Bakis (2007):

$$s_{\max} = 1.15\frac{E_f}{f_{fs}}\frac{w_{cr}}{k_b} - 2.5c_c \le 0.92\frac{E_f}{f_{fs}}\frac{w_{cr}}{k_b} \tag{6.29}$$

Equation (6.28) forms the basis of Eq. (6.29). where s_{max} is the maximum allowable bar spacing for flexural-crack control (mm); f_{fs} is the stress level induced in FRP bars at service loads (MPa); w_{cr} is the maximum permissible crack width (mm); c_c is the clear concrete cover (mm); and k_b is the bond-dependent coefficient, which calculates the bond between the FRP bars and surrounding concrete. The value of k_b is calculated experimentally. When experimental data is not available, ACI 440.1R-15 (ACI 2015) suggests a conservative value of 1.4 for FRP bars. The evaluation of the maximum allowable bar spacing is based on a d_c value that complies with the following equation:

$$d_c \leq \frac{E_f w}{2 f_{fs} \beta k_b} \tag{6.30}$$

6.4.9.2 Predicted Crack-Width to Experimental Results

The accuracy of the crack-control equations using the k_b values recommended in ACI 440.1R-15 (ACI 2015) and CSA S6-19 (CSA 2019) was assessed by comparing their theoretical and experimental results. In this study, the width of the first flexural crack was considered as the critical crack, as reported by El-Nemr et al. (2016). Table 6.7 provides the experimental-to-predicted crack-width values ($w_{cr\text{-}exp}/w_{cr\text{-}pred}$) based on ACI 440.1R-15 (ACI 2015) and CSA S6-19 (CSA 2019). The comparison was conducted at $0.30M_n$ (the service-load level) and at $0.67M_n$ (the average load level at which the crack patterns stabilized). In the absence of test data, the value of k_b in ACI 440.1R-15 (ACI 2015) was considered in the predictions as 1.4 for the sand-coated and helically grooved GFRP bars. As recommended in CSA S6-19 (CSA 2019), k_b was taken 0.8 and 1.0 for the sand-coated and helically grooved GFRP bars, respectively. The results indicate that the predicted crack widths were generally higher than the experimental results at $0.30M_n$ and $0.67M_n$. The ACI 440.1R-15 (ACI 2015) equation overestimated the predicted crack widths of the GFRP-LWSCC beams at $0.30M_n$ and $0.67M_n$, on average, with $w_{cr\text{-}exp}/w_{cr\text{-}pred}$ of 0.59 and 0.61, respectively, with corresponding COVs of 16.30% and 16.90%. The conservative value of k_b (1.4 for all types of GFRP bars), as suggested in ACI 440.1R-15 (ACI 2015) when the experimental data is not available, contributed to overestimating the crack widths. On the other hand, the CSA S6-19 (CSA 2019) equation yielded more accurate predictions of the crack widths at $0.30M_n$ and $0.67M_n$, on average, with $w_{cr\text{-}exp}/w_{cr\text{-}pred}$ of 0.96 and 0.99, respectively, with corresponding COVs of 15.60% and 15.75%. The recommended value of k_b (0.8 and 1.0 for sand-coated and helically grooved GFRP bars, respectively, resulted in more accurate predictions of the crack widths. In addition, the ACI 440.1R-15 (ACI 2015) and CSA S6-19 (CSA 2019) equations were compared using a k_b equal to 1.0 for both approaches. Table 6.7 shows that using a k_b value of 1.0 for both approaches provided similar values of the $w_{cr\text{-}exp}/w_{cr\text{-}pred}$ at $0.30M_n$ and $0.67M_n$, on average, with $w_{cr\text{-}exp}/w_{cr\text{-}pred}$ of 0.83 and 0.85, respectively. In conclusion, the difference between the ACI 440.1R-15 (ACI 2015) and CSA S6-19 (CSA 2019) predictions resulted from the difference in the k_b values recommended in each approach.

Table 6.7 –Experimental-to-predicted crack widths of the GFRP-LWSCC specimens

Beam ID	$w_{cr\text{-}exp}$ (mm)		$w_{cr\text{-}exp}/w_{cr\text{-}pred}$							
			ACI 440.1R-15 (2015)				CSA S6-19 (2019)			
	$0.30M_n$	$0.67M_n$	k_b=1.0		k_b =1.4		k_b =1.0		k_b =0.8 (Sand coated) k_b =1.0 (Helically grooved)	
			$0.30M_n$	$0.67M_n$	$0.30M_n$	$0.67M_n$	$0.30M_n$	$0.67M_n$	$0.30M_n$	$0.67M_n$
LS-GI-3#8	0.19	0.42	0.83	0.82	0.61	0.60	0.83	0.82	1.06	1.04
LS-GI-4#6	0.23	0.52	0.69	0.70	0.47	0.48	0.68	0.69	0.83	0.84
LS-GI-3#6	0.28	0.61	0.89	0.89	0.63	0.63	0.89	0.89	1.09	1.09
LS-GI-3#5	0.34	0.81	0.88	0.95	0.63	0.68	0.87	0.95	1.09	1.19
LS-GI-2#5	0.47	1.06	0.71	0.71	0.50	0.51	0.71	0.72	0.87	0.88
LS-GII-3#5	0.44	1.00	1.08	1.11	0.77	0.80	1.08	1.11	1.08	1.11
LS-GII-2#5	0.51	1.20	0.73	0.79	0.52	0.56	0.73	0.78	0.73	0.78
Average			0.83	0.85	0.59	0.61	0.83	0.85	0.96	0.99
SD			0.14	0.14	0.10	0.11	0.14	0.15	0.15	0.16
COV (%)			16.30	16.90	16.30	16.90	16.35	17.00	15.60	15.75

The experimental results were used to assess the k_b values. The k_b factor was calculated in accordance with CSA S6-19 (CSA 2019). The k_b was determined at $0.30M_n$, at $0.67M_n$, and at a crack width of 0.7 mm (the upper crack-width limit for interior exposure provided in CSA S6-19 (CSA 2019)). Table 6.8 presents the calculated k_b values for the GFRP bars (sand-coated and helically grooved). For the sand-coated GFRP bars, the k_b values ranged from 0.55 to 0.91, with an overall average of 0.73, which is lower than the recommendation in CSA S6-19 (CSA 2019) for sand-coated FRP bars. On the other hand, the k_b values determined for the helically grooved GFRP bars ranged from 0.62 to 0.99, with an overall average of 0.84, which is lower than the recommendation in CSA S6-19 (CSA 2019) for deformed FRP bars.

Table 6.8 –The predicted k_b values at different limits for GFRP bars

Beam ID	k_b			Average k_b
	$0.30M_n$	$0.67M_n$	0.7 mm	
LS-GI-3#8	0.79	0.69	0.77	0.75
LS-GI-4#6	0.67	0.58	0.55	0.60
LS-GI-3#6	0.79	0.75	0.74	0.76
LS-GI-3#5	0.81	0.88	0.91	0.87
LS-GI-2#5	0.65	0.65	0.74	0.68
LS-GII-3#5	0.87	0.84	0.99	0.90
LS-GII-2#5	0.62	0.72	0.98	0.77

6.5 Conclusions

This paper reports on an experimental and theoretical study of the flexural capacity and serviceability performance of GFRP-LWSCC beams. Based on the experimental results and the theoretical analysis, the main findings of this investigation are as follows:

1. Using LWSCC made it possible to fabricate beams with lower self-weight (density of 1,800 kg/m^3) than with NWC. The tested LWSCC and NWC beams reinforced with GFRP bars all experienced compressive failure, while the steel-LWSCC beam failed due to steel yielding, followed by compressive failure.
2. Using a concrete density reduction factor of 0.8 in the ACI 440.1R-15 (ACI 2015) and CSA S806-12 (CSA 2012) cracking-moment equations to consider the influence of concrete density yielded an appropriate degree of conservatism compared to the NWC beams. On the other hand, the predicted moment capacities for the GFRP-LWSCC specimens using the ACI 440.1R-15 (ACI 2015) were in good agreement with the experimental results with an average accuracy of ≥ 90%.
3. The normalized moment capacity in the specimens cast with LWSCC was proportional to the longitudinal reinforcement ratio of the GFRP. Increasing the GFRP reinforcement ratio from 0.78% to 3.22% increased the normalized moment capacity of the specimens by 85%. On the other hand, the normalized moment capacity at concrete crushing of the GFRP-LWSCC beams was approximately 0.90 times that of the counterpart GFRP-NWC beams with the same amount of reinforcement.
4. The specimens reinforced with sand-coated GFRP bars produced narrower crack widths than those reinforced with helically grooved GFRP bars. This tends to confirm GFRP bars with a sand-coated surface have better flexural bond characteristics.
5. The ACI 440.1R-15 model overestimated I_e and therefore, underestimated the deflections at $0.30M_n$ and $0.67M_n$, with average $\delta_{exp}/\delta_{pred}$ of 1.31 and 1.26, respectively. The Bischoff (2005) and Benmokrane et al. (1996) models' predictions were lower than the predictions of the ACI 440.1R-15 model at $0.30M_n$ and $0.67M_n$, with the average $\delta_{exp}/\delta_{pred}$ of 1.17 and 1.25, respectively, at $0.30M_n$ and 1.22 and 1.23 at $0.67M_n$. The ISIS Canada Research Network (2007) model, however, provided better predictions at $0.30M_n$ and $0.67M_n$, with the average $\delta_{exp}/\delta_{pred}$ of 1.06 and 1.19, respectively.

6. The CSA S806-12 (CSA 2012) provided closer predictions of the deflection at $0.30M_n$ and underestimated the deflection at $0.67M_n$, with average $\delta_{exp}/\delta_{pred}$ of 1.04 and 1.18, respectively.
7. Based on the experimental results, a modified ACI 440.1R-15 (ACI 2015) model was suggested using $0.67M_{cr}$ instead of M_{cr} to predict the actual deflection of the LWSCC specimens.
8. The ACI 440.1R-15 (ACI 2015) design equation overestimated the predicted crack widths for the GFRP-LWSCC beams compared to the experimental crack-width values, where the average $w_{cr\text{-}exp}/w_{cr\text{-}pred}$ was 0.59 and 0.61 at $0.30M_n$ and $0.67M_n$, respectively. On the other hand, the CSA S6-19 (CSA 2019) design equation yielded more accurate predictions of the crack widths at $0.30M_n$ and $0.67M_n$, on average, with $w_{cr\text{-}exp}/w_{cr\text{-}pred}$ of 0.96 and 0.99, respectively. The difference between the ACI 440.1R-15 (ACI 2015) and CSA S6-19 (CSA 2019) predictions resulted from the difference in the k_b values recommended in each approach.
9. The average bond-dependent coefficient (k_b) values were 0.73 and 0.84 for the sand-coated and helically grooved GFRP bars, respectively, which are lower than the recommendation in the CSA S6-19 (CSA 2019) (k_b=0.80 and 1.0) for sand-coated and deformed FRP bars, respectively.

CHAPTER 7

Bond-Dependent Coefficient and Cracking Behavior of Lightweight Self-Consolidating Concrete (LWSCC) Beams Reinforced with Glass- and Basalt-FRP Bars

Foreword

Authors and Affiliation:

- Shehab Mehany: Ph.D. candidate, Department of Civil Engineering, Université de Sherbrooke, Sherbrooke, Quebec, Canada, J1K 2R1.
- Hamdy M. Mohamed: Research Associate/Lecturer, Department of Civil Engineering, Université de Sherbrooke, Sherbrooke, Quebec, Canada, J1K 2R1.
- Adel El-Safty: Professor, Department of Civil Engineering, University of North Florida, Jacksonville, FL, USA.
- Brahim Benmokrane: Professor, Department of Civil Engineering, Université de Sherbrooke, Sherbrooke, Quebec, Canada, J1K 2R1.

Journal Title: *Construction and Building Materials, Elsevier.*

Paper Status: *Under review.*

Abstract

Crack width is one of the issues that can often control the design of flexural elements reinforced with fiber-reinforced polymer (FRP) bars due to the relatively low modulus of elasticity. This paper aims at investigating the cracking behavior of lightweight self-consolidating concrete (LWSCC) beams reinforced with glass- and basalt-FRP (GFRP and BFRP) bars and evaluating the bond-dependent coefficient (k_b) values. Fifteen reinforced concrete (RC) specimens 200 mm in width, 300 mm in height, and 3,100 mm in length were prepared and tested up to failure. Twelve specimens were made using LWSCC, while the other three were made with normal-weight concrete (NWC) as reference specimens. The test variables were concrete density (LWSCC and NWC); reinforcement type (GFRP and BFRP bars) with various surface conditions (sand-coated and helically grooved); and longitudinal reinforcement ratio. The experimental results show that the FRP-reinforced LWSCC (FRP-LWSCC) beams exhibited cracking behavior similar to that of the counterpart FRP-reinforced NWC (FRP-NWC) beams. The FRP-LWSCC beams had a linear crack response up to failure by concrete crushing, regardless of the amount and surface condition of the FRP reinforcement. Moreover, the recorded crack widths of the FRP-LWSCC beams are presented and compared to those predicted according to FRP design provisions. The comparisons indicate that the crack widths of the FRP-LWSCC beams can be estimated with the FRP design provisions with a variable degree of conservativeness. Furthermore, the determination of the k_b factor reveals that the sand-coated GFRP and BFRP bars yielded smaller k_b values than the helically grooved GFRP and BFRP bars.

Keywords: Lightweight self-consolidating concrete (LWSCC) beams; GFRP and BFRP bars; cracking behavior; crack width; bond-dependent coefficient; FRP design codes.

7.1 Introduction

Rapid innovations in concrete technology have increasingly resulted in using lightweight materials such as lightweight self-consolidating concrete (LWSCC) in reinforced concrete (RC) structures such as bridge main girders, composite floor slabs, and precast elements (Okamura and Ouchi 2003; Hubertova and Hela 2007). LWSCC was developed to combine the excellent advantages of self-consolidating concrete (SCC) and lightweight concrete (LWC) in a single package. LWC makes it possible to reduce the self-weight of RC members, thereby leading to lower cost. Moreover, LWC offers better performance in terms of fire/flame resistance, freeze–thaw resistance, and heat and sound insulation (ACI 213-14). SCC is a highly workable concrete that can spread into place under its own weight and fill the formwork without any segregation or bleeding. Using SCC in RC members also reduces labor and machinery costs. Therefore, combining LWC and SCC should enhance workability, produce high-strength LWC, prevent the segregation of lightweight aggregate (LWA), and lead to increased cost savings (Hossain et al. 2020).

Nowadays, the use of fiber-reinforced polymer (FRP) bars in RC elements has been deemed an acceptable alternative to traditional steel bars as an effective solution to corrosion problems (ACI 440.1R-15). In North America, glass-FRP (GFRP) bars are becoming the most common type of FRP bars because they cost less than other types of FRP composite materials. GFRP bars have been used for various applications, such as in high-rise buildings, bridges, and parking garages. Recently, basalt-FRP (BFRP) bars have been introduced in the construction field as a promising addition to the existing FRP-bar family. Similar to GFRP bars, BFRP bars have a high strength-to-weight ratio, good resistance to chemical and electromagnetic attack, excellent bond strength with concrete, and relatively low modulus of elasticity compared to traditional steel bars (Wu et al. 2015; Elgabbas et al. 2017). Basically, the relative low modulus of elasticity of FRP reinforcement should be considered in the design to reduce the crack widths in such members. Although the crack widths of FRP-RC elements can be relaxed because of the excellent corrosion resistance of FRP reinforcement, they need to be controlled to ensure other important serviceability aspects, such as appearance and watertightness. This, in turn, might lead to governing the design of FRP-RC elements according to the limits of crack width at service loads. In general, flexural cracks form in RC elements when the concrete tensile strain reaches its tensile deformation capacity. At the crack locations, the applied load is carried by the flexural bars, while the concrete carries no loads. Between the cracks, however, a portion of the load is

transferred to the concrete due to the bond between the concrete and reinforcement. Accordingly, the crack width in FRP flexural elements is controlled by many parameters, including bar spacing: tensile strain in the FRP bars; the bond-dependent coefficient (k_b), which depends on the surface conditions of the FRP bars; and concrete cover.

Extensive efforts have focused on the cracking and crack control of GFRP- and BFRP-reinforced NWC (GFRP-NWC and BFRP-NWC) flexural elements. As a result, several equations from the current approaches (ACI 440.1R-15, AASHTO-18, CSA S806-12, and CSA S6-19) have been introduced to control the crack widths in RC elements reinforced with FRP bars. Theriault and Benmokrane (1998) conducted an early experimental investigation on the cracking behavior of NWC beam specimens reinforced with FRP bars. The main variables were the amount of reinforcement and the concrete strength. Their results showed that increasing the amount of reinforcement of FRP bars yielded smaller crack widths at the same load levels. Subsequently, numerous studies have been carried out to calculate the relationships between crack width and the aforementioned design parameters (Frosch 1999; Toutanji and Saafi 2000; Toutanji and Deng 2003; El-Salakawy and Benmokrane 2004; Ospina and Bakis 2007; Kassem et al. 2011; El-Nemr et al. 2013; McCallumb2013). Recently, Elgabbas et al. (2016) conducted an investigation on the serviceability performance of NWC beam specimens reinforced with sand-coated BFRP bars. They found that the average k_b value was 0.76 for the sand-coated BFRP bars, which is consistent with the CSA S6-19 recommendation of k_b = 0.8 for sand-coated FRP bars. El-Nemr et al. (2016) reported that the sand-coated GFRP bars tested had lower k_b values than the grooved GFRP bars. In addition, the crack width at service load ($0.30M_n$) was less than 0.7 mm in all the specimens, which satisfies the requirements of CSA S806-12. Henin et al. (2019) carried out an experimental study to determine the k_b factor of the two types of sand-coated BFRP bars (primary and secondary). The experimental results indicate that ACI 440.1R-15 provided a conservative k_b value of 1.4 for BFRP bars regardless of the surface condition, which is conservative compared to the determined value of 0.92 and 0.77 for primary and secondary sand-coated BFRP bars, respectively.

In recent years, limited research has been carried out to assess the influence of FRP reinforcing bars on the serviceability performance of LWC beam specimens. Wu et al. (2019) tested nine RC beam specimens reinforced with GFRP bars under flexural loads. The specimens were made with LWC and steel fiber-reinforced LWC (SFLWC). The test results indicated that the beams made with SFLWC exhibited narrower cracks than those made with LWC. Increasing the

amount of GFRP-bar reinforcement in both the LWC and SFLWC beam specimens yielded narrower crack widths at the same load levels. Liu et al. (2020) studied the applicability of using FRP bars as longitudinal reinforcement in LWC and SFLWC beams. They found that the failure of all specimens occurred by concrete crushing. Moreover, comparing the crack-width predictions revealed that the provisions in ACI 440.1R-06 overestimated the predicted crack widths at service load for the LWC and SFLWC beams, while those in ISIS-07 predicted reasonable crack-width values.

7.2 Research Objectives and Significance

To date, limited research work has focused on the serviceability performance of LWC beams reinforced with FRP bars. No research, however, seems to have investigated the cracking behavior of lightweight self-consolidating concrete (LWSCC) beams reinforced with glass- and basalt-FRP (GFRP and BFRP) bars and evaluating the bond-dependent coefficient (k_b) values. In addition, none of the FRP design standards and guides have provided specific provisions about the serviceability performance of FRP-reinforced LWSCC (FRP-LWSCC) members. This paper focuses on the bond-dependent coefficient k_b and cracking behavior/control of LWSCC beam specimens reinforced with various types of FRP bars with different amounts of reinforcement. Accordingly, this investigation has specific objectives: (1) to assess the bond-dependent coefficient k_b of different surface conditions of GFRP and BFRP bars (sand-coated and helically grooved) in LWSCC; (2) to investigate the cracking behavior of LWSCC beams reinforced with GFRP and BFRP bars; (3) to compare the experimental cracking moment of the GFRP- and BFRP-reinforced LWSCC (GFRP-LWSCC and BFRP-LWSCC) beams with those obtained from predicted with FRP design provisions; (4) to investigate the effect of GFRP and BFRP types and reinforcement amount on k_b coefficient and the cracking behavior of the LWSCC specimens; and (5) to compare the recorded crack widths of LWSCC beams with those predicted by models in the FRP design codes and guides. The outcomes of this study can be used to assess and explore the feasibility of using GFRP and BFRP bars in LWSCC members under flexural loads. In addition, the experimental data and theoretical analysis are valuable for designers, engineers, and members of code committees using GFRP and BFRP reinforcement in LWSCC beams and for the development of codes and standards.

7.3 Experimental Program

7.3.1 Materials

7.3.1.1 Concrete Types

The beams were constructed with LWSCC and ready-mix NWC with a specified 20-day compressive strength of 40 MPa. The NWC was mixed and delivered to the laboratory by a local supplier, while the LWSCC was mixed in the University of Sherbrooke's CME laboratory. A cubic meter of the NWC contained 460 kg of cement; 730 and 272 kg, respectively, of coarse aggregate in sizes ranging from 5 to 20 mm and from 5 to 10 mm; 719 kg of natural sand (NS); 0.08 L/100 kg of entrained air; and 0.3 L/100 kg of water-reducing agent. The water-to-cement ratio (w/c) was 0.35. In contrast, the LWSCC mixtures contained two LWA types—Solite 343 and Solite 307—from the same source. The properties of the LWAs met the requirements of the current version of ASTM C330/C330M-17a (2017). Table 7.1 gives the details of the LWSCC mix proportions. Its density was 1,800 kg/m^3, as measured according to ASTM C567/C567M (2014). The exact concrete compressive and tensile strengths were calculated on the day of testing from three 100 × 200 mm concrete cylinders for each test in accordance with ASTM C39/C39M (2018) and ASTM C496 (2011), respectively. The exact concrete compressive strength for the LWSCC ranged from 42 to 43.8 MPa, while that of the NWC was 41.3 MPa. The average tensile strength was 3.0 and 3.6 MPa for the LWSCC and NWC, respectively.

Table 7.1 – LWSCC mix proportions

LWSCC	
Cement – Type TerC3	520 kg /m^3
w/c	0.34
Lightweight coarse aggregate	369 kg /m^3
Lightweight sand	488 kg /m^3
Natural sand	381 kg /m^3
Air entrainment	70 mL/100 kg
Superplasticizer	3 L/ m^3

7.3.1.2 GFRP and BFRP Bars

Since k_b is influenced by the performance of the bond between the concrete and reinforcement, two types of FRP (GFRP and BFRP) reinforcement with two surface conditions (sand-coated

and helically grooved) were used. The GFRP and BFRP bars were classified as Grade III. The FRP bars are referred to herein as sand-coated GFRP (No. 6 and No. 5), helically grooved GFRP (No. 5), sand-coated BFRP (No. 6), and helically grooved BFRP (No. 5) (see Figure 7.1). The GFRP and BFRP bars were fabricated with a pultrusion process using glass or basalt fibers, respectively, impregnated in a vinyl-ester resin. The FRP bars had fiber contents of 83% and 86% for the sand-coated and helically grooved GFRP, respectively, and 81%, and 80% for the sand-coated and helically grooved BFRP, respectively. The modulus of elasticity, ultimate tensile strength, and strain at rupture of the GFRP and BFRP bars were estimated by testing five specimens in accordance with ASTM D7205 (2011). Table 7.2 summarizes the mechanical characteristics of the GFRP and BFRP bars. In addition, one size (10M) of steel stirrups was fabricated for use as transverse reinforcement in all the beams.

Table 7.2 – Mechanical properties of the GFRP and BFRP reinforcements

RFT Type		Bar Size	d_b (mm)	A_f [a] (mm²)	A_{im} [c] (mm²)	E_f (GPa)	f_{fu} (MPa)	ε_{fu} (%)
GFRP bars	Sand-coated	No. 6	19.1	285	325	64.2	1382	2.15
		No. 5	15.9	199	229	65.3	1451	2.22
	Helically grooved	No. 5	15.9	199	221	59.5	1245	2.09
BFRP bars	Sand-coated	No. 6	19.1	285	346	63.7	1646	2.50
	Helically grooved	No. 5	15.9	199	201	64.8	1724	2.67

[a] Nominal cross-sectional area.

[b] f_y and ε_y are the yield strength and strain of the steel bars, respectively.

[c] Immersed cross-sectional area (measured).

Note: Properties calculated based on the nominal cross-sectional area.

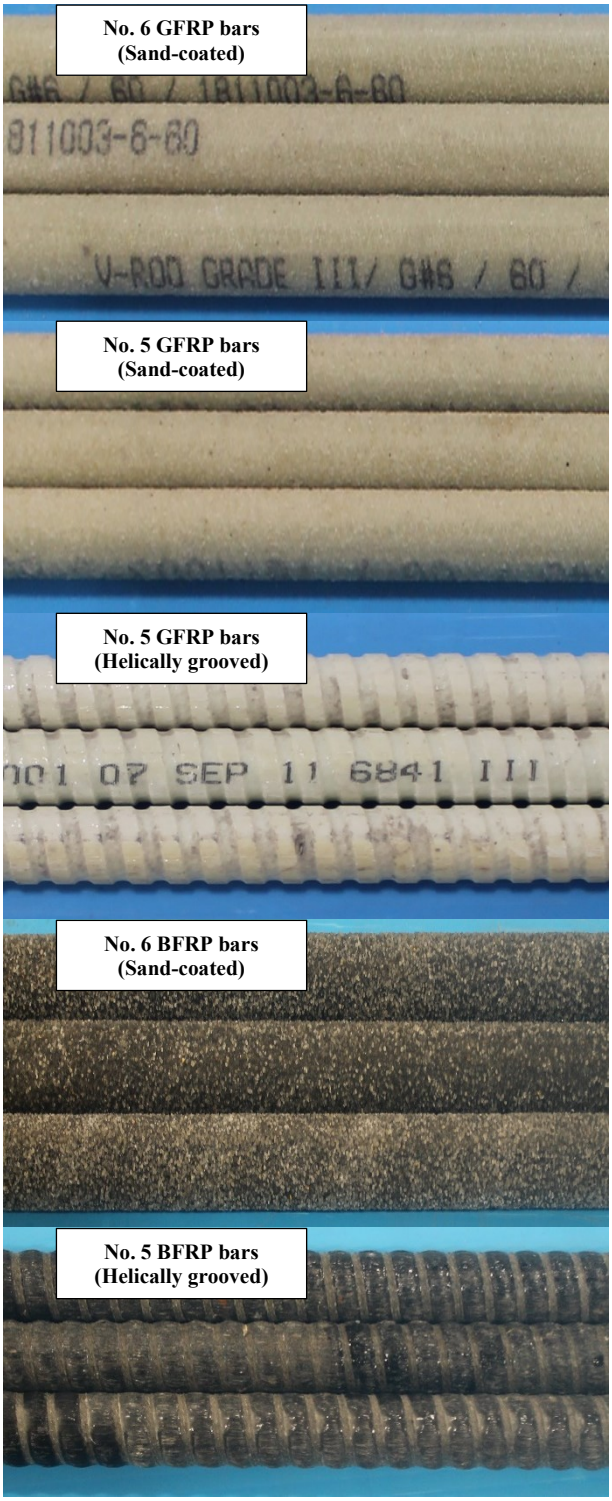

Figure 7.1– FRP bar types and surface characteristics.

7.3.2 Beams Geometry and Test Matrix

Fifteen RC beams with various reinforcement types (GFRP and BFRP bars) were tested under four-point bending load up to failure. The beams measured 3,100 mm in length with a 200 × 300 mm rectangular cross section. Figure 7.2 presents the specimen geometry and reinforcement

details. The total length of the specimens included a 200 mm overhang beyond the two supports to ensure appropriate anchorage of the longitudinal bars. The beams were reinforced with two No. 4 GFRP bars as top reinforcement to hold the stirrups. Shear failure was avoided by using traditional steel stirrups (10 mm in diameter) in the nonconstant-moment regions at a pitch of 100 mm for all beam specimens. Each beam was identified with a tripartite code. The first part—LS or N—refers to the concrete density, i.e., LWSCC and NWC, respectively. The second part—GS, GH, BS, or BH—identifies the beam as being reinforced with sand-coated GFRP, helically grooved GFRP, sand-coated BFRP, or helically grooved BFRP bars, respectively. The third part indicates the number of bars, followed by the bar size. The test parameters were concrete density (LWSCC and NWC), reinforcement type (GFRP and BFRP bars) with two surface conditions (sand-coated and helically grooved), and longitudinal reinforcement ratio. The influence of concrete density on the cracking behavior was considered by testing three NWC beams (N-GS-3#5, N-BS-2#6, and N-BH-3#5) and three LWSCC beams (LS-GS-3#5, LS-BS-2#6, and LS-BH-3#5) (density equal to 1,800 kg/m^3) with the same amount of reinforcement (ρ_f of 1.18%). The influence of reinforcement type on the cracking behavior of the LWSCC beams was studied in Series I by testing two sand-coated GFRP beams (LS-GS-3#5 and LS-GS-2#5) and two helically grooved GFRP beams (LS-GH-3#5 and LS-GH-2#5), and in Series II by testing sand-coated BFRP beam (LS-BS-2#6) and helically grooved GFRP beam (LS-BH-3#5). The influence of the amount of reinforcement on the cracking behavior of the LWSCC beams was studied by testing four specimens reinforced with No. 6 and No. 5 sand-coated GFRP bars with reinforcement amounts of 2.52%, 1.78%, 1.18%, and 0.78%; two specimens reinforced with No. 5 helically grooved GFRP bars with reinforcement amounts of 1.18% and 0.78%; three specimens reinforced with No. 6 sand-coated BFRP bars with reinforcement amounts of 2.52%, 1.78%, and 1.18%; and three specimens reinforced with No. 5 helically grooved BFRP bars with reinforcement amounts of 1.65%, 1.18%, and 0.78%. Table 7.3 provides the test matrix and reinforcement details of the test beams.

Table 7.3 – Test matrix and details of test specimens

Series	Beam ID	f'_c (MPa)	Flexural Reinforcement				Beam Details
			Reinforcing Material	Amount of Reinforcement	ρ_f (%)	E_rA_r, N × 10^6	
I	LS-GS-4#6	43.0	GFRP (Sand-coated)	4#6	2.52	73.20	Sec 1-1
	LS-GS-3#6	43.8	GFRP (Sand-coated)	3#6	1.78	54.90	Sec 2-2
	LS-GS-3#5	43.8	GFRP (Sand-coated)	3#5	1.18	39.00	Sec 5-5
	LS-GS-2#5	43.8	GFRP (Sand-coated)	2#5	0.78	26.00	Sec 6-6
	LS-GH-3#5	43.0	GFRP (Helically grooved)	3#5	1.18	35.50	Sec 5-5
	LS-GH-2#5	43.0	GFRP (Helically grooved)	2#5	0.78	23.70	Sec 6-6
II	LS-BS-4#6	42.0	BFRP (Sand-coated)	4#6	2.52	72.50	Sec 1-1
	LS-BS-3#6	42.0	BFRP (Sand-coated)	3#6	1.78	54.45	Sec 2-2
	LS-BS-2#6	42.0	BFRP (Sand-coated)	2#6	1.18	36.30	Sec 3-3
	LS-BH-4#5	43.0	BFRP (Helically grooved)	4#5	1.65	51.60	Sec 4-4
	LS-BH-3#5	43.0	BFRP (Helically grooved)	3#5	1.18	38.70	Sec 5-5
	LS-BH-2#5	42.0	BFRP (Helically grooved)	2#5	0.78	25.80	Sec 6-6
III	N-GS-3#5	41.3	GFRP (Sand-coated)	3#5	1.18	39.00	Sec 5-5
IV	N-BS-2#6	41.3	BFRP (Sand-coated)	2#6	1.18	36.30	Sec 3-3
	N-BH-3#5	41.3	BFRP (Helically grooved)	3#5	1.18	38.70	Sec 5-5

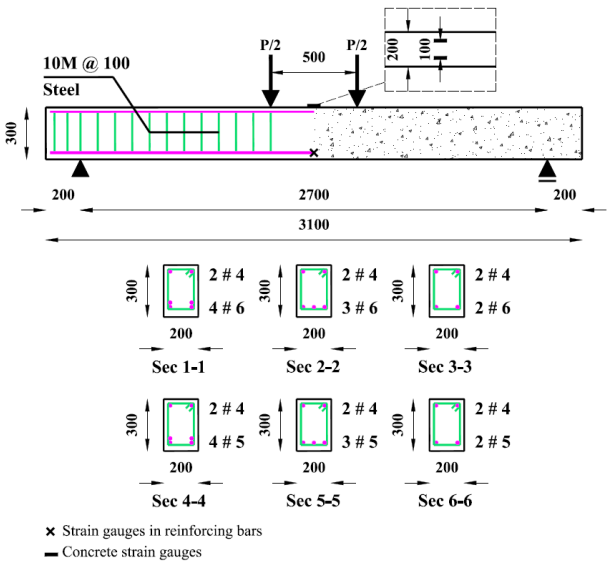

Figure 7.2– Dimensions, reinforcement details, and instrumentation of the specimens (dimensions in mm).

7.3.3 Specimen Fabrication Details

Figure 7.3 presents the fabrication of the GFRP and BFRP cages for the various specimen configurations. All beams were prepared for casting in wooden molds. The clear bottom cover

was 38 mm for No. 5 bars and 50 mm for No. 6 bars, which was determined according to Annex S in CSA S806-12. The reinforcement cages were trimmed 20 mm from each end to fit into the 3,100 mm long forms. The LWSCC and NWC beams were cast and covered after one hour with wet burlap and plastic sheeting for curing. The LWSCC and NWC cylinders were cast and cured under the same conditions as the beams.

Figure 7.3– Fabrication of the of the GFRP and BFRP cages

7.3.4 Instrumentation and Test Setup

The beams were instrumented with two electrical strain gauges with a gauge length of 6 mm at mid-span to measure reinforcement strain. Two electric strain gauges with a gauge length of 60 mm were bonded to the compression surface of each specimen to measure the compressive concrete strains. Epoxy was used to attach the strain gauges to the compression beam surface after it was cleaned. Moreover, three high-accuracy linear variable differential transformers (LVDTs) were placed at the position of the first three flexural cracks to measure the crack widths. Figure 7.2 illustrates the instrumentation details of the test beams. The specimens were stored for two to three months outdoors before being brought back into the laboratory for testing. Prior to testing, all specimens were painted and marked with 100 × 100 mm grid lines to help in observing crack propagation during testing. The beams were subjected to four-point flexural testing on a clear span length of 2,700 mm. The beams were supported by two steel plates measuring 150 mm in width set on hinged and roller supports. The vertical load was applied with a 1,000 kN hydraulic actuator through a steel spreader beam at a stroke-controlled rate of 0.6 mm/min. This rigid steel beam was used to transfer two equal concentrated loads to the specimen. Figure 7.4 shows the details of the test setup. The applied load, strain gauges, and LVDTs readings were automatically recorded during the test on a 20-channel computer data-acquisition system and stored on a personal computer.

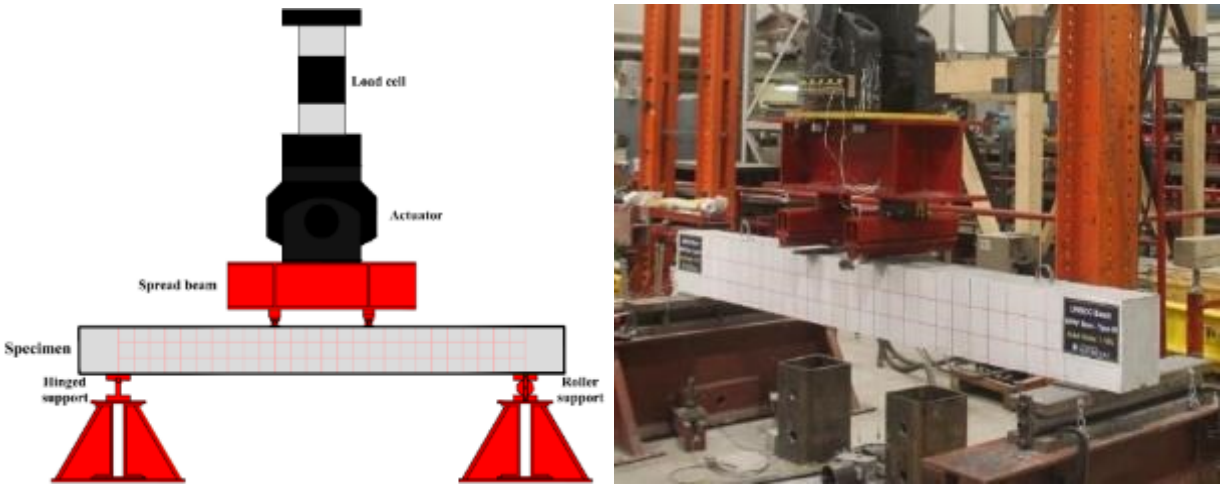

Figure 7.4– Overview of the test setup.

7.4 Test Results and Discussion

7.4.1 Definition of Service Load Level

Since FRP reinforcement is noncorroding, the flexural crack-width limits specified in the FRP-RC design standards are more relaxed than those for steel-RC members. In this investigation, four load levels were defined to estimate the moment at service condition. CSA S6-19 defines the moment at service condition as the moment that corresponds to a crack-width limit of 0.5 for elements subject to aggressive environments (exterior exposure) and 0.7 mm for other elements (interior exposure). ISIS-07 recommends a strain limit of 2,000 $\mu\varepsilon$ for the strain in FRP reinforcement to control crack width. This strain limit of 2,000 $\mu\varepsilon$ was obtained through comparison with the service limit for steel. The allowable strain in steel reinforcement at service condition is equal to 1,200 $\mu\varepsilon$ with a corresponding crack width of 0.3 mm, while the crack width for FRP-RC members was limited to 0.5 mm. Therefore, the allowable strain of 1,200 $\mu\varepsilon$ was modified by the ratio between the crack widths of FRP- and steel-RC members (0.5/0.3 = 1.67), which yielded 1,200×1.67 = 2,000 $\mu\varepsilon$. Several researchers (El-Nemr et al. 2013, 2016; Maranan et al 2015) have used this strain limit to control crack width of FRP-RC structural members. On the other hand, Bischoff et al. (2009) suggested that 30% of the nominal flexural capacity ($0.30M_n$) is a reasonable limit for the service load of FRP-RC elements.

7.4.2 First Cracking Moment

The load at which the first flexural crack occurred was observed and recorded during testing for all specimens. Table 7.4 provides the experimental results for cracking moments at the first flexural crack for each tested beam. The experimental cracking moment ($M_{cr\text{-}exp}$) of the FRP-LWSCC specimens ranged between 7.0 and 9.5 kN.m with an average value of 8.2 kN.m compared to 10.3 kN.m for the FRP-reinforced NWC (FRP-NWC) specimens. The cracking moment (M_{cr}) was estimated with the following equation

$$M_{cr} = \frac{f_r \times I_g}{y_t} \tag{7.1}$$

where I_g is the gross moment of inertia (mm^4); y_t is the distance from the centroidal axis to the extreme tension layer of the gross section (mm); and f_r is the concrete tensile strength, taken as $f_r = 0.62\lambda\sqrt{f_c'}$ for ACI 440.1R-15 and $f_r = 0.6\lambda\sqrt{f_c'}$ for CSA S806-12. For LWC in which the fine aggregate (FA) is a combination of LWA and NS, ACI 318-19 specifies that the concrete density reduction factor (λ) is a linear interpolation from 0.75 to 0.85 based on the absolute volume of NS as a fraction of the total absolute volume of FA. CSA S806-12 specifies that λ = 1.0, 0.85, and 0.75 for normal-density concrete, structural semi-low density concrete in which all the FA is NS, and structural low-density concrete in which none of the FA is NS, respectively. In this study, the value of λ was taken to be equal to 0.8 and 0.75 in estimating the predicted cracking moment according to ACI 440.1R-15 and CSA S806-12 provisions, respectively.

Table 7.4 – Experimental cracking and ultimate moments

Beam ID	Experimental			M_{nor}
	M_{cr} (kN.m)	M_n (kN.m)	Failure mode [a]	
LS-GS-4#6	9.5	85.5	CC	0.196
LS-GS-3#6	8.0	89.0	CC	0.176
LS-GS-3#5	9.0	81.0	CC	0.143
LS-GS-2#5	8.5	67.5	CC	0.119
LS-GH-3#5	8.0	78.0	CC	0.141
LS-GH-2#5	7.0	65.5	CC	0.118
LS-BS-4#6	8.2	87.0	CC	0.203
LS-BS-3#6	8.5	85.5	CC	0.176
LS-BS-2#6	8.0	73.0	CC	0.150
LS-BH-4#5	8.5	87.0	CC	0.174
LS-BH-3#5	8.0	85.0	CC	0.153
LS-BH-2#5	7.5	73.5	CC	0.136
N-GS-3#5	11.0	81.5	CC	0.153
N-BS-2#6	10.3	80.0	CC	0.168
N-BH-3#5	9.5	91.0	CC	0.171

[a] CC = crushing of concrete.

Figures 7.5a and b show the relationship between the $M_{cr\text{-}exp}$ and the corresponding predicted values ($M_{cr\text{-}pred}$) at the first flexural crack for the LWSCC specimens. As shown, the ACI 440.1R-15 equation overestimated the cracking moment of the FRP-LWSCC beam specimens, as the average value of the $M_{cr\text{-}exp}/M_{cr\text{-}pred}$ is 0.80 with a standard deviation and coefficient of variation equal to 0.06 and 7.35%, respectively. On the other hand, using λ = 0.75 in the CSA S806-12 equation provided more accurate predictions for the cracking moment of the LWSCC beams. The average value of the $M_{cr\text{-}exp}/M_{cr\text{-}pred}$ is 0.88 with a standard deviation and coefficient of variation equal to 0.06 and 7.25%, respectively. El-Nemr et al. (2013) reported a similar observation for GFRP-NWC beam specimens where the $M_{cr\text{-}exp}$ was lower than the $M_{cr\text{-}pred}$.

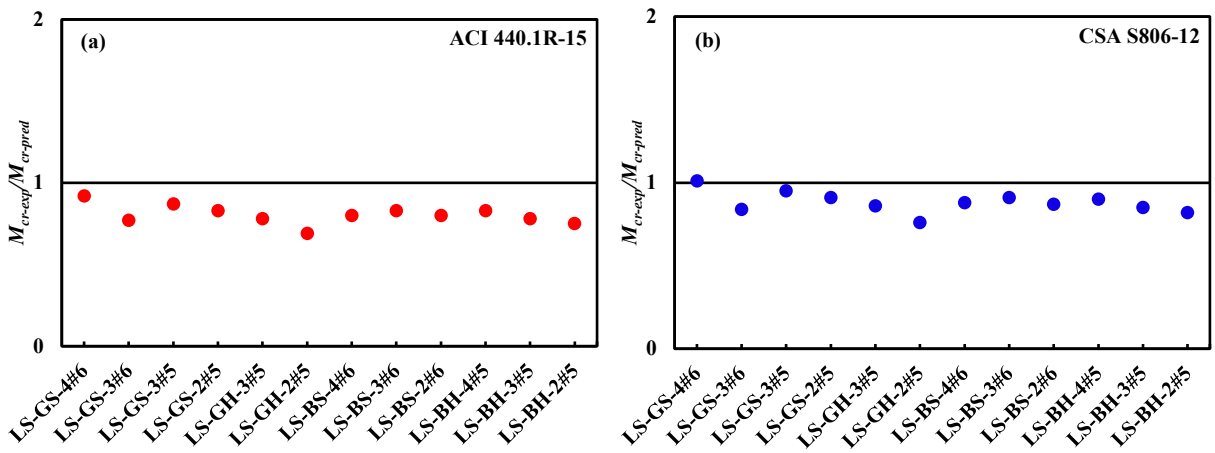

Figure 7.5– Comparison between $M_{cr-exp}/M_{cr-pred}$ for the LWSCC specimens according to: (a) ACI 440.1R-15; (b) CSA S806-12.

7.4.3 Crack Propagation, Flexural Capacity, and Mode of Failure

Figure 7.6 presents the crack patterns and failure modes of the test specimens. Few vertical cracks were observed within the pure bending region where shear stress is zero and pure bending (flexural) stress is highest. As more load was applied, these cracks became wider and propagated progressively vertically, while new cracks appeared in the flexural span and along the specimens' shear span. With further loading, the inclined cracks formed along the shear span propagated towards the two loading points. Table 7.4 presents the failure mode for each specimen in the experimental program. The LWSCC and NWC specimens reinforced with GFRP and BFRP bars clearly failed in flexure mode by concrete compression between the two loading points, regardless of the amount of reinforcement and concrete density. ACI 440.1R-15 and CSA S806-12 recommend this failure mode for FRP-RC members since it is more gradual, less brittle, and less catastrophic than the tensile rupture of FRP bars. The same failure sequence with GFRP- and BFRP-NWC members has been reported in past studies (Elgabbas et al. 2016; El-Nemr et al. 2016).

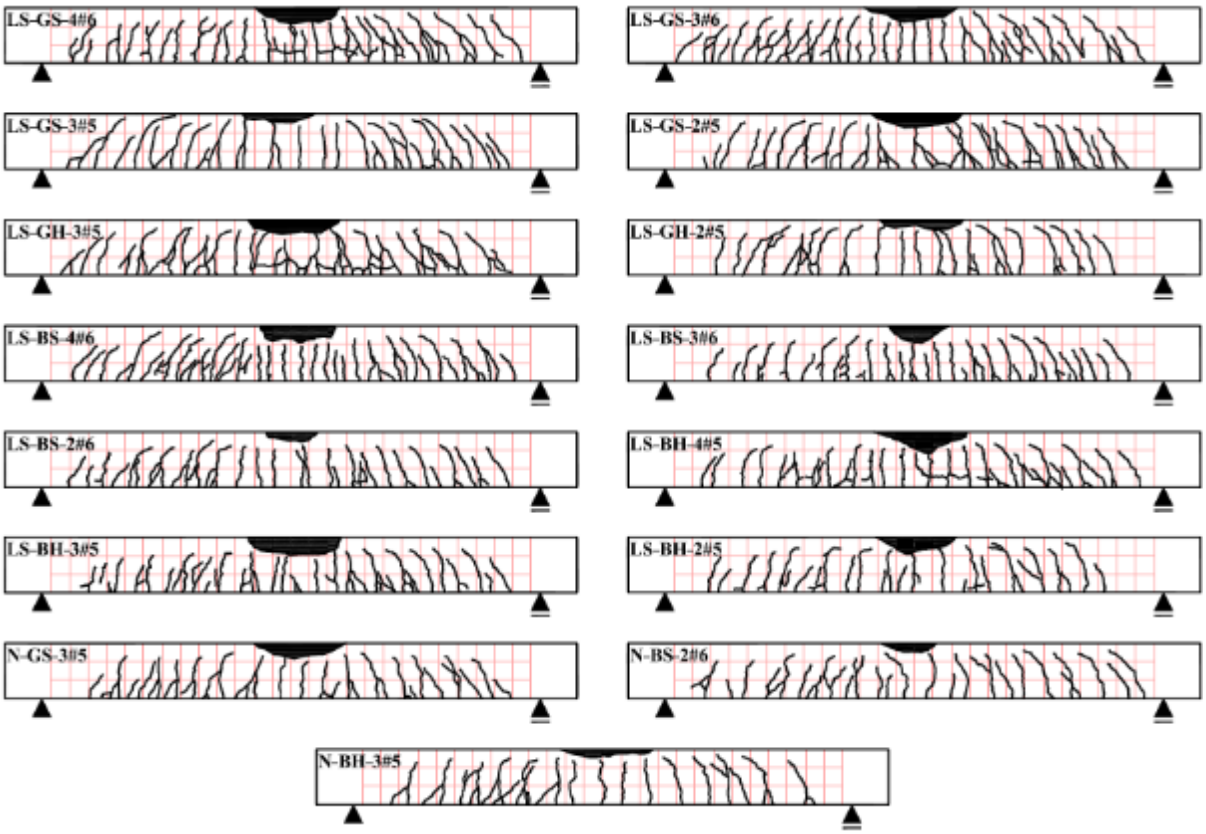

Figure 7.6– Crack pattern and failure modes of the tested beams.

Table 7.4 also provides the influence of the amount of FRP-bar reinforcement on the normalized moment capacity (M_{nor}) of the LWSCC beams**.** As can be seen, the M_{nor} increased when the amount of reinforcement of GFRP bars was increased, with respect to the surface condition. In other words, increasing the sand-coated GFRP reinforcement ratio by 50%, 130%, and 220% (from 0.78% in LS-GS-2#5 to 1.18%, 1.78%, and 2.52%) increased the M_{nor} of specimens LS-GS-3#5, LS-GS-3#6, and LS-GS-4#6 by 20%, 50%, and 65%, respectively. Similarly, the increase in M_{nor} for the LWSCC specimens reinforced with helically grooved GFRP bars (LS-GH-2#5 and LS-GH-3#5) was 20% for an approximately 50% increase in the helically grooved GFRP reinforcement ratio from 0.78% to 1.18%. The same behavior was observed for LWSCC specimens reinforced with the BFRP bars. In that case, the increase in the M_{nor} for the LWSCC specimens reinforced with the helically grooved BFRP bars (LS-BH-2#5, LS-BH-3#5, and LS-BH-4#5) was 13% and 30% for approximately 50% and 110% increases in the amount of reinforcement from 0.78% to 1.18% and 1.65%, respectively. On the other hand, the concrete density was not significantly affected by the M_{nor}. The M_{nor} of the LWSCC beams (LS-GS-3#5, LS-BS-2#6, and LS-BH-3#5) was 0.143, 0.150, and 0.153, respectively, approximately 10% less

than their NWC counterparts (N-GS-3#5, N-BS-2#6, and N-BH-3#5) with values of 0.153, 0.168, and 0.171, respectively (see Table 7.4).

7.4.4 Crack Spacing

The LWSCC beams with a higher amount of reinforcement—regardless of the FRP reinforcement type—experienced a higher number of flexural cracks. Figure 7.6 reveals that increasing the amount of reinforcement in the GFRP- and BFRP-LWSCC beams increased the total number of cracks that formed between the two loading points and, therefore, decreased the crack spacing. In other words, increasing the amount of reinforcement by 40% (from 1.78% in LS-GS-3#6 to 2.52% in LS-GS-4#6) decreased the average crack spacing by 7%. Similarly, the average crack spacing in beam LS-BS-4#6 (ρ_f of 2.52%) was approximately 11% and 37% narrower than the average crack spacing observed in beams LS-BS-3#6 (ρ_f of 1.78%) and LS-BS-2#6 (ρ_f of 1.18%), respectively. The same behavior was observed with the helically grooved GFRP and BFRP reinforcement. In addition, it should be mentioned that the average crack spacing was affected by the surface conditions of the GFRP and BFRP bars. For instance, the average crack spacing in sand-coated GFRP beam LS-GS-3#5 was approximately 7% narrower than the average crack spacing observed in helically grooved GFRP beam LS-GH-3#5 with the same amount of reinforcement (ρ_f of 1.8%). This could be attributed to the fact that the sand-coated FRP bars bonded better with the concrete than the helically grooved FRP bars. Moreover, the LWSCC beams had larger average crack spacing than the NWC beams with the same amount of reinforcement. For instance, the average crack spacing for the LWSCC beam (LS-GS-3#5) was 5% greater than that observed for the similar NWC beam (N-GS-3#5) with the ρ_f of 1.18%. This can be attributed to the brittle nature of the porous LWA in LWSCC compared to gravel aggregate in the NWC.

7.4.5 Moment-Strain Relationship

Figures 7.7a, b, and c illustrate a typical behavior of the measured tensile strains versus the applied moment. All the beams initially behaved similarly and exhibited linear moment–strain behavior prior to cracking regardless of reinforcement type or ratio. At the appearance of the first crack, a sharp increase in bar strain (from 800 to 1,600 μ_ε) was observed in all the beams. After cracking occurred, the specimens showed nearly linear behavior up to failure with reduced slope. As shown in the figures, the bar strains were significantly affected by the axial stiffness of the FRP reinforcement ($E_f A_f$). As show in Figures 7.7a and b for LWSCC specimens, beams

LS-GS-4#6 ($E_f A_f$ = 73,200 kN) and LS-BS-4#6 ($E_f A_f$ = 72,500 kN)—with almost the same $E_f A_f$—had the same moment–strain relationship. Similarly, beam LS-GS-3#6 ($E_f A_f$ = 54,900 kN) had a moment–strain relationship very close to that of beam LS-BS-3#6 ($E_f A_f$ = 54,450 kN) with almost the same $E_f A_f$. In addition, beam LS-GS-3#5, with higher $E_f A_f$ of 39,000 kN, exhibited strains lower than in the beams with a similar amount of reinforcement (LS-GH-3#5 and LS-BS-2#6 with ρ_f of 1.18%) at the same load level. In conclusion, the measured bar strains decreased when the $E_f A_f$ of the FRP bars increased—regardless of the reinforcement type—at the same load level. In contrast, similar to the influence of the $E_f A_f$ of the FRP bars on the bar strain, the LWSCC beams had higher recorded tensile strains than the NWC beams. For instance, LWSCC beam LS-GS-3#5, with a density of 1,800 kg/m^3, exhibited strains higher than the NWC beam with a similar amount of reinforcement (ρ_f of 1.18%) (N-GS-3#5) at the same load level.

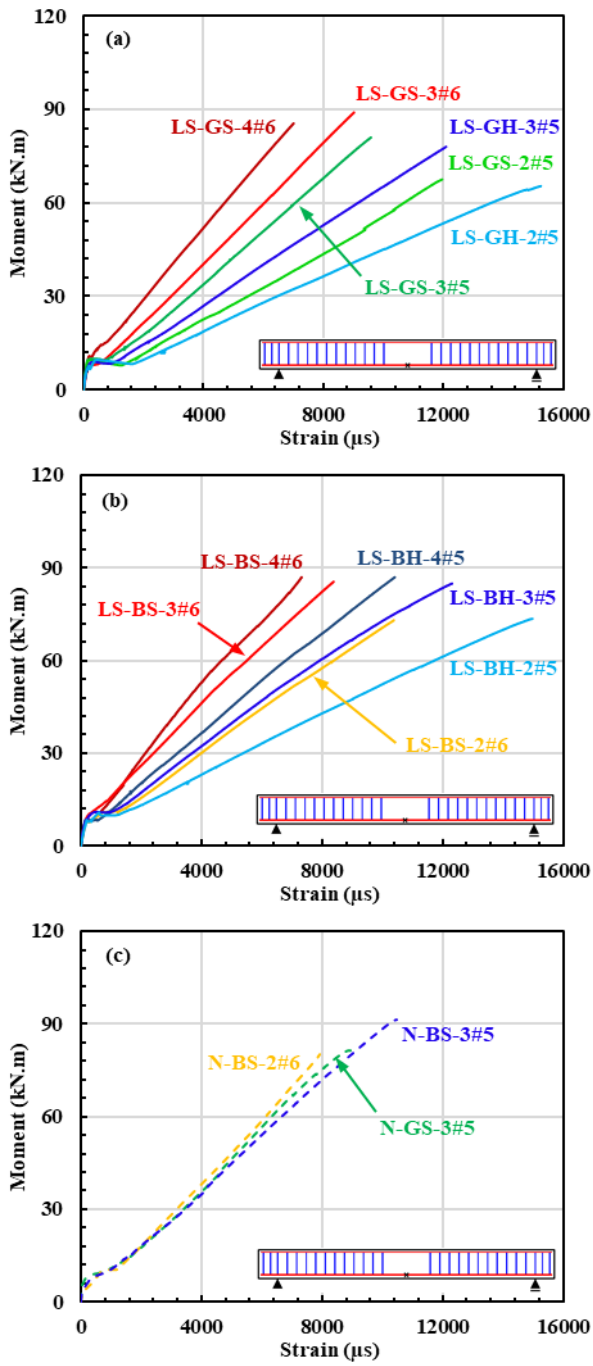

Figure 7.7– Moment-to-bar strain relationships: (a) Series I; (b) Series II; (c) Series III and IV.

7.4.6 Moment-Crack Width Relationship

Figures 7.8a, b, and c present the experimental width of the first crack at the beam center versus the applied moment. The figures show that the width of the first crack varied linearly with the applied moment up to failure. This could be attributed to the linear elastic behavior of the GFRP and BFRP bars. As shown in Figure 7.8a for the GFRP-LWSCC beams, increasing the amount of reinforcement reduced the width of the first crack at the same load level. The crack in LS-GS-

2#5 was wider than in LS-GS-3#5, LS-GS-3#6, and LS-GS-4#6 at the same load level. In addition, beam LS-GH-2#5 with helically grooved GFRP bars also had wider cracks than beam LS-GH-3#5 with the same type of bars. Similar observations were noted for the LWSCC beams reinforced with sand-coated BFRP bars (see Figure 7.8b). Moreover, beam LS-BH-3#5 showed wider crack widths than beam LS-BS-2#6, even though it had higher axial stiffness. This might be related to the fact that the sand-coated FRP bars had a better mechanical bond with the surrounding concrete than the helically grooved FRP bars. On the other hand, the measured crack widths in the LWSCC beams were greater than those of their counterparts made with NWC at the same load level (see Figure 7.8c). The reason behind that is the brittle nature of the porous LWA in the LWSCC compared to the gravel aggregate in the NWC, as reported by Gerritse (1981) for LWC. Hossain et al. (2020) reported a similar observation for LWSCC beams reinforced with steel bars compared to those made with NWC.

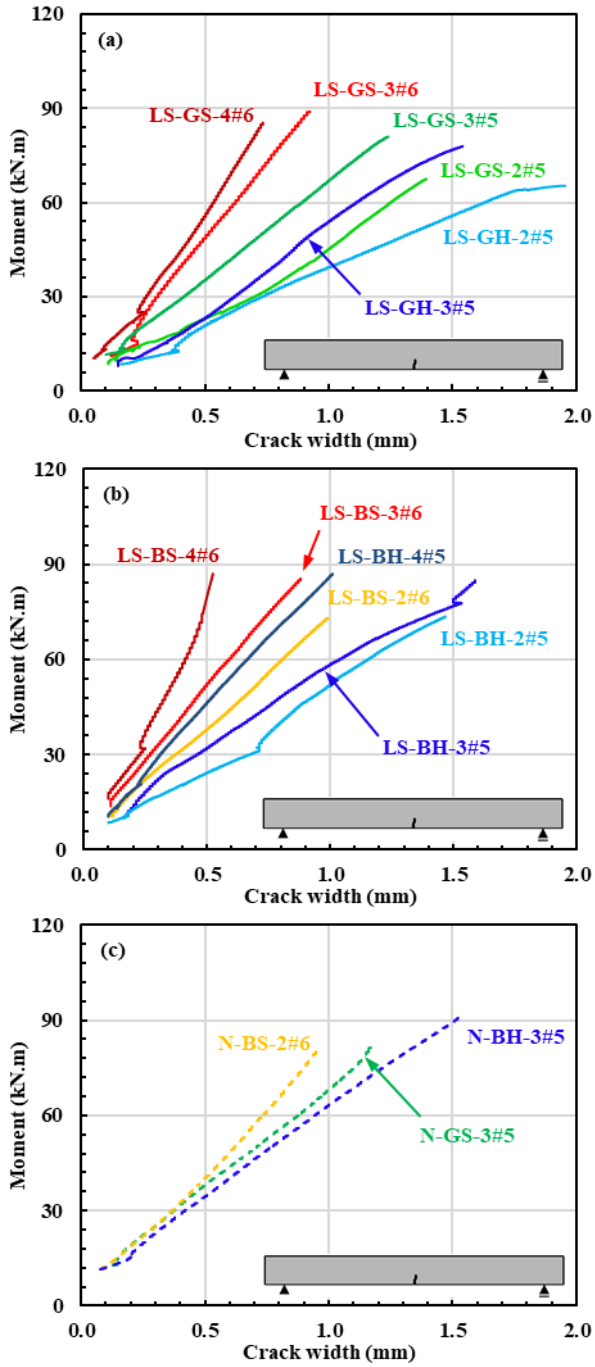

Figure 7.8– Moment-to-crack-width relationships: (a) Series I; (b) Series II; (c) Series III and IV.

7.4.7 Crack Width Prediction

This section presents the theoretical approaches used for calculating the crack-width predictions for the FRP-RC elements, including a direct procedure in which the crack width is estimated and an indirect procedure in which the maximum reinforcing-bar spacing is recommended and a comparison with the experimental results.

7.4.7.1 Crack Width Equations

CSA S6-19 specifies Eq. (7.2) to account for the crack width of flexural elements reinforced with FRP longitudinal bars as:

$$w_{cr} = 2\frac{f_f}{E_f}\frac{h_2}{h_1}k_b\sqrt{d_c^2 + (s/2)^2} \tag{7.2}$$

where h_2 is the distance from the neutral axis to the tension face of the concrete (mm); h_1 is the distance from the neutral axis to the center of the tension bars (mm); and d_c is the distance from the center of the tension bars to the tension face of the concrete (mm). The k_b shall be determined with the test method in CSA S806-12. In the absence of experimental data for k_b, CSA S6-19 recommends a k_b of 0.8 and 1.0 for sand-coated and deformed FRP bars, respectively.

ACI 440.1R-15 specifies an indirect procedure that controls crack width with a maximum bar spacing based on the approach proposed by Ospina and Bakis (2007):

$$s_{\max} = 1.15\frac{E_f}{f_{fs}}\frac{w}{k_b} - 2.5c_c \le 0.92\frac{E_f}{f_{fs}}\frac{w}{k_b} \tag{7.3}$$

where s_{max} is the maximum allowable bar spacing for flexural-crack control (mm); E_f is the modulus of elasticity of the FRP reinforcement (MPa); f_{fs} is the stress level induced in the FRP at service loads (MPa); w is the maximum permissible crack width (mm); and c_c is the clear concrete cover (mm). The k_b is the bond-dependent coefficient, which calculates the bond between the FRP bars and the surrounding concrete. The k_b value shall be determined experimentally, but, when experimental data is not available, ACI 440.1R-15 suggests a conservative value of 1.4 for FRP bars.

A similar equation is currently being considered for the forthcoming *Code requirements for structural concrete reinforced with glass fiber-reinforced polymer (GFRP) bars* (ACI 440X-XX) by controlling and replacing the crack width w in Eq. (7.3) with 0.71 mm to be as follows:

$$s_{\max} = \frac{0.81 \times E_f}{f_{fs}k_b} - 2.5c_c \le \frac{0.66 \times E_f}{f_{fs}k_b} \tag{7.4}$$

The draft of ACI 440X-XX design code recommended k_b values of 1.2 and 1.4 for GFRP bars with sand coating and all GFRP bars without sand coating, respectively, based on a study by

Shield et al. (2019). Recently however, the ACI 440 technical committee approved a single value of 1.35 for k_b for all types of GFRP bars (ACI 440X-XX, draft design code dated of November 2021).

AASHTO (2018) recommends an indirect procedure to control crack width based on the approach proposed by Ospina and Bakis (2007):

$$s \leq \min\left[1.15\frac{C_b E_f w}{f_{fs}} - 2.5c_c; 0.92\frac{C_b E_f w}{f_{fs}}\right] \tag{7.5}$$

where s is the average spacing of FRP bars in layer closest to tension face and C_b is the bond reduction factor that accounts for the degree of bond between FRP bars and surrounding concrete. The term C_b is introduced in the AASHTO-18 in lieu of the traditional k_b, which is equal to $1/C_b$. AASHTO-18 specifies a value of 0.83 for C_b based on test data for three GFRP bar types with different surface conditions (formed, helically wrapped, and sand-coated) (El-Nemr et al. 2013). Less conservative values of C_b may be used for some bar surface treatments. Values of 1.0 to 1.11 have experimental justification for sand-coated GFRP bars.

7.4.7.2 Predicted Crack Width to Experimental Results

The experimental crack-width values of the tested GFRP- and BFRP-LWSCC specimens were compared to the predicted values based on the crack-width equations in ACI 440.1R-15, ACI 440X-XX, AASHTO-18, and CSA S6-19. The value of k_b in ACI 440.1R-15 and ACI 440X-XX was considered in the predictions to be 1.4 and 1.35, respectively, (regardless of the type of FRP bar). On the other hand, the k_b was taken as 0.8 and 1.0 for the sand-coated and helically grooved FRP bars, respectively, as recommended in CSA S6-19. In addition, the value of C_b in AASHTO-18 was considered in the predictions as 0.83. Figure 7.9 presents the comparison of the experimental and predicted results according to ACI 440.1R-15, ACI 440X-XX, AASHTO-18, and CSA S6-19. Table 7.5 shows the average, standard deviation, and coefficient of variation for the ratios of the experimental-to-predicted crack-width values ($w_{cr\text{-}exp}/w_{cr\text{-}pred}$) at 2,000 $\mu\varepsilon$ as well as at $0.30M_n$. The results indicate that the predicted crack widths were generally higher than the experimental results at 2,000 $\mu\varepsilon$ and $0.30M_n$ in most cases. As indicated in Figure 7.9, the ACI 440.1R-15 equation overestimated the predicted crack widths of the FRP-LWSCC beams with a k_b of 1.4. The average $w_{cr\text{-}exp}/w_{cr\text{-}pred}$ was 0.67 with a coefficient of variation of 14.50% at 2,000 $\mu\varepsilon$, while, at $0.30M_n$, the average $w_{cr\text{-}exp}/w_{cr\text{-}pred}$ was 0.70 with a coefficient of variation of

19.50% (see Table 7.5). The conservative value of k_b (1.4 for all types of FRP bars, as suggested in ACI 440.1R-15) contributed to overestimating the crack-width values. Similarly, using a k_b value of 1.35, which is currently being considered for ACI 440X-XX, provided conservative predictions of the crack-width values, on average, with a $w_{cr\text{-}exp}/w_{cr\text{-}pred}$ of 0.70 with a coefficient of variation of 15.10% and 0.73 with a coefficient of variation of 19.65% at 2,000 $\mu\varepsilon$ and $0.30M_n$, respectively. The AASHTO-18 equation provided better predictions of the maximum crack-width values with a k_b of 1.2. The average value of the $w_{cr\text{-}exp}/w_{cr\text{-}pred}$ was 0.78 with a coefficient of variation of 14.20% at 2,000 $\mu\varepsilon$ and 0.82 with a coefficient of variation of 19.20% at $0.30M_n$. It should be mentioned that the equation in ACI 440X-XX is the same as the equation in AASHTO-18 when a crack width w of 0.71 mm is used. AASHTO-18, however, recommends a k_b value of 1.2, compared to a more conservative k_b value of 1.35 in ACI 440X-XX for all types of GFRP bars. In contrast, the k_b of 0.8 and 1.0 for sand-coated and helically grooved FRP bars, respectively, provided in CSA S6-19 yielded very slightly unconservative crack-width predictions of the GFRP- and BFRP-LWSCC beams. The $w_{cr\text{-}exp}/w_{cr\text{-}pred}$ ranged between 0.92 and 1.19 at 2,000 $\mu\varepsilon$ with an average of 1.04 and a coefficient of variation of 9.50%, and ranged between 0.86 and 1.40 at $0.30M_n$ with an average of 1.08 and a coefficient of variation of 17.50% (see Table 7.5).

Table 7.5 – Experimental-to-predicted crack-width ($w_{cr\text{-}exp}/ w_{cr\text{-}pred}$) for LWSCC specimens

Beam ID	$w_{cr\text{-}exp}/ w_{cr\text{-}pred}$							
	ACI 440.1R-15 k_b=1.4		ACI 440X-XX k_b=1.35		CSA S6-19 k_b= 0.8 and 1.0		AASHTO-18 C_b=0.83	
	$2000\mu_\varepsilon$	$0.30M_n$	$2000\mu_\varepsilon$	$0.30M_n$	$2000\mu_\varepsilon$	$0.30M_n$	$2000\mu_\varepsilon$	$0.30M_n$
LS-GS-4#6	0.64	0.61	0.66	0.63	1.06	1.00	0.74	0.72
LS-GS-3#6	0.68	0.68	0.71	0.71	1.07	1.06	0.79	0.81
LS-GS-3#5	0.65	0.79	0.69	0.82	1.14	1.40	0.75	0.93
LS-GS-2#5	0.63	0.74	0.65	0.76	1.10	1.31	0.73	0.86
LS-GH-3#5	0.86	0.96	0.91	1.00	1.19	1.33	1.00	1.10
LS-GH-2#5	0.65	0.87	0.67	0.91	0.92	1.24	0.75	1.02
LS-BS-4#6	0.58	0.57	0.60	0.59	0.94	0.94	0.67	0.67
LS-BS-3#6	0.64	0.55	0.67	0.57	1.00	0.88	0.74	0.64
LS-BS-2#6	0.55	0.51	0.57	0.52	0.94	0.86	0.64	0.59
LS-BH-4#5	0.69	0.72	0.71	0.75	0.97	1.00	0.80	0.84
LS-BH-3#5	0.86	0.78	0.91	0.82	1.19	1.08	1.00	0.91
LS-BH-2#5	0.65	0.63	0.68	0.65	0.94	0.90	0.77	0.73
Average	0.67	0.70	0.70	0.73	1.04	1.08	0.78	0.82
SD	0.10	0.14	0.10	0.14	0.10	0.19	0.11	0.16
COV (%)	14.50	19.50	15.10	19.65	9.50	17.50	14.20	19.20

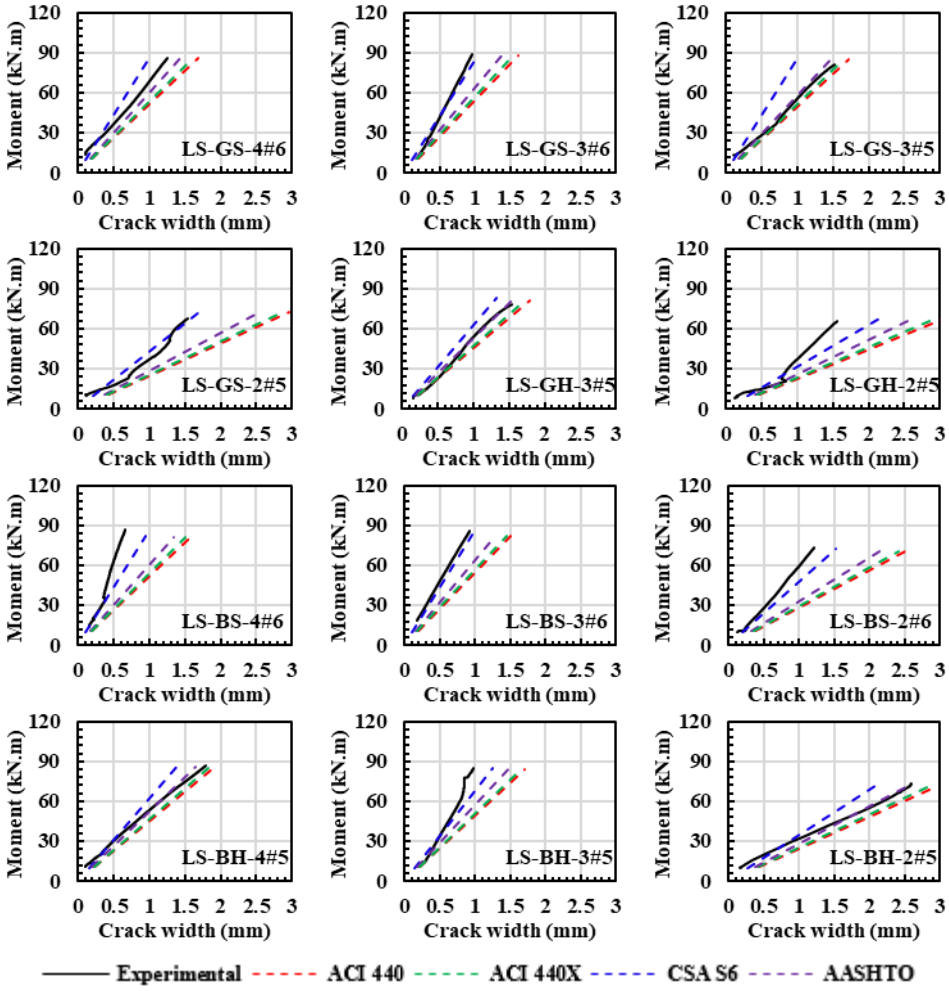

Figure 7.9– Predicted moment-to-crack-width relationships according to ACI 440.1R-15, ACI 440X-XX, AASHTO-18, and CSA S6-19 for LWSCC beams.

7.4.8 Evaluation of the Bond-Dependent Coefficient (k_b)

As discussed in the preceding section, the predicted crack-width values of the FRP-LWSCC beam specimens using the k_b values recommended in the FRP design standards and guides were overestimated in most cases. In addition, using the same k_b value for different surface conditions of FRP bars in standards was not appropriate. Therefore, in this section, the experimental results were used to evaluate the k_b values. The k_b coefficient was calculated in accordance with CSA S6-19 from Eq. (7.2). Equations (7.3), (7.4), and (7.5) in ACI 440.1R-15, ACI 440X-XX, and AASHTO-18, respectively, were also used to assess the k_b values for comparison. The k_b values were calculated at a FRP strain of 2,000 $\mu\varepsilon$, $0.30M_n$ (the service-load level suggested by Bischoff et al. (2009)), at a crack-width of 0.5 mm (the upper crack-width limit for exterior exposure provided in CSA S6-19), and at a crack-width of 0.7 mm (the upper crack-width limit for interior exposure provided in CSA S6-19). Figures 7.10 and 7.11 present the calculated k_b values for the

GFRP and BFRP bars. As shown, the k_b values calculated at the different load levels were somewhat close. Therefore, any of those load levels could be used as the recommended level when determining k_b values.

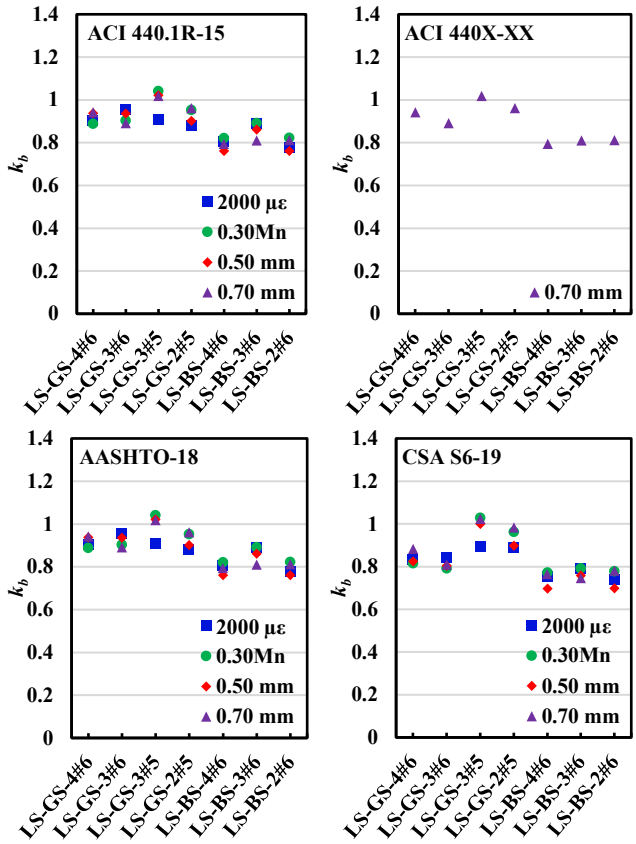

Figure 7.10– Predicted k_b values at different limits for sand-coated GFRP and BFRP bars.

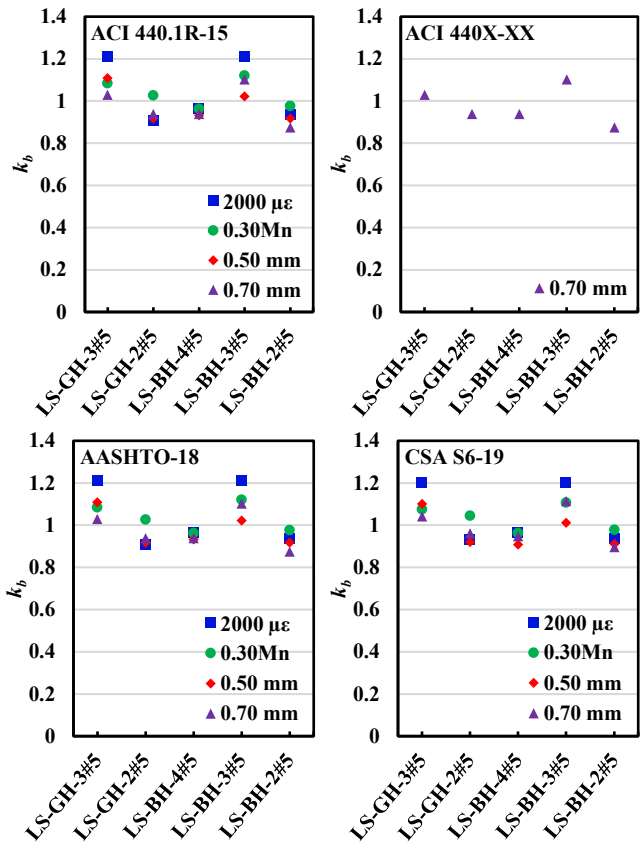

Figure 7.11– Predicted k_b values at different limits for helically grooved GFRP and BFRP bars.

Tables 7.6 and 7.7 list the average calculated k_b values for the GFRP and BFRP bars (sand-coated and helically grooved) based on the wider crack width of the first three flexural cracks in the tested beams. For the sand-coated GFRP bars, the average k_b values yielded by ACI 440.1R-15 were 0.92, 0.92, 1.0, and 0.92 for LS-GS-4#6, LS-GS-3#6, LS-GS-3#5, and LS-GS-2#5, respectively, with an overall average of 0.94, while the overall average k_b values for the same specimens calculated according to ACI 440X-XX, AASHTO-18, and CSA S6-19 were 0.95, 0.94, and 0.89, respectively. For the sand-coated BFRP bars, the average k_b values based on ACI 440.1R-15 ranged from 0.79 to 0.86, with an overall average of 0.82, whereas the overall average k_b value for the same beams determined according to ACI 440X-XX was 0.80. The average k_b values determined according to AASHTO-18 and CSA S6-19 ranged from 0.79 to 0.86, with an overall average of 0.82 and from 0.75 to 0.77, with an overall average of 0.76, respectively, for the same beam specimens. The overall average k_b values for sand-coated FRP (GFRP and BFRP) bars according to ACI 440.1R-15, ACI 440X-XX, AASHTO-18, and CSA S6-19 were 0.89 ± 0.07, 0.89 ± 0.09, 0.89 ± 0.07, and 0.84 ± 0.09, respectively (see Table 7.6). Thus, a k_b value of 0.9 seems to serve well for sand-coated FRP bars in LWSCC beams. In contrast, the overall average k_b values for the helically grooved GFRP bars were 1.03 and 0.99 according to ACI

440.1R-15 and ACI 440X-XX, respectively, whereas the overall average k_b values for the same beams determined according to AASHTO-18 and CSA S6-19 were 1.03 and 1.02, respectively. Lastly, for the helically grooved BFRP bars, the average k_b values according to ACI 440.1R-15 were 0.95, 1.11, and 0.93 for LS-BH-4#5, LS-BH-3#5, and LS-BH-2#5, respectively, with an overall average k_b of 1.0, whereas the overall average k_b value for the same beams determined with ACI 440X-XX was 0.97. The average k_b values determined according to AASHTO-18 and CSA S6-19 ranged from 0.93 to 1.11 and from 0.93 to 1.10, respectively, for the same beam specimens. The overall average k_b values for helically grooved FRP (GFRP and BFRP) bars according to ACI 440.1R-15, ACI 440X-XX, AASHTO-18, and CSA S6-19 were 1.01 ± 0.09, 0.98 ± 0.09, 1.01 ± 0.09, and 1.01 ± 0.09, respectively (see Table 7.7). Thus, a k_b value of 1.1 seems to serve well for helically grooved FRP bars in LWSCC beams. Future experimental and theoretical investigations are recommended with more measurements and calculations to evaluate and improve the current k_b values in FRP standards.

Table 7.6 – Average predicted k_b values for sand-coated GFRP and BFRP bars

Beam ID	ACI 440.1R-15	ACI 440X-XX	AASHTO-18	CSA S6-19
LS-GS-4#6	0.92	0.94	0.92	0.84
LS-GS-3#6	0.92	0.89	0.92	0.81
LS-GS-3#5	1.00	1.02	1.00	0.99
LS-GS-2#5	0.92	0.96	0.92	0.93
LS-BS-4#6	0.80	0.79	0.80	0.75
LS-BS-3#6	0.86	0.81	0.86	0.77
LS-BS-2#6	0.79	0.81	0.79	0.75
Overall Average	0.89 ± 0.07	0.89 ± 0.09	0.89 ± 0.07	0.84 ± 0.09

Note: The ACI 440X-XX equation is based on limiting crack width to 0.71 mm, Therefore, the k_b factor was calculated according to ACI 440X-XX at a crack-width of 0.7 mm only.

Table 7.7 – Average predicted k_b values for helically grooved GFRP and BFRP bars

Beam ID	ACI 440.1R-15	ACI 440X-XX	AASHTO-18	CSA S6-19
LS-GH-3#5	1.11	1.03	1.11	1.10
LS-GH-2#5	0.95	0.94	0.95	0.95
LS-BH-4#5	0.95	0.94	0.95	0.95
LS-BH-3#5	1.11	1.10	1.11	1.10
LS-BH-2#5	0.93	0.87	0.93	0.93
Overall Average	1.01 ± 0.09	0.98 ± 0.09	1.01 ± 0.09	1.01 ± 0.09

Note: The ACI 440X-XX equation is based on limiting crack width to 0.71 mm, Therefore, the k_b factor was calculated according to ACI 440X-XX at a crack-width of 0.7 mm only.

7.5 Summary and Conclusions

This paper aimed at investigating the cracking behavior of LWSCC beams reinforced with GFRP and BFRP bars and evaluating the bond-dependent coefficient (k_b) values. Fifteen RC beam specimens (200 mm wide × 300 mm high × 3,100 long), including three NWC specimens, were prepared and tested under four-point bending up to failure. Based on the experimental results and the theoretical analysis, the main findings of this investigation led to the following conclusions.

1. The experimental results show that the FRP-LWSCC beams exhibited cracking behavior similar to that of the counterpart FRP-NWC beams. The FRP-LWSCC beams, however, had a larger average crack spacing and wider crack widths than those of the NWC beams with the same amount of reinforcement.
2. The cracking moments of the FRP-LWSCC beam specimens were 20% and 12% lower, respectively, than those predicted with the ACI 440.1R-15 and CSA S806-12 equations when using λ equal to 0.8 and 0.75 in the cracking-moment equations, respectively, to consider the effect of concrete density.
3. The GFRP- and BFRP-LWSCC beams exhibited a linear crack response up to failure by concrete crushing, regardless of the amount and surface conditions of the FRP reinforcement. The ACI 440.1R-15 and CSA S806-12 provisions recommend this failure mode for FRP-RC members since it is more gradual, less brittle, and less catastrophic than the tensile rupture of FRP bars.
4. The amount and surface conditions of FRP reinforcement significantly affected the cracking behavior of the LWSCC specimens. Increasing the amount of reinforcement resulted in smaller crack widths and an increase in the total number of cracks between the two loading points and, therefore, decreased the crack spacing. In addition, the specimens reinforced with the sand-coated GFRP and BFRP bars produced smaller crack widths than those reinforced with the helically grooved GFRP and BFRP bars, respectively. This tends to confirm that GFRP and BFRP bars with a sand-coated surface have better flexural bond characteristics.
5. The ACI 440.1R-15 equation overestimated the predicted crack widths for the FRP-LWSCC beams using a k_b of 1.4. The average $w_{cr\text{-}exp}/w_{cr\text{-}pred}$ was 0.67 at 2,000 $\mu\varepsilon$, while, at $0.30M_n$, the average $w_{cr\text{-}exp}/w_{cr\text{-}pred}$ was 0.70. The conservative value of k_b (1.4 for all

types of FRP bars, as suggested in ACI 440.1R-15) attributed to overestimating the crack-width values.

6. Using a k_b value of 1.35 for the FRP bars regardless of surface conditioning—which is currently considered for ACI 440X-XX—provided conservative predictions of the crack-width values, on average, with a $w_{cr\text{-}exp}/w_{cr\text{-}pred}$ of 0.70 and 0.73 at 2,000 $\mu\varepsilon$ and at $0.30M_n$, respectively.
7. The AASHTO-18 equation provided better predictions of the maximum crack-width values, where the average value of the $w_{cr\text{-}exp}/w_{cr\text{-}pred}$ was 0.78 and 0.82 at 2,000 $\mu\varepsilon$ and $0.30M_n$, respectively. It is recommended that the ACI 440X-XX adopts the same value for the k_b as that of the AASHTO-18, i.e. 1.2.
8. The k_b of 0.8 and 1.0 for the sand-coated and helically grooved FRP bars, respectively, provided by the CSA S6-19 equation yielded very slightly unconservative crack-width predictions for the GFRP- and BFRP-LWSCC beams.
9. The k_b values calculated at a FRP strain of 2,000 $\mu\varepsilon$, at $0.30M_n$, and at crack widths of 0.5 and 0.7 mm were somewhat close for the LWSCC beams. Therefore, any of those load levels could be used as the recommended levels when calculating k_b values for LWSCC beams.
10. Based on the experimental results, there was a distinct difference in the values of k_b for the FRP bars with a sand-coated surface and FRP bars with a helically grooved surface. The overall average k_b values were close to 0.9 and 1.1 for the sand-coated and helically grooved FRP (GFRP and BFRP) bars, respectively. Thus, the k_b values of 0.9 and 1.1 are recommended for the sand-coated and helically grooved FRP bars in LWSCC beams, respectively.

CHAPTER 8

Conclusions and Recommendations

8.1 Summary

The current research aimed at investigating the shear and flexural behaviour of lightweight self-consolidating concrete (LWSCC) beams reinforced with fiber-reinforced-polymer (FRP) bars. The experimental program was completed through two phases. The first phase was conducted to investigate the behavior and concrete shear strength of FRP-reinforced LWSCC beams. 14 full-scale RC beams, including nine LWSCC beams reinforced with FRP bars, one LWSCC beam reinforced with steel bars, and four normal-weight concrete (NWC) beams reinforced with FRP bars, were tested up to failure. The beams were 3,100 mm long × 200 mm wide × 400 mm deep with a clear shear span of 1,000 mm. The second phase included testing of 20 full-scale RC beams of 3100 mm long × 200 mm wide × 300 mm deep to investigate the flexural behavior and serviceability performance of FRP bars in LWSCC beams. The beams—including 16 LWSCC beams reinforced with various reinforcement ratios of either FRP or steel bars and four NWC beams reinforced with FRP bars as reference beams—were fabricated and tested under four-point bending up to failure. The test variables included the concrete density (LWSCC and NWC); the longitudinal reinforcement type (glass-FRP (GFRP), basalt-FRP (BFRP), and steel bars); and the longitudinal reinforcement ratio. The experimental results are discussed in terms of cracking behavior, deflection, flexural capacity, concrete shear strength, and mode of failure. The experimental results were compared to the shear and flexural capacity predictions produced with the design equations of the American Concrete Institute (ACI), and the Canadian Standards Association (CSA). The theoretical approaches used for calculating the crack width predictions for the FRP-RC elements, including direct and indirect procedures, and comparison with the experimental results. Finally, the recorded deflections and experimental values of the effective moment of inertia (I_e) were presented, analyzed and compared with those predicted using available models.

8.2 Conclusion

Based on the experimental results and the theoretical analysis, the following conclusions were drawn as follows:

8.2.1 Part I: RC Beams with GFRP and BFRP Bars without stirrups under shear loads

8.2.1.1 Experimental Results

1. Using LWSCC made it possible to fabricate beams with lower self-weight (density of 1,800 kg/m^3) than with NWC. The LWSCC beams with LWA and NS behaved similarly to the NWC beams.
2. Diagonal tension failure was the dominant failure mode of the tested LWSCC beams reinforced with GFRP and BFRP bars.
3. The experimental results show that the GFRP- and BFRP-reinforced LWSCC beams exhibited cracking behavior similar to that of the counterpart GFRP- and BFRP-reinforced NWC beams, with the exception of an earlier onset of flexural cracking.
4. Using high reinforcement ratios and/or moduli of elasticity reduced the crack width in the LWSCC beams. This increased the contribution of uncracked concrete and the interface shear by increasing the depth of compression zone, the aggregate interlock in the cracked surface, and the residual tensile stress.
5. The normalized shear strength in the beams cast with LWSCC was proportional to the GFRP longitudinal reinforcement ratio. Increasing the GFRP reinforcement ratio from 0.58% to 1.75% increased the normalized shear strength of the beams by 30%. On the other hand, increasing the GFRP longitudinal reinforcement ratio increased the number of cracks.

8.2.1.2 Theoretical Results and Design Recommendations

6. Comparing the concrete shear strengths of the LWC beams with their predicted strengths based on a concrete density reduction factor of 0.75 in the CSA S806-12 design equation revealed that this equation yielded the most accurate predictions of LWC beams reinforced with FRP bars, as the safety margin was 1.12.

7. Using a concrete density reduction factor of 0.8 in the ACI 440.1R-15 equation to consider the influence of concrete density yielded a degree of conservatism equal to that of the equation for NWC beams. ACI 440.1R-15, however, yielded the most conservative predictions for LWC and NWC beams.
8. The Hoult et al. (2008) equation provided less conservative results for LWC beams reinforced with FRP bars than did the CSA S6-19 equation. Moreover, the safety margin was 1.02 in LWC beams, indicating that the concrete density reduction factor of the shear strength for LWC beams is not required when using the Hoult et al. (2008) equation.

8.2.2 Part II: RC Beams with GFRP and BFRP Bars under flexural loads

8.2.2.1 Experimental Results

9. The tested LWSCC and NWC beams reinforced with GFRP and BFRP bars failed due to concrete crushing as they were designed as over-reinforced, while the steel-reinforced LWSCC beam failed due to steel yielding, followed by compressive failure.
10. The experimental results showed that the FRP-reinforced LWSCC beams exhibited cracking behavior similar to that of the counterpart FRP- reinforced NWC beams. The FRP-reinforced LWSCC beams, however, had a larger average crack spacing and wider crack widths than those of NWC beams with the same amount of reinforcement.
11. The normalized moment capacity was proportional to the amount of FRP reinforcement bars. Increasing the FRP reinforcement ratio from 0.78% to 3.22% increased the normalized moment capacity of the beams by 85%. In addition, the normalized moment capacity of the LWSCC beams was not significantly affected (approximately 10% less) compared to the NWC beam.
12. The amount and surface conditions of FRP reinforcement significantly affected the cracking behavior of the LWSCC specimens. Increasing the amount of reinforcement resulted in smaller crack widths and an increase in the total number of cracks between the two loading points and, therefore, decreased the cracks' spacing. In addition, the specimens reinforced with sand-coated GFRP and BFRP bars produced smaller crack widths than those reinforced with helically grooved GFRP and BFRP bars. This tends to confirm GFRP and BFRP bars with a sand-coated surface have better flexural bond characteristics.

8.2.2.2 Theoretical Results and Design Recommendations

13. The predicted moment capacities for the GFRP-LWSCC specimens using the ACI 440.1R-15 equation were in good agreement with the experimental results with an average accuracy of ≥ 90%.
14. The cracking moments of the FRP-reinforced LWSCC beam specimens were 20% and 12% lower, respectively, then those predicted with the ACI 440.1R-15 and CSA S806-12 equations when using λ equal to 0.8 and 0.75 in the cracking-moment equations, respectively, to consider the effect of concrete density.
15. The ACI 440.1R-15 equation overestimated the predicted crack widths for the GFRP- and BFRP-reinforced LWSCC beams compared to the experimental crack width values, where the average value of the $w_{cr\text{-}exp}/w_{cr\text{-}pred}$ was 0.67 and 0.70 at 2,000 με and $0.30M_n$, respectively. Similarly, the ISIS-07 provided conservative predictions of the crack width values, on average, with a $w_{cr\text{-}exp}/w_{cr\text{-}pred}$ of 0.68 and 0.70 at 2,000 με and at $0.30M_n$, respectively.
16. The AASHTO-18 yielded good yet conservative predictions of the maximum crack width values, where the average value of the $w_{cr\text{-}exp}/w_{cr\text{-}pred}$ was 0.78 and 0.82 at 2,000 με and $0.30M_n$, respectively. On the other hand, the k_b of 0.8 and 1.0 for sand-coated and helically grooved FRP bars, respectively, provided by the CSA S6-19 yielded very slightly unconservative crack width predictions of the GFRP- and BFRP-reinforced LWSCC beams.
17. The k_b values calculated at a FRP strain of 2,000 με, at $0.30M_n$, and at crack-widths of 0.5 and 0.7 mm were somewhat close for LWSCC beams. Therefore, any of those load levels can be used as the recommended levels when calculating k_b values for LWSCC beams. Furthermore, the crack widths at 2,000 με and $0.30M_n$ were less than 0.7 mm in all the beam specimens, which satisfies the requirements of CSA S806-12 of keeping 0.7 mm as the maximum crack width in calculating k_b values.
18. The ACI 440.1R-15 and ISIS-07 provide conservative k_b values of 1.4 and 1.2, respectively, for FRP bars regardless of the surface condition.
19. The average k_b values were close to 0.90 and 1.10 for the sand-coated FRP (GFRP and BFRP) and helically grooved FRP (GFRP and BFRP) bars, respectively. Thus, the k_b values of 0.90 and 1.10 seem to serve well for the sand-coated and helically grooved FRP bars in LWSCC beams, respectively.

20. The ACI 440.1R-15 underestimated the predicted deflections of the BFRP-reinforced LWSCC beams at both $0.30M_n$ and $0.67M_n$, with an average $\delta_{exp}/\delta_{pred}$ of 1.26 and 1.11, respectively. In contrast, CSA S806-12 provided reasonable predictions at $0.30M_n$ and $0.67M_n$, where the average $\delta_{exp}/\delta_{pred}$ was 0.95 and 1.04, respectively.
21. The ACI 440.1R-15 model overestimated I_e for the GFRP-reinforced LWSCC beams and therefore, underestimated the deflections at $0.30M_n$ and $0.67M_n$, with average $\delta_{exp}/\delta_{pred}$ of 1.31 and 1.26, respectively. The Bischoff and Benmokrane et al. models' predictions were lower than the predictions of the ACI 440.1R-15 model at $0.30M_n$ and $0.67M_n$, with the average $\delta_{exp}/\delta_{pred}$ of 1.17 and 1.25, respectively, at $0.30M_n$ and 1.22 and 1.23 at $0.67M_n$. The ISIS Canada Research Network model, however, provided better predictions at $0.30M_n$ and $0.67M_n$, with the average $\delta_{exp}/\delta_{pred}$ of 1.06 and 1.19, respectively.
22. The CSA S806-12 model provided closer predictions of the deflection for the GFRP-reinforced LWSCC beams at $0.30M_n$ and overestimated the deflection at $0.67M_n$, with average $\delta_{exp}/\delta_{pred}$ of 1.04 and 1.18, respectively.
23. Based on the experimental results, a modified ACI 440.1R-15 model was suggested using $0.67M_{cr}$ instead of M_{cr} to predict the actual deflection of the LWSCC specimens.

8.3 Recommendations for Future Work

Results of the current research represent a promising step toward using FRP bars as flexural reinforcement in LWSCC members. The information presented improves understanding of how LWSCC beams reinforced with FRP bars can be expected to behave. However, additional research on LWSCC members is recommended based on the findings of the current study to cover the following points:

1. Investigate the shear strength of different types of LWC members reinforced with FRP bars with and without stirrups.
2. An additional experimental investigation should be conducted to examine the impact of different types of FRP reinforcement and different *a/d* ratios of slender and deep beams on shear strength of LWC members.
3. Investigate the flexural behavior and serviceability performance of FRP-reinforced LWSCC beams using different types of LWC.

4. The bond-dependent coefficient (k_b) values were investigated in this research for FRP-reinforced LWSCC beams. Experimental and theoretical investigations, however, are recommended with more measurements and calculations to evaluate and improve the current k_b values adopted in FRP standards.
5. Performance of FRP-reinforced LWSCC members subjected to fatigue and cyclic loads at service conditions should be investigated
6. Investigate the performance of prestressed LWSCC members reinforced with FRP tendons.

French version of this section is presented below:

8.4 Sommaire

La recherche actuelle visait à étudier le comportement à l'effort tranchant et en flexion des poutres en béton autoplaçant (BAP) léger armé de barres en polymère renforcé de fibres (PRF). Le programme expérimental s'est déroulé en deux phases. La première phase a été menée pour étudier le comportement et la résistance à l'effort tranchant de poutres en BAP léger FRP. Quatorze (14) poutres en béton armé grandeur nature, dont neuf poutres en BAP léger armé de barres en PRF, une poutre en BAP léger armé d'acier et quatre poutres en béton normal (BN) armé de barres de PRF, ont été testées jusqu'à la rupture. Les poutres mesuraient 3 100 mm de long × 200 mm de large × 400 mm de profondeur avec une portée de cisaillement libre de 1 000 mm. La deuxième phase comprenait des tests de 20 poutres en BAP léger armé à grande échelle de 3100 mm de long × 200 mm de large × 300 mm de profondeur pour étudier le comportement en flexion et les performances de service des barres en PRF dans des poutres en BAP léger. Seize (16) poutres en BAP léger armé avec divers taux d'armature en PRF (PRF en fibre de verre -PRFV- et PRF en fibre de basalte -PRFB-) ou de barres d'acier et quatre poutres en béton normal (BN) armé de barres de PRF comme poutres de référence - ont été fabriquées et testées sous des charges de flexion. Les variables d'essai comprenaient la densité du béton (BAP léger et BN) ; le type d'armature longitudinale (PRFV -fibre de verre), PRFB – fibre de basalte et barres d'acier); et le taux d'armature longitudinale. Les résultats expérimentaux sont discutés en termes de comportement à la fissuration, de flèche, de résistance à la flexion, de résistance à l'effort tranchant et du mode de rupture. Les résultats expérimentaux portant sur la résistance à l'effort tranchant et a ; a flexion ont été comparés aux prévisions des équations de calcul des normes de

conception l'American Concrete Institute (ACI) et de l'Association canadienne de normalisation (CSA). Des approches théoriques ont été utilisées pour calculer la largeur de fissure pour les éléments en béton armé de PRF, y compris les procédures directes et indirectes, incluant une comparaison avec les résultats expérimentaux. Enfin, les flèches mesurées et les valeurs expérimentales du moment d'inertie effectif (Ie) ont été analysées et comparées à celles prédites à l'aide des modèles disponibles.

8.5 Conclusions

8.5.1 Phase I : Poutres en béton armé avec des barres en PRFV et barres en PRFB sans étriers soumises à l'effort tranchant

8.5.1.1 Résultats expérimentaux

1. L'utilisation du BAP léger a permis de fabriquer des poutres avec un poids propre plus bas (densité de 1 800 kg/m3) comparativement au béton normal (BN). Les poutres en BAP léger et en BN ont eu un comportement similaire.
2. La rupture par traction diagonale était le mode de rupture dominant des poutres en BAP léger armé de PRFV ou de PRFB.
3. Les résultats expérimentaux montrent que les poutres en BAP léger armé en PRFV et PRFB présentaient un comportement de fissuration similaire à celui des poutres homologues en BN armé de PRFV ou de PRFB, à l'exception d'un début plus précoce de fissuration par flexion.
4. L'utilisation de taux d'armature et/ou de modules d'élasticité élevés a réduit la largeur des fissures dans les poutres en BAP léger. Cela a augmenté la contribution du béton non fissuré et la résistance à l'effort tranchant en augmentant la profondeur de la zone du béton comprimé (zone de compression), l'imbrication des granulats dans la surface fissurée et la contrainte de traction résiduelle.
5. La résistance à l'effort tranchant normalisée dans les poutres coulées avec BAP léger était proportionnelle au taux d'armature longitudinal en PRFV. L'augmentation du taux d'armature du PRFV de 0,58 % à 1,75 % a augmenté la résistance à l'effort tranchant normalisée des poutres de 30 %. D'autre part, l'augmentation du taux d'armature longitudinal en PRFV a augmenté le nombre de fissures.

8.5.1.2 Résultats théoriques et recommandations de conception

6. La comparaison des résistances à l'effort tranchant des poutres en BAP léger avec leurs résistances calculées sur la base d'un facteur de réduction de la densité du béton de 0,75 dans l'équation de conception CSA S806-12 a révélé que cette équation résulte en des prédictions plus précises pour les poutres en BAL léger armé de PRF, avec une marge de sécurité de 1,12.
7. L'utilisation d'un facteur de réduction de la densité du béton de 0,8 dans l'équation ACI 440.1R-15 pour considérer l'influence de la densité du béton a résulté en une prédiction sécuritaire et comparable à celle obtenue pour les poutres en BN armé de PRF. Cependant, l'ACI 440.1R-15 a donné les prévisions les plus sécuritaires pour les pour les poutres en BAP léger et BN.
8. L'équation de Hoult et al. (2008) a fourni des résultats moins sécuritaires pour les poutres en BAP léger armé de PRF que l'équation du CSA S6-19. De plus, la marge de sécurité était de 1,02 dans les poutres en BAP léger, indiquant que le facteur de réduction de la densité du béton pour la résistance à l'effort tranchant pour les poutres en BAP léger n'est pas requis lors de l'utilisation de l'équation de Hoult et al. (2008).

8.5.2 Phase II : Poutres en béton armé avec des barres en PRFV et PRFB sous charges de flexion

8.5.2.1 Résultats expérimentaux

9. Les poutres en BAP léger et BN armé de barres en PRFV et PRFB ont rompu par écrasement du béton car elles ont été conçues comme étant surarmées, tandis que la poutre en BAP léger armé d'acier a rompu par plastification de l'acier, suivie d'une rupture par écrasement du béton.
10. Les résultats expérimentaux ont montré que les poutres en BAP léger armé de PRF présentaient un comportement à la fissuration similaire à celui des poutres homologues en BN armé de PRF. Les poutres en BAP léger armé de PRF ont montré cependant un espacement moyen des fissures plus grand et des largeurs de fissures plus larges que celles des poutres en BN avec la même quantité d'armature.
11. La résistance en flexion normalisée était proportionnelle à la quantité de barres d'armature en PRF. L'augmentation du taux d'armature en PRF de 0,78 % à 3,22 % a

augmenté la la résistance en flexion normalisée des poutres de 85 %. De plus, la résistance en flexion normalisée des poutres en BAP léger n'a pas été affectée de manière significative (environ 10 % de moins) par rapport à la poutre en BN.

12. La quantité et les conditions de surface de l'armature en PRF ont affecté de manière significative le comportement à la fissuration des poutres en BAP léger. L'augmentation du taux d'armature a conduit à des largeurs de fissures plus petites et une augmentation du nombre total de fissures entre les deux points de chargement et, par conséquent, une diminution de l'espacement des fissures. De plus, les poutres avec des barres en PRFV ou des barres en PRFB saupoudrées de sable ont montré des largeurs de fissures plus petites que celles des poutres en béton armé avec des barres en PRFV ou en PRFB à rainures hélicoïdales. Cela tend à confirmer que les barres en PRFV ou des barres en PRFB saupoudrées de sable ont de meilleures caractéristiques d'adhérence en flexion.

8.5.2.2 Résultats théoriques et recommandations de conception

13. Les capacités de moment prédites pour les échantillons GFRP-LWSCC en utilisant l'équation ACI 440.1R-15 étaient en bon accord avec les résultats expérimentaux avec une précision moyenne ≥ 90 %.

14. Les moments de fissuration des poutres en BAP léger armé de barres en PRF étaient respectivement de 20 % et 12 % inférieurs à ceux prédits avec les équations de l'ACI 440.1R-15 et CSA S806-12 en utilisant λ égal à 0,8 et 0,75, respectivement, pour considérer l'effet de la densité du béton.

15. L'ACI 440.1R-15 a surestimé les largeurs de fissure prédites pour les poutres en BAP léger armé de PRFV ou de PRFB par rapport aux valeurs expérimentales de largeur de fissure, où la valeur moyenne de $w_{cr\text{-}exp}/w_{cr\text{-}pred}$ était de 0,67 et 0,70 à 2 000 et 0,30Mn, respectivement. De même, l'ISIS-07 a fourni des prévisions sécuritaires des valeurs de largeur de fissure, en moyenne, avec un $w_{cr\text{-}exp}/w_{cr\text{-}pred}$ de 0,68 et 0,70 à 2 000 $\mu\varepsilon$ et à 0,30 Mn, respectivement.

16. L'AASHTO-18 a donné de bonnes prédictions pour le calcul de la largeur de fissure, où la valeur moyenne de $w_{cr\text{-}exp}/w_{cr\text{-}pred}$ était de 0,78 et 0,82 à 2 000 $\mu\varepsilon$ et 0,30Mn, respectivement. D'un autre côté, les valeurs de k_b de 0,8 et 1,0 pour les barres en PRF saupoudrées de sable et à rainures hélicoïdales, respectivement, fournies par la CSA S6-

19 ont donné des prédictions non conservatrices de la largeur de fissure pour les poutres en BAP léger armé de PRF (PRFV ou PRFB).

17. Les valeurs de k_b calculées à une déformation du PRF de 2 000 με, à 0,30 Mn et à des largeurs de fissure de 0,5 et 0,7 mm étaient assez proches pour les poutres en BAP léger. Par conséquent, n'importe lequel de ces niveaux de charge peut être utilisé comme niveaux recommandés lors du calcul des valeurs k_b pour les poutres en BAP léger. De plus, les largeurs de fissure à 2 000 με et 0,30 Mn étaient inférieures à 0,7 mm dans tous les spécimens de poutres, ce qui satisfait aux exigences de la CSA S806-12 de conserver 0,7 mm comme largeur de fissure maximale dans le calcul des valeurs de k_b.
18. L'ACI 440.1R-15 et l'ISIS-07 fournissent des valeurs k_b conservatrices de 1,4 et 1,2, respectivement, pour les barres en PRF, quel que soit l'état de la surface.
19. Les valeurs moyennes de k_b étaient proches de 0,9 et 1,10 pour les barres en PRF saupoudrées de sable et à rainure hélicoïdale, respectivement. Ainsi, les valeurs k_b de 0,9 et 1,10 sont recommandées pour les barres PRF saupoudrées de sable et rainurées en hélice dans les membrures en BAP léger, respectivement.
20. L'ACI 440.1R-15 a sous-estimé les déflexions prévues des poutres en BAP léger armé de PRFB à $0,30M_n$ et $0,67\ M_n$, avec un $\delta_{exp}/\delta_{pred}$ moyen de 1,26 et 1,11, respectivement. En revanche, CSA S806-12 a fourni des prévisions raisonnables à $0,30M_n$ et $0,67\ M_n$, où la moyenne $\delta_{exp}/\delta_{pred}$ était de 0,95 et 1,04, respectivement.
21. Le modèle ACI 440.1R-15 surestimait I_e pour les poutres en BAP léger armé de PRFV et, par conséquent, sous-estimait les déflexions à $0,30M_n$ et $0,67\ M_n$, avec une moyenne de $\delta_{exp}/\delta_{pred}$ de 1,31 et 1,26, respectivement. Les équations de Bischoff et Benmokrane et al ont donné de meilleures prédictions que le modèle ACI 440.1R-15 à $0,30M_n$ et $0,67\ M_n$, avec le $\delta_{exp}/\delta_{pred}$ moyen de 1,17 et 1,25, respectivement, à $0,30M_n$ et 1,22 et 1,23 à $0,67\ M_n$. Le modèle d'ISIS Canada, a fourni de bonnes prévisions à $0,30M_n$ et 0,67Mn, avec une moyenne de $\delta_{exp}/\delta_{pred}$ de 1,06 et 1,19, respectivement.
22. Le modèle CSA S806-12 a fourni une prédiction raisonnable pour les poutres en BAP léger armé de PRFV à $0,30\ M_n$ et a surestimé la déflexion à $0,67\ M_n$, avec une moyenne de $\delta_{exp}/\delta_{pred}$ de 1,04 et 1,18, respectivement.
23. Sur la base des résultats expérimentaux, un modèle ACI 440.1R-15 modifié a été suggéré en utilisant $0,67M_{cr}$ au lieu de M_{cr} pour prédire la déflexion réelle des spécimens BAP.

8.6 Recommandations pour les travaux futurs

Les résultats de cette recherche ont mené à une étape prometteuse vers l'utilisation de barres en PRF comme armature dans les structures en BAP léger. Les informations présentées ont aidé à la compréhension du comportement des poutres en BAP léger armé de PRF. Cependant, des recherches supplémentaires sont recommandées sur la base des conclusions de la présente étude pour couvrir les points suivants :

1. Étudier la résistance à l'effort tranchant de différents types d'éléments en BAP léger armé avec des barres en PRF avec et sans étriers.
2. Une étude expérimentale supplémentaire devrait être menée pour examiner l'impact de différents types de renforcement en PRF et de différents rapports a/d de poutres élancées et profondes sur la résistance à l'effort tranchant de membrures en BAP léger armé.
3. Étudier le comportement en flexion et les performances de service des poutres en BAP léger armé en utilisant différents types de BAP.
4. Les valeurs du coefficient d'adhérence (k_b) ont été étudiées dans cette recherche pour les poutres en BAP léger armé de PRF. Des investigations expérimentales et théoriques sont cependant recommandées avec plus d'expérimentations et de calculs pour évaluer et améliorer les valeurs k_b actuelles adoptées dans les normes sur les PRF.
5. La performance des éléments en BAP léger armé de PRF soumis à la fatigue et aux charges cycliques dans les conditions de service doit être étudiée.
6. Étudier la performance des éléments en BAP léger précontraints s avec des armatures en PRF.

References

Abdelazim, W., Mohamed, H. M., Afifi, M. Z., and Benmokrane, B. (2020). "Proposed Slenderness Limit for Glass Fiber-Reinforced Polymer-Reinforced Concrete Columns Based on Experiments and Buckling Analysis." ACI Structural Journal, 117(1).

Abdelkarim, O. I., Ahmed, E. A., Mohamed, H. M., and Benmokrane, B. (2019). "Flexural strength and serviceability evaluation of concrete beams reinforced with deformed GFRP bars." Engineering Structures, 186, 282-296.

Abed, F., Al-Mimar, M., and Ahmed, S. (2021). "Performance of BFRP RC beams using high strength concrete." Composites Part C: Open Access, 4, 100107.

Adebar, P., and Collins, M. P. (1996). "Shear strength of members without transverse reinforcement." Canadian Journal of Civil Engineering, 23(1), 30-41.

Ali, A. H., Mohamed, H. M., and Benmokrane, B. (2016). "Shear behavior of circular concrete members reinforced with GFRP bars and spirals at shear span-to-depth ratios between 1.5 and 3.0." Journal of Composites for Construction, 20(6), 04016055.

Ali, A. H., Mohamed, H. M., and Benmokrane, B. (2017a). "Strength and behavior of circular FRP reinforced concrete sections without web reinforcement in shear." Journal of Structural Engineering, 143(3), 04016196.

Ali, A. H., Mohamed, H. M., and Benmokrane, B. (2017b). "Shear Strength of Circular Concrete Beams Reinforced with Glass Fiber-Reinforced Polymer Bars and Spirals." ACI Structural Journal, 114(1).

American Association of State Highway and Transportation Officials. (2018). "AASHTO LRFD bridge design guide specifications for GFRP–reinforced concrete bridge decks and traffic railings." AASHTO (2018), Washington, D.C.

American Concrete Institute (ACI) Committee 213. (2014). "Guide for structural lightweight-aggregate concrete." ACI 213R-14, American concrete institute edition. ACI, Farmington Hills, MI.

American Concrete Institute (ACI) Committee 440. (2001). "Guide for the design and construction of concrete reinforced with FRP bars." ACI 440.1R-01, Farmington Hills, MI.

American Concrete Institute (ACI) Committee 440. (2003). "Guide for the design and construction of concrete reinforced with FRP bars." ACI 440.1R-03, Farmington Hills, MI.

American Concrete Institute (ACI) Committee 440. (2006). "Guide for the design and construction of concrete reinforced with FRP bars." ACI 440.1R-06, Farmington Hills, MI.

American Concrete Institute (ACI) Committee 440. (2015). "Guide for the design and construction of concrete reinforced with FRP bars." ACI 440.1R-15, Farmington Hills, MI.

American Concrete Institute (ACI) Committee 440. (2021). "Code requirements for structural concrete reinforced with glass fiber-reinforced polymer (GFRP) bars and commentary." ACI 440X-XX (2021), Farmington Hills, MI.

American Concrete Institute (ACI) Committee 318. (2019). "Building code requirements for structural concrete and commentary." ACI 318R-19, Farmington Hills, MI.

ASCE-ACI Committee 426. (1973). "The Shear Strength of Reinforced Concrete Members." ASCE Proceedings, Vol. 99, ST6, 1091-1187.

ASCE-ACI Committee 445 on Shear and Torsion. (1998). "Recent approaches to shear design of structures." J. Struct. Eng., 10.1061/ (ASCE) 0733-9445(1998)124:12(1375), 1375–1417.

ASTM C39/C39M-18. (2018). "Standard test method for compressive strength of cylindrical concrete specimens." ASTM International, West Conshohocken, PA.

ASTM C330/C330M-17a. (2017). "Standard specification for lightweight aggregates for structural concrete." ASTM International, West Conshohocken, PA.

ASTM C567/C567M. (2014). "Standard test Method for determining density of structural lightweight concrete." ASTM International, West Conshohocken, PA.

ASTM D7205. (2011). "Tensile properties of fiber reinforced polymer matrix composite bars." ASTM International, West Conshohocken, PA.

ASTM C496 / C496 M. (2011), "Standard test Method for splitting tensile strength of cylindrical concrete specimens." ASTM International, West Conshohocken, PA.

Bakouregui, A. S., Mohamed, H. M., Yahia, A., and Benmokrane, B. (2021). "Axial load–moment interaction diagram of full-scale circular LWSCC columns reinforced with BFRP and GFRP bars and spirals: Experimental and theoretical investigations." Engineering Structures, 242, 112538.

Benmokrane, B., Chaallal, O., and Masmoudi, R. (1996). "Flexural response of concrete beams reinforced with FRP reinforcing bars." ACI Struct. J., 93(1), 46-55.

Bischoff, P. H. (2005). "Re-evaluation of deflection prediction for concrete beams reinforced with steel and fiber reinforced polymer bars." Journal of structural engineering, 131(5), 752-767.

Bischoff, P. H., Gross, S., and Ospina, C. E. (2009). "The story behind proposed changes to ACI 440 deflection requirements for FRP-reinforced concrete." Special Publication, 264, 53-76.

Bischoff, P. H., and Gross, S. P. (2011a). “Equivalent moment of inertia based on integration of curvature.” Journal of Composites for Construction, 15(3), 263-273.

Bischoff, P. H., & Gross, S. P. (2011b). Design approach for calculating deflection of FRP-reinforced concrete. Journal of composites for construction, 15(4), 490-499.

Bischoff, P.H., 2018. "A Plea for Unified Deflection Calculation of Reinforced Concrete Flexural Members," CSCE 2018 6th International Specialty Conference, Fredericton, NB, June 13-16, ST11-1/8.

British Standards Institution (BSI). (1985). “Structural use of concrete: Code of practice for design and construction.” BS 8110-85, London.

Canadian Standards Association (CSA). (2012) – Re-approved in 2017 –. “Design and construction of building components with fiber reinforced polymers.” CSA S806-12. Rexdale, Ontario, Canada.

Canadian Standards Association (CSA). (2019). “Canadian highway bridge design code.” CSA S6-19, Rexdale, Ontario, Canada.

Canadian Standards Association (CSA). (2019). “Specification for fibre-reinforced polymers.” CSA S807-19, Rexdale, Ontario, Canada.

Canadian Standards Association (CSA). (2019). “Design of concrete structures.” CSA A23.3-19, Mississauga, Ontario, Canada.

Clark, J. L., (1993). “Structural lightweight aggregate concrete.” Blackie Academic and Professional, London.

Collins, M. P., and Mitchell, D. (1997). “Prestressed concrete structures.” Response Publications. Toronto, Canada, ISBN 0 9681958 0 6, 766p.

Elgabbas, F., Ahmed, E. A., and Benmokrane, B. (2015). “Physical and mechanical characteristics of new basalt-FRP bars for reinforcing concrete structures.” Construction and Building Materials, 95, 623-635.

Elgabbas, F., Vincent, P., Ahmed, E. A., and Benmokrane, B. (2016). “Experimental testing of basalt fiber-reinforced polymer bars in concrete beams.” Composites Part B: Engineering, 91, 205-218.

Elgabbas, F., Ahmed, E. A., and Benmokrane, B. (2017). “Flexural behavior of concrete beams reinforced with ribbed basalt-FRP bars under static loads.” Journal of Composites for Construction, 21(3), 04016098.

El-Nemr, A., Ahmed, E. A., and Benmokrane, B. (2013). "Flexural Behavior and Serviceability of Normal-and High-Strength Concrete Beams Reinforced with Glass Fiber-Reinforced Polymer Bars." ACI structural journal, 110(6).

El-Nemr, A., Ahmed, E. A., Barris, C., and Benmokrane, B. (2016). "Bond-dependent coefficient of glass-and carbon-FRP bars in normal-and high-strength concretes." Construction and Building Materials, 113, 77-89.

El-Nemr, A., Ahmed, E. A., El-Safty, A., and Benmokrane, B. (2018). "Evaluation of the flexural strength and serviceability of concrete beams reinforced with different types of GFRP bars." Engineering Structures, 173, 606-619.

El Refai, A., and Abed, F. (2015). "Concrete contribution to shear strength of beams reinforced with basalt fiber-reinforced bars." Journal of Composites for Construction, 20(4), 04015082.

El-Salakawy, E. F., and Benmokrane, B. (2004). "Serviceability of concrete bridge deck slabs reinforced with FRP composite bars." ACI Structural Journal, 101(5), 727-736.

El-Sayed, A. K., El-Salakawy, E. F., and Benmokrane, B. (2006). "Shear strength of FRP-reinforced concrete beams without transverse reinforcement." ACI Structural Journal, 103(2), 235.

El-Sayed, A. K., and Benmokrane, B. (2008). "Evaluation of the new Canadian highway bridge design code shear provisions for concrete beams with fiber-reinforced polymer reinforcement." Canadian Journal of Civil Engineering, 35(6), 609-623.

Frosch, R. J. (1999). "Another look at cracking and crack control in reinforced concrete." ACI Struct. J., 96(3), 437–442.

Gao, D., Masmoudi, R., and Benmokrane, B. (1998). "A calculating method of flexural properties of FRP-reinforced concrete beam: Part 1: crack-width and deflection." Technical Report, Department of Civil engineering, University of Sherbrooke, Sherbrooke, Quebec, Canada, 24p.

Gergely, P., and Lutz, L. A. (1968). Maximum crack width in RC flexural members, causes, mechanism and control of cracking in concrete. SP20, American Concrete Institute, 87-117.

Gerritse, A. (1981). "Design considerations for reinforced lightweight concrete." International Journal of Cement Composites and Lightweight Concrete, 3(1), 57-69.

Hadhood, A., Mohamed, H. M., Ghrib, F., and Benmokrane, B. (2017). "Efficiency of glass-fiber reinforced-polymer (GFRP) discrete hoops and bars in concrete columns under combined axial and flexural loads." Composites Part B: Engineering, 114, 223-236.

Hadhood, A., Mohamed, H. M., and Benmokrane, B. (2018). “Flexural stiffness of GFRP-and CFRP-RC circular members under eccentric loads based on experimental and curvature analysis.” ACI Structural Journal, 115(4), 1185-1198.

Hadhood, A., Mohamed, H. M., Benmokrane, B., Nanni, A., and Shield, C. K. (2019). “Assessment of design guidelines of concrete columns reinforced with glass fiber-reinforced polymer bars.” ACI Structural Journal, 116(4), 193-207.

Henin, E., Tawadrous, R., and Morcous, G. (2019). “Effect of surface condition on the bond of Basalt Fiber-Reinforced Polymer bars in concrete.” Construction and Building Materials, 226, 449-458.

Hossain, K. M. A. (2004a). “Properties of volcanic pumice based cement and lightweight concrete.” Cement and concrete research, 34(2), 283-291.

Hossain, K. M. A. (2004b). “Properties of volcanic scoria based lightweight concrete.” Magazine of Concrete Research, 56(2), 111-120.

Hossain, K. M. A., Sathiyamoorthy, K., Manzur, T., and Lotfy, A. (2020). “Shear Behavior of Lightweight Slag Aggregate Self-Consolidating Concrete Beams.” ACI Structural Journal, 117(5), 259-268.

Hoult, N. A., Sherwood, E. G., Bentz, E. C., and Collins, M. P. (2008). “Does the use of FRP reinforcement change the one-way shear behavior of reinforced concrete slabs?.” Journal of Composites for Construction, 12(2), 125-133.

Hubertova, M., and Hela, R. (2007). “The effect of metakaolin and silica fume on the properties of lightweight self consolidating concrete.” ACI Materials Journal, American Concrete Institute, Detroit, 243, 35-48.

Hwang, C. L., and Hung, M. F. (2005). “Durability design and performance of self-consolidating lightweight concrete.” Construction and building materials, 19(8), 619-626.

ISIS Canada Research Network (2007). “Reinforced Concrete Structures with Fibre Reinforced Polymers” ISIS Manual No.3, University of Manitoba, Winnipeg, MB, Canada.

Issa, M. A., Ovitigala, T., and Ibrahim, M. (2015). “Shear behavior of basalt fiber reinforced concrete beams with and without basalt FRP stirrups.” Journal of Composites for Construction, 20(4), 04015083.

Jaeger, L. G., Mufti, A. A., and Tadros, G. (1997, October). “The concept of the overall performance factor in rectangular-section reinforced concrete members.” In Proceedings of the 3rd International Symposium on Non-Metallic (FRP) Reinforcement for Concrete Structures, Sapporo, Japan (Vol. 2, pp. 551-559).

Japan Society of Civil Engineers (JSCE). (1997). "Recommendations for design and construction of concrete structures using continuous fiber reinforced materials." Research committee on continuous fiber reinforced materials, A. Machida, ed., Tokyo.

Kassem, C., Farghaly, A. S., and Benmokrane, B. (2011). "Evaluation of flexural behavior and serviceability performance of concrete beams reinforced with FRP bars." Journal of composites for construction, 15(5), 682-695.

Kim, C. H., and Jang, H. S. (2014). "Concrete shear strength of normal and lightweight concrete beams reinforced with FRP bars." Journal of Composites for Construction, 18(2), 04013038.

Kuchma, D. A., and Collins, M. P. (1998). "Advances in understanding shear performance of concrete structures." Progress in Structural Engineering and Materials, 1(4), 360-369.

Liu, R., and Pantelides, C. P. (2013). "Shear strength of GFRP reinforced precast lightweight concrete panels." Construction and Building Materials, 48, 51-58.

Liu, X., Sun, Y., Wu, T., and Liu, Y. (2020). "Flexural cracks in steel fiber-reinforced lightweight aggregate concrete beams reinforced with FRP bars." Composite Structures, 253, 112752.

MacGregor, J. G., and Wight, J. K. (2005). "Reinforced concrete: Mechanics and design." 4th Ed., Prentice-Hall, Upper Saddle River, NJ.

Machial, R., Alam, M. S., and Rteil, A. (2010). "Shear strength contribution of transverse FRP reinforcement in bridge girders." In Proceedings of the IABSE-JSCE Joint Conference on Advances in Bridge Engineering-II.

Maranan, G. B., Manalo, A. C., Benmokrane, B., Karunasena, W., and Mendis, P. (2015). "Evaluation of the flexural strength and serviceability of geopolymer concrete beams reinforced with glass-fibre-reinforced polymer (GFRP) bars." Engineering Structures, 101, 529-541.

McCallum, B. (2013). "Experimental evaluation of the bond dependent coefficient and parameters which influence crack width in GFRP reinforced concrete." M.S. thesis, Dept. of Civil and Resource Engineering, Dalhousie Univ.

McSaveney, L. G. (2000). "The Wellington Stadium, New Zealand.s first use of high strength lightweight precast concrete." Proc. 2nd Int. Symp. Structural Lightweight Aggregate Concrete, Kristiansand, Norway, pp. 385.395.

Mehany, S., Mohamed, H. M., and Benmokrane, B. (2019). "Strength and behavior of HSC concrete beams reinforced with sand-coated basalt FRP bars." Proceedings of the Canadian Society for Civil Engineering (CSCE), Annual Conference, QC, Canada.

Mehany, S., Mohamed, H. M., & Benmokrane, B. (2021). Contribution of lightweight self-consolidated concrete (LWSCC) to shear strength of beams reinforced with basalt FRP bars. Engineering Structures, 231, 111758.

Mehta, P. K. et Monteiro, P. J. M. (2013). “Concrete: microstructure, properties, and materials, 4e édition.” McGraw-Hill Education, New York.

Mindess, S., Young, J. F., and Darwin, D. (2002). “Concrete, 2nd edition.” Pearson, Upper Saddle River, NJ.

Mohamed, H. M., and Benmokrane, B. (2014). “Design and performance of reinforced concrete water chlorination tank totally reinforced with GFRP bars:” Case study. Journal of Composites for Construction, 18(1), 05013001.

Mota, C., Alminar, S., and Svecova, D. (2006). Critical review of deflection formulas for FRP-RC members. Journal of Composites for Construction, 10(3), 183-194.

Mousa, S., Mohamed, H. M., and Benmokrane, B. (2019). Strength and deformability aspects of circular concrete members reinforced with hybrid carbon-FRP and glass-FRP under flexure. Journal of Composites for Construction, 23(2), 04019005.

Naaman, A. E., and JEONG, M. (1995). “Structural ductility of concrete beams prestressed with FRP tendons.” In Non-Metallic (FRP) Reinforcement for Concrete Structures: Proceedings of the Second International RILEM Symposium (Vol. 29, p. 379). CRC Press.

Newhook, J., Ghali, A., and Tadros, G. (2002). “Concrete flexural members reinforced with fiber reinforced polymer: design for cracking and deformability.” Canadian Journal of Civil Engineering, 29 (1), 125-134.

Okamura, H., and Ouchi, M. (2003). “Self-compacting concrete.” Journal of advanced concrete technology, 1(1), 5-15.

Ospina, C. E., and Bakis, C. E. (2007). “Indirect flexural crack control of concrete beams and one-way slabs reinforced with FRP bars.” Proceedings of FRPRCS, 8.

Ovitigala, T., and Issa, M. (2013). “Mechanical and bond strength of basalt fiber reinforced polymer (BFRP) bars for concrete structures.” Proc., 11th Int. Symp. on Fiber Reinforced Polymer for Reinforced Concrete Structures (FRPRCS-11), J. Barros, and J. Sena-Cruz, eds., Univ. of Minho, Guimaraes, Portugal, 10, 10.

Pantelides, C. P., Besser, B. T., and Liu, R. (2012a). “One-way shear behavior of lightweight concrete panels reinforced with GFRP bars.” Journal of Composites for Construction, 16(1), 2-9.

Pantelides, C. P., Liu, R., and Reaveley, L. D. (2012b). "Lightweight concrete precast bridge deck panels reinforced with glass fiber-reinforced polymer bars." ACI Structural Journal, 109(6), 879.

Razaqpur, A. G., Isgor, B. O., Greenaway, S., and Selley, A. (2004). "Concrete contribution to the shear resistance of fiber reinforced polymer reinforced concrete members." Journal of Composites for Construction, 8(5), 452-460.

Razaqpur, A. G., and Isgor, O. B. (2006). "Proposed shear design method for FRP-reinforced concrete members without stirrups." ACI Structural Journal, 103(1), 93.

Razaqpur, A. G., Shedid, M., and Isgor, B. (2011). "Shear strength of fiber-reinforced polymer reinforced concrete beams subject to unsymmetric loading." Journal of Composites for Construction, 15(4), 500-512.

Reineck, K. H. (1991). "Ultimate shear force of structural concrete members without transverse reinforcement derived from a mechanical model." Structural Journal, 88(5), 592-602.

Roy, B. K. B. (1995). "Lightweight aggregate concrete in UK." Proc. 1st Int. Symp. Structural Lightweight Aggregate Concrete, Sandfjörd, Norway, pp. 52.69.

Sanni, B. A., Mohamed, H. M., Yahia, A., and Benmokrane, B. (2021). "Behavior of Lightweight Self-Consolidating Concrete Columns Reinforced with Glass Fiber-Reinforced Polymer Bars and Spirals under Axial and Eccentric Loads." ACI Structural Journal, 118(3), 241-254.

Sathiyamoorthy, K. (2016). "Shear and flexural behavior of lightweight self-consolidating concrete beams." M.Sc. Thesis, Department of Civil Engineering, Ryerson University, Toronto, Canada, 106 pp.

Shideler, J. J., (1957). "Lightweight aggregate concrete for structural use." ACI Journal Proceedings, V. 54, No. 10, Oct., pp. 298-328.

Shi C. and Wu Y. (2005). "Mixture proportioning and properties of self-consolidating lightweight concrete containing glass powder." ACI Materials Journal, Vol. 102, No. 5, pp.355–63.

Shield, C., Brown, V., Bakis, C. E., and Gross, S. (2019). "A recalibration of the crack width bond-dependent coefficient for GFRP-reinforced concrete." Journal of Composites for Construction, 23(4), 04019020.

Shioya, T., Iguro, M., Nojiri, Y., Akiyama, H., and Okada, T. (1989). “Shear strength of large reinforced concrete beams. Fracture Mechanics: Application to Concrete.” SP 118, American Concrete Institute, Detroit, 309 pp.

Soltanzadeh, F., Edalat-Behbahani, A., Barros, J. A., and Mazaheripour, H. (2016). “Effect of fiber dosage and prestress level on shear behavior of hybrid GFRP-steel reinforced concrete I-shape beams without stirrups.” Composites Part B: Engineering, 102, 57-77.

Taylor, H. P. J. (1970). “Investigation of the forces carried across cracks in reinforced concrete beams in shear by interlock of aggregate.” Cement and Concrete Association, London, England.

Theriault, M., and Benmokrane, B. (1998). “Effects of FRP reinforcement ratio and concrete strength on flexure behavior of concrete beams.” J. Compos. Constr., 2(1), 7-16.

Tomlinson, D., and Fam, A. (2015). “Performance of concrete beams reinforced with basalt FRP for flexure and shear.” Journal of composites for construction, 19(2), 04014036.

Toutanji H. A. and Saafi M. (2000). “Flexural behavior of concrete beams reinforced with glass fiber-reinforced polymer (GFRP) bars.” ACI Struct. J., 97(5), 712-719.

Toutanji H. and Deng Y. (2003). “Deflection and crack-width prediction of concrete beams reinforced with glass FRP rods.” J. Constr. Build. Mater.,17, 69-74.

Tureyen, A. K., and Frosch, R. J. (2002). “Shear tests of FRP-reinforced concrete beams without stirrups.” ACI Struct. J., 99(4), 427–434.

Vecchio, F. J., and Collins, M. P. (1986). “The Modified Compression Field Theory for Reinforced Concrete Elements Subjected to Shear.” ACI Structural Journal, Marc/April, 219-231.

Wang, H. Y. (2009). “Durability of self-consolidating lightweight aggregate concrete using dredged silt.” Construction and building materials, 23(6), 2332-2337.

Wei, B., Hailin, C., and Shenhua, S. (2010). “Environmental resistance and mechanical performance of basalt and glass fibers.” Mater. Sci. Eng. A, 527(18–19), 4708–4715.

Wight J.K. and Macgregor J.G. (1997). “Reinforced concrete mechanics and design, sixth edition.” Upper Saddle River, NJ, Prentice Hall, U.S.A, pp.1143.

Wu, G., Dong, Z. Q., Wang, X., Zhu, Y., and Wu, Z. S. (2015). “Prediction of long-term performance and durability of BFRP bars under the combined effect of sustained load and corrosive solutions.” Journal of Composites for Construction, 19(3), 04014058.

Wu, T., Sun, Y., Liu, X., and Wei, H. (2019). "Flexural behavior of steel fiber–reinforced lightweight aggregate concrete beams reinforced with glass fiber–reinforced polymer bars." Journal of Composites for Construction, 23(2), 04018081.

Xiao, L., Liu, Q., and Li, J. (2016). "Basalt fiber on cinder strength of lightweight aggregate concrete." In 2016 2nd International Conference on Advances in Energy, Environment and Chemical Engineering (AEECE 2016). Atlantis Press.

Yost, J. R., Gross, S. P., and Dinehart, D. W. (2001). "Shear strength of normal strength concrete beams reinforced with deformed GFRP bars." Journal of composites for construction, 5(4), 268-275.

Appendix. Example: Bond-dependent coefficient (k_b)

A simply supported beam with a cross-sectional width and height of 200 mm and 300 mm, respectively, was tested up to failure. The beam was reinforced with three No. 5 GFRP bars as longitudinal reinforcement.

The GFRP bars had a helically grooved surface with a diameter of 15.9 mm and E_f = 59,500 MPa. The clear concrete cover was 38 mm. Determine the bond-dependent coefficient at the service load of $0.30M_n$ using ACI 440.1R-15, AASHTO-18, and CSA S6-19. The ε_f and ε_c at $(M_s=0.30M_n)$ =0.0037 and 0.001045, respectively.

Given:

b = 200 mm, h = 300 mm, c = 38 mm.

E_f = 59500 MPa, # *bars*= 3 bars, d_b= 15.9 mm.

At $M_s=0.30M_n$: w_{cr} = 0.53 mm, ε_f = 0.0037, ε_c = 0.001045.

Solution:

$$d = h - c - (d_b / 2) = 300 - 38 - (15.9 / 2) = 254.05 \text{ mm}$$

$$z = \frac{\varepsilon_c d}{\varepsilon_f + \varepsilon_c} = \frac{0.001045 \times 254.05}{0.0037 + 0.001045} = 55.95 \text{ mm}$$

$$d_c = c + (d_b / 2) = 38 + (15.9 / 2) = 45.95 \text{ mm}$$

$$h_2 = h - z = 300 - 55.95 = 244.05 \text{ mm}$$

$$h_1 = h_2 - d_c = 244.05 - 45.95 = 198.10 \text{ mm}$$

s_{max} = (200-50-20-15.9)/2= 57.05 mm

$$f_{fs} = E_f \times \varepsilon_f = 59500 \times 0.0037 = 220.15 \text{ MPa}$$

ACI 440.1R-15

$$k_b = \frac{1.15 E_f w}{(s_{\max} + 2.5c_c) f_{fs}}$$

$$k_b = \frac{1.15 \times 59500 \times 0.53}{(57.05 + 2.5 \times 38) \times 220.15} = 1.08$$

Check (1):

$$s_{\max} \le 0.92 \frac{E_f}{f_{fs}} \frac{w}{k_b}$$

$$57.05 \text{ mm} \le 0.92 \times \frac{59500}{220.15} \times \frac{0.53}{1.08}$$

57.05 mm < 122.02 mm OK.

Check (2):

$$d_c \le \frac{E_f w}{2 f_{fs} \beta k_b}$$

$$\beta = \frac{h_2}{h_1} = \frac{244.05}{198.10} = 1.23$$

$$45.95 \text{ mm} \le \frac{59500 \times 0.53}{2 \times 220.15 \times 1.23 \times 1.08}$$

45.95 mm < 54.0 mm OK.

AASHTO-18

$$k_b = \frac{1}{C_b} = \frac{1.15 E_f w}{(s_{\max} + 2.5 c_c) f_{fs}}$$

$$k_b = \frac{1}{C_b} = \frac{1.15 \times 59500 \times 0.53}{(57.05 + 2.5 \times 38) \times 220.15} = 1.08$$

Check (1):

$$s_{\max} \le 0.92 \frac{C_b E_f w}{f_{fs}}$$

$$57.05 \text{ mm} \leq 0.92 \times \frac{0.93 \times 59500 \times 0.53}{220.15}$$

57.05 mm < 122.02 mm OK.

Check (2):

$$d_c \leq \frac{C_b E_f w}{2 f_{fs} \xi}$$

$$\xi = \frac{h - kd}{d - kd} = \frac{244.05}{198.10} = 1.23$$

$$45.95 \text{ mm} \leq \frac{0.93 \times 59500 \times 0.53}{2 \times 220.15 \times 1.23}$$

45.95 mm < 54.0 mm OK.

CSA S6-19

$$k_b = \frac{w_{cr}}{2 \frac{f_f}{E_f} \frac{h_2}{h_1} \sqrt{d_c^2 + (s/2)^2}}$$

$$k_b = \frac{0.53}{2 \times \frac{220.15}{59500} \times \frac{244.05}{198.10} \times \sqrt{45.95^2 + (57.05/2)^2}} = 1.07$$